UNIVERSITY OF CALIFORNIA, SAN DIEGO

The Importance of Latent Inputs for Analyzing the Human Brain

A dissertation submitted in partial satisfaction of the
requirements for the degree
Doctor of Philosophy

in

Electrical Engineering (Signal and Image Processing)

by

Anup Das

Committee in charge:

Professor Kenneth Kreutz-Delgado, Co-Chair
Professor Terrence J. Sejnowski, Co-Chair
Professor Vikash Gilja
Professor Eric Halgren
Professor Paul H. Siegel

2018

The dissertation of Anup Das is approved, and it is acceptable in quality and form for publication on microfilm and electronically:

_____

_____

_____

_____
Co-Chair

_____
Co-Chair

University of California, San Diego

2018

DEDICATION

To my parents.

TABLE OF CONTENTS

LIST OF FIGURES

LIST OF TABLES

ACKNOWLEDGEMENTS

First of all, I would like thank God who makes everything possible. And, my parents, Mr. Pravat Kumar Das and Mrs. Anupama Das, who brought me into this world and all the family members for their love and support. I was very lucky to have professor Terrence J. Sejnowski as my advisor and this thesis would not have been possible without him. I am also thankful to my committee members who gave valuable feedback on the research in this thesis. I would also like to thank Dr. Sydney S. Cash who generously provided the electrocorticography recordings for analysis in my thesis. I also thank Dr. David J. C. MacKay for interesting discussions on the spring-mass model, Dr. John C. Doyle for discussions on the precision matrix and the RC circuit models, Dr. Mark A. Kramer and Dr. Giovanni Piantoni for discussions on the preprocessing steps in the electrocorticography recordings, and Dr. Giovanni Piantoni for his help in using the FieldTrip toolbox. Also thanks to all the professors in the department of electrical and computer engineering, University of California, San Diego under whom I finished all my course work and who have helped me in my academics through out my stay here at the University of California, San Diego. Last, but not least, I would like to thank all the members of the computational neurobiology laboratory whose help and encouragement significantly improved the quality of this thesis.

Chapter 2.1, in full, and chapter 3, in full, are reprints of some of the material in Das, Anup; Sampson, Aaron L.; Lainscsek, Claudia; Muller, Lyle; Lin, Wutu; Doyle, John C.; Cash, Sydney S.; Halgren, Eric; Sejnowski, Terrence J.,"Interpretation of the precision matrix and its application in estimating sparse brain connectivity during sleep spindles from human electrocorticography recordings," Neural Computation, vol. 29, no. 3, pp. 603–642, 2017. The author of this thesis was the primary author of this material.

Chapter 2.2, in full, and chapter 4, in part, are currently being prepared for submission for possible publication of some of the material in Das, Anup; Sexton, Daniel; Lainscsek, Claudia; Cash, Sydney S.; Sejnowski, Terrence J.,"Characterizing brain connectivity during epileptic seizures from human electrocorticography recordings with unobserved inputs". The author of this thesis is the primary author of this material.

VITA

2013	B. Tech. Electrical Engineering (Signal Processing), Indian Institute of Technology
2015	M. S. Electrical Engineering (Signal and Image Processing), University of California, San Diego, William S. Hodgkiss, Ph. D.
2016	C. Ph. Electrical Engineering (Signal and Image Processing), University of California, San Diego, Terrence J. Sejnowski, Ph. D.
2018	Ph. D. Electrical Engineering (Signal and Image Processing), University of California, San Diego, Terrence J. Sejnowski, Ph. D.

ABSTRACT OF THE DISSERTATION

The Importance of Latent Inputs for Analyzing the Human Brain

by

Anup Das

Doctor of Philosophy in Electrical Engineering (Signal and Image Processing)

University of California, San Diego, 2018

Professor Kenneth Kreutz-Delgado, Co-Chair
Professor Terrence J. Sejnowski, Co-Chair

In human brain imaging studies, researchers have predominantly used the correlation method to estimate the "functional connectivity". However, spurious correlations can be measured between two brain regions without even having direct connection or interaction between them. This high correlation can be due to the strong interactions of the two brain regions with common input from a third region which may or may not be observed. One previously proposed solution to this problem is to use a sparse-regularized inverse covariance matrix or precision matrix (SRPM) when all the regions are observed. The SRPM method yields partial correlations to measure strong direct interactions between pairs of observed regions while simultaneously removing the influence of the rest of the observed regions thus identifying observed regions that are conditionally independent.

However, in most brain studies, especially in electrocorticography (ECoG), simultaneously recording all brain regions is a near impossible task using existing imaging technologies. Hence researchers have recently proposed to use a sparse-plus-latent-regularized precision matrix (SLRPM) when there are unobserved or latent regions interacting with the observed regions. The SLRPM method yields partial correlations of the conditional statistics of the observed regions given the latent regions thus identifying observed regions that are conditionally independent of both the observed and latent regions.

In the first contribution of the thesis, we evaluate the performance of the SRPM and SLRPM methods using simple artificial networks. In the second contribution of the thesis, we demonstrate the application of the SRPM method for estimating brain connectivity during stage 2 sleep spindles from human ECoG recordings from a patient with complex partial epilepsy. We only consider sleep spindles occurring in long seizure-free periods. Sleep spindles are automatically detected using delay-differential analysis (DDA), then analyzed with SRPM and the Louvain method for community detection (LMCD). The performance of the SLRPM method is found to be similar to that of the SRPM method for this application. In the third contribution of the thesis, we demonstrate the application of the SLRPM method to estimate brain connectivity during epileptic seizures from human ECoG recordings. Seizures from 12 patients having complex partial epilepsy were analyzed using SLRPM and brain connectivity has been quantified using modularity index (MI), clustering coefficient (CC), and eigenvector centrality (EC). These applications will enhance our understanding of the global connectivity pattern of the human brain and may help us in finding better treatments in epilepsy.

Chapter 1

Introduction

1.1 The caveat in the correlation, precision matrix (PM) and sparse-regularized precision matrix (SRPM) methods

The correlation method is the most widely used method for estimating brain functional connectivity (Biswal et al., 1995; Uddin et al., 2009; Vertes et al., 2012; Rubinov et al., 2010; Zhou et al., 2009; Anand et al., 2005; Siegle et al., 2007; Smith et al., 2011; Chu et al., 2015; Shafi et al., 2014; Lynall et al., 2010). Researchers (Biswal et al., 1995; Xiong et al., 1999; Cordes et al., 2000) have analyzed the functional connectivity of the resting state human brain from functional magnetic resonance imaging (fMRI) data using the correlation method and found functionally connected regions in the primary sensory motor cortex. Other studies (Greicius et al., 2003; Fox et al., 2006, 2005) of the resting state human brain using the correlation method have shown that the posterior cingulate cortex (PCC) and ventral anterior cingulate cortex (vACC) are functionally connected within themselves and also with each other. In (Uddin et al., 2009), researchers have identified positively correlated and anticorrelated brain networks with PCC and vACC by using the correlation method on resting state data and found significant heterogeneity within the default mode network. Authors in (Anand et al., 2005) have carried out a study, by using the correlation method, to explore the effect of antidepressant on the functional connectivity of human brain from fMRI data and found

that antidepressant treatment increases corticolimbic connectivity in depressed patients. In another study (Hampson et al., 2002) of the human brain functional connectivity in low frequency using the correlation method, researchers have found existence of connection between Broca's area and Wernicke's area in healthy subjects at rest. The authors in (Supekar et al., 2008) have analyzed brain functional connectivity in Alzheimer's disease (AD) from fMRI using the correlation method. They collected task-free fMRI data from 21 AD patients and 18 controls and found relatively low small-world properties in AD patients as compared to the healthy controls indicating disrupted organization of functional brain networks in AD.

Connectivity estimation using the correlation method can be misleading or wrong since brain regions might show high correlation due to a common input, which may or may not be measured or observed, and not due to strong physical connections between themselves (Stevenson et al., 2008; Wang et al., 2016). In a recent study (Glasser et al., 2016) of the multi-modal magnetic resonance images from 210 healthy young adults in the Human Connectome Project (HCP), researchers have been able to identify many new areas in the human cortex using a machine learning classifier. Pairs of these areas with a high degree of functional connectivity also received common input from other areas of the human brain. The authors in (Honey et al., 2009) measured the functional connectivity from fMRI in 5 individuals using the correlation method and several brain regions showed high degree of functional connectivity without having direct connections. This provides further evidence that brain regions can have high correlations due to common inputs rather than direct interactions.

Due to this major drawback of the correlation method, researchers have suggested to use *partial correlations* to measure strong direct interactions between pairs of brain regions while simultaneously removing the influence of the rest of the brain regions (Whittaker, 1990; Lauritzen, 1996; Dempster, 1972; Das et al., 2017) assuming all the regions can be measured. Partial correlations help identify pairwise brain regions which are *conditionally independent* given all the other brain regions. When the output of the brain regions follows a multivariate Gaussian distribution, the inverse covariance matrix (ICM) or precision matrix (PM) can be used to calculate these partial correlations (Dempster, 1972). A value zero or very close to zero in the PM will indicate that the

two brain regions are conditionally independent given the rest of the brain regions. Researchers (Salvador et al., 2005; Marrelec et al., 2007) have previously used the PM to estimate the human brain functional connectivity from fMRI.

However, a major drawback of the PM method is that, under the regime of relatively small number of time samples, the sample covariance matrix might not be directly invertible. Even if there are sufficient number of samples such that the sample covariance matrix is invertible, the estimated PM might produce large errors in connections in a given brain network since the sample covariance matrix is a poor estimator of the eigenvalues of the covariance matrix (Das et al., 2017). Hence researchers have proposed to use a sparse-regularized precision matrix (SRPM) to calculate the pairwise partial correlations (Friedman et al., 2008). The SRPM $\mathbf{X}$ can be estimated by solving the following L_1 regularized optimization problem

$$\underset{\mathbf{X} s.t. \mathbf{X} \succ 0}{\arg\min} \left[-\log\det(\mathbf{X}) + \mathrm{tr}(\mathbf{S}\mathbf{X}) + \lambda \|\mathbf{X}\|_1 \right] \tag{1.1}$$

where λ is the regularization parameter balancing the error in the maximum likelihood estimate (MLE) of the precision matrix and the sparsity (The MLE of the precision matrix is the inverse of the sample covariance matrix according to the invariance principle) and $\mathbf{S}$ is the sample covariance matrix. The effect of the L_1 regularization term $\lambda\|\mathbf{X}\|_1$ is twofold. First, it helps make the estimation of the precision matrix problem well posed since direct inversion of the sample covariance matrix is ill-posed when finite number of time samples is available as mentioned before. Second, since it promotes sparsity, it can incorporate this assumption while estimating the human brain network which is known to be sparse (Steriade et al., 1993; Laughlin et al., 2003). Observe that the optimization problem in (1.1) is a convex optimization problem and several algorithms (Friedman et al., 2008; Banerjee et al., 2008; Hsieh et al., 2011, 2013; Yuan et al., 2007; Oztoprak et al., 2012; Rothman et al., 2008; Scheinberg et al., 2010) have been proposed in literature for solving this optimization problem. For the analysis in this thesis, we use the QUIC algorithm (Hsieh et al., 2011, 2013) to estimate the SRPM.

Researchers in (Hsieh et al., 2011, 2013) have applied the SRPM method on a voxels data set collected from the human brain. After applying modularity-based clustering (Newman et al., 2004, 2006; Brandes et al., 2008; Blondel et al., 2008; Reichardt et al., 2006; Ronhovde et al., 2009; Sun et al., 2009; Sporns, 2010) to the regularized precision matrix, they found strong functionally connected regions in gray matter regions in the human brain along with identification of resting-state networks such as "default mode" and sensorimotor networks. The modules detected by the SRPM method were similar to those identified using independent components analysis (ICA) on the same dataset. In another study (Ryali et al., 2012), researchers have applied the SRPM method to resting state fMRI data and found a modular architecture characterized by strong inter-hemispheric links, distinct ventral and dorsal stream pathways, and a major hub in the posterior medial cortex. The authors in (Varoquaux et al., 2010) analyzed human brain functional connectivity using the SRPM method and after clustering, found regions corresponding to important brain areas such as the primary visual system (medial visual areas), the dorsal visual pathway, the occipital pole and the intra-parietal areas comprising the default mode network, the fronto-parietal networks, the ventral visual pathway, the lateral visual areas, and the inferior temporal lobe. Researchers in (Monti et al., 2014) have analyzed human brain functional connectivity using the SRPM method in healthy patients and found that the Right Inferior Frontal Gyrus and the Right Inferior Parietal lobe play a key role in the attention and executive function during cognitively demanding tasks and may be fundamental in regulating the balance between other brain regions. Researchers (Rosa et al., 2015) also have applied the SRPM method to distinguish patients with major depressive disorder from healthy control subjects by analyzing brain functional connectivity from fMRI data. The authors in (Allen et al., 2012) have analyzed brain functional connectivity using SRPM and clustering algorithms from resting state data in young adults and found connections between regions in lateral parietal and cingulate cortex. They also found that the dynamic functional connectivity of the human brain was markedly different than the stationary brain connectivity. The SRPM method has also been used to estimate the brain functional connectivity at a neuronal level in the mouse visual cortex in (Yatsenko et al., 2015) where it found more biologically plausible brain networks

than the correlation method. In another research (Wang et al., 2016), the authors have applied the SRPM method to estimate human brain functional connectivity from fMRI data and compared it with the same estimated by the correlation method. They found that the SRPM method was able to remove considerable between-module connections which were estimated by the correlation method. In particular, 34% of the significant connections found in the correlation method became insignificant after calculating the partial correlations from the SRPM method. Recently, (Glasser et al., 2016), using multi-modal magnetic resonance images of the human cerebral cortex from 210 healthy young adults, found 97 new cortical areas, along with 83 previously existing cortical areas, using the SRPM method. The authors concluded that their study presents a picture of the structural and functional organization of the human cerebral cortex and its variation across individuals and in development, aging, and disease.

Even though the application of the SRPM method to identify functionally connected networks in the human brain is promising, one major shortcoming of this method is that it assumes that all the brain regions are measurable or observed. This assumption might lead to incorrect estimation of brain connectivity since most brain regions remain unobserved (also known as latent regions) using current imaging technologies, especially in electrocorticography (ECoG) recordings, which are used in our analysis.

1.2 Proposed method – the sparse-plus-latent regularized precision matrix (SLRPM) method

Hence researchers (Chandrasekaran et al., 2012) have recently proposed to use a sparse-plus-latent-regularized precision matrix (SLRPM) when there are unobserved or latent regions interacting with the observed regions which is typical of brain imaging. The SLRPM method yields partial correlations of the conditional statistics of the observed regions given the latent regions thus identifying observed regions that are conditionally independent of both the observed and latent regions. Here we assume that the observed and latent variables jointly follow a multivariate

Gaussian distribution. Also assume that we have p number of observed variables and h number of latent variables. Let the covariance matrix $\mathbf{\Sigma}$ of this joint distribution be represented by

$$\mathbf{\Sigma} = \begin{bmatrix} \mathbf{\Sigma}_P & \mathbf{\Sigma}_{P,H} \\ \mathbf{\Sigma}_{H,P} & \mathbf{\Sigma}_H \end{bmatrix} \tag{1.2}$$

where $\mathbf{\Sigma}_P$ is of dimension $p \times p$ representing the covariances of the observed variables, $\mathbf{\Sigma}_{P,H}$ is of dimension $p \times h$ representing the covariances between the observed and latent variables, and $\mathbf{\Sigma}_H$ is of dimension $h \times h$ representing the covariances of the latent variables. Let the inverse $\mathbf{\Sigma}^{-1}$ of this covariance matrix be represented by

$$\mathbf{\Sigma}^{-1} \triangleq \mathbf{K} = \begin{bmatrix} \mathbf{K}_P & \mathbf{K}_{P,H} \\ \mathbf{K}_{H,P} & \mathbf{K}_H \end{bmatrix} \tag{1.3}$$

where $\mathbf{K}_P$ is of dimension $p \times p$ representing the dependencies of the observed variables, $\mathbf{K}_{P,H}$ is of dimension $p \times h$ representing the dependencies between the observed and latent variables, and $\mathbf{K}_H$ is of dimension $h \times h$ representing the dependencies of the latent variables. The marginal precision matrix $\mathbf{\Sigma}_P^{-1}$ of the observed variables can be given by the Schur complement w.r.t. to $\mathbf{K}_H$ as (Chandrasekaran et al., 2012)

$$\widetilde{\mathbf{K}}_P \triangleq \mathbf{\Sigma}_P^{-1} = \mathbf{K}_P - \mathbf{K}_{P,H}\mathbf{K}_H^{-1}\mathbf{K}_{H,P}. \tag{1.4}$$

The matrix $\mathbf{K}_P$ is the precision matrix of the conditional statistics of the observed variables given the latent variables. Hence if the underlying brain network is sparse, then $\mathbf{K}_P$ is a sparse matrix. The matrix $\mathbf{K}_{P,H}\mathbf{K}_H^{-1}\mathbf{K}_{H,P}$ summarizes the effect of marginalization over the latent variables. Note that the rank of $\mathbf{K}_{P,H}\mathbf{K}_H^{-1}\mathbf{K}_{H,P}$ can be at most h and hence it will be of small rank if the number of latent variables is relatively small. Thus the marginal precision matrix $\widetilde{\mathbf{K}}_P$ is not sparse, in general, due to the presence of the term $\mathbf{K}_{P,H}\mathbf{K}_H^{-1}\mathbf{K}_{H,P}$ and the SRPM method for the observed variables might not be able to correctly identify the brain connectivity. Since from (1.4), the marginal precision

matrix is decomposed as a sum of a sparse matrix and a low rank matrix, we will impose the L_1 norm on the precision matrix of the conditional statistics (also known as the SLRPM) and nuclear norm on the low rank matrix. The SLRPM $\mathbf{X}$ can be estimated by solving the following regularized optimization problem

$$\underset{\mathbf{X},\mathbf{L}\, s.t\, \mathbf{X}-\mathbf{L}\succ 0, \mathbf{L}\succeq 0}{\arg\min} [-\log\det(\mathbf{X}-\mathbf{L}) + \mathrm{tr}(\mathbf{S}(\mathbf{X}-\mathbf{L})) + \alpha\|\mathbf{X}\|_1 + \beta\,\mathrm{tr}(\mathbf{L})] \tag{1.5}$$

where α and β are the regularization parameters balancing the error in the likelihood and the sparse and low rank terms and $\mathbf{S}$ is the sample covariance matrix. In (1.5), $\mathbf{X}$ provides an estimate of the sparse matrix $\mathbf{K}_P$ and $\mathbf{L}$ provides an estimate of the low rank matrix $\mathbf{K}_{P,H}\mathbf{K}_H^{-1}\mathbf{K}_{H,P}$. The L_1 regularization term $\alpha\|\mathbf{X}\|_1$ imposes sparsity on the underlying brain connectivity and the trace or nuclear norm regularization term $\beta\,\mathrm{tr}(\mathbf{L})$ imposes low rankness on the common inputs from the latent or unobserved brain regions. Furthermore, these regularizations make the optimization problem well behaved when we have finite number of samples. Observe that the optimization problem in (1.5) is a convex optimization problem and we use the alternating direction method of multipliers (ADMM) (Ma et al., 2013) to estimate the SLRPM for our analysis. Note that the SRPM and SLRPM have to be normalized to obtain the partial correlations (Whittaker, 1990).

1.3 Prior research on human brain connectivity estimation using the SLRPM method

Research on the application of the SLRPM method on brain functional connectivity estimation has been limited and the author of this thesis is not aware of any comprehensive analysis on the application of the SLRPM method for human brain connectivity estimation. To the best of the author's knowledge, the only comprehensive analysis of the SLRPM method has been done by researchers in (Yatsenko et al., 2015) where they have applied the method to infer connectivity in the mouse visual cortex. Their simulation results showed that the SLRPM method has the potential

to outperform both the correlation method and the SRPM method. However, there was a major flaw in their simulations. They generated the data from the same optimization problem that they solved to estimate the connectivity matrix for the SRPM and SLRPM methods. A more reasonable way to these analyses is to generate data independently of the methods and then validate the methods by estimating the connectivity matrices from the data. This was the approach taken in our simulations for validating the methods. From the experimental analysis using 3D random-access laser scanning microscopy of calcium signals in the mouse visual cortex, the authors found more physiologically interpretable functionally connected brain regions by the SLRPM method than the correlation and SRPM methods. Our effort in this thesis on the use of the SLRPM method to characterize brain connectivity in humans from ECoG recordings is the first.

1.4 First contribution – simple artificial networks to evaluate the performance of the methods

In the first contribution of the thesis, we evaluate the performance of the SRPM and SLRPM methods via simulation using simple artificial networks. We first demonstrate conditions under which the SRPM method can indeed find the true physical connection between a pair of nodes using synthetic data from two physical models: (i) a mechanical model which considers a cascade connection of a number of springs and masses, and (ii) an electrical circuit model which consists of resistors (R) and capacitors (C), assuming that all the nodes can be observed. The purpose here is to demonstrate that the connectivity pattern of the spring-mass model can be obtained from the SRPM associated with the displacements of the masses and the connectivity pattern of the RC circuit model can be obtained from the SRPM associated with the voltages measured at the nodes. The SRPM method is shown to give superior performance compared with the correlation and PM methods and is also able to find the ground truth connection. In other words, it is shown that the correlation and PM methods may not be able to recover the true connectivity of the associated network in the simulated models in contrast to the SRPM method. Note that PM and SRPM have to be normalized

to obtain the partial correlations (Whittaker, 1990). The recovery of the connectivity structure via the SRPM method can be explained by energy models using the Boltzmann distribution. This shows that theoretically if PM can estimate the connectivity structure between regions under consideration, then the SRPM method should be used to estimate the regularized version of PM to avoid false positive and false negative connections when a finite number of samples is available.

We next test the performance of the SLRPM method by using the spring-mass example and assuming that there can be some nodes which cannot be observed thus constituting the latent variables in the example. Several different cases have been considered including both sparse and dense connections, short-range and long-range connections, and varying the number of latent variables. For comparison, we consider the correlation, PM, and SRPM methods. The SLRPM method is shown to have superior performance compared with the other methods.

1.5 Second contribution – application of SRPM in analyzing brain connectivity in presence and absence of sleep spindles

In our second contribution, we demonstrate the application of the SRPM method for estimating brain connectivity during sleep spindles from human ECoG data using an 8×8 electrode array. The ECoG recordings that we analyzed were from a male patient of age 32 with long-standing pharmaco-resistant left temporal lobe complex partial epilepsy. Sleep spindles have a major role in learning and memory consolidation. Our purpose in this thesis is to find and understand the functional organization of the brain areas in the presence and absence of sleep spindles. We find that the brain connectivity during the spindles are highly spatially localized in contrast to the case when sleep spindles are not present. We believe that this can give us further insight into the functioning of brain areas during spindles in stage 2 sleep. We can find the connectivity pattern in the presence and absence of sleep spindles by the SRPM method.

For the detection of sleep spindles, we employ a novel method called DDA (Kremliovsky et al., 1997; Lainscsek et al., 2013; Sampson et al., 2015; Lainscsek et al., 2015). DDA is a time

domain classification framework based on embedding theory in nonlinear dynamics. Given a recording (here ECoG data) from some unknown dynamical system (here the brain), an embedding will reveal the nonlinear invariant properties of the system, even from a single time series. The embedding in DDA provides a low-dimensional nonlinear functional basis onto which the data are mapped. Since this basis is built on the dynamical structure of the data, preprocessing of the data (such as filtering) is not necessary. DDA yields a low number of features (around 4), as compared with traditional spectral techniques, which greatly reduces the risk of overfitting. Frequency-based approaches which have often been used for detecting spindles are sensitive to certain artifacts involving transient increases in spectral power in the band of interest; with DDA, we train on the real data to find the relevant dynamical features for spindle identification.

1.6 Third contribution – application of SLRPM for epileptic seizure analysis

Epilepsy is the world's one of the most common brain disorder, characterized by sudden occurrence of unprovoked seizures, affecting more than 50 million people worldwide. There is plenty of evidence of significantly altered brain connectivity during epilepsy, especially during seizure periods, in the human brain (Stam, 2014; Diessen et al., 2013; Kramer et al., 2012). However, research on characterization of human brain functional connectivity during epileptic seizures have only been limited to the use of the correlation method. These results might be flawed since existing brain imaging technologies cannot simultaneously record from the entire human brain and brain regions which are observed can receive common inputs from latent or unobserved brain regions. Furthermore, it is known that there can be dopaminergic, norepinephrine or cholinergic fiber projections to the cortex, from which electroencephalography (EEG) or ECoG recordings are usually taken, during seizures (Krimer et al., 1998; Lado et al., 2008; Sato et al., 1992; Attwell et al., 2002; Giorge et al., 2004) and these neuromodulatory projections serve as common latent inputs to the cortex and induce spurious correlations among the EEG or ECoG electrodes. But

the SLRPM method calculates the precision matrix of the conditional statistics of the observed brain regions given the latent brain regions and this helps to remove the influence of common observed and latent inputs on the EEG or ECoG recordings. In this way, we may be able to find more accurate brain connectivity from the recordings and this will help us analyze the brain activity during epileptic seizures. In our third contribution, we demonstrate the application of the SLRPM method to estimate brain connectivity during epileptic seizures from human ECoG recordings. Continuous ECoG recordings from 12 patients with long-standing pharmaco-resistant complex partial epileptic seizures were analyzed using SLRPM and brain connectivity was quantified using modularity index (MI), clustering coefficient (CC), and eigenvector centrality (EC).

1.7 Organization of the thesis

The rest of the thesis is organized as follows. In Chapter 2, we test our methods using simple artificial networks. In Chapter 3, we first describe the DDA method for automatically detecting sleep spindles from human ECoG data and then proceed on to the application of SRPM to recover the connectivity among the brain regions during sleep spindles. In Chapter 4, we demonstrate the application of the SLRPM method for estimating brain connectivity during epileptic seizures from human ECoG recordings. Implication of the results of this thesis are given in Chapter 5.

Chapter 2

Simple models to evaluate the performance of the methods

2.1 Evaluation of the sparse-regularized precision matrix (SRPM) method

We first demonstrate conditions under which the sparse-regularized precision matrix (SRPM) method can indeed find the true physical connection between a pair of nodes using synthetic data from two physical models: (i) a mechanical model which considers a cascade connection of a number of springs and masses, and (ii) an electrical circuit model which consists of resistors (R) and capacitors (C), assuming that all the nodes can be observed. The purpose here is to demonstrate that the connectivity pattern of the spring-mass model can be obtained from the SRPM associated with the displacements of the masses and the connectivity pattern of the RC circuit model can be obtained from the SRPM associated with the voltages measured at the nodes.

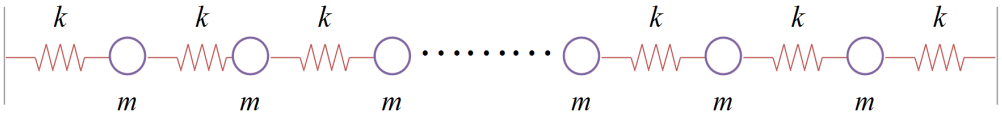

Figure 2.1: The spring-mass model. The black dots denote continuation of springs and masses.

2.1.1 The spring-mass model

The spring-mass model that we use in our simulation is shown in Figure 2.1. We assume that we can measure the displacements of the masses in the model. There are 50 equal masses m connected in cascade via springs each of which has a spring constant k. The leftmost and the rightmost springs are connected to a rigid wall. For our simulation (hereafter all units are in mks), we use $m = 0.1$ and $k = 1$. We assume that this spring-mass model is subject to thermal perturbation. In addition, we also assume that each spring is subjected to external force and we model this external force as a white noise process with variance σ^2. For our simulation we use $\sigma^2 = 0.000025$. We denote the displacements of the masses as $x_1, x_2, \ldots, x_{50}$ and the external forces associated with each of them as $w_1, w_2, \ldots, w_{50}$ respectively. Using Newton's second law of motion and Hooke's law, we can write the displacement equations of the masses as

$$\begin{aligned} m\ddot{x}_1 &= -kx_1 + k(x_2 - x_1) + w_1 \\ m\ddot{x}_2 &= -k(x_2 - x_1) + k(x_3 - x_2) + w_2 \\ &\vdots \\ m\ddot{x}_{50} &= -k(x_{50} - x_{49}) - kx_{50} + w_{50}. \end{aligned} \tag{2.1}$$

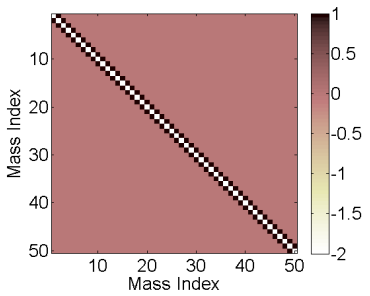

Figure 2.2: The connectivity matrix or the ground truth matrix **C** for the spring-mass model.

In matrix-vector form, the above set of equations can be written as

$$m\begin{bmatrix}\ddot{x}_1\\ \ddot{x}_2\\ \ddot{x}_3\\ \ddot{x}_4\\ \vdots\\ \ddot{x}_{50}\end{bmatrix} = k\begin{bmatrix}-2 & 1 & 0 & 0 & \cdots & 0\\ 1 & -2 & 1 & 0 & \cdots & 0\\ 0 & 1 & -2 & 1 & \cdots & 0\\ 0 & 0 & 1 & -2 & \cdots & 0\\ \vdots & \vdots & \vdots & \vdots & \ddots & \vdots\\ 0 & 0 & 0 & \cdots & 1 & -2\end{bmatrix}\begin{bmatrix}x_1\\ x_2\\ x_3\\ x_4\\ \vdots\\ x_{50}\end{bmatrix} + \begin{bmatrix}w_1\\ w_2\\ w_3\\ w_4\\ \vdots\\ w_{50}\end{bmatrix}. \tag{2.2}$$

In compact form, (2.2) can be represented as

$$m\ddot{\mathbf{x}} = k\mathbf{C}\mathbf{x} + \mathbf{w} \tag{2.3}$$

where $\mathbf{x}$ is the displacement vector, $\mathbf{w}$ is the white noise vector and $\mathbf{C}$ is the connectivity (or ground truth) matrix and is shown in Figure 2.2. Using a second order approximation of the double derivative on the left hand side in (2.3), we have

$$m\left[\frac{\mathbf{x}(t+h) - 2\mathbf{x}(t) + \mathbf{x}(t-h)}{h^2}\right] = k\mathbf{C}\mathbf{x}(t) + \mathbf{w}(t) \tag{2.4}$$

where h is the step size and t denotes the time instant. We use a random initialization of $\mathbf{x}$ with variance $\sigma_{\mathbf{x}}^2 = 0.000001$. We then solve (2.4) repeatedly to generate N samples of the displacement vector $\mathbf{x}$ corresponding to N consecutive time points. For our simulation, we choose $h = 0.007$ and

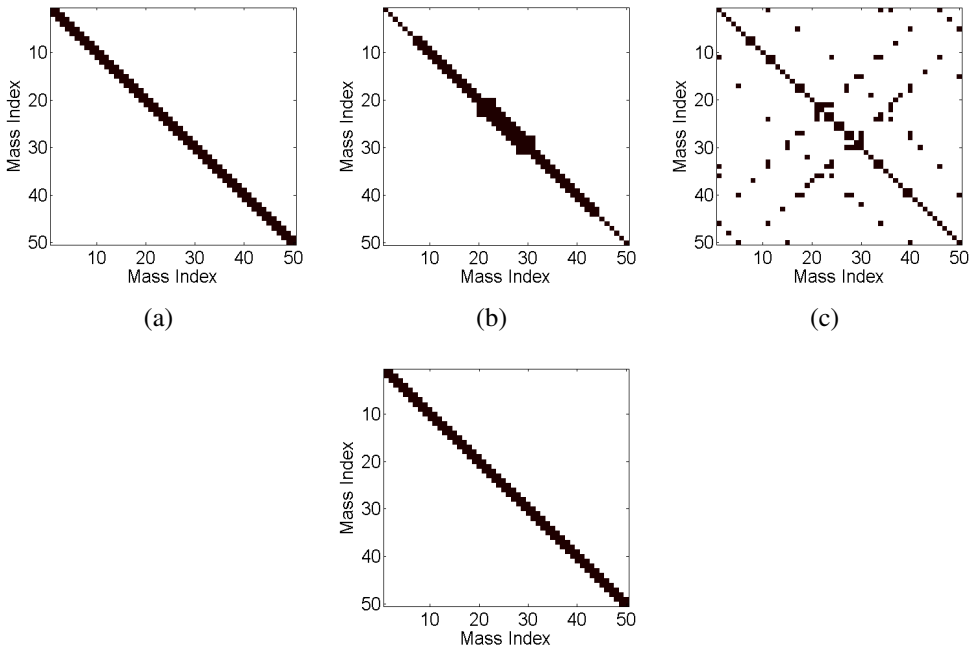

Figure 2.3: Results of the estimation methods for the spring-mass model. (a) The ground truth matrix. (b) The estimated connection matrix from the correlation method (16% error). (c) The estimated connection matrix from the PM method (53% error). (d) The estimated connection matrix from the SRPM method (0% error). In each panel (a), (b), (c), and (d), black denotes either a diagonal element or a connectivity between two masses via a spring and white denotes no connectivity.

$N = 50000$. We use these N samples to form the sample covariance matrix.

We next apply the correlation, PM, and SRPM methods to recover the connectivity pattern of the spring-mass system. The value of λ for the SRPM method is chosen to be 0.0009. The results are shown in Figure 2.3. Note that the ground truth matrix in Figure 2.3 is binarized such that a one denotes either a diagonal element or a connectivity between two masses via a spring and a zero denotes no connectivity. For all three methods, we first estimate the connection matrix and choose the M largest elements (in absolute value) in the estimated connection matrix where M is the number of nonzero elements in the ground truth matrix. In Figure 2.3, for each method, we denote these M largest elements as ones and the rest as zeros. The binarization is done for clarity and better visualization. The error percentage in the figures for a particular method is calculated as the fraction of false positive and false negative connections between the binarized ground truth matrix and the binarized estimated connection matrix for that method.

From Figure 2.3(b) we note that the correlation method is not able to fully recover the true connectivity structure of the spring-mass system. Since the sample covariance matrix is a poor estimator of the true covariance matrix, the PM method is even worse than the correlation method and results in a large number of false positive and false negative connections. The SRPM method is able to recover successfully the true connectivity pattern of the spring-mass model.

Explanation for the recovery of the connectivity structure via the SRPM method in the spring-mass model

Assuming that the spring-mass model is only subject to thermal perturbation, i.e., if we assume $\mathbf{w} = 0$ in (2.3), then the probability distribution of the displacement vector $\mathbf{x}$ can be given by the Boltzmann distribution (MacKay, 2002) as

$$P(\mathbf{x}) = \frac{1}{Z}\exp[-\beta E(\mathbf{x})] \tag{2.5}$$

where $\beta = 1/(kT)$, k is the Boltzmann constant and T is the temperature, and Z is a normalization factor. In (2.5), $E(\mathbf{x})$ is the energy of the spring-mass system. For the model in Figure 2.1, the energy $E(\mathbf{x})$ can be written as

$$\begin{aligned} E(\mathbf{x}) &= \frac{1}{2}kx_1^2 + \frac{1}{2}k(x_2 - x_1)^2 + \frac{1}{2}k(x_3 - x_2)^2 + \cdots + \frac{1}{2}kx_{50}^2 \\ &= \frac{1}{2}\mathbf{x}^T\widetilde{\mathbf{C}}\mathbf{x} \end{aligned} \tag{2.6}$$

where $\mathbf{x}^T$ denotes the transpose of $\mathbf{x}$ and $\widetilde{\mathbf{C}} = -\mathbf{C}$. Hence we have

$$P(\mathbf{x}) = \frac{1}{Z}\exp[-\beta\mathbf{x}^T\widetilde{\mathbf{C}}\mathbf{x}]. \tag{2.7}$$

We note that $P(\mathbf{x})$ in (2.7) is a multivariate Gaussian distribution in $\mathbf{x}$ whose PM differs from $\widetilde{\mathbf{C}}$ only by a scalar multiple, implying that the PM in (2.7) is just a scaled version of the connectivity matrix $\mathbf{C}$ in (2.3). Hence PM can recover the connectivity structure of the cascade connection of springs and masses given in Figure 2.1.

Since the sample covariance matrix is a poor estimator of the eigenvalues of the covariance matrix, the inverse of the covariance matrix or PM produces a large number of false positive and false negative connections as shown in Figure 2.3(c). In contrast, since the connectivity structure is sparse, we can use the SRPM method to recover the connectivity pattern of the spring-mass system.

Remark 1

The performance (in terms of error percentage) of the correlation method, the covariance method, and the SRPM method in the spring-mass model does not change under different types of noise distributions. We have tested the performance of these methods under Gaussian, Poisson, and uniform distributions and have obtained similar performance to that given in Figure 2.3 for the three methods.

Remark 2

The performance (in terms of error percentage) of the three methods in the spring-mass model does not change for signal-to-noise ratio up to 30 dB and the performance is very similar to that given in Figure 2.3 for the three methods.

These two results are not surprising. Note that in the spring-mass model, we model the noise as an external force. So no matter how "forcefully" (noise variance) or in what way (noise distribution) we wobble the spring-mass system, the connectivity pattern won't change. Noise is not responsible for the connectivity pattern and the connectivity patterns for different methods shown in Figure 2.3 are due to the methods themselves.

2.1.2 The RC circuit model

The RC circuit model is taken from (Sojoudi et al., 2014) which applied the graphical LASSO algorithm for the SRPM method. Two different network topologies are considered: (i) the tree network, and (ii) the mesh network. We assume that the voltages at the nodes are available for measurement and estimate the connectivity by the three methods from these measured voltages. An edge between a pair of nodes denotes a parallel resistor-capacitor (RC) circuit as shown in Figure 2.4(a). We assume that the circuit is activated only by the thermal current (i.e., there is no supply of external current) and each node is subject to thermal current as shown in Figure 2.4(b). We model this thermal current as white noise known as the Johnson-Nyquist noise. These stochastic currents produce stochastic voltages at the nodes which in turn cause the charging and discharging of the capacitors in the network.

The tree network

This network is shown in Figure 2.5 where the nodes are denoted as numbers and each edge represents a parallel RC circuit as in Figure 2.4(a). We consider a total of 10 nodes in this example. Let $\mathbf{v}$ denote the vector of voltages at the nodes and $\mathbf{i}$ denote the vector of stochastic

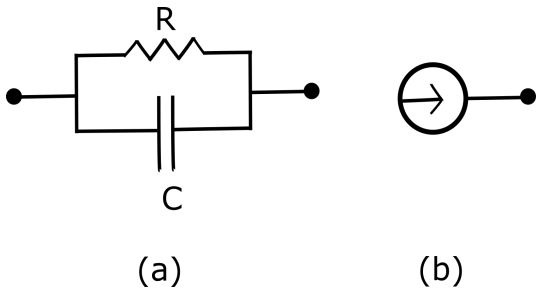

Figure 2.4: Elements of the RC circuit model. (a) Parallel RC circuit between a pair of nodes. (b) Thermal current associated with a node.

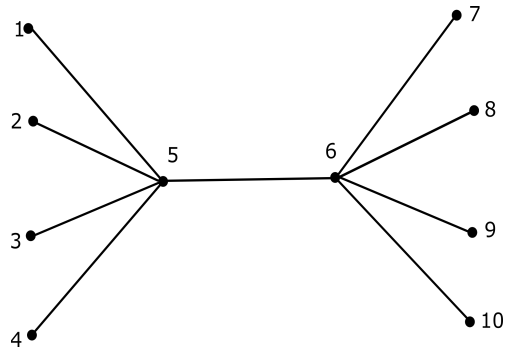

Figure 2.5: The tree network.

currents injected to the nodes by some external device. Using Kirchoff's law, we have,

$$\mathbf{A}\dot{\mathbf{v}} = -\mathbf{G}\mathbf{v} + \mathbf{i} \tag{2.8}$$

where $\mathbf{A}$ is the capacitance matrix and $\mathbf{G}$ is the conductance matrix (see (Sojoudi et al., 2014) regarding how to construct the matrices $\mathbf{A}$ and $\mathbf{G}$). For our simulation, we assume that each of the values of the capacitances and conductances denoted as edges in Figure 2.5 has a value of 1. Moreover, the node 5 of the circuit is grounded through a parallel RC circuit and for this, the values of both the capacitance and the conductance are taken to be 4. Hence, in this case, $\mathbf{A} \equiv \mathbf{G}$ and we call $\mathbf{A}$ or $\mathbf{G}$ the connectivity matrix or the ground truth matrix of the RC circuit. Note that the values of the capacitances and conductances in the tree network are chosen such that the connectivity matrix $\mathbf{A}$ ($\equiv \mathbf{G}$) is positive definite. The connectivity matrix for the given tree network is shown in Figure 2.6. Assuming that the current vector $\mathbf{i}$ is due to the stochastic currents from the white

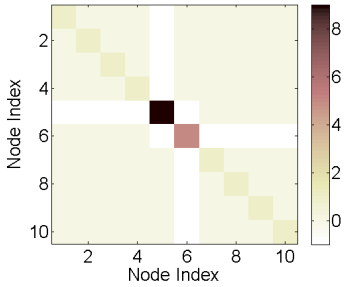

Figure 2.6: The connectivity matrix or the ground truth matrix $\mathbf{A}$ ($\equiv \mathbf{G}$) for the tree network.

thermal noise, we can write (2.8) as (Sojoudi et al., 2014)

$$\mathbf{A}\dot{\mathbf{v}} = -\mathbf{G}\mathbf{v} - \mathbf{G}^{\frac{1}{2}}\mathbf{w} \tag{2.9}$$

where $\mathbf{G}^{\frac{1}{2}}$ is the square root (not the elementwise square root) of the matrix $\mathbf{G}$. For our simulation we choose variance $\sigma^2 = 4$ for the white noise process $\mathbf{w}$ in (2.9). Using a first-order approximation of the derivative on the left hand side in (2.9), we have,

$$\mathbf{A}\left[\frac{\mathbf{v}(t) - \mathbf{v}(t-h)}{h}\right] = -\mathbf{G}\mathbf{v}(t) - \mathbf{G}^{\frac{1}{2}}\mathbf{w}(t) \tag{2.10}$$

where h is the step size and t denotes the time instant. For our simulation we choose $h = 0.5$. We use a random initialization of $\mathbf{v}$ with variance $\sigma_{\mathbf{v}}^2 = 0.0001$. As done in the spring-mass example, we solve (2.10) iteratively to generate N samples for the voltages. For our simulation we choose $N = 282$.

We next apply the correlation, PM, and SRPM methods to recover the connectivity pattern of the tree network. The value of λ for the SRPM method is chosen to be 0.01. The results are shown in Figure 2.7. As done in the spring-mass example, we show only the binarized results for better visualization.

We note that the correlation and PM methods are not able to recover the true connectivity pattern of the tree network. The correlation method in particular has having a large percentage of false positive and false negative connections. This is due to the fact that node 5 is connected

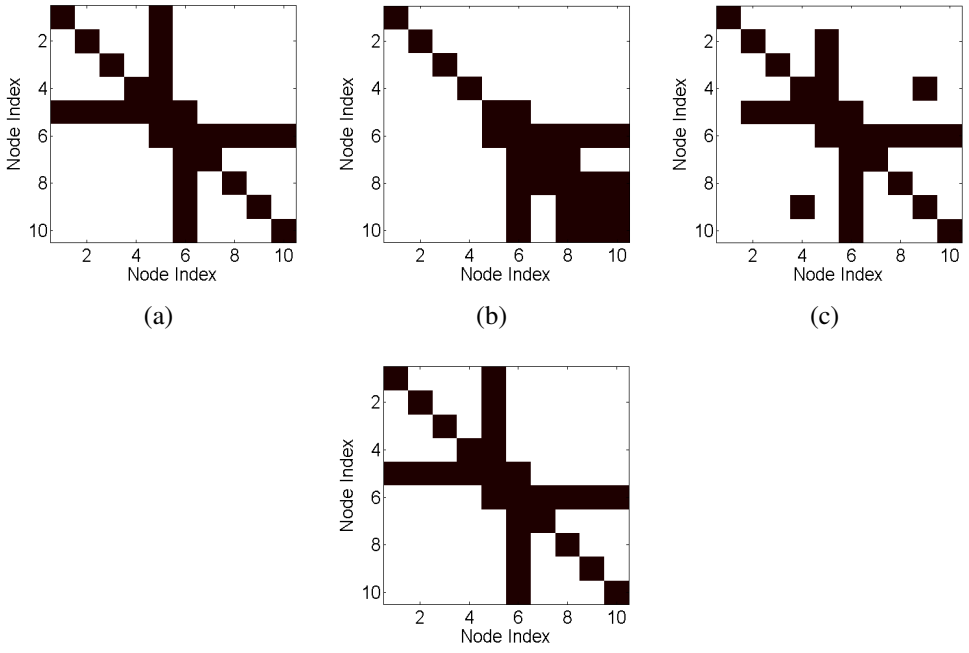

Figure 2.7: Results of the estimation methods for the tree network in the RC circuit model. (a) The ground truth matrix. (b) The estimated connection matrix from the correlation method (29% error). (c) The estimated connection matrix from the PM method (7% error). (d) The estimated connection matrix from the SRPM method (0% error). In each panel (a), (b), (c), and (d), black denotes either a diagonal element or a connectivity between two nodes and white denotes no connectivity.

to ground via a parallel RC circuit with relatively high conductance and capacitance. Thus the grounded node and its neighbors will have low correlation and the ungrounded nodes and their neighbors will have high correlation even though they are not connected (Sojoudi et al., 2014). In contrast, the SRPM method is able to recover successfully the ground truth of the tree network.

Explanation for the recovery of the connectivity structure via the SRPM method in the tree network

Since we have assumed that the tree network is only subject to thermal perturbation, the probability distribution of the voltage vector $\mathbf{v}$ can be given by the Boltzmann distribution as

$$P(\mathbf{v}) = \frac{1}{Z}\exp[-\beta E(\mathbf{v})] \tag{2.11}$$

where $E(\mathbf{v})$ is the energy of the capacitors in the tree network and Z is the corresponding normalization factor. For the given tree network in Figure 2.5, the energy $E(\mathbf{v})$ can be written as

$$\begin{aligned} E(\mathbf{v}) = \frac{1}{2}\big[&(v_5-v_1)^2+(v_5-v_2)^2+(v_5-v_3)^2 \\ &+(v_5-v_4)^2+4v_5^2+(v_5-v_6)^2+(v_6-v_7)^2 \\ &+(v_6-v_8)^2+(v_6-v_9)^2+(v_6-v_{10})^2\big] \\ =\ &\frac{1}{2}\mathbf{v}^T\mathbf{A}\mathbf{v} \end{aligned} \tag{2.12}$$

where v_i denotes the voltage at the ith node, $i = 1,2,\ldots,10$ and $\mathbf{A}$ is the connectivity matrix of the tree network given in (2.15). Hence we have

$$P(\mathbf{v}) = \frac{1}{Z}\exp[-\beta\mathbf{v}^T\mathbf{A}\mathbf{v}] \tag{2.13}$$

which is a multivariate Gaussian distribution in $\mathbf{v}$ whose PM differs from $\mathbf{A}$ only by a scalar multiple. Hence PM can recover the connectivity pattern of the tree network given in Figure 2.5. But since the sample covariance matrix is a poor estimator of the eigenvalues of the covariance matrix, the

inverse of the covariance matrix or PM produces false positive and false negative connections as shown in Figure 2.7(c). In contrast, since the connectivity structure is sparse, the SRPM method is able to recover successfully the connectivity pattern of the tree network.

The mesh network

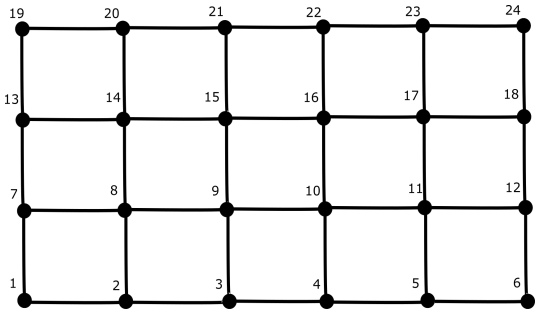

Figure 2.8: The mesh network.

This network is shown in Figure 2.8 where the nodes are denoted as numbers and each edge represents a parallel RC circuit as in the tree network. We consider a total of 24 nodes in this example. Equations (2.9) and (2.10) remain the same for this network with the corresponding $\mathbf{A}$, $\mathbf{G}$, and $\mathbf{v}$. For our simulation, we assume that each of the values of the capacitances and conductances denoted as edges in Figure 2.8 has a value of 1. Moreover, all the nodes indexed from 1 to 18 of the circuit are grounded through parallel RC circuits as is done for node 5 in the tree network and the value of both the capacitance and the conductance are taken to be 5 for each parallel RC circuit connected to ground. Hence in this case $\mathbf{A} \equiv \mathbf{G}$ and this is the connectivity matrix or the ground truth matrix for the mesh network. Once again note that the values of the capacitances and conductances in the mesh network are chosen such that the connectivity matrix $\mathbf{A}$ ($\equiv \mathbf{G}$) is positive definite. The connectivity matrix for the given mesh network is shown in Figure 2.9. We again choose $\sigma^2 = 4$ for the white noise process $\mathbf{w}$ in (2.9). The value of step size is chosen to be $h = 0.5$. We also use a random initialization of $\mathbf{v}$ with variance $\sigma_{\mathbf{v}}^2 = 1$. As done in the tree network, we solve (2.10) iteratively to generate N samples for the voltages and in this case, we choose $N = 2000$.

We again apply the correlation, PM, and SRPM methods to recover the connectivity pattern

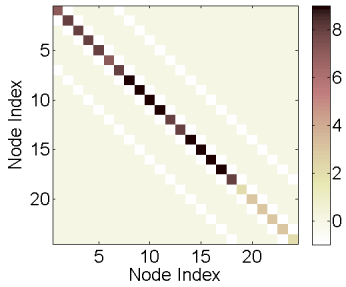

Figure 2.9: The connectivity matrix or the ground truth matrix $\mathbf{A}$ ($\equiv \mathbf{G}$) for the mesh network.

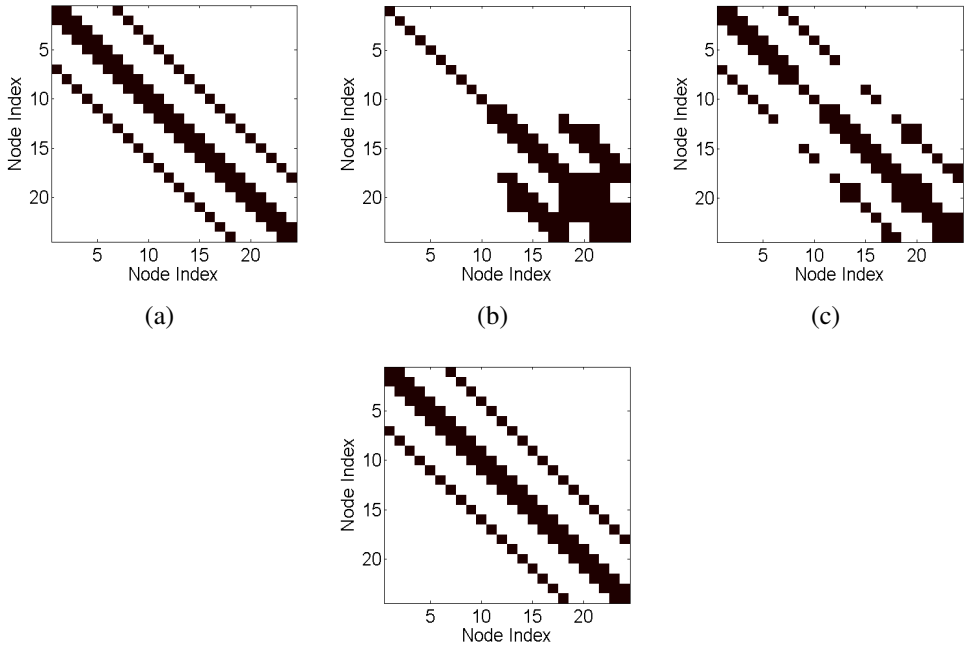

Figure 2.10: Results of the estimation methods for the mesh network in the RC circuit model. (a) The ground truth matrix. (b) The estimated connection matrix from the correlation method (40% error). (c) The estimated connection matrix from the PM method (11% error). (d) The estimated connection matrix from the SRPM method (0% error). In each panel (a), (b), (c), and (d), black denotes either a diagonal element or a connectivity between two nodes and white denotes no connectivity.

of the mesh network. The value of λ for the SRPM method is chosen to be 0.005. The results are shown in Figure 2.10. As done in the tree network, we show only the binarized results.

We note that the correlation and PM methods are not able to recover the true connectivity pattern of the mesh network with the correlation method having a large percentage of false positive and false negative connections. We also observe that the ungrounded nodes and their neighbors have high correlation even though they are not connected. Once again, the SRPM method is able to recover successfully the ground truth of the mesh network.

Explanation for the recovery of the connectivity structure via the SRPM method in the mesh network

Following the procedure in the tree network, if we assume that the mesh network is only subject to thermal perturbation, it is straightforward to show that the voltage vector $\mathbf{v}$ in the mesh network follows a multivariate Gaussian distribution whose PM differs from the connectivity matrix $\mathbf{A}$ of the mesh network shown in Figure 2.8 only by a scalar multiple. Hence PM can recover the connectivity pattern of the mesh network. Once again, the direct inverse of the covariance matrix produces false positive and false negative connections as shown in Figure 2.10(c). In contrast, since the connectivity structure is sparse, the SRPM method is able to recover successfully the connectivity structure of the mesh network.

Also note that for the voltage vector $\mathbf{v}$ to follow a multivariate normal distribution whose PM differs from the connectivity matrix $\mathbf{A}$ only by a scalar multiple, the RC circuit network need not be one of the specific structures (tree and mesh) given in Figure 2.5 and Figure 2.8. It is straightforward to show (following the steps as before via the Boltzmann distribution) that PM can recover the connectivity pattern of an arbitrarily connected RC circuit network in the limit as the number of samples increases to infinity.

Remark 1

The performance (in terms of error percentage) of the correlation method, the covariance method, and the SRPM method in the tree network and the mesh network does not change under different types of noise distributions. We have tested the performance of these methods under Gaussian, Poisson, and uniform distributions and have obtained similar performance to that given in Figure 2.7 for the tree network and in Figure 2.10 for the mesh network for the three methods.

Remark 2

The performance (in terms of error percentage) of the three methods in the tree network and the mesh network does not change for signal-to-noise ratio up to 30 dB and the performance is very similar to that given in Figure 2.7 for the tree network and in Figure 2.10 for the mesh network for the three methods.

Once again, these two results are not surprising. Note that in the RC networks, we have modeled the noise as stochastic current from white thermal noise. If current goes up and down or changes direction, the connectivity pattern won't change. Noise is not responsible for the connectivity pattern and the connectivity patterns for different methods shown in Figure 2.7 and Figure 2.10 are due to the methods themselves.

2.2 Evaluation of the sparse-plus-latent regularized precision matrix (SLRPM) method

We next test the performance of the SLRPM method by using the spring-mass example and assuming that there can be some nodes which cannot be observed thus constituting the latent variables in the example. Several different cases have been considered including both sparse and dense connections, short-range and long-range connections, and varying the number of latent variables.

2.2.1 The spring-mass model

Consider once again the spring-mass model shown in Figure 2.1. We assume that we can measure the displacements of the masses in the model. Also assume there are 200 equal masses m connected in cascade via springs, i.e., the ith mass is connected to its neighbors $i-1$ and $i+1$, via springs. First consider each spring to have a restoring force characteristics (RFC) of the form kx, where k is the spring constant and x is the amount by which the spring is displaced from its relaxed position. Note that the RFC is linear in this case. The leftmost and the rightmost springs are connected to a rigid wall. For our simulations (hereafter all units are in mks), we use $m = 0.1$ and $k = 1$. We assume that this spring-mass model is subject to thermal perturbation. In addition, we also assume that each mass is subject to external force and we model this external force as a white noise process with variance σ^2. For our simulation we use $\sigma^2 = 0.000025$. We denote the displacements of the masses as $x_1, x_2, \ldots, x_{200}$ and the external forces associated with each of them as $w_1, w_2, \ldots, w_{200}$ respectively. As before, we can write the displacement equations of the masses as

$$\begin{aligned} m\ddot{x}_1 &= -kx_1 + k(x_2 - x_1) + w_1 \\ m\ddot{x}_2 &= -k(x_2 - x_1) + k(x_3 - x_2) + w_2 \\ &\vdots \\ m\ddot{x}_{200} &= -k(x_{200} - x_{199}) - kx_{200} + w_{200}. \end{aligned} \tag{2.14}$$

In matrix-vector form, the above set of equations can be written as

$$m\begin{bmatrix}\ddot{x}_1\\ \ddot{x}_2\\ \ddot{x}_3\\ \ddot{x}_4\\ \vdots\\ \ddot{x}_{200}\end{bmatrix} = k\begin{bmatrix}-2 & 1 & 0 & 0 & \cdots & 0\\ 1 & -2 & 1 & 0 & \cdots & 0\\ 0 & 1 & -2 & 1 & \cdots & 0\\ 0 & 0 & 1 & -2 & \cdots & 0\\ \vdots & \vdots & \vdots & \vdots & \ddots & \vdots\\ 0 & 0 & 0 & \cdots & 1 & -2\end{bmatrix}\begin{bmatrix}x_1\\ x_2\\ x_3\\ x_4\\ \vdots\\ x_{200}\end{bmatrix} + \begin{bmatrix}w_1\\ w_2\\ w_3\\ w_4\\ \vdots\\ w_{200}\end{bmatrix}. \tag{2.15}$$

In compact form, (2.15) can be represented as

$$m\ddot{\mathbf{x}} = k\mathbf{C}\mathbf{x} + \mathbf{w} \tag{2.16}$$

where $\mathbf{x}$ is the displacement vector, $\mathbf{w}$ is the white noise vector and $\mathbf{C}$ is the connectivity (or ground truth) matrix of the entire spring-mass network. Using a second order approximation of the double derivative on the left hand side in (2.16), we have

$$m\left[\frac{\mathbf{x}(t+h) - 2\mathbf{x}(t) + \mathbf{x}(t-h)}{h^2}\right] = k\mathbf{C}\mathbf{x}(t) + \mathbf{w}(t) \tag{2.17}$$

where h is the step size and t denotes the time instant. We use a random initialization of $\mathbf{x}$ with variance $\sigma_{\mathbf{x}}^2 = 0.000001$. We then solve (2.17) repeatedly to generate N samples of the displacement vector $\mathbf{x}$ corresponding to N consecutive time points. For our simulation, we choose $h = 0.0007$ and $N = 50000$. We can use these N samples to form the sample covariance matrix of the entire spring-mass network.

However, we assume that we can observe only a part of the entire network, i.e., some of the displacements are not available for measurement. Hence, the only available data is the sample covariance matrix of the displacements which are available for measurement. From this sample covariance matrix, we wish to recover the connectivity of the observable masses using the correlation method, the precision matrix (PM) method, the SRPM method and the SLRPM method.

We study the recovery performance of the methods by varying the number of observable variables p (hence varying the number of latent variables h). The values of p are taken to be 60, 100, and 150 for this example. This example is shown in Figure 2.11. The connections in the ground truth matrix of the observed network are shown in black dots. We choose the M largest elements (in absolute value) in the estimated connection matrix from each method, where M is the number of connections in the ground truth matrix, and check whether the estimated connection corresponds to the connection in the ground truth matrix. For each method, we show a correctly identified connection in black dot and an incorrectly identified connection in red dot in Figure 2.11. The error percentage for a particular method is the percentage of incorrectly identified connections expressed as a fraction of the total number of connections in the ground truth matrix. The value of the regularization parameter λ for the SRPM method and the values of the regularization parameters α and β for the SLRPM method are also mentioned in Figure 2.11. These values were fine tuned for this example. From this figure, we observe that the PM method, which directly inverts the sample covariance matrix, results in extremely poor performance for the three cases considered. The SLRPM method has comparable or better performance than the other methods for the three cases considered in Figure 2.11.

Next, we consider an example with a non-linear RFC of the form $kx+\gamma x^3$. Non-linear RFC is considered since brain dynamics during seizures is well known to be highly non-linear (see Stam (2005) and the references therein). We vary the number of observable masses and keep the other parameters the same as the previous example. The value of γ is set to 1 for our simulations. The results of the application of different methods for this example is shown in Figure 2.12. Note that the SLRPM method has comparable or better performance than the other methods for varying number of observed variables. We also have considered a non-linear RFC of the form $kx+\gamma x^9$ and in that case too, the SLRPM method was able to outperform the correlation and SRPM methods (results not shown here). In Figure 2.13, we have also plotted the performance of the methods in terms of number of samples N for $p = 100$. We note that the performance of the correlation, SRPM, and SLRPM methods does not improve with increase in N with the SLRPM method outperforming

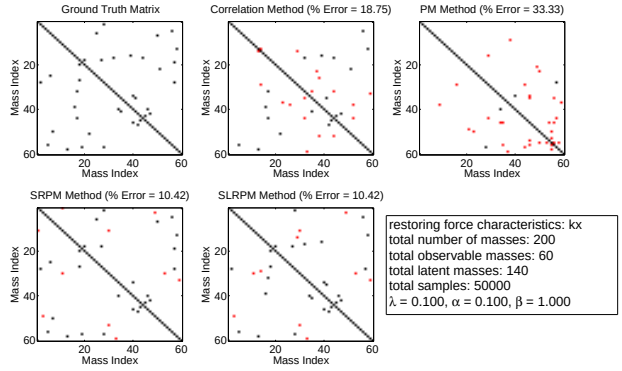

(a)

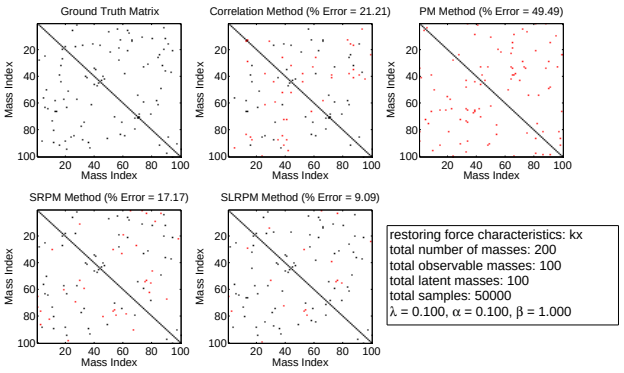

(b)

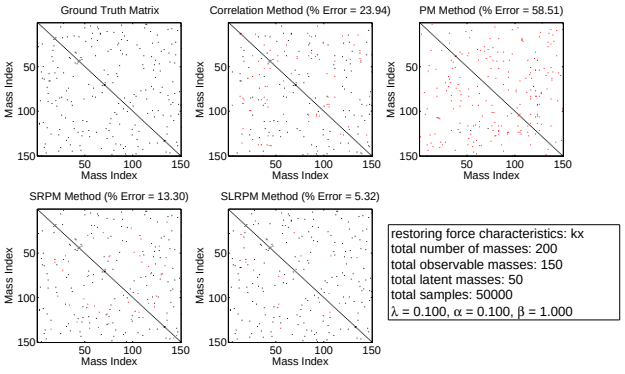

(c)

Figure 2.11: Results of the estimation methods for the spring-mass model of 200 masses when only a part of the network is observable and a linear RFC is considered. Connections in the observed network (ground truth matrix) are shown in black dots. For the methods, correct identification of a connection is shown in black dot and incorrect identification of a connection is shown in red dot. (a) $p = 60$. (b) $p = 100$. (c) $p = 150$.

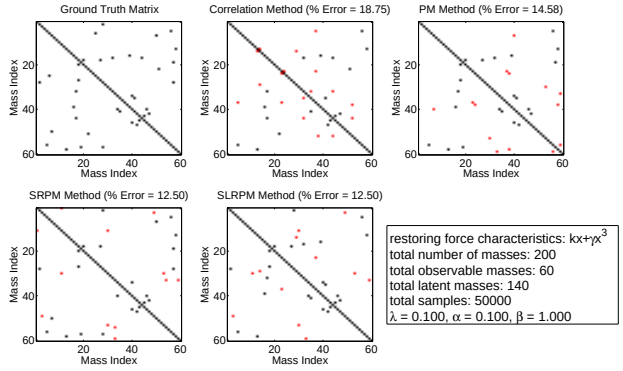

(a)

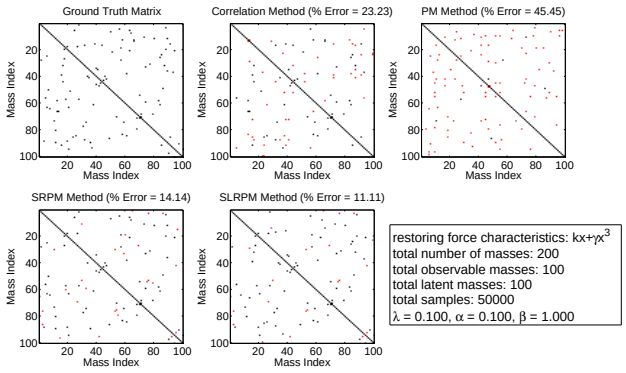

(b)

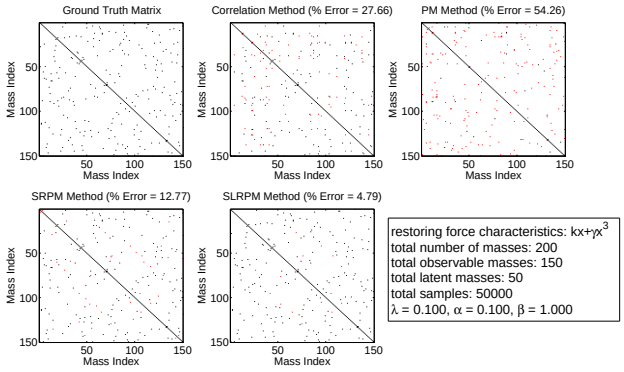

(c)

Figure 2.12: Results of the estimation methods for the spring-mass model of 200 masses when only a part of the network is observable and a non-linear RFC is considered. Connections in the observed network (ground truth matrix) are shown in black dots. For the methods, correct identification of a connection is shown in black dot and incorrect identification of a connection is shown in red dot. (a) $p = 60$. (b) $p = 100$. (c) $p = 150$.

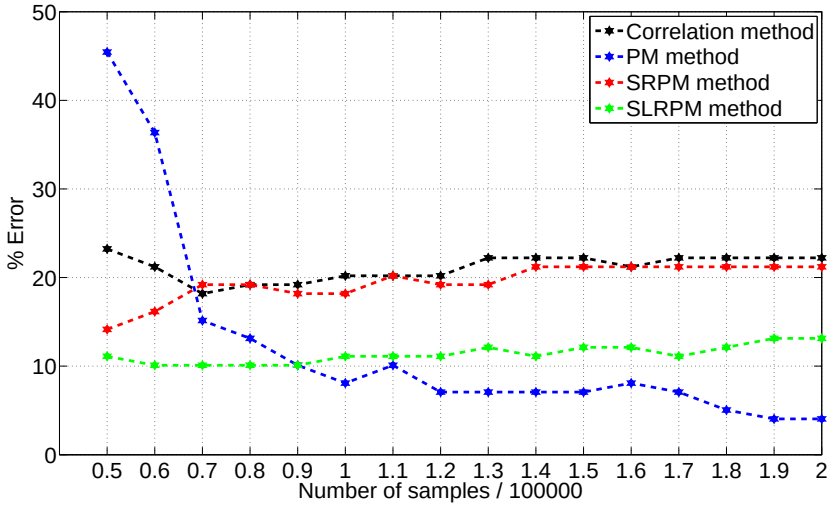

Figure 2.13: Plot of error percentage of the estimation methods vs. N with $p = 100$ and when a non-linear RFC is considered.

the correlation and SRPM methods. The correlation and SRPM methods also have comparable performance. It is also worth noting that even though the SLRPM method performs much better and the PM method is the worst when the sample size is small, the PM method is able to outperform all the other methods when we increase the sample size.

In the previous two examples, the considered network was sparse (all masses were connected only to their immediate neighbors). For an epileptic human brain, this sparseness assumption might not remain valid (Steriade et al., 1993). Hence, we now consider relatively denser networks and evaluate the performance of the methods. In the next two examples, we will consider the spring-mass network to have long range connections. First assume that this range is $40n$, where n is a natural number, i.e., the ith mass, besides being connected to its immediate neighbors $i+1$ and $i-1$, is now also connected to masses with indices $i+40$, $i-40$, $i+80$, $i-80$, and so on. Note that, even though mechanically such connections are not possible for one dimensional spring-mass motion, we make such hypothetical connections for simulation purposes. We also assume a linear RFC for this example. Using Newton's second law of motion and Hooke's law, we can easily write the displacement equations of the masses for this modified spring-mass network as done for the two previous examples in (2.14). We can then iteratively solve these equations to generate N samples of

the displacement vector. We assume $N = 100000$ samples for this example. All other parameters are same as before. Like the previous examples, the values of observable masses p are taken to be 60, 100, and 150. The performance of the methods for this example is shown in Figure 2.14. The values of the regularization parameters are also indicated in that figure. We note that the SLRPM method is able to outperform the other methods. It is also worth noting that the SRPM method is able to have comparable performance to that of the SLRPM method.

Next, assume that the range is $20n$, i.e., the ith mass, besides being connected to its immediate neighbors $i+1$ and $i-1$, is now also connected to masses with indices $i+20$, $i-20$, $i+40$, $i-40$, and so on. We vary the number of observable masses and keep the other parameters the same as the previous example. The performance of different methods for this example is shown in Figure 2.15. The SLRPM method is able to outperform the other methods. Furthermore, in Figure 2.16, we have plotted the performance of the methods in terms of number of samples N for $p = 100$. Note that the PM method is not able to estimate the observable network resulting in large errors. The SLRPM method is able to perform better than the correlation and SRPM methods. It is also worth noting that the correlation and SRPM methods have comparable performance.

In the next example, we still consider relatively dense connections, but we assume the spring-mass network to have short range connections. We assume a neighborhood of 3, i.e., the ith mass, is now connected to masses with indices $i+1$, $i-1$, $i+2$, $i-2$, $i+3$, and $i-3$. Once again, even though mechanically such connections are not possible for one dimensional spring-mass motion, we make such hypothetical connections for simulation purposes. We also assume $N = 100000$ samples and a linear RFC. As before, the values of observable masses p are taken to be 60, 100, and 150. The performance of the methods for this example is shown in Figure 2.17. The values of the regularization parameters are also mentioned in that figure. We note that the SLRPM method is able to outperform the correlation and PM methods and has comparable performance to that of the SRPM method. We have also plotted the performance of the methods in terms of number of samples N for $p = 100$ in Figure 2.18. The PM method is not able to have any useful estimate of the observed network. The SLRPM method is able to outperform the correlation method and have

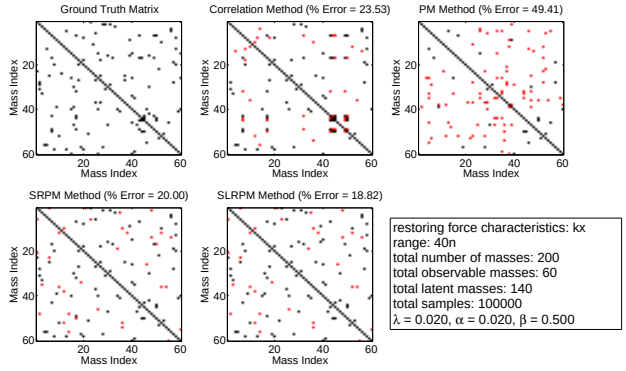

(a)

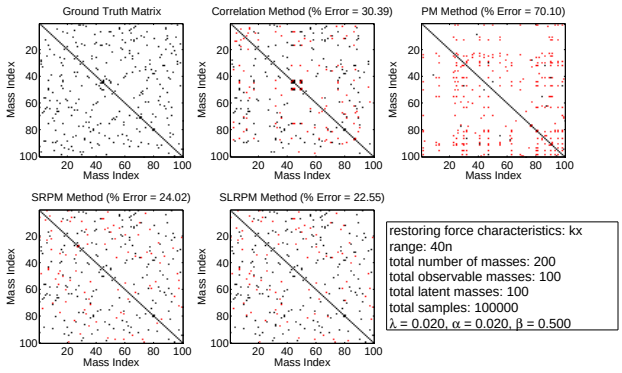

(b)

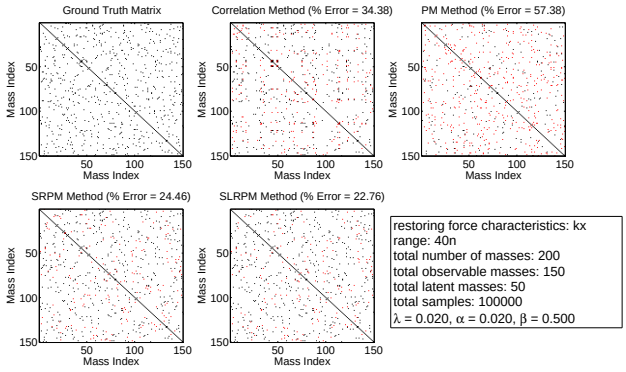

(c)

Figure 2.14: Results of the estimation methods for the spring-mass model of 200 masses when only a part of the network is observable and there are long range connections with range $40n$. Connections in the observed network (ground truth matrix) are shown in black dots. For the methods, correct identification of a connection is shown in black dot and incorrect identification of a connection is shown in red dot. (a) $p = 60$. (b) $p = 100$. (c) $p = 150$.

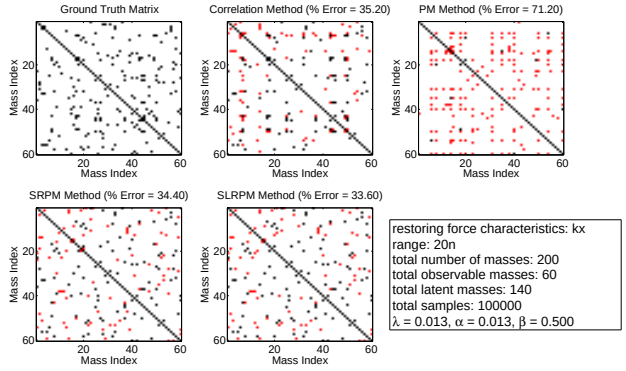

(a)

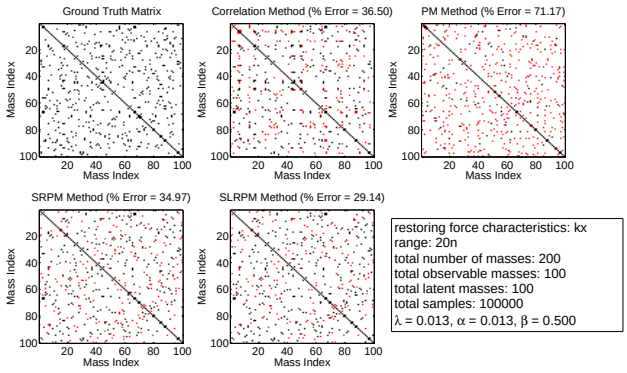

(b)

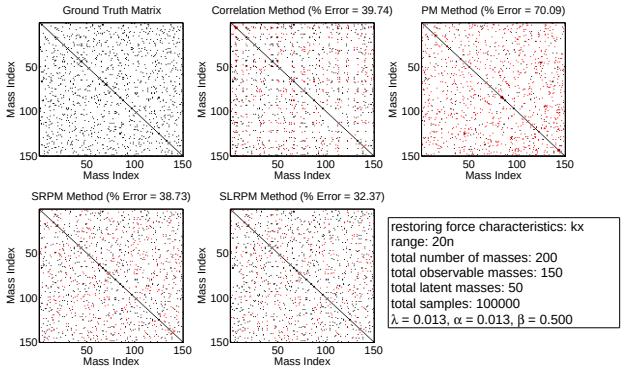

(c)

Figure 2.15: Results of the estimation methods for the spring-mass model of 200 masses when only a part of the network is observable and there are long range connections with range $20n$. Connections in the observed network (ground truth matrix) are shown in black dots. For the methods, correct identification of a connection is shown in black dot and incorrect identification of a connection is shown in red dot. (a) $p = 60$. (b) $p = 100$. (c) $p = 150$.

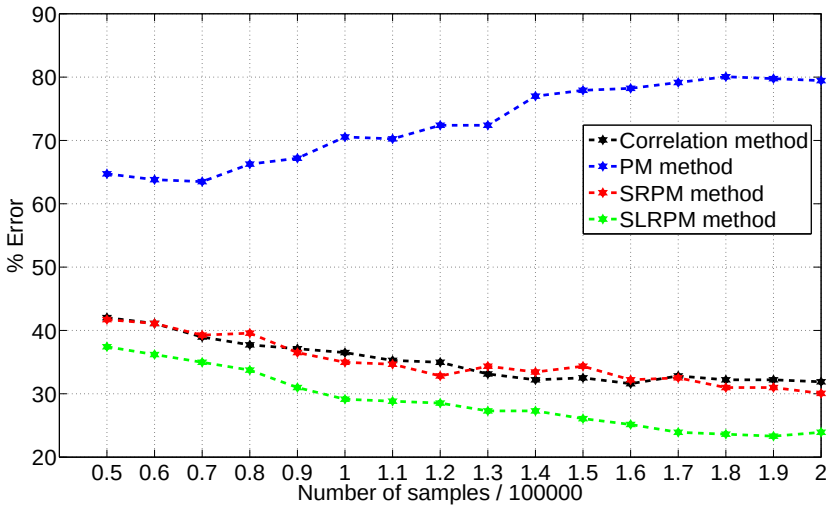

Figure 2.16: Plot of error percentage of the estimation methods vs. N with $p = 100$ and densely connected network with long range connections of range $20n$.

comparable performance to the SRPM method.

Remark 1

Even though for each case we have considered only one random subset of network to be observable, considering different random subsets of network (but fixing all the parameters) to be observable does not change the *trends* of the results reported here and the SLRPM method is able to outperform the other methods for different random subsets observed variables.

Remark 2

The performance (in terms of error percentage) of each method for network recovery in the spring-mass model does not change under different types of noise distributions. We have tested the performance of these methods under Gaussian, Poisson, and uniform distributions and each method has similar performance under these different noise distributions.

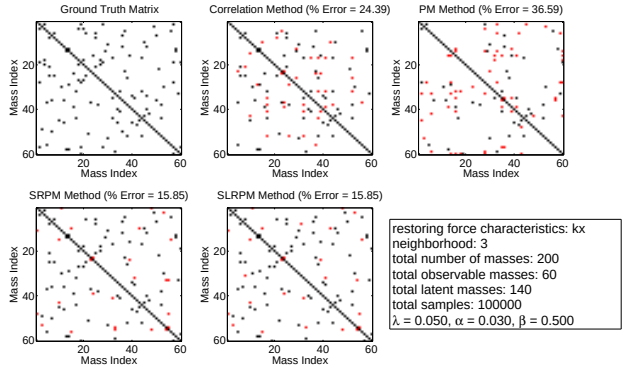

(a)

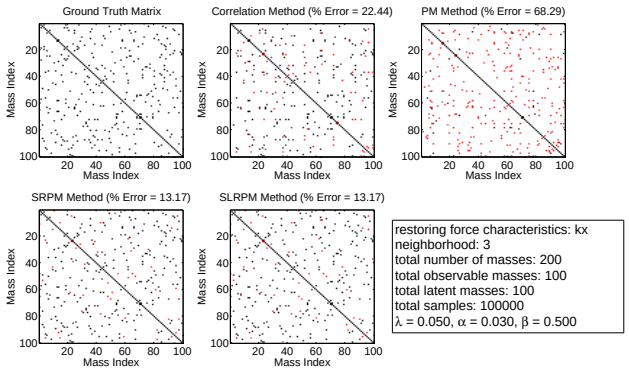

(b)

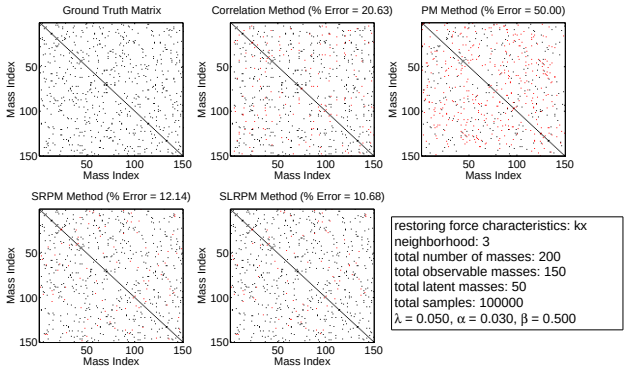

(c)

Figure 2.17: Results of the estimation methods for the spring-mass model of 200 masses when only a part of the network is observable and there are short range connections with a neighborhood of 3. Connections in the observed network (ground truth matrix) are shown in black dots. For the methods, correct identification of a connection is shown in black dot and incorrect identification of a connection is shown in red dot. (a) $p = 60$. (b) $p = 100$. (c) $p = 150$.

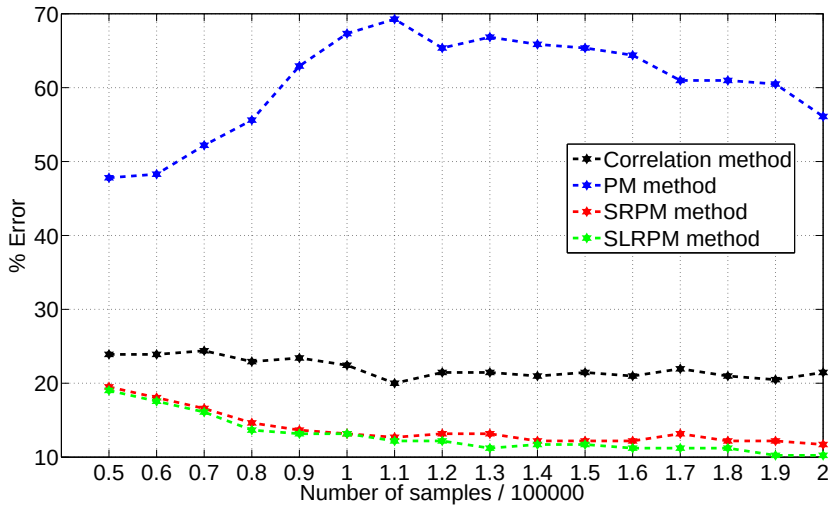

Figure 2.18: Plot of error percentage of the estimation methods vs. N with $p = 100$ and densely connected network with short range connections of neighborhood 3.

Remark 3

The performance (in terms of error percentage) of each method for network recovery in the spring-mass model does not change for change in signal-to-noise ratio up to 30 dB.

Remarks 2 and 3 are not surprising. Note that in the spring-mass model, we model the noise as an external force. So no matter how "forcefully" (noise variance) or in what way (noise distribution) we wobble the spring-mass system, the connectivity pattern won't change. Noise is not responsible for the connectivity pattern and the connectivity patterns estimated by the different methods shown here are due to the methods themselves.

2.3 Acknowledgement

Chapter 2.1, in full, is reprint of some of the material in Das, Anup; Sampson, Aaron L.; Lainscsek, Claudia; Muller, Lyle; Lin, Wutu; Doyle, John C.; Cash, Sydney S.; Halgren, Eric; Sejnowski, Terrence J.,"Interpretation of the precision matrix and its application in estimating sparse brain connectivity during sleep spindles from human electrocorticography recordings," Neural Computation, vol. 29, no. 3, pp. 603–642, 2017. The author of this thesis was the primary

author of this material. Chapter 2.2, in full, is currently being prepared for submission for possible publication of some of the material in Das, Anup; Sexton, Daniel; Lainscsek, Claudia; Cash, Sydney S.; Sejnowski, Terrence J.,"Characterizing brain connectivity during epileptic seizures from human electrocorticography recordings with unobserved inputs". The author of this thesis is the primary author of this material.

Chapter 3

Application in estimating brain connectivity during sleep spindles from human electrocorticography (ECoG) recordings

3.1 The significance of sleep and sleep spindles

During sleep, our brains are highly active. The low-amplitude, high-frequency activity in the neocortex characteristic of the awake state is replaced with a sequence of distinct phases with generally high-amplitude, low-frequency activity. Soon after the onset of sleep, brief episodes of 10-14 Hz synchronized spindling occur in the thalamus and cortex, producing large-scale spatiotemporal coherence throughout the forebrain. Throughout the night, the cortex alternates between periods of slow-wave sleep in the 2-4 Hz range and episodes of rapid eye movement sleep (REM), characterized by sharp waves of activity in the pons, the thalamus and in the occipital cortex, while also passing through intermediate nonREM sleep stages (Sejnowski, 1995; Sejnowski et al., 2000).

Activity in the sleeping brain is largely hidden from us because very little content of the brain activity that occurs during sleep directly enters consciousness. Hence it becomes important

to understand the patterns of electrical activity of neurons that occur in the brain during sleep. It has been suggested that the important functions of sleep are adaptive strategies, physical recovery, energy conservation, and information processing among others. There is also evidence supporting the role of sleep in learning and memory consolidation, and neuronal plasticity (Sejnowski, 1995; Sejnowski et al., 2000; Stickgold et al., 2005, 2007).

In (Fogel et al., 2007), researchers have made effort concerning the functional significance of the considerable interindividual differences in sleep spindles. The pattern of the sleep spindles within individuals is quite stable and varies little from night to night. Because of the remarkable intra-individual stability in sleep spindles from night to night, it was hypothesized that sleep spindles may serve as a "fingerprint" to account for inter-individual differences.

Three separate studies were performed to broadly examine the relationship between spindles and learning potential as measured by an intelligence quotient (IQ) test. In all the three studies, it was found that the number of sleep spindles was positively correlated with Performance IQ. Power in the $12-18$ Hz frequency band, a more objective indicator of the level of stage 2 spindle activity displayed even stronger correlations with Performance IQ. These results indicated that Performance IQ can be predicted simply by knowing the number of spindles and sigma power. This suggested that sleep spindles and sigma power may be biological markers for the specific abilities that are assessed by Performance IQ. This relationship might reflect the efficiency of information processing that is dependent on thalamocortical communication. In other words, richer cortical representations would require more thalamocortical interconnectedness. Maintenance and encoding of new information in a more complex system may require more thalamocortical activity or a more efficient thalamocortical system. This efficiency or added complexity may be reflected in the higher number of sleep spindles in the cortical areas underlying perceptual or analytical abilities in individuals with a higher Performance IQ.

In (Fogel et al., 2006), a study examined the learning-dependent changes in sleep, including stage 2 sleep spindles where subjects went through an intense period of simple motor procedural learning. Overall, the results from the study supported the hypothesis that sleep spindles are

intimately involved with the consolidation of simple motor procedural memory and may be important for the off-line reprocessing of recently acquired simple procedural tasks. It was found that there was an increase in the density of sleep spindles. Furthermore, it was found that the overall improvement on the motor tasks was positively correlated with the increase in sleep spindle density. In addition, there was an increase in the duration of stage 2 sleep following new learning. The magnitude of this change was very large: overall, there was a 15.8% increase in stage 2 sleep. The increase in the duration of Stage 2 sleep would be expected to increase the total number of sleep spindles alone. However, in addition to the increased duration of stage 2 sleep, there was an increase in spindle density. This suggested that motor learning-dependent changes in sleep spindles are independent of the time spent in stage 2 sleep. To determine if the changes to sleep following simple procedural memory were limited to stage 2 sleep and sleep spindles, REM density was also considered in this experiment. It was found that the duration of REM sleep did not change following new learning, nor did the density of REM, which suggested that the changes to sleep following new simple procedural learning affected only stage 2 sleep, and is specific to sleep spindles.

In (Schabus et al., 2004) researchers studied the functional significance of stage 2 sleep spindle activity for declarative memory consolidation. This study measured spindle activity during stage 2 sleep following a (declarative) word-pair association task as compared to a control task. Participants performed a cued recall in the evening after learning (160 word pairs) as well as in the subsequent morning after 8 hours of undisturbed sleep with full polysomnography. Overnight change in the number of recalled words correlated significantly with increased spindle activity during the experimental night. The results also suggested that the increase in spindle activity cannot simply be accounted for by changes in (stage 2) sleep architecture, or subjects' tiredness. They found that the relationship between memory performance and spindle activity was not an indirect effect of sleep-stage durations. Even when all sleep stages were controlled, the correlation between memory performance and spindle activity changes remained significant. Thus their findings provided evidence for the involvement of sleep spindle activity in memory consolidation as measured by the declarative memory task performed before and after the experimental night. The fact that spindle

activity was only related to changes in memory performance (increase or decrease over the night) was consistent with the hypothesis that spindle activity is specifically related to the consolidation of recently established memory traces. In other words, the findings of the study were in good agreement with the role of sleep spindles for memory consolidation. Several other researchers (Gais et al., 2002, 2004; Marshall et al., 2007) also have reported similar results.

Researchers in (Walker et al., 2002) found that improvement in motor skill performance in humans was due to sleep. They found evidence that continued improvement on a motor skill task occurs only across a night of sleep, while an equivalent period of wake offers no significant benefit to performance. Furthermore, more than half the variance in overnight improvement was explained by the amount of stage 2 sleep obtained during night. The authors further speculated that the enhancement in motor skill was due to the sleep spindles which are thought to cause massive calcium entry into pyramidal cells of the cerebral cortex, triggering intracellular calcium-dependent mechanisms required for synaptic plasticity (Sejnowski et al., 2000) and have been shown to increase following training on a motor task (Fogel et al., 2007, 2006) as described previously. These implications become most significant in the broader context of acquiring real life skillful actions duch as learning motor patterns required for movement based sports, learning a musical instrument, or developing artistic movement control. All such learning of new actions may require sleep before the maximum benefit of practice is expressed.

The authors in (Smith et al., 1994) have found impaired motor memory for a pursuit rotor task following stage 2 sleep loss in college students. Among the subjects considered, one group was subjected to REM sleep deprivation and the other group was subjected nonREM sleep deprivation following acquisition of a pure motor task, the pursuit rotor. Results showed that the REM sleep deprivation group had excellent memory for the task whereas the nonREM sleep deprivation group had a deficit in memory for the task. It was concluded that stage 2 sleep (where sleep spindles occur) rather than REM sleep was the important stage of sleep for efficient memory processing of the pursuit motor task. In other words, the newly acquired pure motor skill was most efficient when post-training stage 2 sleep was allowed and was impaired when this stage of sleep was reduced or

interrupted in the sleep night following the training session.

In (Meier-Koll et al., 1999), researchers have tried to link the storing of spatial information and episodic memory to sleep stages. Two city mazes, a simple and a complex one, were created by means of a computer program and were presented to the subjects on a TV screen. The task was to find various end points and to find the way back to the starting point via the help of a PC mouse. After the task, the subjects slept and the sleep stages were measured polygraphically. The subjects exposed to this experiment had significantly enhanced sleep spindle activities in comparison to subjects who had experienced neither maze. It was concluded that there is a functional linkage between stage 2 sleep spindles and learning or information processing in cortical areas.

Furthermore, because of its well-organized and consistent structure, sleep can be a valuable instrument for the investigation of neurological disorders such as Alzheimer's disease, progressive supranuclear palsy, REM sleep behavior disorder, Parkinson's disease, dementia with Lewy bodies, multiple system atrophy MSA, Huntington's disease and Creutzfeldt-Jakob disease (Petit et al., 2004). For example, the researchers in (Ferrarelli et al., 2007) have investigated whether sleep spindles differ between schizophrenia subjects, healthy individuals, and a psychiatric control group with a history of depression. The authors found a decrease in sleep spindle number, amplitude, duration, and integrated spindle activity in schizophrenia patients. Furthermore, integrated spindle activity had an effect size corresponding to 93.0% or 90.2% separation of the schizophrenia from the comparison or depression group. Since sleep spindles are generated by the thalamic reticular nucleus in conjunction with specific thalamic nuclei and are modulated by corticothalamic and thalamocortical connections, it was concluded that the deficit in sleep spindles in schizophrenia subjects may reflect dysfunction in thalamic-reticular and thalamocortical mechanisms and could represent a biological marker of illness. Hence finding the functional pattern in the brain during sleep spindles can provide valuable information for understanding the pathophysiology and for assisting the diagnosis of neurodegenerative diseases.

From these studies, it is quite clear that sleep and sleep spindles play a vital role in memory and learning and in investigation of neurological disorders in the human brain. Thus finding

connectivity during sleep will surely give us insights into the strong activity regions in the brain areas and how they are organized which may be responsible for information processing. Unfortunately, there has been very little research regarding the brain connectivity pattern during sleep. Moreover, researchers have termed the correlation of brain activity between brain regions as "functional connectivity" and have drawn conclusions based on that. These conclusions are flawed since the correlation method fails to identify the true connectivity pattern of a physical network as we have shown via extensive simulations using artificial networks.

3.2 Prior work in analyzing human brain connectivity during sleep spindles

In (Spoormaker et al., 2010), researchers have characterized the human functional brain network during nonREM sleep by using the correlation method on functional magnetic resonance imaging (fMRI) recordings. In this study, the authors used the correlation method to explore how physiological changes during sleep are reflected in functional connectivity and small-world network properties of a large-scale, low-frequency functional brain network. They observed that in the transition from wakefulness to light sleep, thalamocortical connectivity was sharply reduced, whereas corticocortical connectivity increased; corticocortical connectivity subsequently broke down in slow-wave sleep. Local clustering values were closest to random values in light sleep, whereas slow-wave sleep was characterized by the highest clustering ratio (gamma). The authors claimed that the changes in consciousness in the descent to sleep are subserved by reduced thalamocortical connectivity at sleep onset and a breakdown of general connectivity in slow-wave sleep, with both processes limiting the capacity of the brain to integrate information across functional modules.

The authors in (Larson-Prior et al., 2009) studied the cortical network functional connectivity during sleep using the correlation method. They examined the functional connectivity using conventional seed-based analyses in 3 primary sensory and 3 association networks as normal young adults transitioned from wakefulness to light sleep. They found that functional connectivity in

nonREM sleep was maintained in each network throughout all examined states of arousal. Further, these networks were consistent across subjects. The authors were surprised that they did not find any evidence of change in functional connectivity in the sensory (visual, auditory, and somatomotor) or cognitive (dorsal attention, default and executive control) networks examined.

In (Andrade et al., 2011), the authors also have investigated the functional connectivity between the hippocampal and neocortical regions of the human brain in nonREM sleep using the correlation method. They found increased connectivity between hippocampal and neocortical regions of the brain during stage 2 sleep spindles suggesting an increased capacity for global information transfer during sleep spindles.

Though the results of these studies are interesting, further experimental validation is necessary to support their claims and to derive a more thorough physiological interpretation. A flaw in these analyses is the use of the correlation method to characterize the brain functional connectivity pattern during sleep since two brain regions might show very high correlation even if there is not strong physical connection between them, rather the correlation could be due to a common input. Hence the motivation for the application of the sparse regularized precision matrix (SRPM) method in connectivity estimation during sleep.

3.3 Automatic detection of sleep spindles using delay differential analysis (DDA)

In order to detect sleep spindles reliably in the ECoG data, we used DDA. In Figure 3.1(a), DDA is introduced as a time domain classification framework based on embedding theory in nonlinear dynamics (Kremliovsky et al., 1997; Lainscsek et al., 2013; Sampson et al., 2015; Lainscsek et al., 2015, 2013). Given a recording (here ECoG data) from some unknown dynamical system (here the brain), an embedding will reveal the nonlinear invariant properties of the system, even from a single time series (Takens, 1981). The embedding in DDA provides a low-dimensional nonlinear functional basis onto which the data are mapped. Since this basis is built on the dynamical

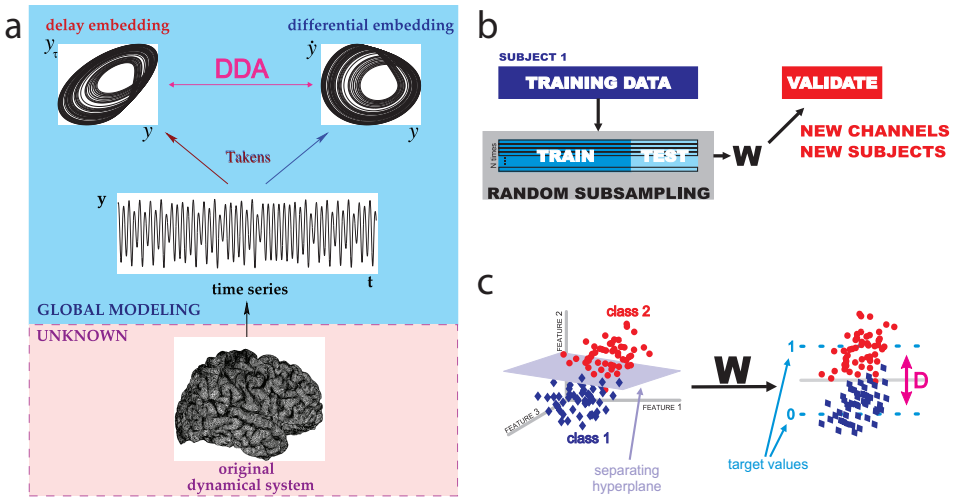

Figure 3.1: Delay Differential Analysis (DDA). (a) For an unknown dynamical system (such as the brain) from which we can record the value of a single variable over time (such as ECoG data), embedding theory states that we can recover the nonlinear invariant properties of the original system. DDA combines delay and differential embeddings in a functional form which allows time-domain classification of the data. (b) Performance of DDA model forms is evaluated with repeated random subsampling cross-validation. The data is repeatedly divided at random into training and testing sets. (c) Applying the weights (set by SVD) to the DDA features transforms from the feature space to a one-dimensional distance from the hyperplane of separation. This value is used as a measure of performance for classification.

structure of the data, preprocessing of the data (such as filtering) is not necessary. DDA yields a low number of features (around 4), as compared with traditional spectral techniques, which greatly reduces the risk of overfitting.

Another way of viewing DDA models is as sparse Volterra series (Volterra, 1887, 1959). A general nonlinear real-valued function can be expressed as a Taylor series expansion of functionals of increasing complexity around a fixed point. When the function represents the behavior of a dynamical system the expansion becomes a Volterra series. DDA restricts the complexity of the analysis by using a low-dimensional sparse delay differential equation model. In such a model, linear and nonlinear data components are analyzed in an interconnected manner. This reduces the computational load, and, leaving some of the non-relevant dynamics unmodeled highly reduces the effect of artifacts and other signals unrelated to those we aim to detect.

All of these properties make DDA well-suited to the problem of spindle detection. Frequency-based approaches which have often been used for detecting spindles are sensitive to artifacts

involving transient increases in spectral power in the band of interest and parameters often have to be adjusted to fit individual subjects. In DDA, we train on real data from a single subject and a single electrode and find the relevant dynamical features for spindle identification that are highly generalizable to a wide class of subjects and recordings.

In practice, DDA (see Figure 3.1(a)) combines a differential embedding with a delay embedding by relating them in a polynomial function

$$\dot{x}(t) = \sum_{i=1}^{I} a_i \prod_{n=1}^{N} x(t-\tau_n)^{m_{n,i}} \text{ for } \tau_n, m_{n,i} \in \mathbb{N}_0 \tag{3.1}$$

where I is the number of monomials in the model, N is the number of delays in each monomial, and $m_{n,i}$ is the order of the nth term in the ith monomial. The time derivative of the data, $\dot{x}(t)$, is computed with a five-point center derivative (Miletics et al., 2005). The estimated coefficients a_i for the model, as well as the least-squares error, form the low-dimensional feature space used for classifying the data (here, for detecting spindles). The least-squares error is defined as

$$\rho = \sqrt{\frac{1}{K} \sum_{k=1}^{K} \left(\dot{x} - \sum_{i=1}^{I} a_i \prod_{n=1}^{N} x_{\tau_n}^{m_{n,i}} \right)^2} \tag{3.2}$$

where K denotes the number of time points, $\dot{x}$ denotes $\dot{x}(t)$, and x_{τ_n} denotes $x(t-\tau_n)$.

The particular form of the polynomial in (3.1) was chosen after an exhaustive search of all model forms subject to the following constraints: model forms were constrained to two delays ($N \leq 2$), three terms ($I \leq 3$), and third-order nonlinearity ($\sum_n m_{n,i} \leq 3$), and the delays were constrained to values up to 150 time points ($\tau_n \leq 150$). For model selection, we used a training data set with human expert-scored spindles in stereoelectroencephalogram (SEEG) data sampled at 500 Hz. As shown in Figure 3.1(b), the best-performing model was selected using repeated random subsampling cross-validation (Kohavi, 1995). This method involves repeatedly dividing the data at random into training and testing sets. Each random split assigns 70% of the data to the training set and 30% to the testing set. The model form and values of the delays τ_1 and τ_2 in (3.3) were chosen to maximize the separation between spindle and non-spindle epochs. For spindle detection, we used

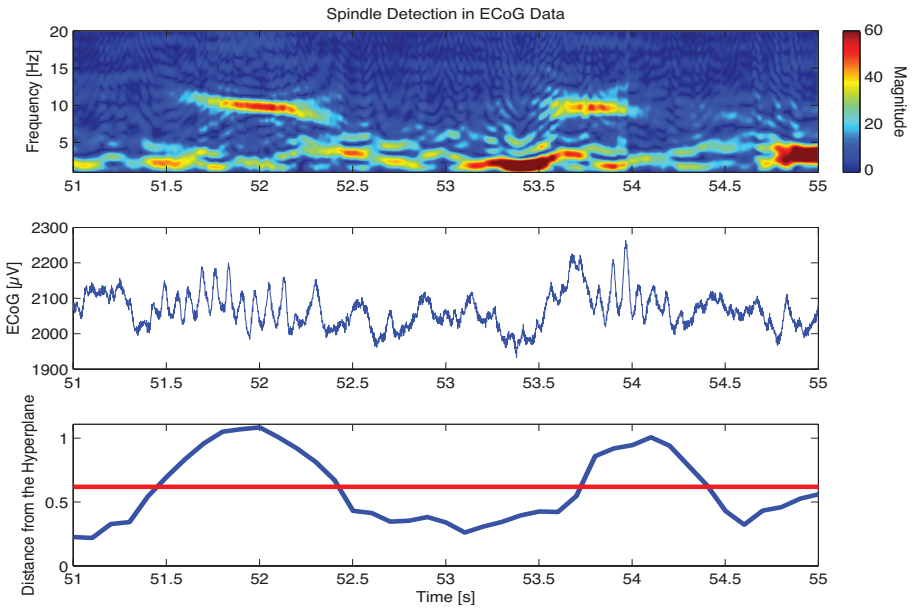

Figure 3.2: DDA spindle detection. The top panel shows a spectrogram of the ECoG data for a four-second time period in which two sleep spindles are detected. The middle panel shows the same data in the time domain after the application of a 60 Hz notch filter for visualization. The bottom panel shows the spindle detection index from DDA, higher values above the set threshold, in red, correspond to the presence of spindles.

the model

$$\dot{x} = a_1 x_{\tau_1} + a_2 x_{\tau_2} + a_3 x_{\tau_1}^2 \tag{3.3}$$

with $\tau_1 = 19\ \delta t$ and $\tau_2 = 12\ \delta t$, where $\delta t = 1/f_s = 2$ ms. Different values of the delays would be selected for a different sampling rate. From the cross-validation procedure, we obtain weights using singular-value-decomposition (SVD), which we apply to the four features from this model, a_1, a_2, a_3, and ρ, to transform the four-dimensional feature space to a one-dimensional distance from a hyperplane of separation. This transformation is illustrated in Figure 3.1(c). The small number of features is a general feature of DDA, which has the advantages of minimizing overfitting and reducing the influences of artifacts in the recordings. DDA is also more sensitive than traditional methods based on frequency analysis and thresholding, allowing spindles to be detected in most electrodes.

After selecting the model based on the SEEG training data, its performance was evaluated

on a set of twenty recordings from SEEG, ECoG, and laminar electrodes. Across this data set, our DDA-based spindle detector agrees with the expert scoring with a mean area of 0.84 under the receiver operating characteristic (ROC) curve and a mean F_1 score of 0.9. This is comparable to or better than typical inter-rater agreement between human experts. Researchers in (Warby et al., 2014) found a mean F_1 score of 0.75 for marked-spindles for a group of 24 experts as compared with the group consensus (designed to maximize mean individual F_1 score). This finding is similar to those of other studies of human-expert sleep-scoring, where typical inter-rater agreement is in the range of 72% (Basner et al., 2008; Danker et al., 2009; Iber et al., 2007).

For detecting the spindles used in this analysis, we treat each channel separately, and use sliding windows of 0.25 seconds, with a 0.05 second step size. In each window we obtain a distance from the hyperplane as described above, which serves as an index indicating the presence of a spindle when it exceeds a set threshold. The threshold was set to maximize agreement with human scoring in the training data, as measured by area under the ROC curve. Figure 3.2 shows, for two example spindles, the output detection index from DDA along with the raw waveform and spectrogram for reference from one channel of ECoG data.

It is important to note that DDA is used here only to identify spindle epochs for study, and the outputs of DDA are not used in any of the subsequent analysis.

3.4 Sparse connectivity estimation using SRPM during sleep spindles

ECoG recordings from a male patient of age 32 with long-standing pharmaco-resistant left temporal lobe complex partial epilepsy were analyzed. Recordings were performed using a standard clinical recording system (XLTEK, Natus Medical Inc., San Carlos, CA) with a 500 Hz sampling rate. The reference channel was a strip of electrodes placed outside the dura and facing the skull at a region remote from the other grid and strip electrodes. Subdural electrode arrays were placed to confirm the hypothesized seizure focus and locate epileptogenic tissue in relation to essential cortex,

Table 3.1: Medication information of the patient.

Day	Medication
Home medications	Keppra 1000 bid
Day 1	Levetiracetam 1000 bid
Day 2	Levetiracetam 1000 bid
Day 3	Levetiracetam 500 bid
Day 4	Levetiracetam 500 bid
Day 5	off
Day 9	Levetiracetam 1500 qhs, lorazepam 1mg IV
Day 10	Levetiracetam 1000 bid

thus directing surgical treatment. The decision to implant, the electrode targets, and the duration of implantation were made entirely on clinical grounds with no input from this research study. All data acquisition was performed under protocols monitored by Institutional Review Board of the Massachusetts General Hospital according to National Institutes of Health guidelines. Data selected for use in this study were exclusively from stage 2 sleep, during time periods when no seizures were occurring. The medication information for the patient is given in Table 3.1. The recordings analyzed here are from Day 10.

After detecting the sleep spindles for each channel (see Figure 3.3) as described above, we selected only those time windows in which spindles were present in a relatively large number of channels. We selected 10 such time windows in total and estimated the SRPM for each of them. The average number of channels in which sleep spindles were present in the selected time windows was found to be 32.10 ± 6.78. We then applied the Louvain method for community detection (LMCD) (Newman et al., 2004, 2006; Brandes et al., 2008; Blondel et al., 2008; Reichardt et al., 2006; Ronhovde et al., 2009; Sun et al., 2009; Sporns, 2010) on the SRPM to cluster similar electrodes together. The regularization parameter λ in the SRPM method was chosen to be large enough to minimize the inter-cluster connectivity after applying the LMCD, thus clustering the brain regions with the strongest connectivity. The range of values of λ used for the analysis was between 0.035 and 0.054. The SRPM method was found to be fairly robust to the regularization parameter and small changes in the values of the regularization parameters did not significantly alter the results

reported here. Figure 3.3 shows the clustered brain regions in the 10 time windows considered. Note that in all the panels in Figure 3.3 the clusters are spatially localized, indicating spatially localized connectivity among brain regions. The average modularity index (MI) Q across the 10 panels was found to be 0.41 defined as

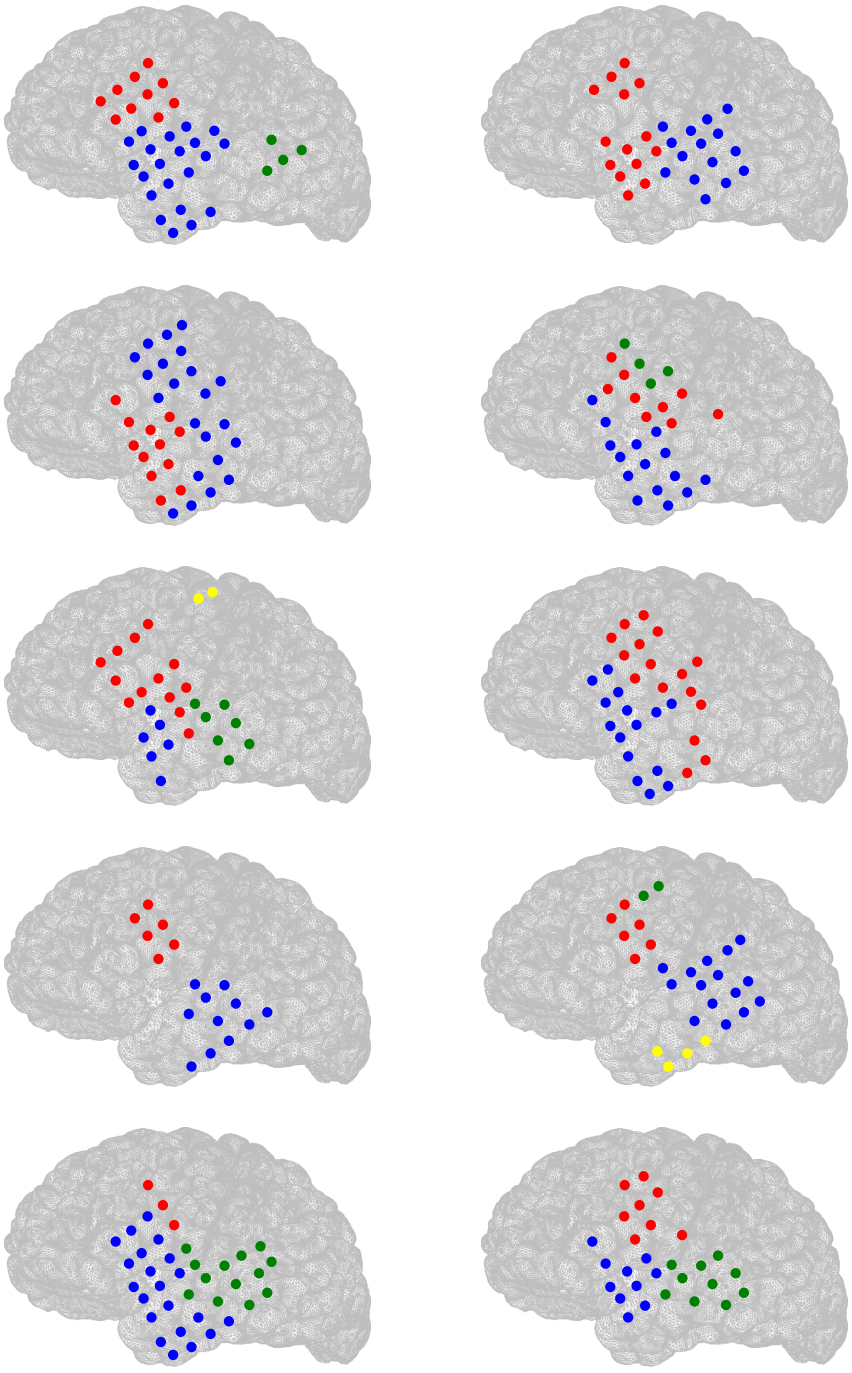

Figure 3.3: Estimating brain connectivity during sleep spindles from human ECoG data by the SRPM method in 10 epochs from a patient. Circles denote electrode locations and clusters (of strongest activity) put together by the LMCD have the same color. For example, in the left top panel, there are three clusters of strongest activity denoted by red, blue, and green.

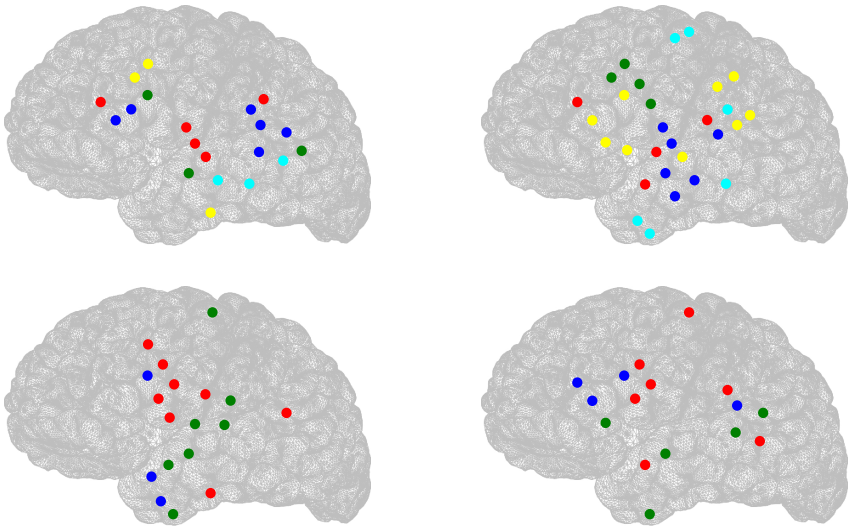

Figure 3.4: Estimating brain connectivity during absence of spindles from human ECoG data by the SRPM method in 4 epochs from a patient. Circles denote electrode locations and clusters (of strongest activity) put together by the LMCD have the same color. For example, in the left top panel, there are five clusters of strongest activity denoted by red, blue, green, yellow, and cyan.

$$Q = \frac{1}{2M} \sum_{i,j} \left[B_{ij} - \frac{s_i s_j}{2M} \right] \delta(\sigma_i, \sigma_j) \tag{3.4}$$

where B_{ij} denotes the strength of connectivity (obtained from the SRPM) between brain regions i and j, $s_i = \sum_j B_{ij}$ denotes the sum of connectivity strengths between brain region i and the rest of the brain regions, σ_i denotes the cluster to which brain region i belongs to, $M = \frac{1}{2} \sum_{ij} B_{ij}$, and $\delta(\sigma_i, \sigma_j)$ is 1 if $\sigma_i = \sigma_j$ and 0 otherwise (Blondel et al., 2008; Reichardt et al., 2006). Also, the number of clusters is not the same in the panels. Also, observe that in different panels, different brain regions show the strongest connectivity.

We next analyzed the time windows in which sleep spindles were not present in any of the 64 channels. We selected 21 such time windows in total and observed that the clustered brain regions were not as spatially localized as that of the time windows where sleep spindles were present. Figure 3.4 shows the clustered brain regions in 4 time windows in which there were no spindles. The average modularity across all the nonspindle time windows (including those not shown here) was found to be 0.49. The number of clusters is not the same in the panels, and in different panels, different brain regions show the strongest connectivity.

In order to quantify the degree of spatial localization in spindle and nonspindle cases, we calculated the average relative surface area (ARSA) for both the cases. The ARSA for the spindle case was defined to be the average of the relative surface areas (RSAs) of all clusters across all time windows in which spindles were present and the ARSA for the nonspindle case was defined similarly. The RSA of a cluster was defined as

$$\text{RSA} = \frac{\text{SA}}{\text{TA} \times \text{NA}} \tag{3.5}$$

where SA denotes the surface area spanned by the cluster, TA denotes the total surface area spanned by all the electrodes, and NA denotes the number of electrodes in that particular cluster. The ARSA for the spindle case was found to be 0.010 ± 0.006 and the ARSA for the nonspindle case was found to be 0.031 ± 0.009 which is significantly higher than that of the spindle case. This indicates that

the brain networks during sleep spindles are highly spatially localized in comparison to that during absence of spindles.

Moreover, we applied the correlation method and almost all brain regions showed very strong connectivity after applying the LMCD on the correlation matrix indicating that the correlation method does not result in sparse connectivity between brain regions.

3.5 Discussion

The correlation method cannot find true physical connections in a network since two brain regions might show very high correlation even when the two regions are not directly connected, rather the high correlation could be due to the strong interaction of the two regions with common input from a third region. Even though past research has primarily focused on the correlation method and conclusions have been drawn based on the results, those experiments need to be repeated using our proposed approach to validate the correctness of the findings. Researchers have proposed solutions to this problem and have suggested using SRPM assuming that the connectivity structure is sparse. This method yields partial correlations to measure strong direct interactions between pairs of regions while simultaneously removing the influence of the rest of the regions thus identifying conditionally independent regions. Even though the SRPM and PM methods have been previously applied in brain research to identify functionally connected networks in the human brain and conclusions have been drawn regarding how the brain processes information, more experimental analyses are necessary to verify these claims.

Thus we generated simple artificial networks via simulation and demonstrated through extensive analysis that the SRPM method can indeed find the true physical connection in a network. The spring-mass model and the two network topologies in the RC circuit model were used to evaluate the performance of the SRPM method. We showed successfully that, as long as the connectivity structure is sparse, the SRPM method has the potential to outperform the correlation and PM methods. For these two linear problems, SRPM recovered the exact network connectivity.

This result is in contrast to the results in (Sojoudi et al., 2016, 2014) where the correlation and PM methods gave equivalent or better performance than the SRPM method, although a different algorithm was used to solve the optimization problem in SRPM. Even though the algorithm in (Sojoudi et al., 2016, 2014) promoted sparsity, it did not successfully recover the connectivity pattern in a physical network.

The superior performance of the SRPM method on the artificial networks encouraged us to apply the same for analyzing the human brain. We applied the SRPM method for estimating brain connectivity during sleep spindles from human ECoG data using an 8×8 electrode array. For sleep spindle detection we used DDA, which is a time domain classification framework based on embedding theory in nonlinear dynamics. After obtaining the SRPM during the sleep spindles, we clustered similar brain regions of strongest activity together using the LMCD and found spatially localized brain networks during spindles. Moreover, analyzing the time windows in which sleep spindles were not present, we found that the clusters were not as compact compared with that of the time windows where sleep spindles were present. These findings suggest that regional interactions in the cortex are stronger during sleep spindles. Moreover, this gives us insight into the local information processing during spindle activity in brain. During sleep spindles, the connectivity pattern in the brain was transiently synchronized thus providing evidence for globally organized coherence patterns. These findings on spatial localization during spindles provide us with new insights into how sleep spindles have a major role in learning, memory consolidation, and neuronal plasticity.

Furthermore, the clusters shown in Figure 3.3 obtained during sleep spindles were large and in 7 out of the 10 epochs, there was a cluster that included regions of both the temporal and prefrontal cortices. This suggests that some of the connectivity underlying the clustering are association fiber bundles that project between the major cortical lobes. It is worth noting that the comparison we are making is between spindle epochs and all other epochs during this recording of stage 2 sleep. These non-spindle epochs, then, can be quite heterogeneous, with various other phenomena such as K-complexes or other slow oscillations occuring at different times throughout. As such, we expect

that the connectivity pattern to change accordingly throughout these periods. By including a number of different non-spindle epochs in our analysis then, we establish a broad baseline for connectivity during stage 2 sleep that we can then compare to the specific connectivity patterns observed during spindles. Although the data was from a patient with epilepsy, the recordings we analyzed were during long seizure-free periods. Nonetheless, there is concern that the cortical sleep states may not be normal and further work is needed to confirm our results in healthy control subjects. Another issue is that, the ECoG recordings that we analyzed were from a single patient and hence there is a need to test our methods in a large number of epileptic patients. It is important to note that the inputs from the thalamus also act as common inputs to the cortex and constitute latent (unobserved) variables in our analysis. In order to estimate the connectivity by modeling the latent inputs, we have also applied the SLRPM method (Chandrasekaran et al., 2012) on the same ECoG recordings shown here and found very similar results to the SRPM method which is surprising. The author of this thesis does not have an explanation for the similar performance of the two methods for sleep spindle analysis.

In a recent work (Brunton et al., 2016), the authors used the dynamic mode decomposition algorithm and clustering methods to characterize brain networks during sleep spindles. Similar to our results, the researchers found that the brain networks during sleep spindles are spatially localized. However, no results were reported in the absence of sleep spindles. Other researchers (Andrillon et al., 2011) also have found similar results. In a recent study (Muller et al., 2016), by analyzing the phase coherence, we have found that sleep spindles are associated with traveling waves which provide further support for our findings.

The analytical and experimental advances made in this thesis on sleep, learning and information processing in the brain are exciting because they suggest a possible resolution to one of the greatest mysteries in biology, the nature and function of sleep. The experimental results so far are incomplete and tentative, but they should lead us toward further advances that will widen our understanding of sleep. Additional analysis is needed to test these conclusions and these are reserved for future research.

Finally, the same SRPM method we have used to analyze ECoG recordings could also be applied to single unit recordings, local field potentials, and fMRI data.

3.6 Acknowledgement

Chapter 3, in full, is reprint of some of the material in Das, Anup; Sampson, Aaron L.; Lainscsek, Claudia; Muller, Lyle; Lin, Wutu; Doyle, John C.; Cash, Sydney S.; Halgren, Eric; Sejnowski, Terrence J.,"Interpretation of the precision matrix and its application in estimating sparse brain connectivity during sleep spindles from human electrocorticography recordings," Neural Computation, vol. 29, no. 3, pp. 603–642, 2017. The author of this thesis was the primary author of this material.

Chapter 4

Application in estimating brain connectivity during epileptic seizures from human electrocorticography (ECoG) recordings

Epilepsy is the world's one of the most common brain disorder, characterized by sudden occurrence of unprovoked seizures, affecting more than 50 million people worldwide. There is plenty of evidence of significantly altered brain connectivity during epilepsy, especially during seizure periods, in the human brain (Stam, 2014; Diessen et al., 2013; Kramer et al., 2012). However, research on characterization of human brain functional connectivity during epileptic seizures have only been limited to the use of the correlation method.

4.1 Prior work in analyzing human brain connectivity during epileptic seizures

The authors in (Vega-Zelaya et al., 2015) have estimated the brain functional connectivity during partial seizures from foramen ovale electrode (FOE) and electroencephalogram (EEG) recordings in 22 temporal lobe epilepsy (TLE) patients using the correlation method. Brain network

connectivity was characterized using average clustering coefficient (ACC) and modularity index (MI). The ACC increased and the MI decreased after the seizure onset. Researchers in (Kramer et al., 2010) have analyzed brain functional connectivity in 48 seizures from electrocorticography (ECoG) recordings in 11 epilepsy patients using the correlation method. They found that the ACC increased after the seizure onset. A research study in (Ponten et al., 2007) have characterized, via the correlation method, the functional connectivity from EEG recordings in 7 patients suffering from mesial TLE (MTLE) and reported increase in ACC after seizure onset. In another study (Schindler et al., 2008), researchers have carried out an analysis of the brain activity from EEG recordings in 100 epileptic seizures from 60 patients using the correlation method. They characterized functional connectivity by ACC and found that it increased after seizure onset. Furthermore, in (Burns et al., 2014), researchers have characterized brain functional connectivity in terms of eigenvector centrality (EC), from ECoG recordings in 12 patients before and after seizure onset via the correlation method. They found that the brain functional connectivity significantly changed before and after seizure onset and they were able to successfully localize the seizure onset zones by analyzing this change in connectivity (EC) of the ECoG electrodes.

As mentioned previously, these results of the human brain functional connectivity during epileptic seizures measured using the correlation method might be flawed since existing brain imaging technologies cannot simultaneously record from the entire human brain and brain regions which are observed can receive common inputs from latent or unobserved brain regions. Furthermore, it is known that there can be dopaminergic, norepinephrine or cholinergic fiber projections to the cortex, from which EEG or ECoG recordings are usually taken, during seizures (Krimer et al., 1998; Lado et al., 2008; Sato et al., 1992; Attwell et al., 2002; Giorge et al., 2004) and these neuromodulatory projections serve as common latent inputs to the cortex and induce spurious correlations among the EEG or ECoG electrodes. But the SLRPM method calculates the precision matrix of the conditional statistics of the observed brain regions given the latent brain regions and this helps to remove the influence of common observed and latent inputs on the EEG or ECoG recordings. In this way, we may be able to find more accurate brain connectivity from the recordings and this will help us

analyze the brain activity during epileptic seizures.

We demonstrate the application of the SLRPM method to estimate brain connectivity during epileptic seizures from human ECoG recordings. These recordings are analyzed using SLRPM and brain connectivity has been quantified using modularity index (MI), clustering coefficient (CC), and eigenvector centrality (EC).

4.2 Epileptic seizure analysis from human ECoG recordings using SLRPM

4.2.1 ECoG data acquisition and protocol

Continuous ECoG recordings from 12 patients (see Table 4.1 for details) with long-standing pharmaco-resistant complex partial epileptic seizures were analyzed. Recordings were performed using a standard clinical recording system (XLTEK, Natus Medical Inc., San Carlos, CA) with a 500 Hz sampling rate. The reference channel was a strip of electrodes placed outside the dura and facing the skull at a region remote from the other grid and strip electrodes. Subdural electrode arrays were placed to confirm the hypothesized seizure focus and locate epileptogenic tissue in relation to essential cortex, thus directing surgical treatment. The decision to implant, the electrode targets, and the duration of implantation were made entirely on clinical grounds with no input from this research study. All data acquisition was performed under protocols monitored by Institutional Review Board of the Massachusetts General Hospital according to National Institutes of Health guidelines.

4.2.2 Preprocessing and referencing

ECoG recordings were first low pass filtered at 125 Hz using a 6th order Butterworth filter to remove high frequency artifacts. Line frequencies 60 Hz and 120 Hz were then notch filtered using a 4th order Butterworth filter. Next, to reduce the signals from the reference electrode, at

Table 4.1: Patients' details.

Patient	Age	Sex (Male (M)/Female (F))
1	46	F
2	55	F
3	29	M
4	45	F
5	25	M
6	23	M
7	28	M
8	35	M
9	32	M
10	23	F
11	19	F
12	32	M

each time point, the average signal of all electrodes was subtracted from each electrode (Nunez et al., 2006; Kramer et al., 2010; Cimenser et al., 2011) (this process is also known as the common average referencing (CAR)). Finally, recordings were z-scored (mean-variance normalization) for each channel (Varsavsky et al., 2010).

After the preprocessing steps, we can now apply our methods on the ECoG recordings for comparison. We used MI, CC, and EC to quantify brain connectivity. These three measures are widely used for characterizing activity in brain imaging studies. These three measures are described next. All these measures are directly applied on the estimated connectivity matrix from the methods considered. In order to calculate the measures, we used the brain connectivity toolbox (BCT) (Sporns, 2010).

4.2.3 Description of brain connectivity measures

Modularity index (MI)

For clustering of brain regions, we use MI (Newman et al., 2004, 2006; Brandes et al., 2008; Blondel et al., 2008; Reichardt et al., 2006; Ronhovde et al., 2009; Sun et al., 2009; Sporns, 2010), which was also previously used in sleep spindle analysis. We define it here again for completeness.

MI Q is defined as

$$Q = \frac{1}{2M} \sum_{i,j} \left[B_{ij} - \frac{s_i s_j}{2M} \right] \delta(\sigma_i, \sigma_j) \tag{4.1}$$

where B_{ij} denotes the strength of connectivity (obtained from the methods) between brain regions i and j, $s_i = \sum_j B_{ij}$ denotes the sum of connectivity strengths between brain region i and the rest of the brain regions, σ_i denotes the cluster to which brain region i belongs to, $M = \frac{1}{2} \sum_{ij} B_{ij}$, and $\delta(\sigma_i, \sigma_j)$ is 1 if $\sigma_i = \sigma_j$ and 0 otherwise. Note that MI measures the fraction of the strengths of the connectivities belonging to the same cluster minus the probability of the strengths of random connectivities belonging to the same cluster. Hence, in order to have positive MI, the strengths of the connectivities belonging to the same cluster has to be better than random. Extraction of brain networks is based on MI optimization and we use the Louvain method for community detection (LMCD) (Newman et al., 2004, 2006; Brandes et al., 2008; Blondel et al., 2008; Reichardt et al., 2006; Ronhovde et al., 2009; Sun et al., 2009; Sporns, 2010), which is a fully automatic method, for this optimization. In other words, LMCD maximizes the strengths of connectivities within clusters, and minimizes the strengths of connectivities between clusters. Clustering of brain regions based on MI optimization is a widely used method in human brain imaging data analysis (Rubinov et al., 2010; Bassett et al., 2011; Meunier et al., 2010; Zuo et al., 2012; Rubinov et al., 2011; Bassett et al., 2010; Sporns, 2011; Cole et al., 2014; Bruno et al., 2017).

Clustering coefficient (CC)

The CC (Onnela et al., 2005; Saramaki et al., 2007) of a brain region in a network quantifies how well its neighboring brain regions are connected. CC C_i of the ith brain region is defined as

$$C_i = \frac{1}{k_i(k_i - 1)} \sum_{j,h} (B_{ij} B_{jh} B_{hi})^{1/3} \tag{4.2}$$

where k_i is the number of neighboring brain regions of the ith brain region and B_{ij} is the strength of connectivity (obtained from the methods) between brain regions i and j. The average CC (ACC) C

of an entire brain network can be defined as

$$C = \frac{1}{M}\sum_i C_i \tag{4.3}$$

where M is the total number of observed brain regions. CC is also a widely used measure in human brain imaging data analysis (Vega-Zelaya et al., 2015; Kramer et al., 2010; Ponten et al., 2007; Schindler et al., 2008; Rubinov et al., 2010; Wang et al., 2017; Bruno et al., 2017).

Eigenvector centrality (EC)

The EC (Newman et al., 2010) is a measure of the influence or importance of a brain region in the entire brain network. This is based on the concept that a brain region more strongly connected to high influential brain regions will have relatively higher EC. Mathematically, the relative EC e_i of the ith brain region can be written as

$$e_i = \frac{1}{\kappa}\sum_j B_{ij}e_j \tag{4.4}$$

where B_{ij} is the strength of connectivity (obtained from the methods) between brain regions i and j and e_j is the relative EC of the jth brain region. In matrix-vector notation, the above set of equations can be compactly written as a eigenvector equation as

$$\mathbf{Be} = \kappa\mathbf{e} \tag{4.5}$$

where $\mathbf{B}$ is the estimated connectivity matrix from the methods and $\mathbf{e}$ is its eigenvector which contains the relative influences of the brain regions. Hence, the relative ECs can be found by solving the eigenvector equation in (4.5). But note that (4.5) has multiple solutions. The relative ECs are always assumed to be non-negative. The following two theorems help us find EC from (4.5). These theorems are valid for an estimated connectivity matrix $\mathbf{B}$ which is real, symmetric, and with all elements non-negative (we take the absolute values of the elements of the estimated connectivity

matrix to make them non-negative).

Theorem 1. *The largest positive eigenvalue* κ_1 *of* $\mathbf{B}$ *is always greater than or equal to the magnitude of its most negative eigenvalue.*

Proof: See p. 346 in (Newman et al., 2010).

Theorem 2. *There exists an eigenvector with eigenvalue* κ_1 *all of whose elements are non-negative.*

Proof: This follows from Theorem 1. See p. 347 in (Newman et al., 2010) for details.

And since there can be at most one eigenvector with all elements non-negative, the eigenvector corresponding to the largest positive eigenvalue contains the relative ECs of the brain regions. The optimization problem in (4.5) can be solved by using the *power method* (Newman et al., 2010). The EC measure has been previously used by researchers to quantify connectivity in human brain imaging studies (Burns et al., 2014; Zuo et al., 2012; Lohmann et al., 2010; Joyce et al., 2010).

4.2.4 Seizure analysis

After preprocessing of the ECoG recordings, the methods are applied on 4 s non-overlapping time-windows and brain connectivity is then quantified using the described measures. Total 25 minutes time-segment has been analyzed for each seizure which includes 10 minutes preictal time-segment. Note that even though it is difficult to characterize the preictal period of seizures which vary from seizure-to-seizure within a patient and in seizures from different patients (Rozman, 2015), we define the 10 minute preseizure period as our preictal period for all seizures in all patients. Information regarding the number and type of seizures analyzed for each patient is given in Table 4.2 (total 214 seizures out of which 133 were clinical seizures).

The regularization parameter λ in the SRPM method was set to 0.02 and the regularization parameters α and β in the SLRPM method were set to 0.02 and 0.2 respectively for all seizures and all patients. The SRPM and SLRPM methods were found to be robust to changes in the regularization parameters and small changes in the values of these did not change the results and implications of the thesis.

Table 4.2: Number and type of seizures for each patient. Clinical and sub-clinical seizures are denoted by "C" and "SC" respectively.

Patient	Number of seizures analyzed
1	5 C and 2 SC
2	5 C
3	7 C
4	3 C
5	62 C
6	10 C
7	1 C and 2 SC
8	7 C and 4 SC
9	19 C
10	10 C
11	1 C and 4 SC
12	3 C and 69 SC

Table 4.3: Medication information of patient 1.

Day	Medication
On admission	Trileptal 300 tid + 150mg OD, Clonazepam 0.25mg tds
Day 1	Trileptal 300 bid; Clonazepam 0.25mg tds
Day 2	Trileptal 300 od; Clonazepam 0.25mg tds
Day 3	Clonazepam 0.25mg tds
Day 4	Clonazepam 0.25mg bid
Day 5	Clonazepam 0.25mg od
Day $6-9$	no AEDs
Day $10-11$ and on discharge	Trileptal 300 tid + 150mg OD, Clonazepam 0.25mg tds

Patient 1

Medication information of this patient is shown in Table 4.3. Electrode locations are shown in Figure 4.1. As shown, there were two grids, one over the anterior temporal and fronto-parietal region and the other was placed over the posterior temporal-parietal region. There were three strips placed in the frontopolar region, the subfrontal region and the subtemporal region. There were also depth electrodes inserted in the inferior frontal, and the anterior and posterior temporal regions. We analyzed 5 clinical seizures and 2 sub-clinical seizures from this patient. Among the five clinical

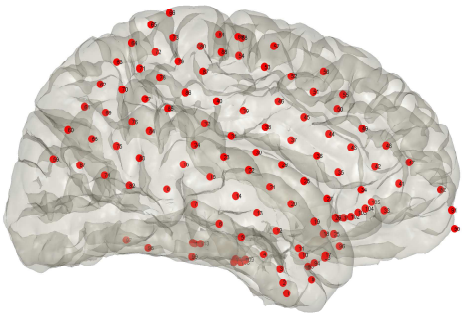

Figure 4.1: Electrode locations in patient 1.

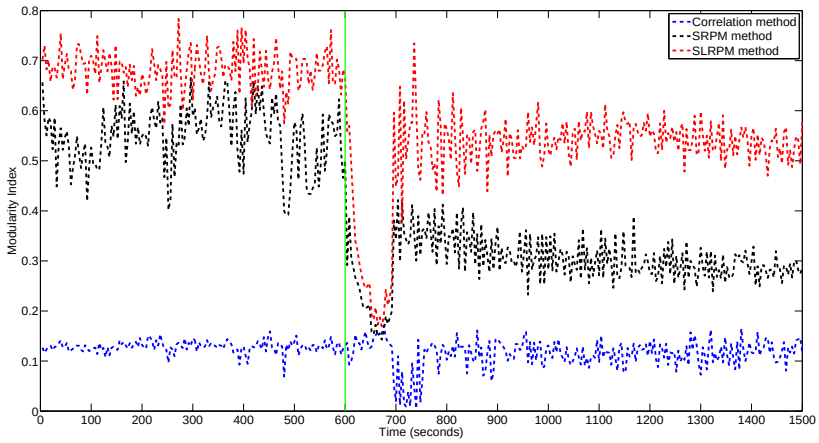

Figure 4.2: MI plots for the three methods for seizure 1 in patient 1. Green line denotes the seizure onset time.

seizures, seizure 1 corresponds to day 7, seizures 2 and 3 correspond to day 8, and seizures 4 and 5 correspond to day 9. Among the two sub-clinical seizures, seizure 1 belongs to day 7 and seizure 2 belongs to day 9 respectively.

The MI plots for the three methods for clinical seizure 1 are shown in Figure 4.2. This seizure lasted for approximately 90 seconds (this was determined by the clinician). Observe that the MI estimated by the SRPM and SLRPM methods during the seizure are relatively lower than the preictal and post-ictal MI estimated by the same methods respectively. Furthermore, the preictal and post-ictal MI in the SLRPM method are relatively higher than those in the SRPM method respectively and both methods have higher MI than the correlation method. Since the SLRPM

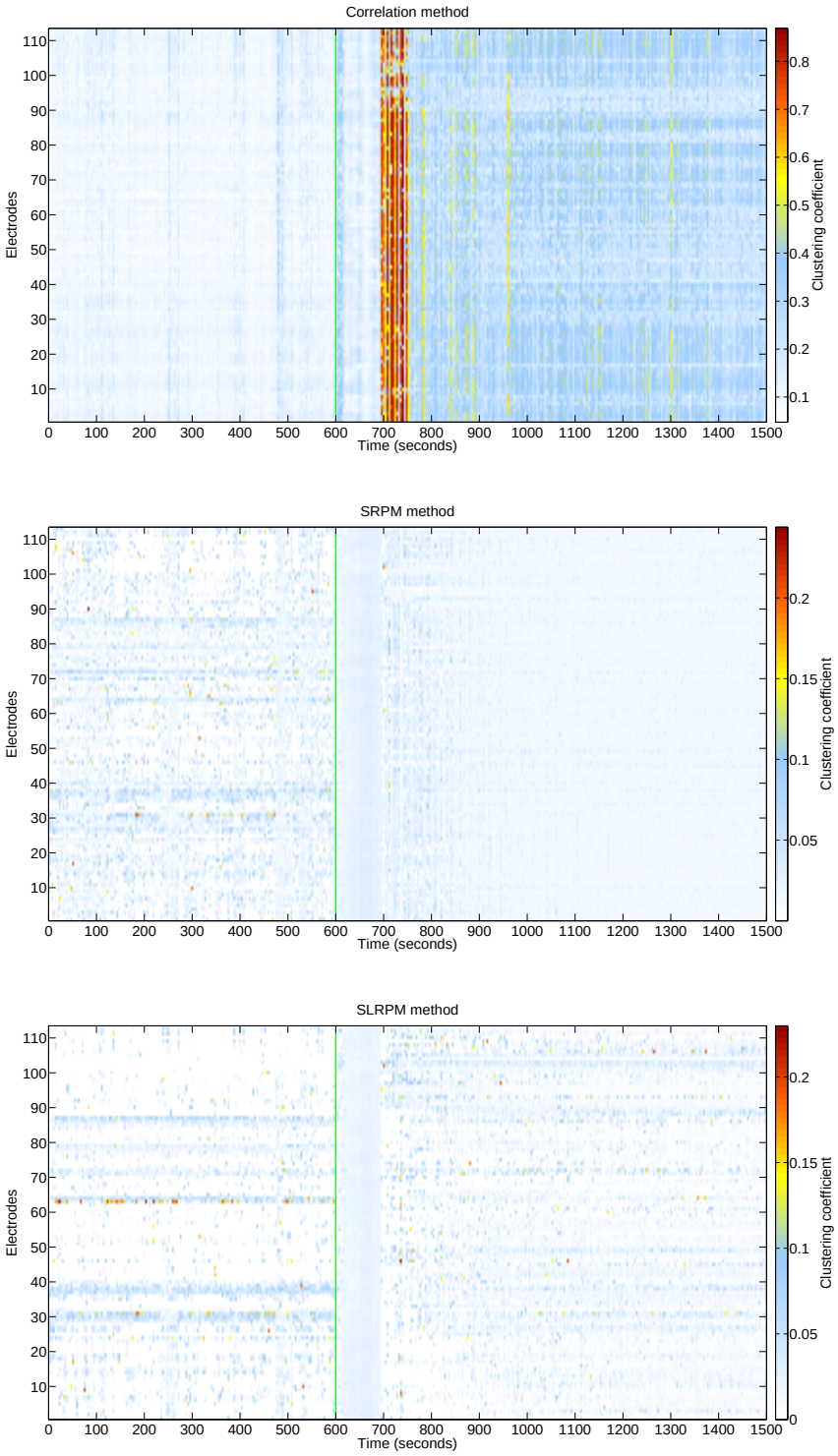

Figure 4.3: CC plots for the three methods for seizure 1 in patient 1. Green line denotes the seizure onset time.

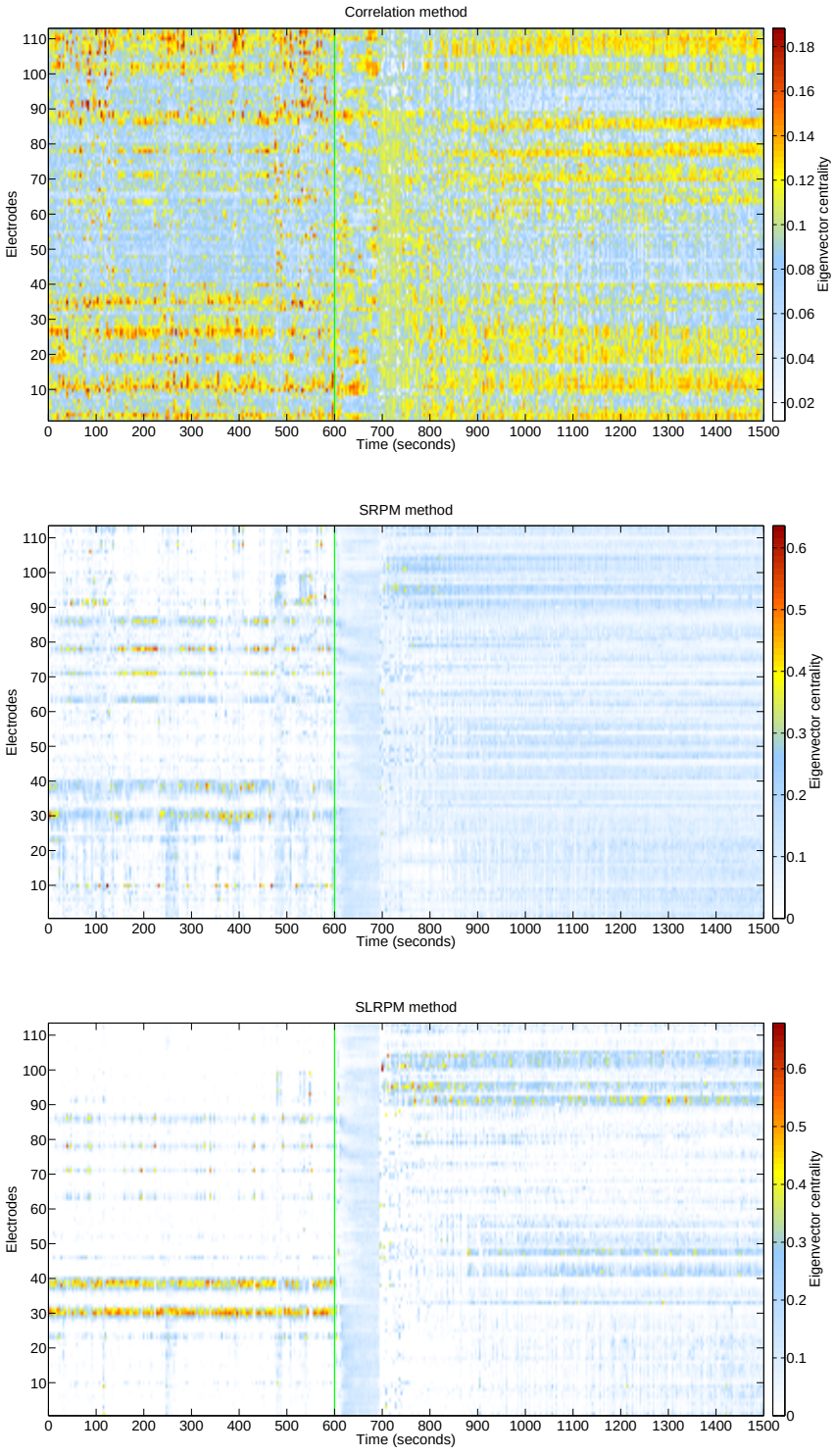

Figure 4.4: EC plots for the three methods for seizure 1 in patient 1. Green line denotes the seizure onset time.

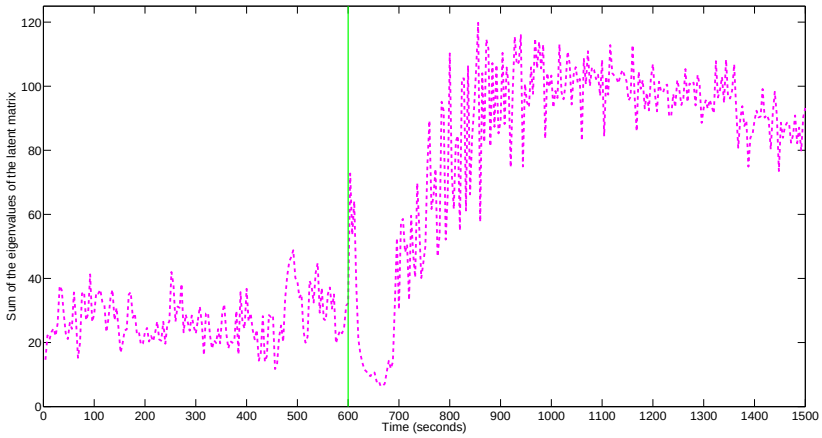

Figure 4.5: Plot of the latent inputs estimated by the SLRPM method for seizure 1 in patient 1. Green line denotes the seizure onset time.

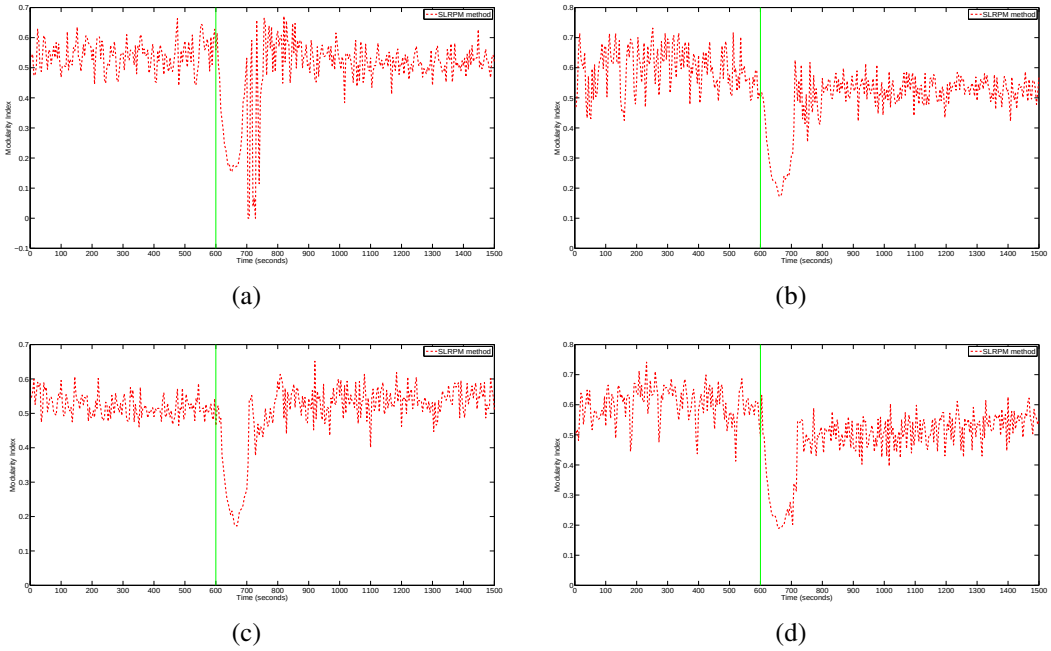

(a) (b)

(c) (d)

Figure 4.6: MI plots for the SLRPM method for clinical seizures 2, 3, 4, and 5 (shown in (a), (b), (c), and (d) respectively) in patient 1. Green lines in all plots denote the seizure onset time.

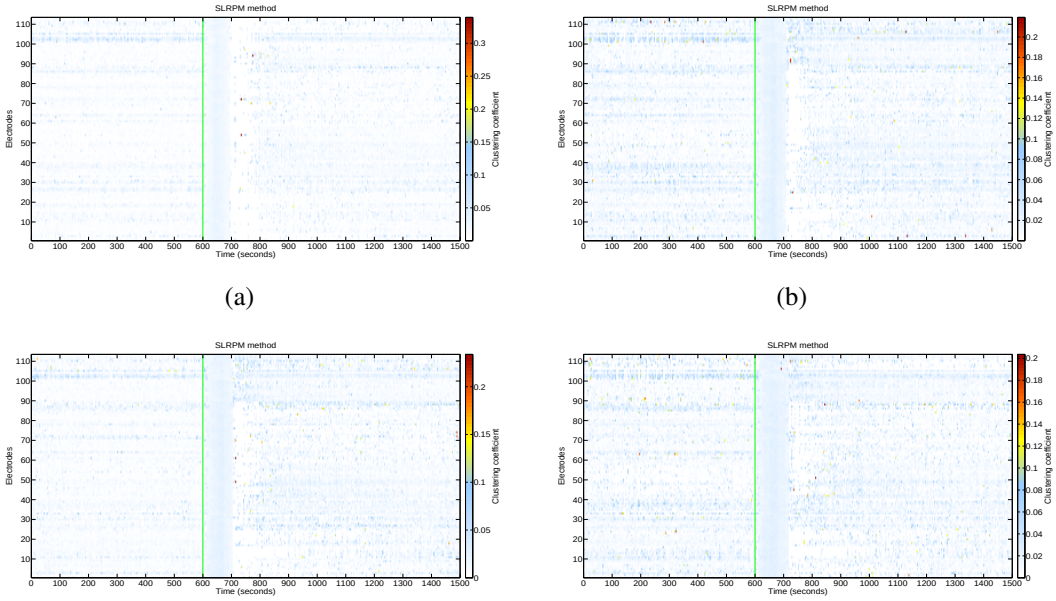

(a) (b) (c) (d)

Figure 4.7: CC plots for the SLRPM method for clinical seizures 2, 3, 4, and 5 (shown in (a), (b), (c), and (d) respectively) in patient 1. Green lines in all plots denote the seizure onset time.

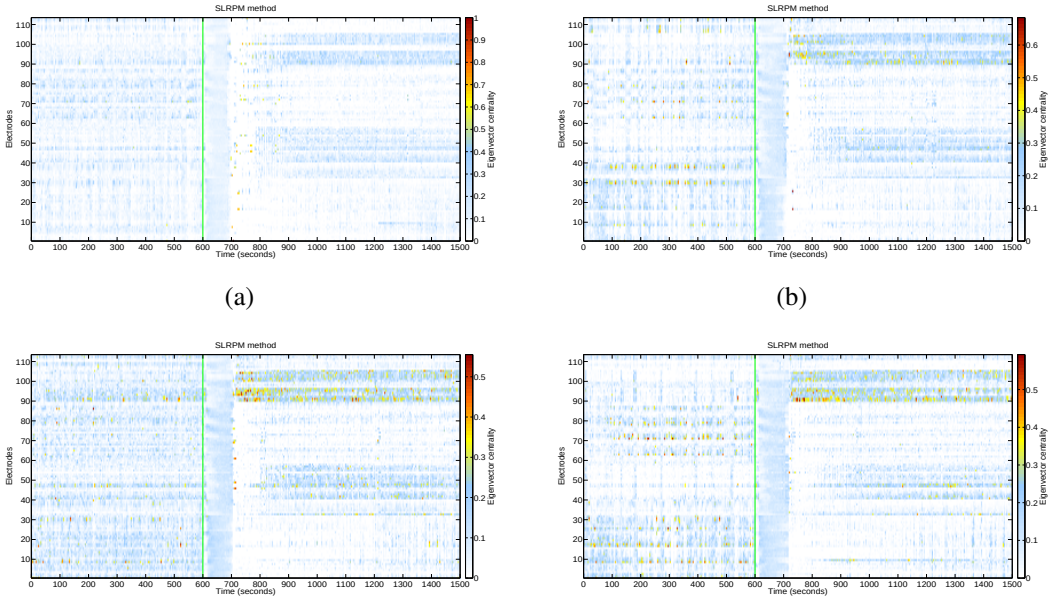

(a) (b) (c) (d)

Figure 4.8: EC plots for the SLRPM method for clinical seizures 2, 3, 4, and 5 (shown in (a), (b), (c), and (d) respectively) in patient 1. Green lines in all plots denote the seizure onset time.

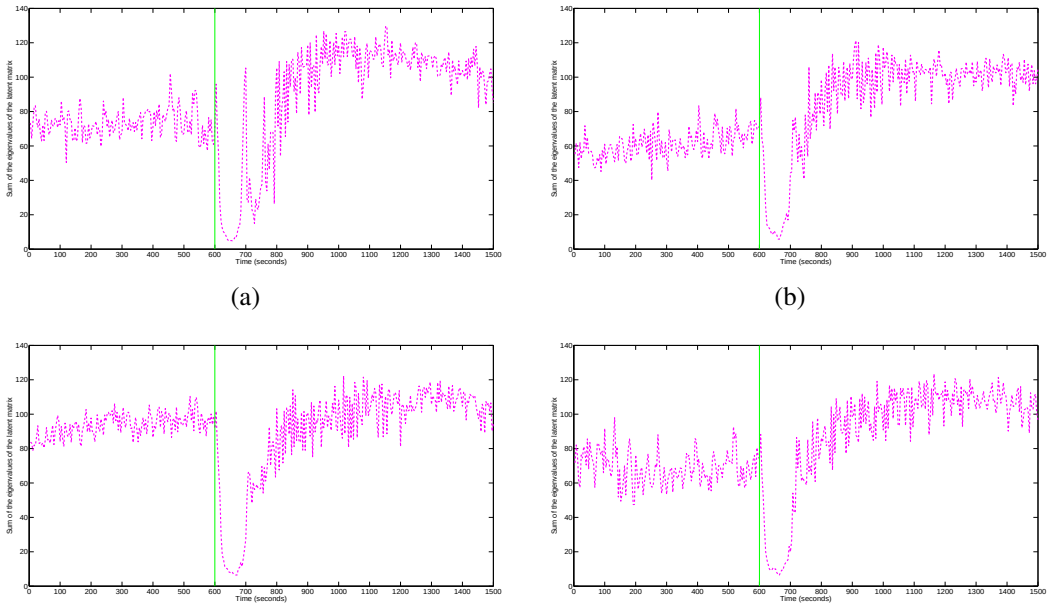

(a) (b)

(c) (d)

Figure 4.9: Plots of the latent inputs estimated by the SLRPM method for clinical seizures 2, 3, 4, and 5 (shown in (a), (b), (c), and (d) respectively) in patient 1. Green lines in all plots denote the seizure onset time.

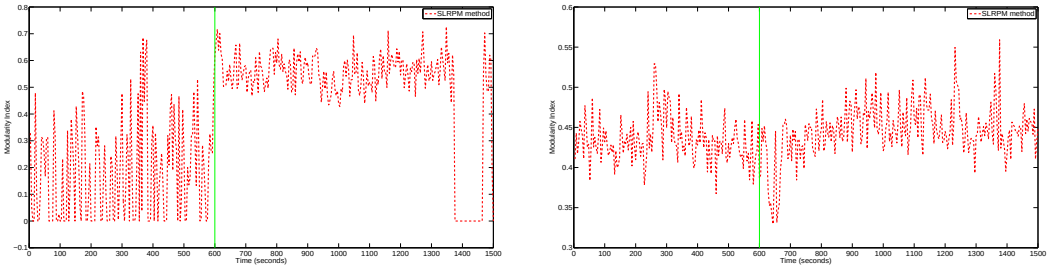

(a) (b)

Figure 4.10: MI plots for the SLRPM method for the two sub-clinical seizures in patient 1. Green lines in all plots denote the seizure onset time.

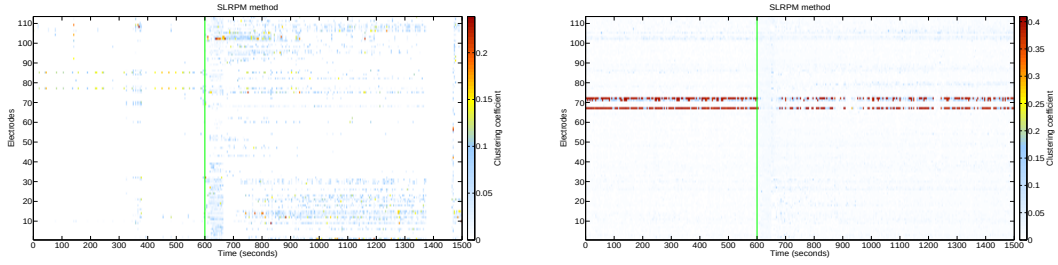

(a) (b)

Figure 4.11: CC plots for the SLRPM method for the two sub-clinical seizures in patient 1. Green lines in all plots denote the seizure onset time.

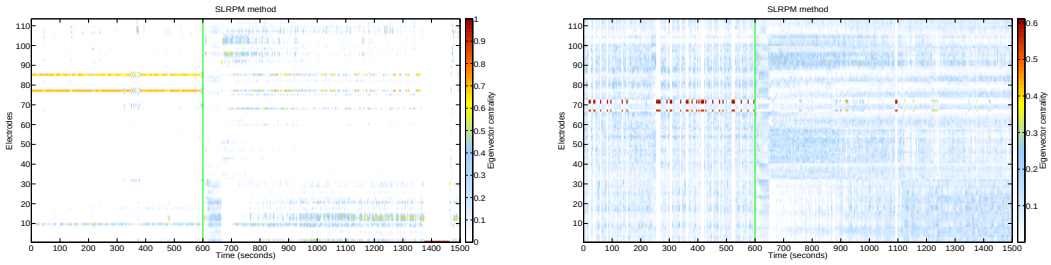

(a) (b)

Figure 4.12: EC plots for the SLRPM method for the two sub-clinical seizures in patient 1. Green lines in all plots denote the seizure onset time.

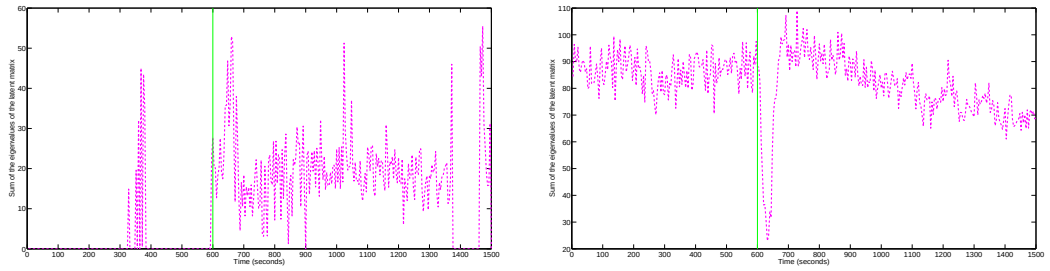

(a) (b)

Figure 4.13: Plots of the latent inputs estimated by the SLRPM method for the two sub-clinical seizures in patient 1. Green lines in all plots denote the seizure onset time.

method estimates brain connectivity by considering both the common observable and latent inputs, it removes considerable between module connectivity and the estimated brain network by this method is highly modular. Also note that the MI shown in the correlation method slightly increases during the seizure and then decreases for the first few seconds of the post-ictal period. These dynamics estimated by the three methods can be more clearly interpreted if we visualize the latent inputs to the electrodes from which brain activity was recorded. In order to have a measure for the latent inputs, we calculate the sum of the eigenvalues of the low rank matrix estimated by the SLRPM method. This plot is shown in Figure 4.5. We see that the latent inputs are relatively low in the ictal period than the preictal period, but are relatively high in the post-ictal period. For the first few seconds of the post-ictal period, the latent inputs start increasing and make the observed brain regions more correlated and hence we see a decrease in MI in the correlation method for this period. Also, since the effect of the latent inputs is relatively higher in the preictal and post-ictal periods than the ictal period, it becomes essential to estimate the precision matrix of the conditional statistics in order to remove the influence of these inputs on the recorded activity. SRPM and correlation methods have lower MI in preictal and post-ictal periods than the SLRPM method since they cannot model the latent inputs and might produce erroneous connections among the brain regions hence resulting in an erroneous estimate of MI.

The low MI values in the SRPM and SLRPM methods can be explained by the CC and EC plots for the individual electrodes which are shown in Figure 4.3 and 4.4 respectively. Note from the CC and EC plots of SRPM and SLRPM methods that the brain regions are uniformly active in the ictal period in contrast to the preictal and post-ictal periods. This relatively more uniform activity explains the lower MI shown in these two methods since during the ictal period the entire brain network behaves as one big module. For both CC and EC measures, the SLRPM method shows relatively more sparse activity than the SRPM and correlation methods during the preictal and postictal periods which is again a consequence of the ability of the SLRPM method to model the latent inputs. The estimates by the SRPM and correlation methods in these periods might be erroneous due to the inability of these two methods to capture the effect of the latent inputs on

the observed brain regions. For the first few seconds of the post-ictal period, the EC measure in the correlation method shows that the electrodes are relatively highly active. This phenomena is also observed in the CC measure of the correlation method to some extent in which we see that a relatively large number of electrodes are uniformly active. These probably are erroneous estimates due to the presence of the common inputs as explained before. In contrast, examining the CC and EC measures in the SLRPM method during this period, we see that relatively few electrodes are active. All these results demonstrate the superior ability of the SLRPM method to capture brain dynamics which might be the closest to the ground truth.

Plots of MI, CC, EC and latent inputs measures from the SLRPM method for the other 4 clinical seizures are shown in Figures 4.6, 4.7, 4.8, and 4.9 respectively. Clinical seizures 2, 3, 4, and 5 are shown in (a), (b), (c), and (d) in each of the Figures 4.6, 4.7, 4.8, and 4.9 respectively. Each of these seizures lasted for approximately 90 seconds. We note that ictal dynamics for all these seizures for each measure are very similar to each other and seizure 1 and can be explained as before.

Plots of MI, CC, EC and latent inputs measures from the SLRPM method for the 2 sub-clinical seizures are shown in Figures 4.10, 4.11, 4.12, and 4.13 respectively. Sub-clinical seizures 1 and 2 are shown in (a) and (b) in each of the Figures 4.10, 4.11, 4.12, and 4.13 respectively. MI for sub-clinical seizure 1 was relatively high for a relatively large period of time after seizure onset. However, no obvious ictal dynamics was seen in the MI plot of sub-clinical seizure 2. In the CC and EC plots of sub-clinical seizure 1, electrodes 77 and 85 were relatively more active than the other electrodes in the preictal period and electrode 85 was marked as one of the onset channels by the clinician. In the CC plot of sub-clinical seizure 2, electrodes 67 and 72 were relatively more active than the other electrodes in the preictal period and in the EC plot of sub-clinical seizure 2, electrodes 67, 71, and 72 were relatively more active than the other electrodes in the preictal period. But none of these electrodes were marked as onset channels by the clinician. Ictal dynamics can be seen in the first few seconds after seizure onset in the CC and EC plots in sub-clinical seizure 2 where a relatively large number of electrodes became uniformly active, however no such dynamics

can be seen in those plots for sub-clinical seizure 1. However, there was change in activity in a relatively large number of electrodes after the onset of sub-clinical seizure 2 as can be seen from its CC and EC plots. From the plots of the latent inputs, we see that they were relatively high for a relatively large period of time after sub-clinical seizure 1 onset and were relatively low for the first few seconds of sub-clinical seizure 2 onset like the clinical seizures.

Due to the consistency of dynamics of all 5 clinical seizures in the SLRPM method, we were able to write a seizure detection algorithm for this patient. For seizure detection, we considered the latent inputs measure. Overall, we found this measure to be the most sensitive to seizures from the analysis of all seizures from all patients and hence used it for seizure detection. We used both threshold criterion, i.e., when the latent inputs become lower than a specified threshold and duration criterion, i.e., when the duration of the latent inputs lower than the specified threshold is higher than some specified lower limit and lower than some specified higher limit. We declare that a seizure is detected when the latent inputs satisfy both of these criteria. Using these criteria, we were able to detect all 5 clinical seizures with zero false positives.

Patient 2

Medication information of this patient is shown in Table 4.4. Electrode locations are shown in Figure 4.14. As shown, there were depth electrodes inserted in right and left anterior temporal regions, right and left posterior temporal regions, right and left cingulate regions, and right and left subfrontal regions. We analyzed 5 clinical seizures from this patient. Seizures 1 and 2 correspond to day 2, seizure 3 corresponds to day 3, and seizures 4 and 5 correspond to day 8.

Plots of MI, CC, EC and latent inputs measures from the SLRPM method for 5 seizures of this patient are shown in Figures 4.15, 4.16, 4.17, and 4.18 respectively. From the MI plots of these seizures, ictal dynamics is visible, to varying extent, by the relative lowering of MI for the first few seconds of seizure onset and this phenomena is similar to the ictal dynamics seen in patient 1. A relatively large number of electrodes are uniformly active for the first few seconds of seizure onset in each of the CC and EC plots which is similar to those observed in patient 1. It is also

Table 4.4: Medication information of patient 2.

Day	Medication
Home doses	Levetiracetam 1500 – 1500, Oxcarbazepine 600 – 600, Clonazepam 0.25 – 0.25
Day 1	Levetiracetam 1500 – 1500, Oxcarbazepine 600 – 600, Clonazepam 0.25 – 0.25
Day 2	Levetiracetam 1500 – 1500, Oxcarbazepine 300 – 300, Clonazepam 0.25 – 0.25
Day 3	Levetiracetam 1500 – 1500, Oxcarbazepine 300 – 600, Clonazepam 0.25 – 0.25
Day 4	Levetiracetam 1500 – 1500, Oxcarbazepine 600 – 600, Clonazepam 0.25 – 0.25
Day 5	Levetiracetam 1500 – 750, Oxcarbazepine 600 – 300, Clonazepam 0.25 – 0.25
Day 6	Levetiracetam 750 – 750, Oxcarbazepine 300 – 0, Clonazepam stopped
Day 7	Levetiracetam stopped, Oxcarbazepine stopped, Clonazepam stopped
Day 8	Levetiracetam 750 – 750, Oxcarbazepine stopped, Clonazepam stopped
Day 9	Levetiracetam 1500 – 1500, Oxcarbazepine 600 – 600, Clonazepam 0.25 – 0.25

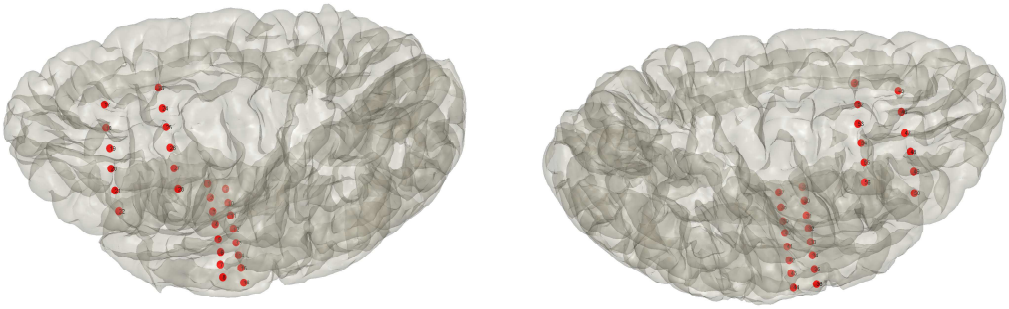

(a) (b)

Figure 4.14: Electrode locations in patient 2. (a) Left hemisphere. (b) Right hemisphere.

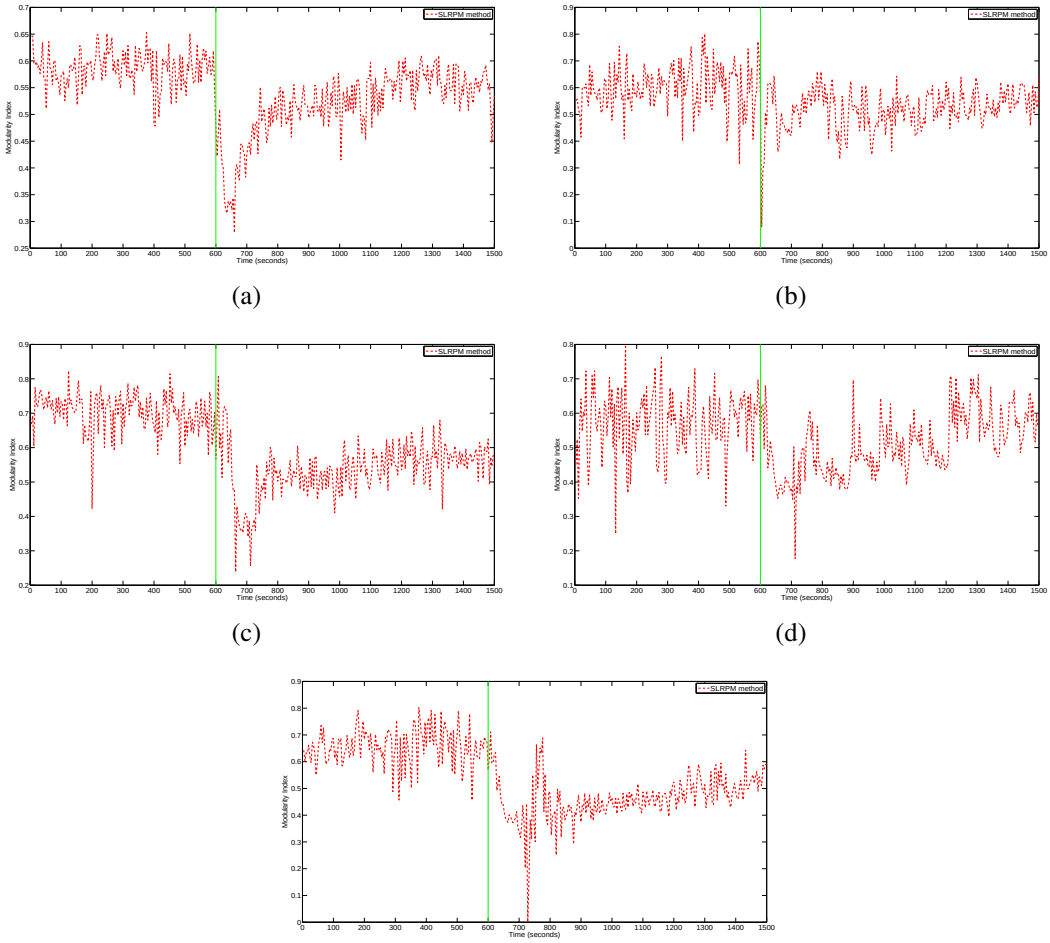

Figure 4.15: MI plots for the SLRPM method for seizures 1, 2, 3, 4, and 5 (shown in (a), (b), (c), (d), and (e) respectively) in patient 2. Green lines in all plots denote the seizure onset time.

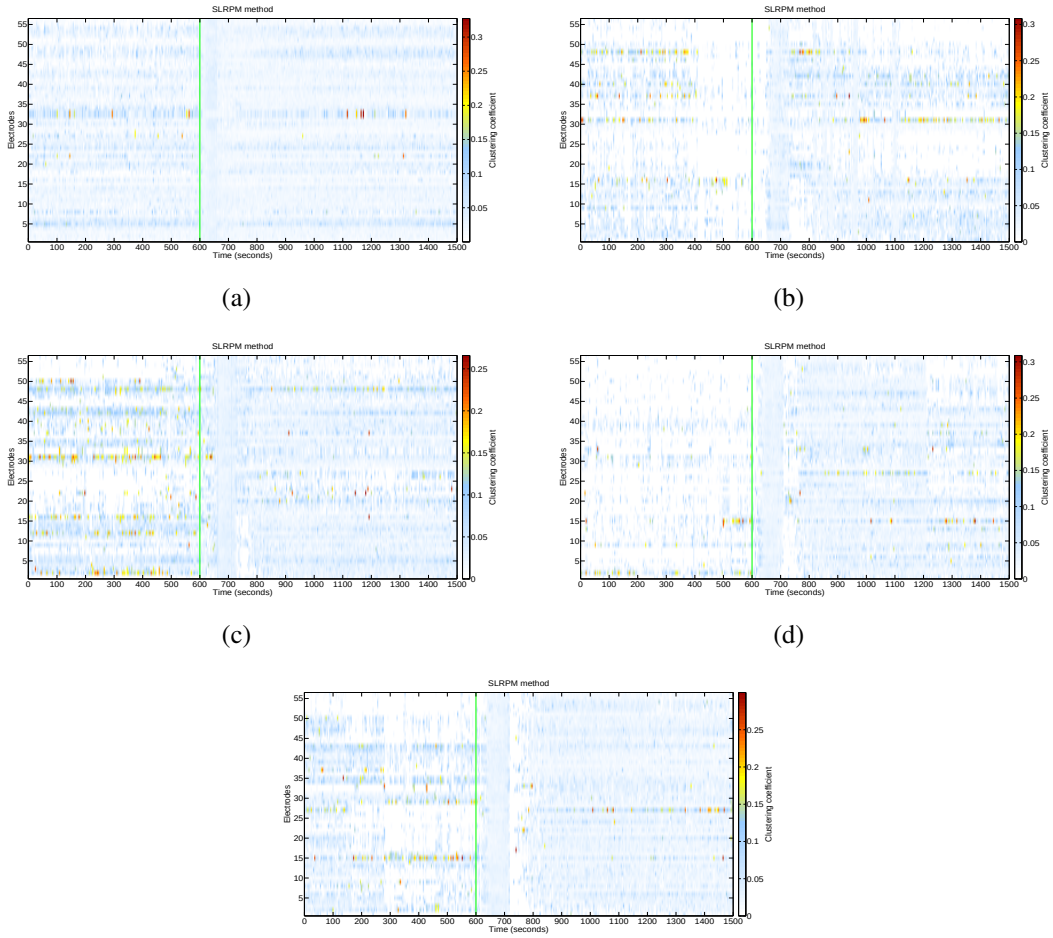

(a) (b)

(c) (d)

(e)

Figure 4.16: CC plots for the SLRPM method for seizures 1, 2, 3, 4, and 5 (shown in (a), (b), (c), (d) and (e) respectively) in patient 2. Green lines in all plots denote the seizure onset time.

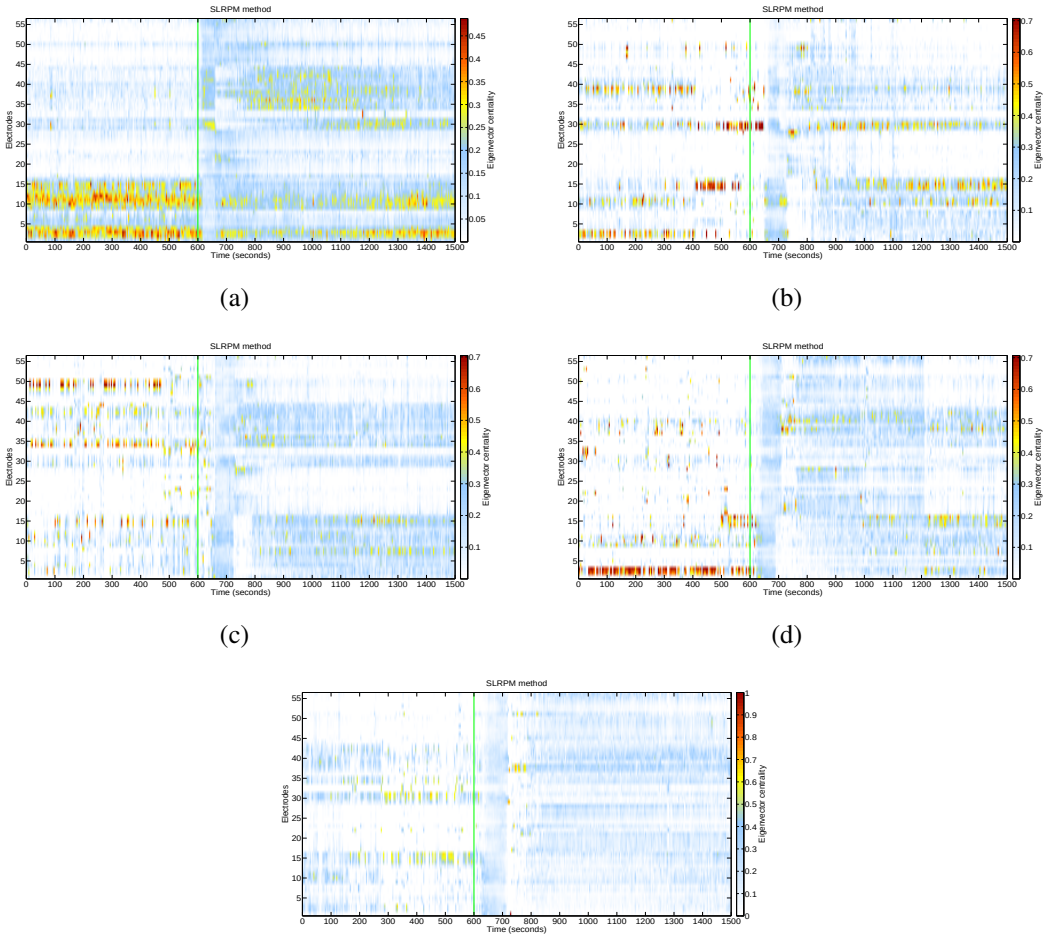

Figure 4.17: EC plots for the SLRPM method for seizures 1, 2, 3, 4, and 5 (shown in (a), (b), (c), (d), and (e) respectively) in patient 2. Green lines in all plots denote the seizure onset time.

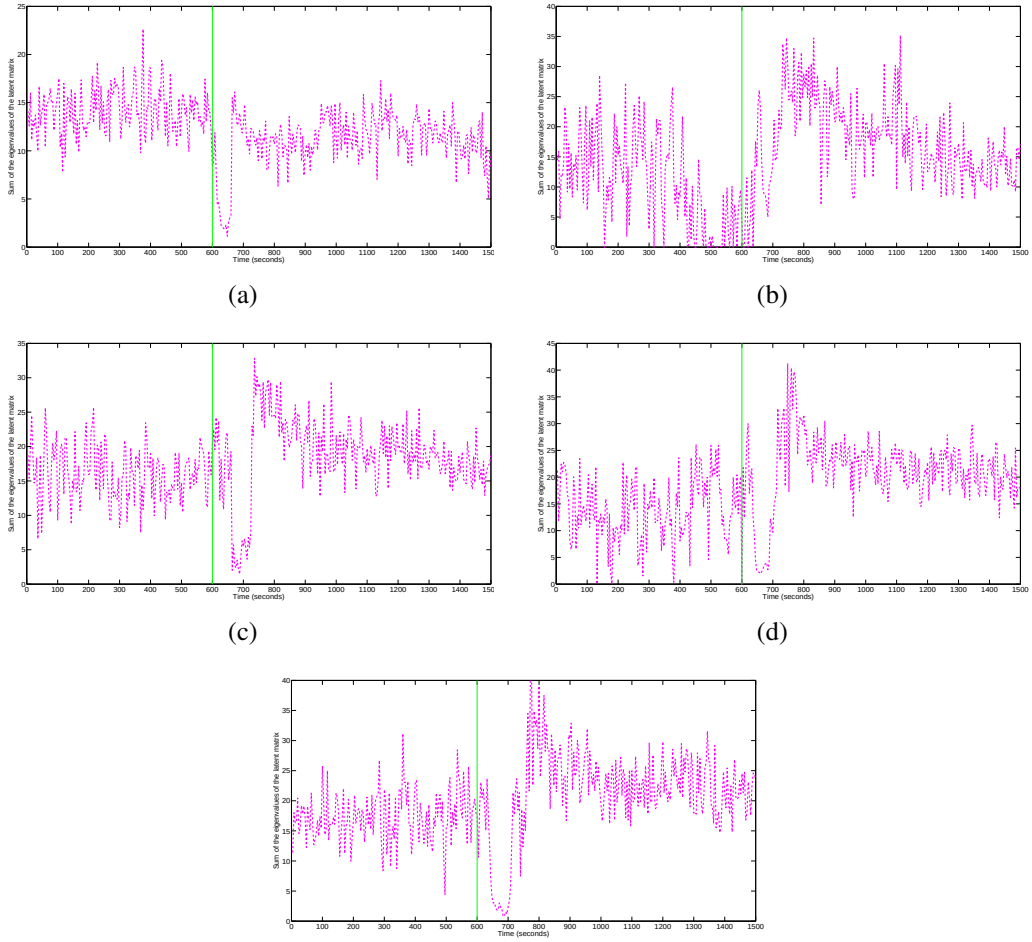

(a) (b)

(c) (d)

(e)

Figure 4.18: Plots of the latent inputs estimated by the SLRPM method for seizures 1, 2, 3, 4, and 5 (shown in (a), (b), (c), (d), and (e) respectively) in patient 2. Green lines in all plots denote the seizure onset time.

Table 4.5: Medication information of patient 3.

Day	Medication
Home doses	Keppra 1500 – 1500, Lamotrigine 200 – 200, Zonegran 300 – 300
Day 1	Keppra 1500 – 1500, Lamotrigine 200 – 200, Zonegran 300 – 300
Day 2	Keppra 750 – 750, Lamotrigine 100 – 100, Zonegran 200 – 200
Day 3	Keppra 375 – 375, Lamotrigine 50 – 50, Zonegran 100 – 100
Day 4 – 8	Off medications

noteworthy that the number of preictal active electrodes is relatively more sparse in the EC plots than those in the corresponding CC plots. We also observe the relative lessening of the latent inputs, to varying extent, after seizure onset, a phenomena which is also observed in patient 1. We also used the threshold and duration criteria on the latent inputs measure for seizure detection in this patient (the threshold and duration values for this patient were different from those selected for patient 1) and were able to detect all 5 seizures with zero false positives.

Patient 3

Medication information of this patient is shown in Table 4.5. Electrode locations are shown in Figure 4.19. As shown, there were depth electrodes inserted in right and left anterior temporal regions, right and left posterior temporal regions, right and left cingulate regions, right and left subfrontal regions, and right and left posterior frontal regions. We analyzed 7 clinical seizures from this patient. Seizure 1 corresponds to day 2, seizures 2, 3, 4, and 5 correspond to day 7, and seizures 6 and 7 correspond to day 8.

Plots of MI, CC, EC and latent inputs measures from the SLRPM method for 7 seizures of this patient are shown in Figures 4.20, 4.21, 4.22, and 4.23 respectively. Ictal dynamics is clearly visible from these plots and similar to that in patients 1 and 2. Using the threshold and duration criteria on the latent inputs for seizure detection in this patient, we were able to detect all 7 seizures with two false positives.

Patient 4

Electrode locations are shown in Figure 4.24. As shown, there were depth electrodes inserted in anterior temporal, posterior temporal, subfrontal, cingulate, and parietal regions. We analyzed 3 clinical seizures from this patient.

Plots of MI, CC, EC and latent inputs measures from the SLRPM method for 3 seizures of this patient are shown in Figures 4.25, 4.26, 4.27, and 4.28 respectively. Ictal dynamics is clearly visible from these plots and similar to that in patients 1, 2, and 3. Large variation in MI and latent inputs plots is also observed starting from the 700 s mark and lasting for a few seconds in seizure 3 and seizure 2 to some extent. From all plots for seizure 1, we also see that the duration of ictal dynamics is relatively large as compared to those for the other two seizures. Using the threshold and duration criteria on the latent inputs for seizure detection in this patient, we were able to detect all 3 seizures with zero false positives.

Patient 5

The patient's hospital medications included phenobarbital, carbamazepine, ativan, and vimpat. Electrode locations are shown in Figure 4.29. As shown, there were two grids, one placed over the posterior inferior frontal, posterior inferior parietal, superior temporal, and superior posterior temporal regions and the other covered the posterior inferior frontal, inferior parietal, and superior parietal lobe regions. There were two strips placed over the subtemporal and parietal regions. There were also depth electrodes placed into the anterior temporal lobe, the posterior temporal lobe, the superior parietal lobe and encephalomalacia noted on MRI, and through the posterior frontal lobe to reach the cingulate gyrus. We analyzed 62 clinical seizures from this patient.

Among the 62 seizures, 54 seizures showed very similar characteristic and we define them as characteristic seizures. Plots of MI, CC, EC and latent inputs measures from the SLRPM method for 4 of these characteristic seizures are shown in Figures 4.30, 4.31, 4.32, and 4.33 respectively. We note that ictal dynamics is not obvious from the MI plots, but can be seen, to varying extent, in the

Table 4.6: Medication information of patient 6.

Day	Medication
Home doses	Lamotrigine 200 mg-300mg, Lacosamide 100 mg bid
Day 1	Lamotrigine 200 mg-300 mg, Lacosamide 100 mg bid
Day 2	Lamotrigine 200 mg-300 mg, Lacosamine 100 mg am
Day 3	Lamotrigine 200 mg-150 mg
Day 4	Lamotrigine 100 mg-75 mg
Day 5	Lamotrigine 150 mg pm
Day 6	Lamotrigine 150 mg-300 mg, Lacosamide 100 pm
Day 7	Lamotrigine 200 mg-300 mg, Lacosamide 100 am and 200 pm
Day 8	Lamotrigine 200 mg-300 mg, Lacosamide 100 mg pm
Day 9	Lamotrigine 200 mg-300 mg, Lacosamide 100 mg bid
Day 10	Lamotrigine 200 mg-300 mg, Lacosamide 100 mg bid

CC plots where a relatively large number of electrodes become uniformly active. Clear change in preictal dynamics in the EC plots also demonstrate the capability of the SLRPM method to capture ictal dynamics. The latent inputs measure appears to be the most sensitive among all measures in this patient. Ictal dynamics is very clear by relative lowering of the latent inputs followed by a sharp increase. Using the threshold and duration criteria on these 54 seizures, we were able to detect 52 seizures with 2 false positives and 6 were not marked clinically, but showed clear signs of ictal dynamics in the latent inputs plots (and in plots of other measures not shown here) in Figure 4.34 (2 seizures in Figure 4.34 (a) and one each in Figures 4.34 (b)-(e)). This shows the potential of the SLRPM method to detect seizures which were possibly missed by the clinician. The other 8 seizures, which we define as non-characteristic seizures, showed characteristic different to those in characteristic seizures and it was not possible to write a detection algorithm for them. Plots of latent inputs for these seizures are shown in Figure 4.35.

Patient 6

Medication information of this patient is shown in Table 4.6. Electrode locations are shown in Figure 4.36. As shown, there were depth electrodes surgically implanted into subfrontal, prefrontal, cingulate, anterior temporal, and posterior temporal regions of both hemispheres. We analyzed 10 clinical seizures from this patient.

By observing the characteristics of the measures from the SLRPM method, we clustered the seizures into three groups. Group 1 consisted of 5 seizures, group 2 consisted of 4 seizures, and group 3 consisted of 1 seizure.

Plots of MI, CC, EC and latent inputs measures for the group 1 seizures of this patient are shown in Figures 4.37, 4.38, 4.39, and 4.40 respectively. Seizures shown in (a), (b), (c), (d), and (e) in each of Figures 4.37, 4.38, 4.39, and 4.40 belonged to day 5, day 5, day 6, day 6, and day 6 respectively. Ictal dynamics is clearly visible in Figures 4.37 (a), (b), and (d) in the MI plots where the MI was relatively low for the first few seconds of seizure onset. In Figure 4.40 (c), MI first increased and then decreased for a few seconds after seizure onset. In Figure 4.40 (e), ictal dynamics can be seen a few seconds prior to the seizure onset marking. In the CC plots, ictal dynamics can be seen for a few seconds after seizure onset (except for Figure 4.38 (e) where ictal dynamics occurred prior to the seizure onset marking) when a relatively large number of electrodes become uniformly active. Ictal dynamics can also be seen in the EC plots posterior to the seizure onset marking (except for Figure 4.39 (e) where ictal dynamics occured prior to the seizure onset marking) as change in the EC values of a relatively large number of electrodes. Ictal characteristics are difficult to observe in the plots of the latent inputs.

Plots of MI, CC, EC and latent inputs measures for the group 2 seizures of this patient are shown in Figures 4.41, 4.42, 4.43, and 4.44 respectively. Seizures shown in (a), (b), (c), and (d) in each of Figures 4.41, 4.42, 4.43, and 4.44 belonged to day 4, day 5, day 6, and day 7 respectively. From all the MI plots, we see that MI is persistently high after seizure onset in comparison to the preictal period. Ictal dynamics is clearly seen in the CC and EC plots where the CC and EC values of the electrodes were different posterior to seizure onset and the change is persistent in the 15 minute period shown after seizure onset. However, it is difficult to find any clear sings of ictal characteristics from the plots of the latent inputs.

Plots of MI, CC, EC and latent inputs measures for the group 3 seizure of this patient are shown in Figures 4.45 (a), (b), (c), and (d) respectively. This seizure belonged to day 4. The MI was relatively high for the first few seconds prior and posterior to seizure onset. Ictal dynamics can

Table 4.7: Medication information of patient 7.

Day	Medication
Home doses	Keppra 1500 mg twice a day, Dilantin 300 mg twice a day, and p.r.n. Ativan
Day 1	Keppra 1000 mg BID, Dilantin 150 mg BID
Day 2	Keppra 500 mg BID
Day 3	None
Day 21	Home meds

also be seen to some extent in the CC and EC plots as indicated by the change in the activity of a relatively large number of electrodes. However, no clear signs of ictal dynamics is present in the latent inputs plot. Due to the highly heterogeneous nature of the seizures, it was not possible to write a seizure detection algorithm for this patient.

Patient 7

Medication information of this patient is shown in Table 4.7. Electrode locations are shown in Figure 4.46. As shown, there were depth electrodes surgically implanted into subfrontal, posterior frontal, cingulate, anterior temporal, and posterior temporal regions of both hemispheres. We analyzed 3 seizures from this patient. Seizure 1, which was a clinical seizure, corresponds to day 2 and seizures 2 and 3, which were sub-clinical seizures, correspond to day 7 and 14 respectively.

Plots of MI, CC, EC and latent inputs measures for the 3 seizures of this patient are shown in Figures 4.47, 4.48, 4.49, and 4.50 respectively. The Seizure shown in (a) of Figures 4.47, 4.48, 4.49, and 4.50 is the clinical one, the other two are sub-clinical seizures shown in (b) and (c) of these figures respectively. No obvious characteristic of the clinical seizure is seen in the plots of its measures. It is also difficult to characterize the two sub-clinical seizures from the MI plots. Sub-clinical seizure 2 can be seen in the CC plot as a relatively large number of electrodes became uniformly active for the first few seconds of the seizure onset marking. In the EC plot in Figure 4.49 (b), electrodes $65-68$ and $73-75$ are relatively more active than other electrodes starting from approximately 800 s and electrodes $65-68$ and 73 were marked as onset channels by the clinician for this patient. The same set of electrodes were relatively more active than other electrodes for the

Table 4.8: Medication information of patient 8.

Day	Medication
Home doses	Trileptal 900 bid, Lamictal 225 bid, Keppra 1500 bid
Day 1	Trileptal 900 bid, Lamictal 225 bid, Keppra 1500 bid
Day 2	Lamictal 100 bid, Keppra 750 BID, Trileptal 900 BID
Day 3	Lamictal 100 BID, Keppra 500 BID, Trileptal 600 BID
Day 4	Lamictal 100 BID, Keppra 500 AM and off thereafter, Trileptal 600 AM then 300 PM
Day 5	Lamictal 225 BID, Keppra 500 BID, Trileptal 900 BID
Day 6	Lamictal 225 BID, Keppra 500 BID, Trileptal 900 BID
Day 7	Lamictal 225 BID, Keppra 500 BID, Trileptal 900 BID
Day 8 – 11	Lamictal 225 BID, Keppra 1500 BID, Trileptal 900 BID

first few seconds of the seizure onset time for sub-clinical seizure 3 in Figure 4.49 (c). Due to the heterogeneous nature of the seizures, it was not possible to write a seizure detection algorithm for this patient.

Patient 8

Medication information of this patient is shown in Table 4.8. Electrode locations are shown in Figure 4.51. As shown, there were depth electrodes surgically implanted into subfrontal, prefrontal, cingulate, anterior temporal, and posterior temporal regions of both hemispheres. We analyzed 7 clinical and 4 sub-clinical seizures from this patient.

Plots of MI, CC, EC and latent inputs measures for the 7 clinical seizures of this patient are shown in Figures 4.52, 4.53, 4.54, and 4.55 respectively. Seizures shown in (a)-(f) of Figures 4.52, 4.53, 4.54, and 4.55 correspond to day 5 and the seizure shown in (g) in those figures corresponds to day 7. From the MI plots, we observe that MI is relatively low for the first few seconds of seizure onset. Ictal dynamics can be seen in the CC plots for the first few seconds after seizure onset when a relatively large number of electrodes become uniformly active. Ictal dynamics can also be seen in the EC plots posterior to the seizure onset marking as change in the EC values of a relatively large number of electrodes. However, seizure dynamics is not obvious in the plots of the latent inputs.

Plots of MI, CC, EC and latent inputs measures for the 4 sub-clinical seizures of this patient

Table 4.9: Medication information of patient 9.

Day	Medication
Home	Trileptal 600 bid, Keppra 1500 bid, felbamate 1200 mg PO TID
Day 1	Trileptal 600 bid, Keppra 1500 bid, prcedex drip, propofol drip, ativan 1mg q4h, felbamate 1200 mg PO TID
Day 2	prcedex drip, propofol drip, versed drip, ativan prn, Keppra 1500 bid, Trileptal 600 bid, felbamate 1200 mg PO TID
Day 3	prcedex drip, propofol drip, ativan prn, Keppra 1500 bid, Phenobarbital 1400 mg x 1 and 30 mg qhs, Trileptal 600 bid, felbamate 1200 mg PO TID
Day 4	propofol drip, Keppra 1500 bid, midazolam drip, prcedex drip, Trileptal 600 bid, felbamate 1200 mg PO TID
Day 5	Trileptal 600 bid, Keppra 1500 bid, felbamate 1200 mg PO TID, midazolam drip, prcedex drip
Day 6	Trileptal 600 bid, Keppra 1500 bid, felbamate 1200 mg PO TID, midazolam drip, prcedex drip
Day 7	Trileptal 600 bid, Keppra 1500 bid, felbamate 1200 mg PO TID, midazolam drip, prcedex drip
Day 8	Trileptal 600 bid, Keppra 1500 bid, felbamate 1200 mg PO TID, propofol , and versed drips

are shown in Figures 4.56, 4.57, 4.58, and 4.59 respectively. Seizures shown in (a)-(b) of Figures 4.52, 4.53, 4.54, and 4.55 correspond to day 3, the seizure shown in (c) in those figures corresponds to day 6, and the seizure shown in (d) in those figures corresponds to day 8. These seizures were similar in characteristic to the clinical seizures. Due to the heterogeneous nature of the seizures in this patient, it was not possible to write a seizure detection algorithm.

Patient 9

Medication information of this patient is shown in Table 4.9. Electrode locations are shown in Figure 4.60. As shown, in addition to the grid, there were three strips placed in the frontopolar, subtemporal, and posterior regions. There were also depth electrodes inserted in the occipital, prefrontal, and the anterior and posterior temporal regions. We analyzed 19 clinical seizures from this patient. Based on the observed dynamics of these seizures from the measures, we divided them into 3 groups.

Plots of MI, CC, EC and latent inputs measures for the 7 group 1 seizures of this patient are shown in Figures 4.61, 4.62, 4.63, and 4.64 respectively. All these seizures belong to day 1. From the MI plots, we note that MI first relatively increases and then relatively decreases for the first few seconds of seizure onset. Ictal dynamics can be seen in the CC and EC plots for the first few seconds after seizure onset when brain activity changes in a relatively large number of electrodes. However, plots of the latent inputs were highly heterogeneous for these seizures and seizures are not obvious in these plots.

Plots of MI, CC, EC and latent inputs measures for the 7 group 2 seizures of this patient are shown in Figures 4.65, 4.66, 4.67, and 4.68 respectively. Plots of seizures $1-7$ in this group are shown in (a)-(g) in each of the Figures 4.65, 4.66, 4.67, and 4.68 respectively. Seizure 1 corresponds to day 2, seizures $2-4$ correspond to day 3, seizure 5 corresponds to day 4, and seizures 6 and 7 correspond to day 5. The MI plots were highly heterogeneous and ictal dynamics cannot be clearly seen from these plots. Ictal dynamics can be seen in the CC and EC plots for the first few seconds after seizure onset when brain activity changes in a relatively large number of electrodes. Moreover, for the first few seconds of the seizure onset, electrodes $89-93$ and $97-101$ were relatively more active than the other electrodes. These electrodes corresponded to the onset channels as marked by the clinician. However, plots of the latent inputs were highly heterogeneous for these seizures and seizures are not clearly seen in these plots.

Plots of MI, CC, EC and latent inputs measures for the 5 group 3 seizures of this patient are shown in Figures 4.69, 4.70, 4.71, and 4.72 respectively. All these seizures belong to day 8. From the plots of all the measures, we can see that ictal dynamics is highly heterogeneous for these seizures. Also, in the EC plot in Figure 4.71 (a), electrodes $78-80$ and $89-90$ were relatively more active than the other electrodes in the post-seizure period. The same set of electrodes were also relatively more active in the EC plots in Figures 4.71 (c) and (d) in both before and after seizure onset. These electrodes corresponded to the onset channels as marked by the clinician. Due to the highly heterogeneous nature of the seizures in this patient, it was not possible to write a seizure detection algorithm.

Table 4.10: Medication information of patient 10.

Day	Medication
Home doses	Lamictal 300 mg b.i.d., Topamax 400 mg b.i.d.
Day 1	Home medications
Day 2	Topamax 200 BID, Lamictal 300 BID
Day 3	Topamax 100 AM and 0 PM, Lamictal 150 BID
Day 4	Lamictal 75 AM
Day 5	none
Day 6	none
Day 7	none in am, home medications in PM
Day $8-11$	Home medications

Patient 10

Medication information of this patient is shown in Table 4.10. Electrode locations are shown in Figure 4.73. As shown, there were depth electrodes surgically implanted into orbitofrontal, prefrontal, cingulate, anterior temporal, and parietal regions of both hemispheres. We analyzed 10 clinical seizures from this patient. Based on the observed dynamics of these seizures from the measures, we divided them into 2 groups.

Plots of MI, CC, EC and latent inputs measures for the 7 group 1 seizures of this patient are shown in Figures 4.74, 4.75, 4.76, and 4.77 respectively. Seizures $1-7$ are shown in (a)-(g) in each of Figures 4.74, 4.75, 4.76, and 4.77 respectively. Seizure 1 belongs to day 5, seizures 2, 3, 4, and 5 belong to day 7, and seizures 6 and 7 belong to day 8. From the MI plots, we can see the relative lowering of MI for all seizures, except seizures 6, for the first few seconds of seizure onset. Ictal dynamics can be seen in the CC and EC plots for the first few seconds after seizure onset when a relatively large number of electrodes become uniformaly active. However, plots of the latent inputs were highly heterogeneous for these seizures and seizures are not obvious in these plots.

Plots of MI, CC, EC and latent inputs measures for the 3 group 2 seizures of this patient are shown in (a) and (b) in each of the Figures 4.78, 4.79, 4.80, and 4.81 respectively. From the plots of these measures, we can see that the seizures are highly heterogeneous and it is difficult to observe ictal dynamics. Due to the heterogeneous nature of the seizures in this patient, it was not possible to

Table 4.11: Medication information of patient 11.

Day	Medication
Home	GBP 2000/1600/2000, LTG 300/300, LEV 1000/1500, LAC 100/100 (tapered to 50 qhs prior to admission)
Day 1	GBP 2000/1600/2000, LTG 300/300, LEV 1000/1500
Day 2	GBP 2000/1600/2000, LTG 300/300, LEV 1000/1500, LAC 50qhs
Day 3	GBP 2000/1600/2000, LTG 300/300, LEV 1000/1500, LAC 50qhs
Day 4	GBP 2000/1600/2000, LTG 300/300, LEV 1000/1500, LAC 50qhs

write a seizure detection algorithm.

Patient 11

Medication information of this patient is shown in Table 4.11. Electrode locations are shown in Figure 4.82. As shown, there was a grid placed over the lateral temporal cortex. In addition, there were eight strips placed in the anterior subtemporal, middle subtemporal, posterior subtemporal, temporal polar, inferior frontal, superior frontal, parietal, and temporo-occipital regions. We analyzed 5 seizures from this patient. Seizure 3, which was a clinical seizure and lasted for approximately 70 seconds, corresponds to day 2 and seizures 1, 2, and 4, which were sub-clinical seizures, correspond to day 2, 2, and 3 and lasted for approximately 19, 54, and 55 seconds respectively. Seizure 5, which was a sub-clinical seizure, corresponds to day 4.

Plots of MI, CC, EC and latent inputs measures for the 5 seizures of this patient are shown in Figures 4.83, 4.84, 4.85, and 4.86 respectively. Plots (a)-(e) in each of the Figures 4.83, 4.84, 4.85, and 4.86 correspond to seizures $1-5$ respectively. MI was relatively high for a few seconds before and after seizure 1 onset. For seizure 2, MI is relatively high for approximately 650 seconds to 700 seconds. For the clinical seizure, MI first increased for a few seconds and then decreased for a few seconds after its onset. MI was relatively high for approximately 750 seconds to 800 seconds in seizure 4. Ictal dynamics is not visible from the CC plots for the three sub-clinical seizures, but can be clearly seen for the clinical seizure where a relatively large number electrodes become relatively

more active than preictal and post-ictal periods. Electrodes $33-38$ were relatively more active during ictal periods in the EC plots and these electrodes correspond to the onset channels. From the plots of the latent inputs, we note that latent inputs were relatively high for a few seconds before and after seizure 1 onset. For seizure 2, latent inputs were relatively high for approximately 650 seconds to 700 seconds. For the clinical seizure, latent inputs first increased for a few seconds and then decreased for a few seconds after its onset. Latent inputs were relatively high for approximately 750 seconds to 800 seconds in seizure 4. No definite ictal characteristics were observed in the plots of the measures for seizure 5. Due to the heterogeneous nature of the seizures in this patient, it was not possible to write a seizure detection algorithm.

Patient 12

We have previously used recordings from this patient for sleep spindle analysis (see Chapter 3). Medication information of this patient is shown in Table 3.1. Electrode locations are shown in Figure 4.87. As shown, there was a grid covering the frontal-temporal-parietal regions. There were four strips placed in the frontopolar, subfrontal, anterior subtemporal, and posterior subtemporal regions. There were also depth electrodes surgically implanted into the anterior temporal and posterior temporal regions. We analyzed 72 seizures from this patient out of which 3 were clinical seizures and the rest were sub-clinical.

Plots of MI, CC, EC and latent inputs measures for the 3 clinical seizures of this patient are shown in Figures 4.88, 4.89, 4.90, and 4.91 respectively. Plots (a)-(c) in each of the Figures 4.88, 4.89, 4.90, and 4.91 correspond to the clinical seizures $1-3$ respectively. These three clinical seizures correspond to day 3, 6, and 8 respectively. For clinical seizure 1, MI was relatively high for the first few seconds prior and posterior to seizure onset. For clinical seizures 2 and 3, relative lowering of MI can be seen for the first few seconds of seizure onset similar to those in patients $1-4$. Ictal dynamics can be seen in the CC and EC plots for the clinical seizure 1 as change in activity in a relatively large number of electrodes prior and posterior to seizure onset. Furthermore, electrodes $65-67$ in the EC plot were relatively more active than the other electrodes for a few

seconds after clinical seizure 1 onset. Among these electrodes, 65 and 66 were the onset channels as characterized by the clinician. Ictal dynamics can also be seen in the CC and EC plots when a relatively large number of electrodes became uniformly active post seizure 2 and 3 onset. Moreover, in the EC plot of clinical seizure 3, electrodes 73 and 74, which also were characterized by onset channels by the clinician, were relatively more active than the other electrodes from approximately 630 seconds to 660 seconds. Latent inputs for the clinical seizure 1 were relatively high for the first few seconds prior and posterior to seizure onset. For clinical seizures 2 and 3, relative lowering of latent inputs can be seen post seizure onset similar to those in patients $1-4$.

Plots of the measures of the sub-clinical seizures were highly heterogeneous and it was not possible to draw a uniform conclusion regarding their characteristics. EC measure was relatively more sensitive than the CC measure to the onset channels. Onset channels were relatively more active than the other electrodes for a few seconds prior (see Figure 4.92 (a)-(b) for two example seizures) and posterior (see Figure 4.92 (c)-(d) for two example seizures) to seizure onset. Due to the highly heterogeneous nature of the seizures in this patient, it was not possible to write a seizure detection algorithm.

4.3 Heterogeneity analysis

From the results presented for the preictal dynamics, we observe that there is considerable variability in the preictal dynamics of the seizures in some patients. These findings are consistent with findings from other researchers (Kuhnert et al., 2010; Kramer et al., 2010; Rozman, 2015; Truccolo et al., 2011). Researchers in (Kramer et al., 2010) have analyzed 48 seizures from ECoG recordings in 11 epilepsy patients and they found that there is relatively more variability in the preictal period than in the ictal period for seizures within a patient, however no results were reported for variability of seizures in the preictal period for the patients. The authors in (Kuhnert et al., 2010) have analyzed 75 seizures in 13 epilepsy patients and reported significant variability of preictal activity of seizures from patient-to-patient, however, no results were reported regarding variability

of seizures within patients. Rozman (2015) in his doctoral dissertation have analyzed 39 seizures from ECoG recordings in 12 patients suffering from complex partial epilepsy. He analyzed the power spectrum of the recordings of the individual electrodes in the preictal period and found high heterogeneity of seizures within patients. Heterogeneity analysis of preictal activity within patients is important because it might help us for predicting seizures and eventually lead to better understanding of how seizures initiate (Truccolo et al., 2011).

In order to calculate the degree of heterogeneity in the preictal period of seizures for a patient, we first calculated the normalized time-average EC in the preictal period of each seizure and then averaged the resulting ECs across all seizures for that patient. We then found the M most active electrodes from the resulting average EC, where M is the number of onset channels marked by the clinician. We next calculated the coefficient of variability (ratio of standarad deviation to mean) of each active electrode across all seizures for that patient (Truccolo et al., 2011). We define the average coefficient of variability across all active electrodes as the degree of heterogeneity (DH) for the patient. Furthermore, we also reported how many of the active electrodes corresponded to the onset channels marked by the clinician. We also denote "A/O", where "A" stands for *active* and "O" stands for *onset* as the ratio of the number of active electrodes corresponding to the onset channels identified by the clinician to the total number of onset channels identified by the clinician. We also express the values of DH as percentage. For heterogeneity analysis, we only considered those seizures for which the 10 minutes preictal time-segment did not contain another seizure. Hence we had to exclude some seizures from the lot shown in Table 4.2 from analysis. The details about the number of seizures analyzed (total 185 seizures out of which 116 were clinical seizures) for each patient for heterogeneity analysis are shown in Table 4.12.

Table 4.13 shows the heterogeneity statistics for all patients. We observe that DH for SLRPM is higher than that for SRPM for all patients except one (patient 4) and DH for SRPM is higher than that of correlation for all patients. This clearly emphasizes the importance of taking the latent inputs in to consideration while estimating connectivity of brain regions. The relatively low DH in the SRPM and correlation methods is attributable to the common latent inputs. Furthermore

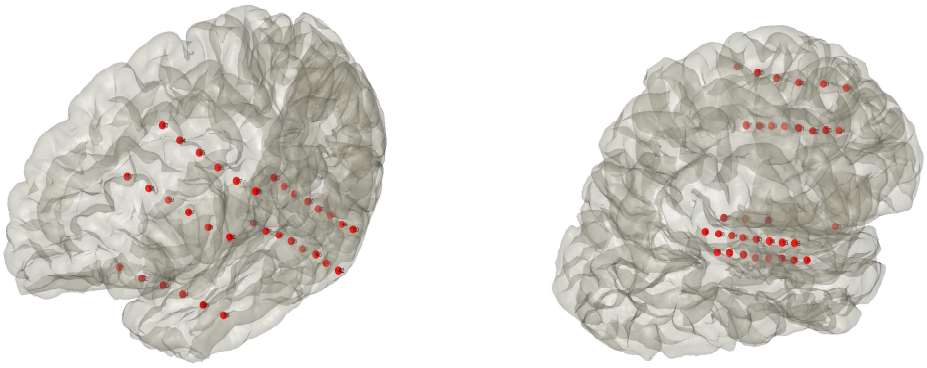

(a) (b)

Figure 4.19: Electrode locations in patient 3. (a) Left hemisphere. (b) Right hemisphere.

Table 4.12: Number and type of seizures analyzed for each patient for heterogeneity analysis. Clinical and sub-clinical seizures are denoted by "C" and "SC" respectively.

Patient	Number of seizures analyzed
1	5 C and 2 SC
2	5 C
3	7 C
4	3 C
5	46 C
6	10 C
7	1 C and 2 SC
8	7 C and 4 SC
9	19 C
10	9 C
11	1 C and 4 SC
12	3 C and 57 SC

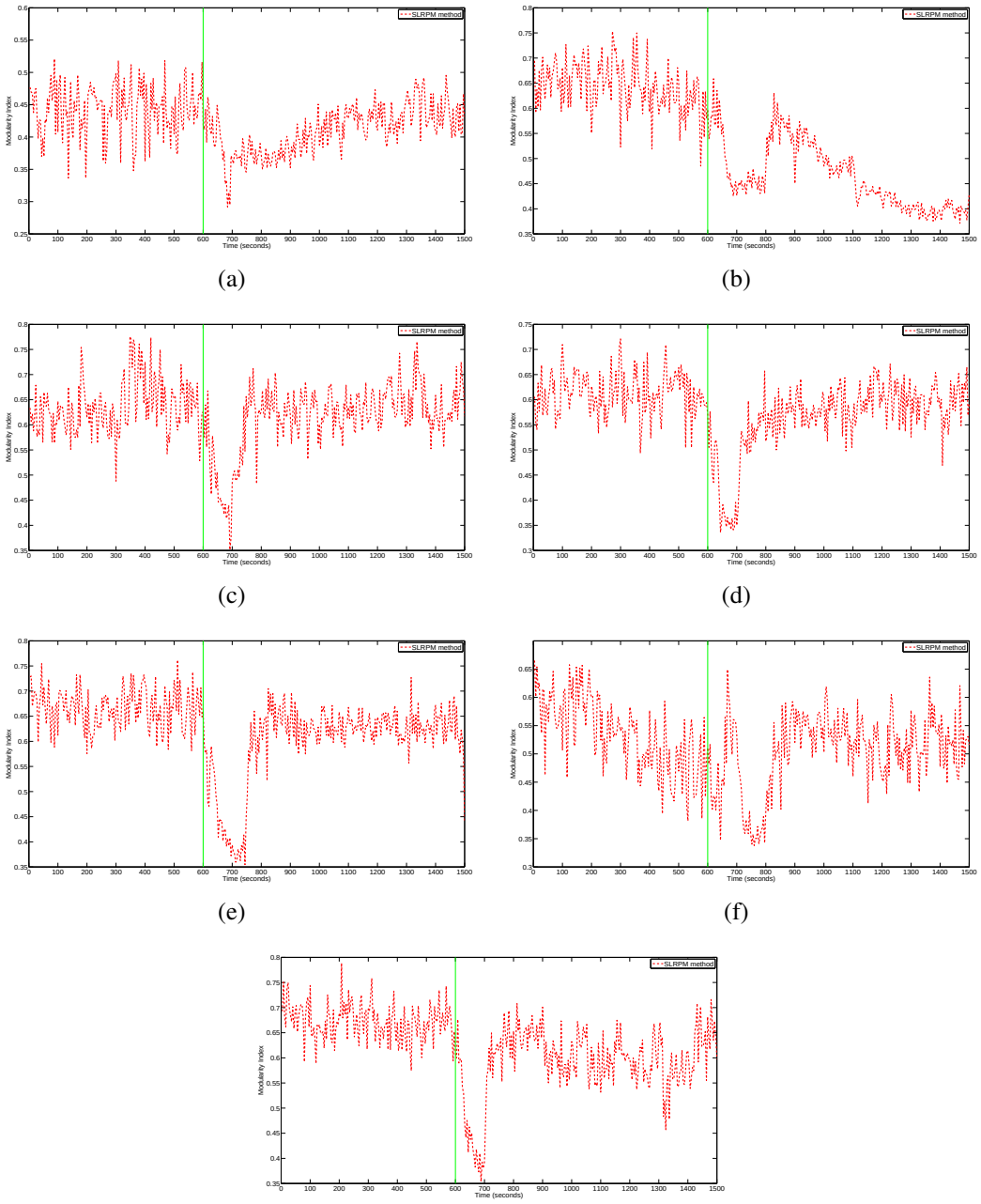

Figure 4.20: MI plots for the SLRPM method for seizures 1, 2, 3, 4, 5, 6, and 7 (shown in (a), (b), (c), (d), (e), (f), and (g) respectively) in patient 3. Green lines in all plots denote the seizure onset time.

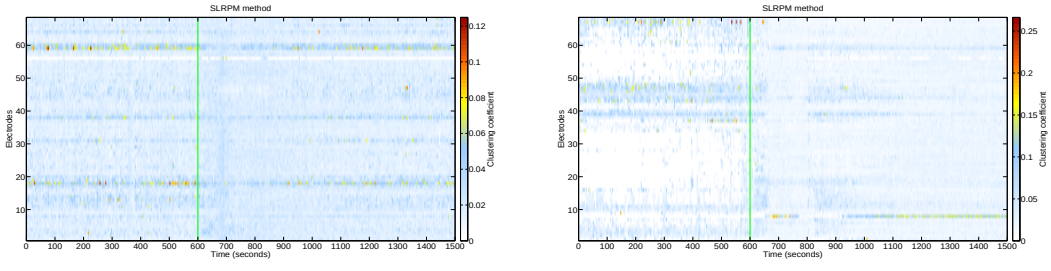

(a)

(b)

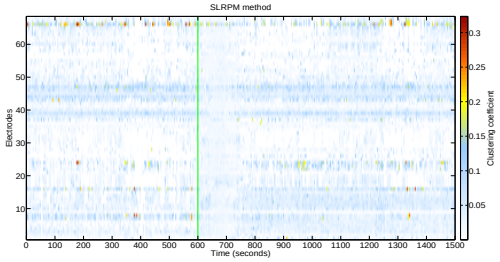

(c)

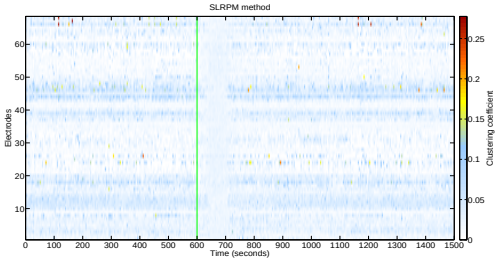

(d)

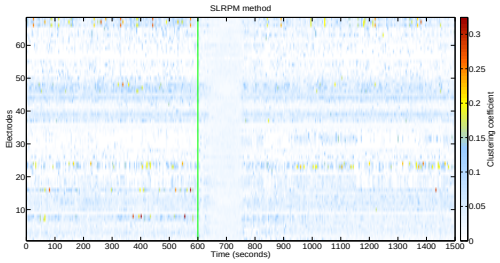

(e)

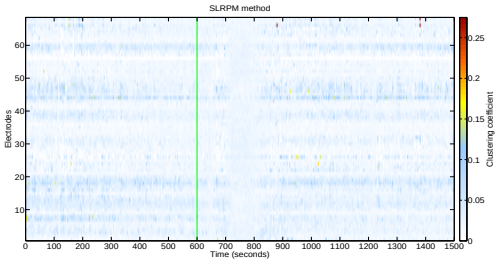

(f)

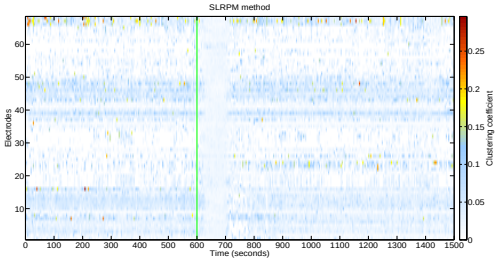

(g)

Figure 4.21: CC plots for the SLRPM method for seizures 1, 2, 3, 4, 5, 6, and 7 (shown in (a), (b), (c), (d), (e), (f), and (g) respectively) in patient 3. Green lines in all plots denote the seizure onset time.

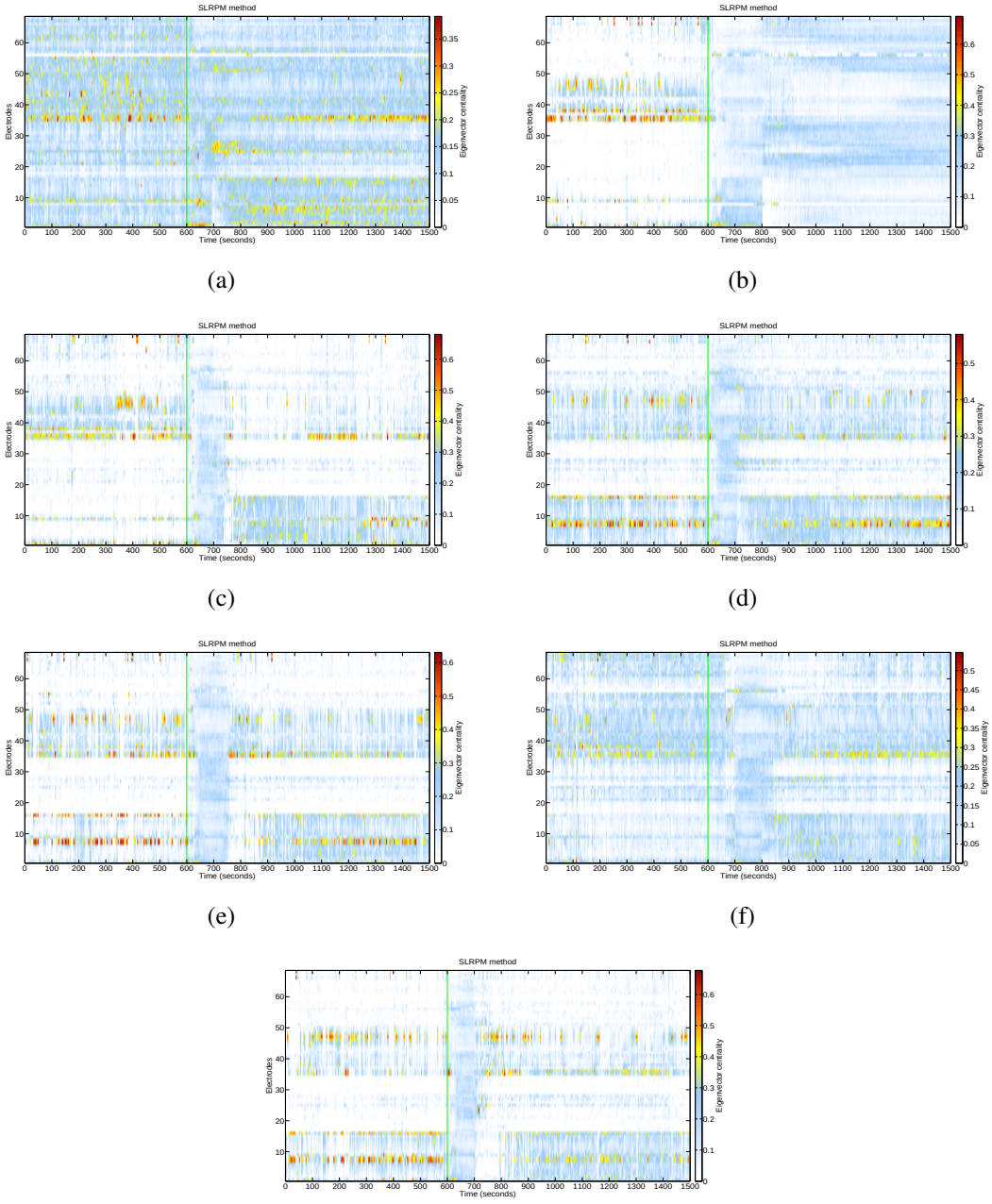

Figure 4.22: EC plots for the SLRPM method for seizures 1, 2, 3, 4, 5, 6, and 7 (shown in (a), (b), (c), (d), (e), (f), and (g) respectively) in patient 3. Green lines in all plots denote the seizure onset time.

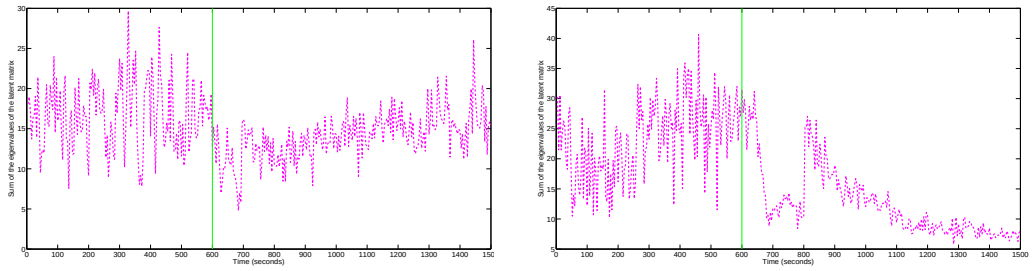

(a)

(b)

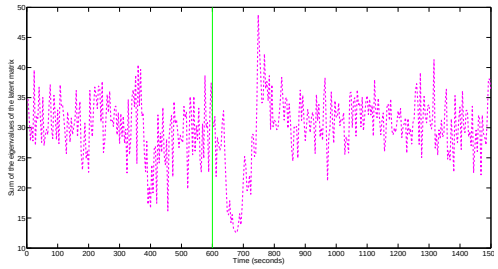

(c)

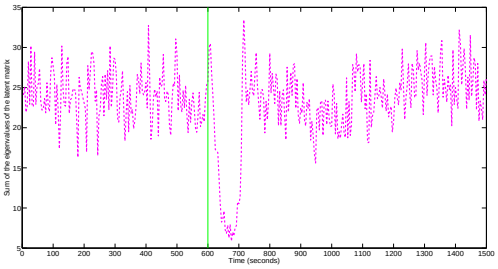

(d)

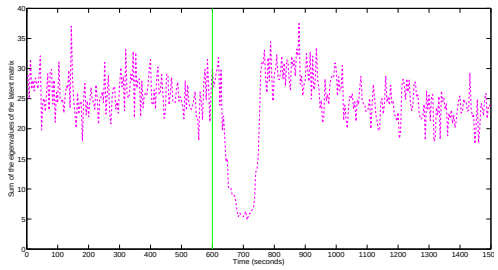

(e)

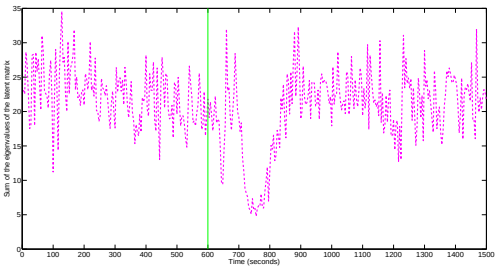

(f)

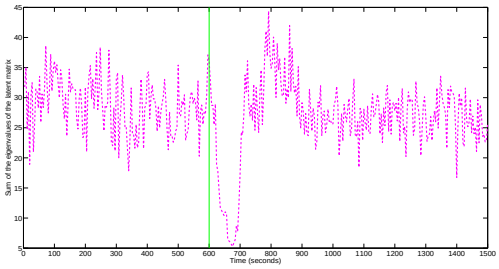

(g)

Figure 4.23: Plots of the latent inputs estimated by the SLRPM method for seizures 1, 2, 3, 4, 5, 6, and 7 (shown in (a), (b), (c), (d), (e), (f), and (g) respectively) in patient 3. Green lines in all plots denote the seizure onset time.

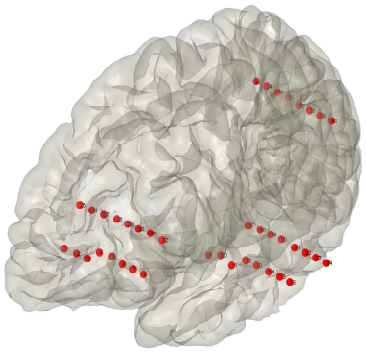

Figure 4.24: Electrode locations in patient 4.

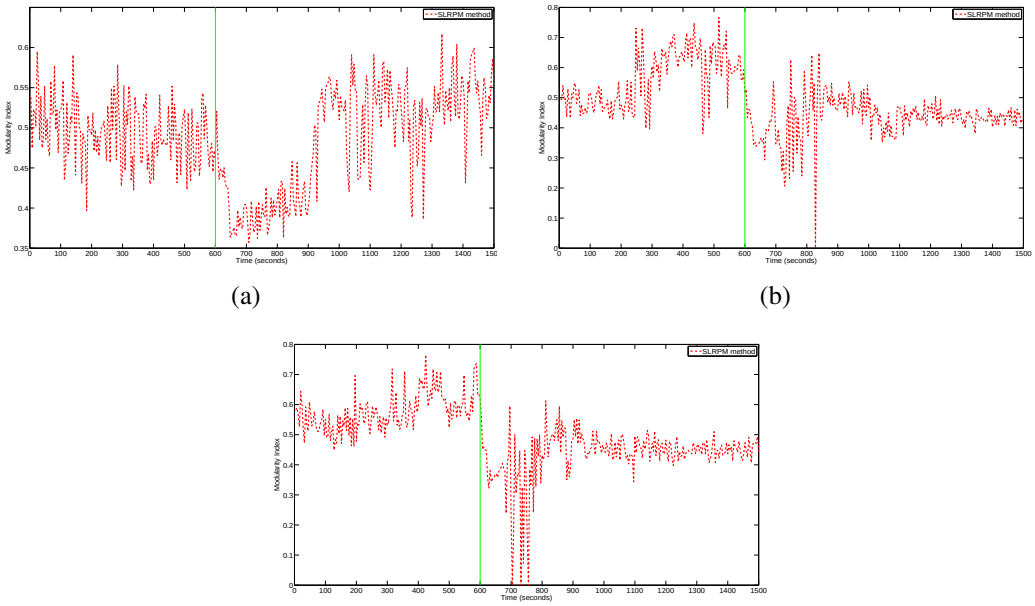

(a) (b)

(c)

Figure 4.25: MI plots for the SLRPM method for seizures 1, 2, and 3 (shown in (a), (b), and (c), respectively) in patient 4. Green lines in all plots denote the seizure onset time.

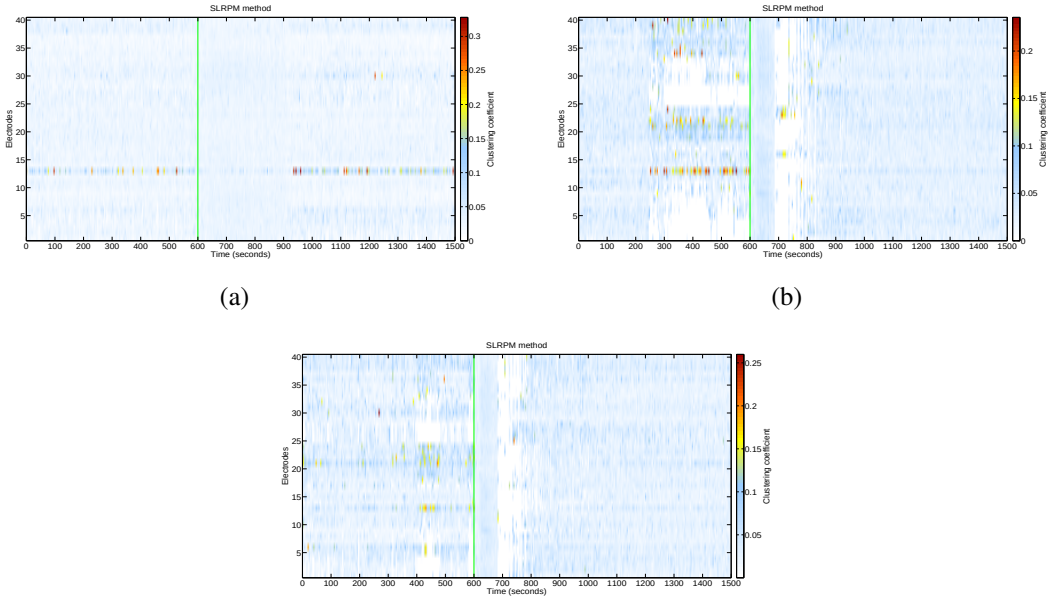

(a) (b)

(c)

Figure 4.26: CC plots for the SLRPM method for seizures 1, 2, and 3 (shown in (a), (b), and (c), respectively) in patient 4. Green lines in all plots denote the seizure onset time.

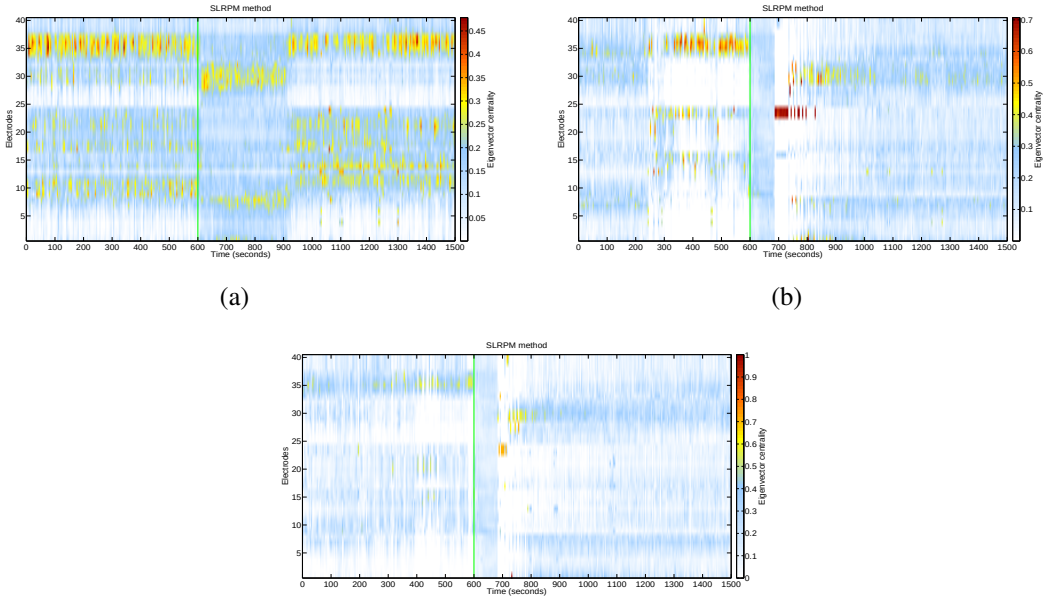

(a) (b)

(c)

Figure 4.27: EC plots for the SLRPM method for seizures 1, 2, and 3 (shown in (a), (b), and (c), respectively) in patient 4. Green lines in all plots denote the seizure onset time.

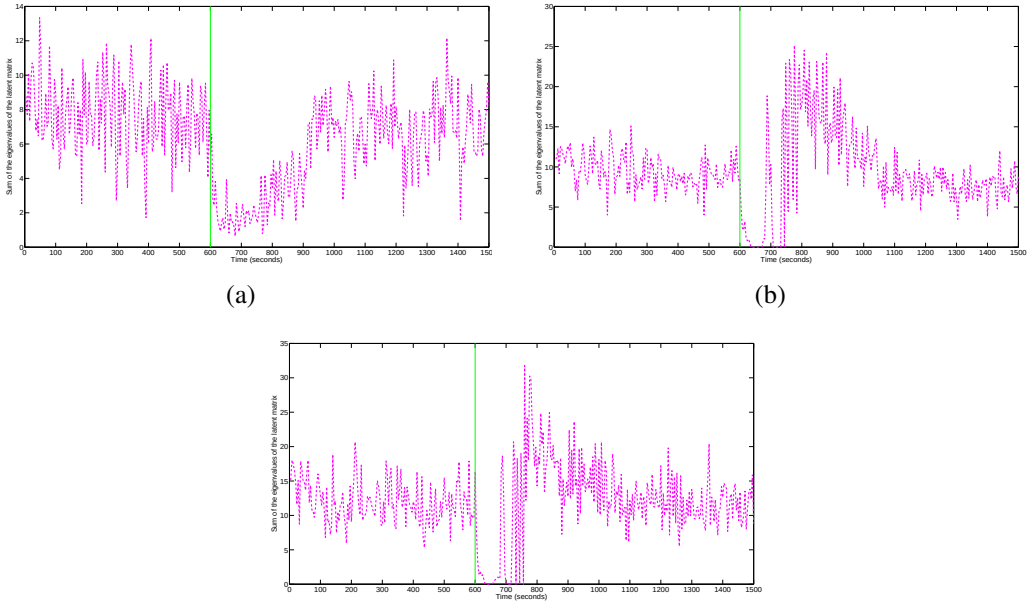

(a) (b)

(c)

Figure 4.28: Plots of the latent inputs estimated by the SLRPM method for seizures 1, 2, and 3 (shown in (a), (b), and (c), respectively) in patient 4. Green lines in all plots denote the seizure onset time.

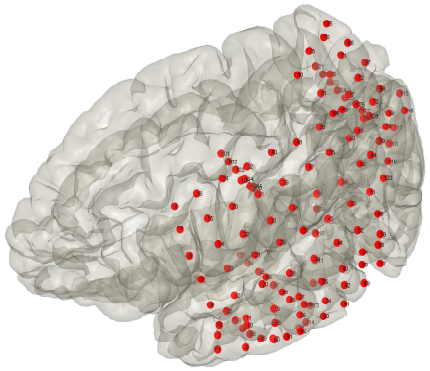

Figure 4.29: Electrode locations in patient 5.

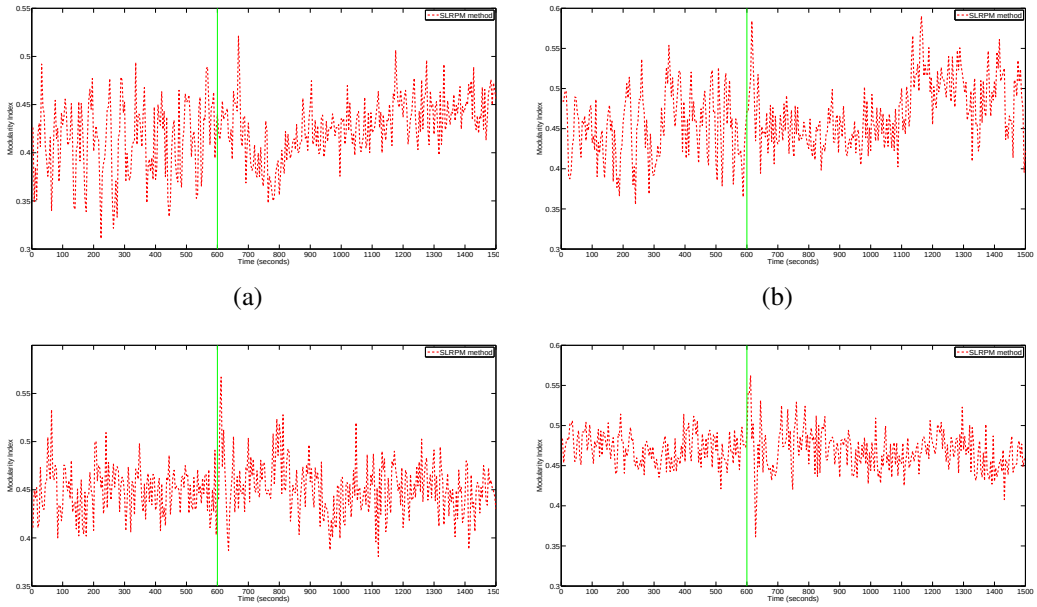

(a) (b)

(c) (d)

Figure 4.30: MI plots for the SLRPM method for four characteristic seizures in patient 5. Green lines in all plots denote the seizure onset time.

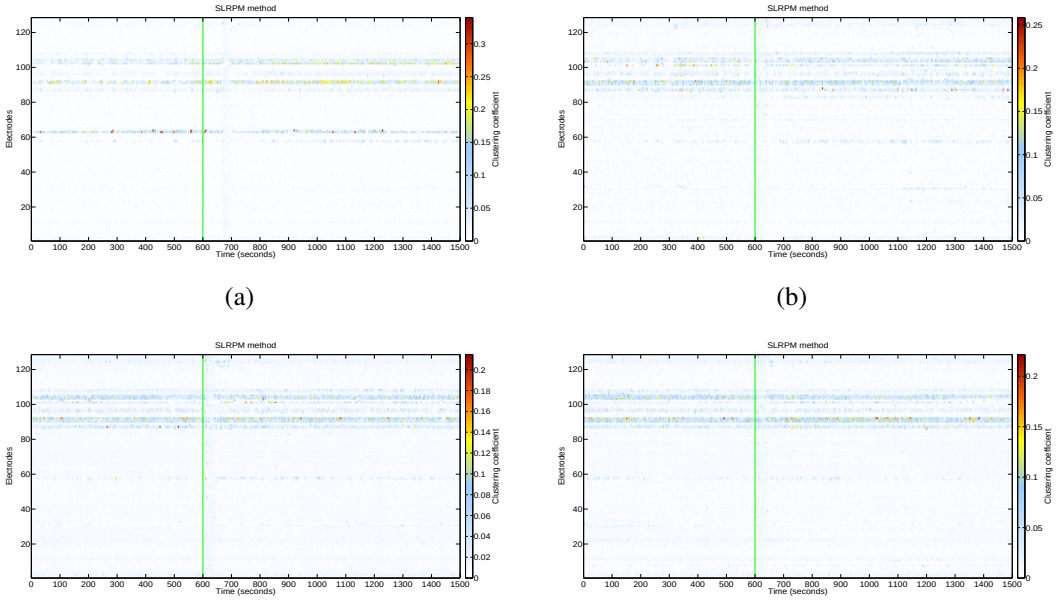

(a) (b)

(c) (d)

Figure 4.31: CC plots for the SLRPM method for four characteristic seizures in patient 5. Green lines in all plots denote the seizure onset time.

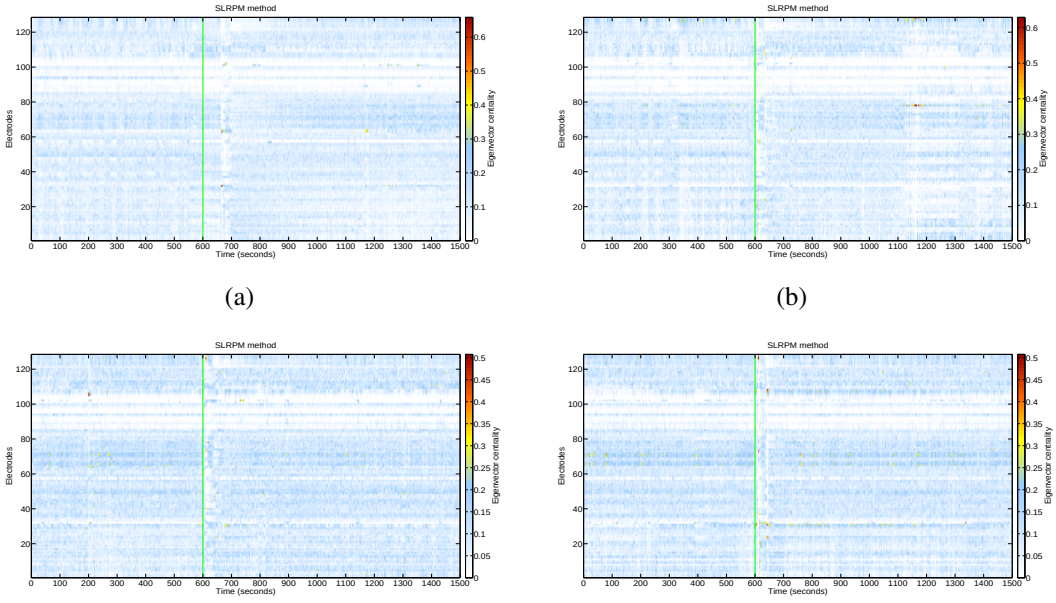

(a) (b)

(c) (d)

Figure 4.32: EC plots for the SLRPM method for four characteristic seizures in patient 5. Green lines in all plots denote the seizure onset time.

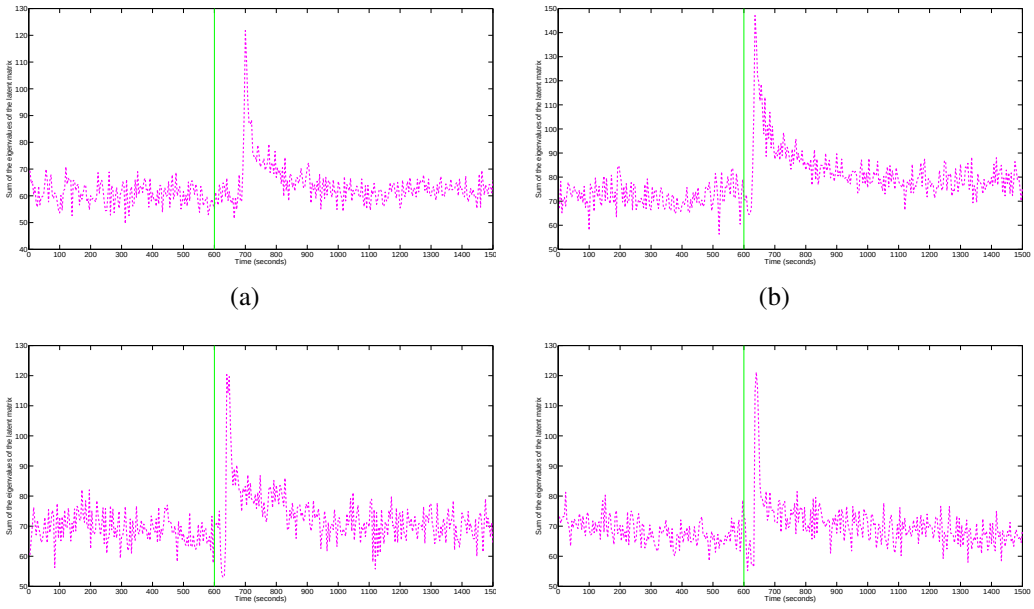

(a) (b)

(c) (d)

Figure 4.33: Plots of the latent inputs estimated by the SLRPM method for four characteristic seizures in patient 5. Green lines in all plots denote the seizure onset time.

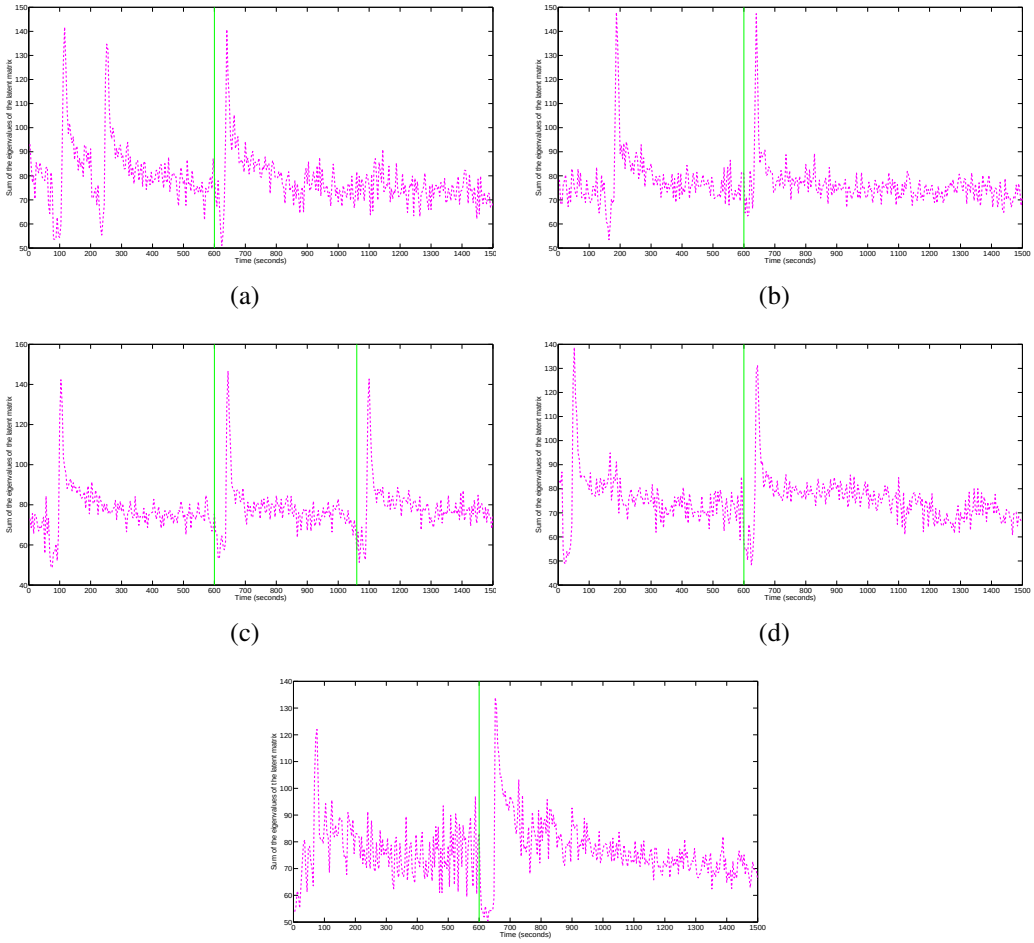

(a) (b)

(c) (d)

(e)

Figure 4.34: Plots of the latent inputs estimated by the SLRPM method for 5 characteristic seizures in patient 5 in which ictal dynamics is also observed at time instants (2 in (a) and one each in (b)-(e)) which were not classified by the clinician as seizure onset times. Green lines in all plots denote the seizure onset time.

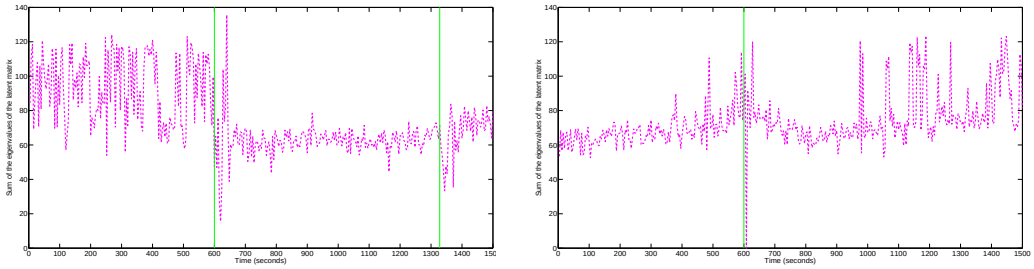

(a)

(b)

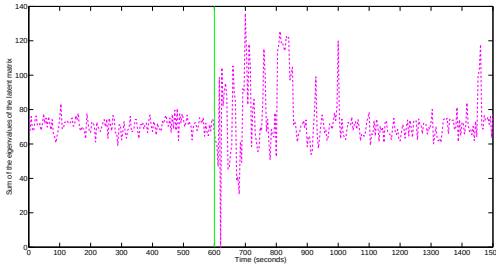

(c)

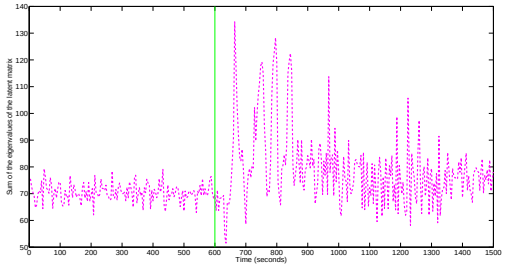

(d)

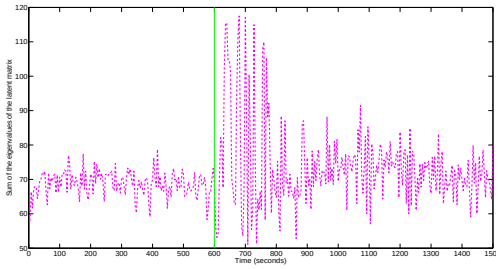

(e)

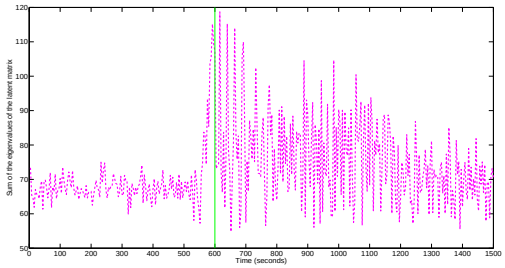

(f)

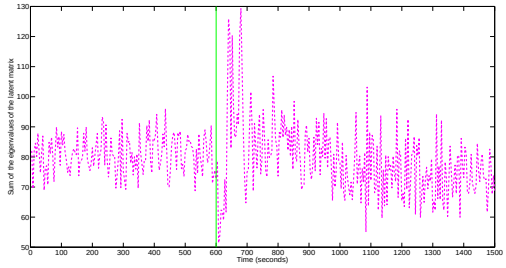

(g)

Figure 4.35: Plots of the latent inputs estimated by the SLRPM method for the 8 non-characteristic seizures in patient 5. Green lines in all plots denote the seizure onset time.

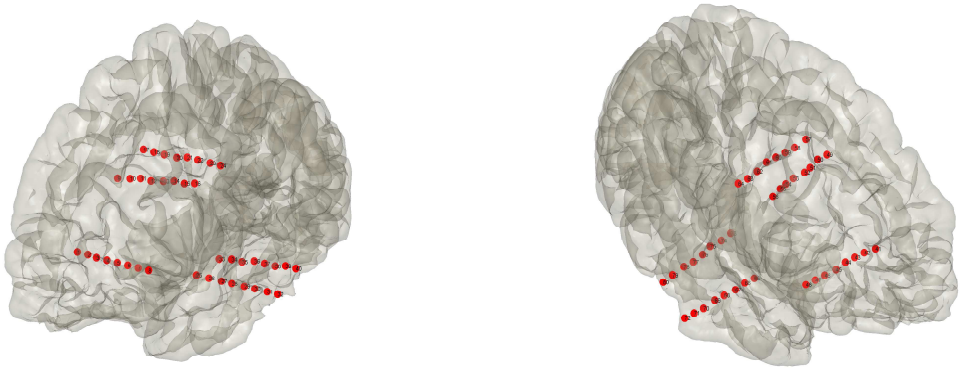

(a) (b)

Figure 4.36: Electrode locations in patient 6. (a) Left hemisphere. (b) Right hemisphere.

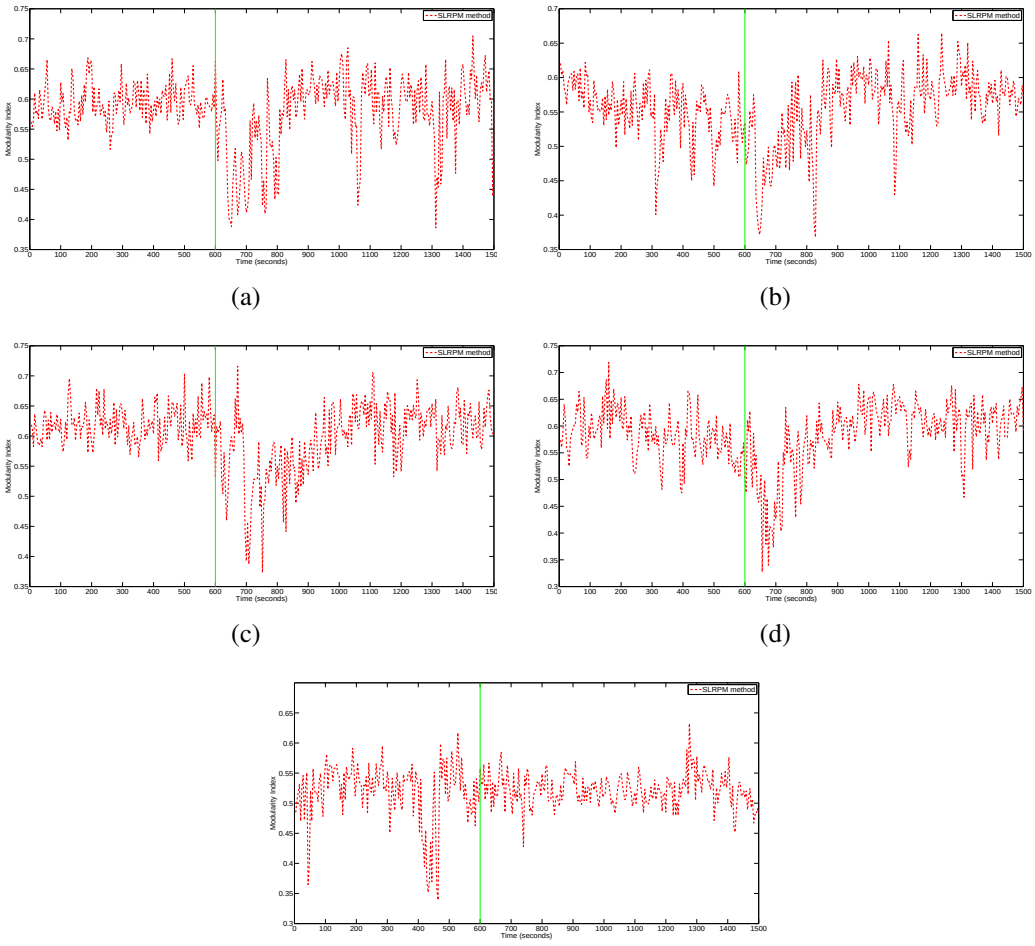

(a) (b)

(c) (d)

(e)

Figure 4.37: MI plots for the SLRPM method for the five group 1 seizures in patient 6. Green lines in all plots denote the seizure onset time.

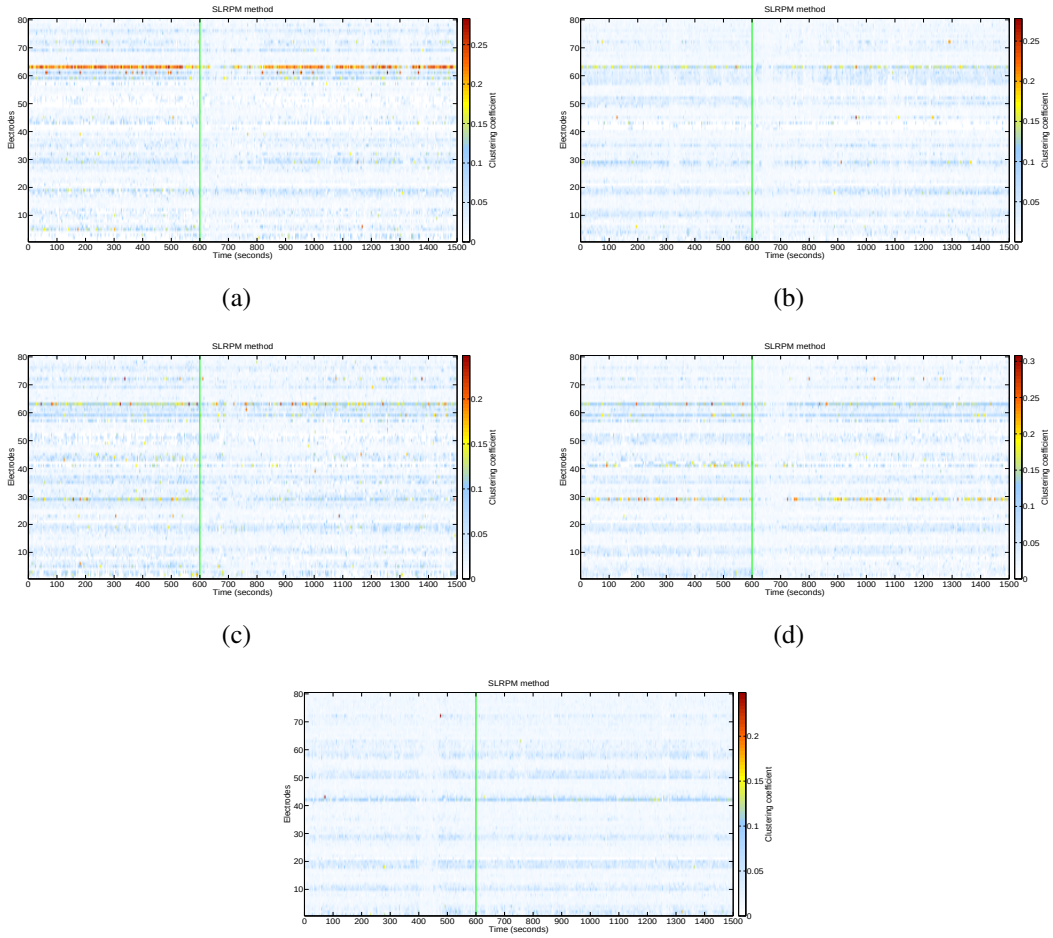

Figure 4.38: CC plots for the SLRPM method for the five group 1 seizures in patient 6. Green lines in all plots denote the seizure onset time.

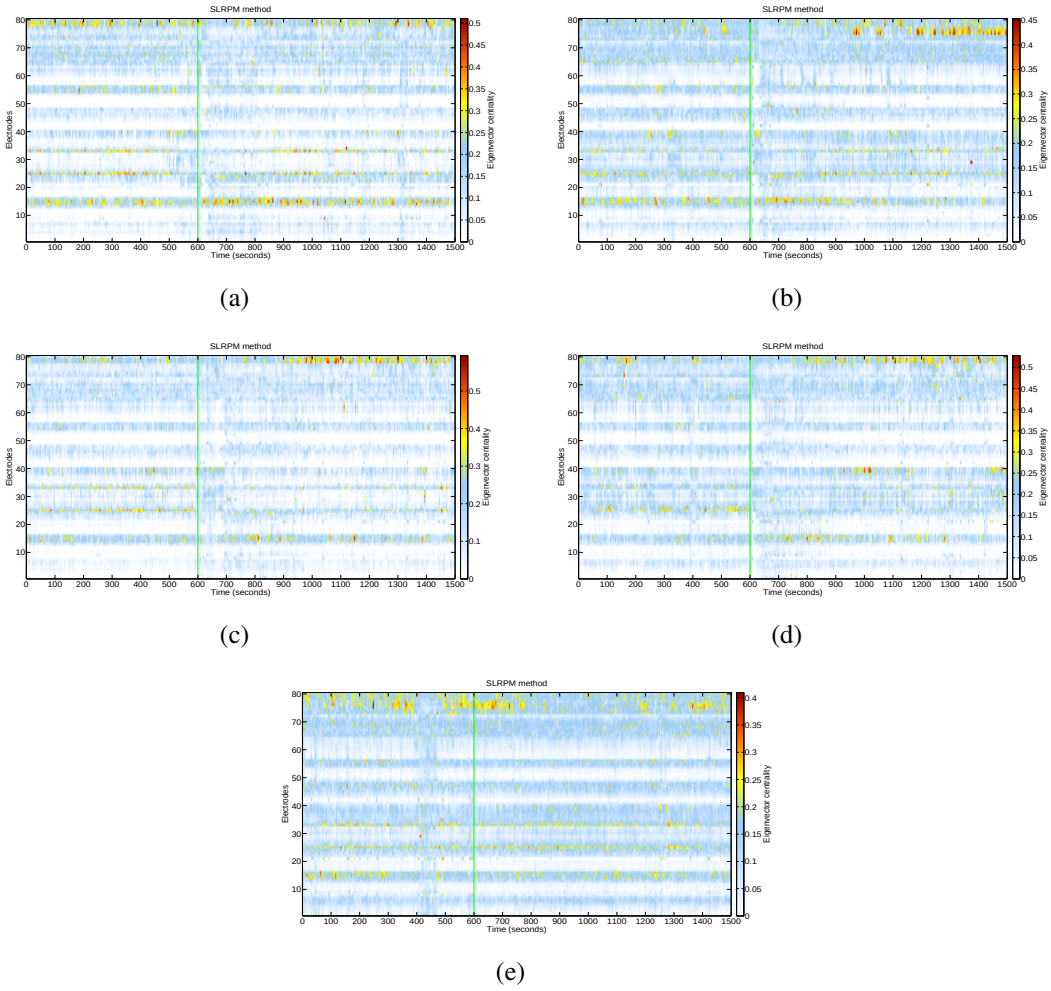

Figure 4.39: EC plots for the SLRPM method for the five group 1 seizures in patient 6. Green lines in all plots denote the seizure onset time.

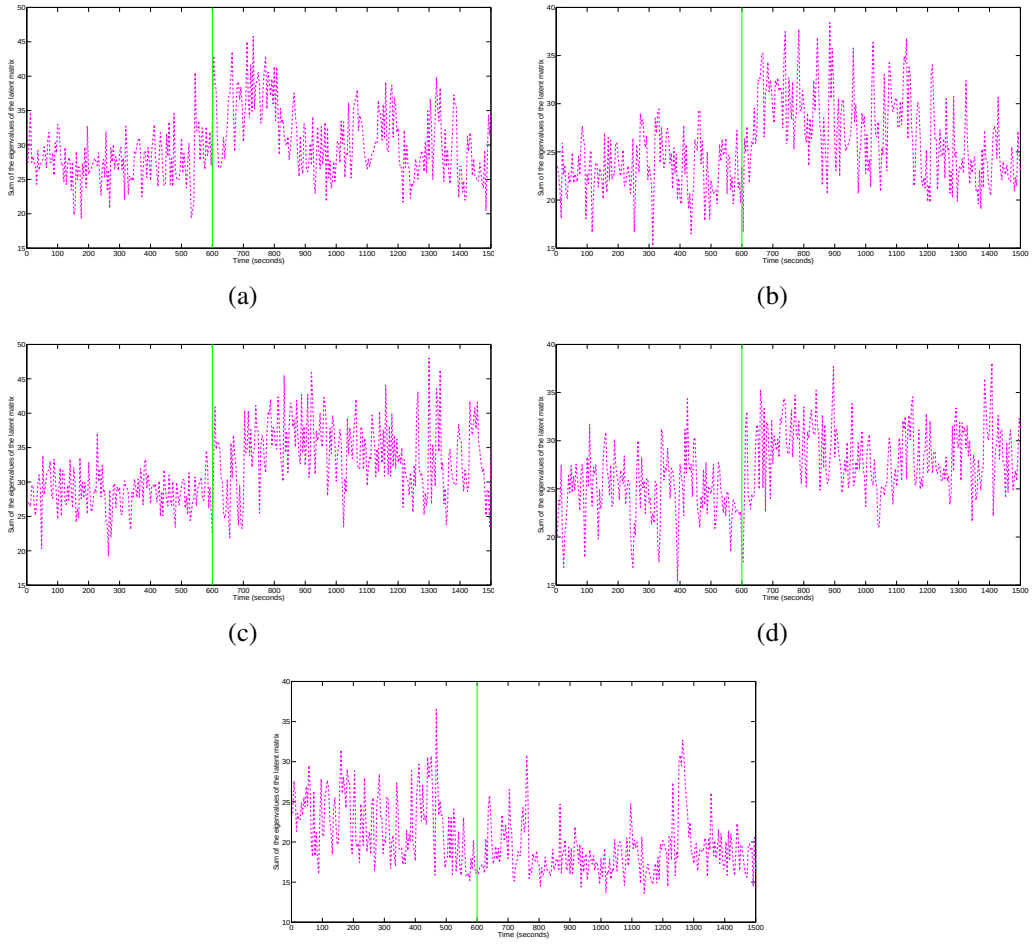

(a) (b)

(c) (d)

(e)

Figure 4.40: Plots of the latent inputs estimated by the SLRPM method for the five group 1 seizures in patient 6. Green lines in all plots denote the seizure onset time.

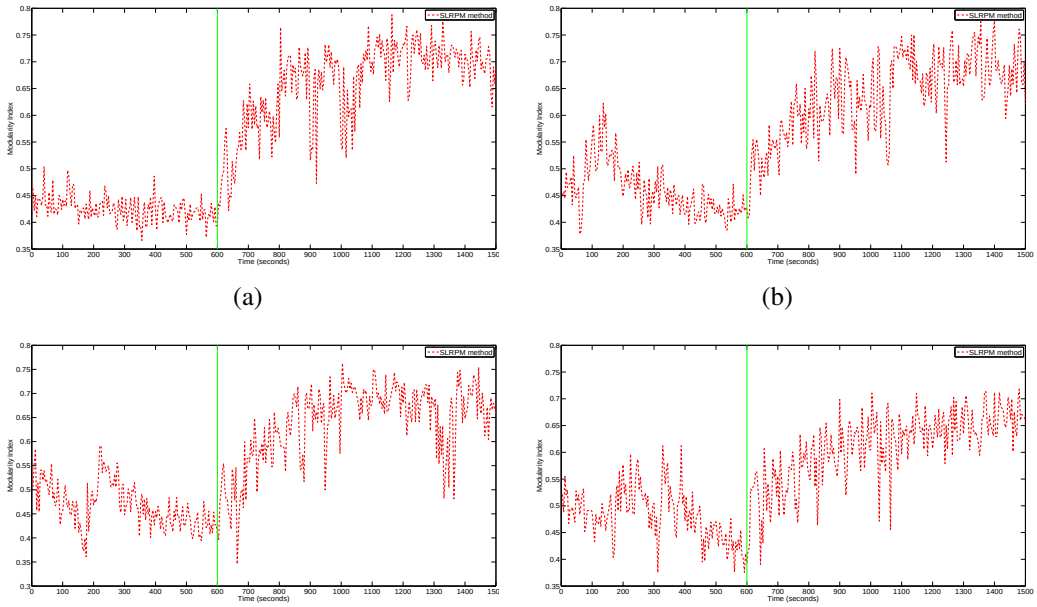

(a) (b)

(c) (d)

Figure 4.41: MI plots for the SLRPM method for the four group 2 seizures in patient 6. Green lines in all plots denote the seizure onset time.

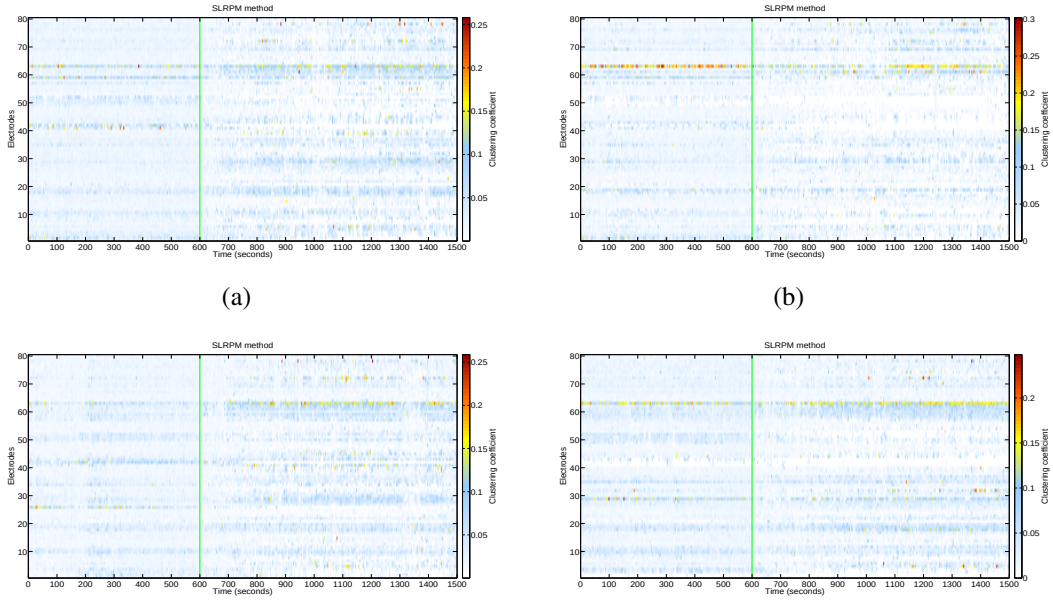

(a) (b)

(c) (d)

Figure 4.42: CC plots for the SLRPM method for the four group 2 seizures in patient 6. Green lines in all plots denote the seizure onset time.

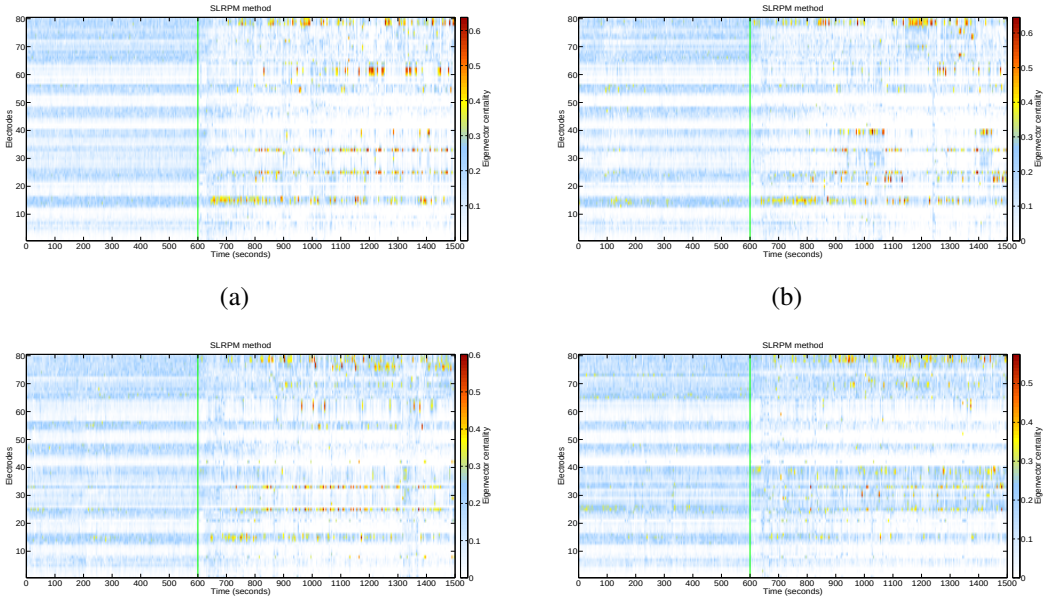

Figure 4.43: EC plots for the SLRPM method for the four group 2 seizures in patient 6. Green lines in all plots denote the seizure onset time.

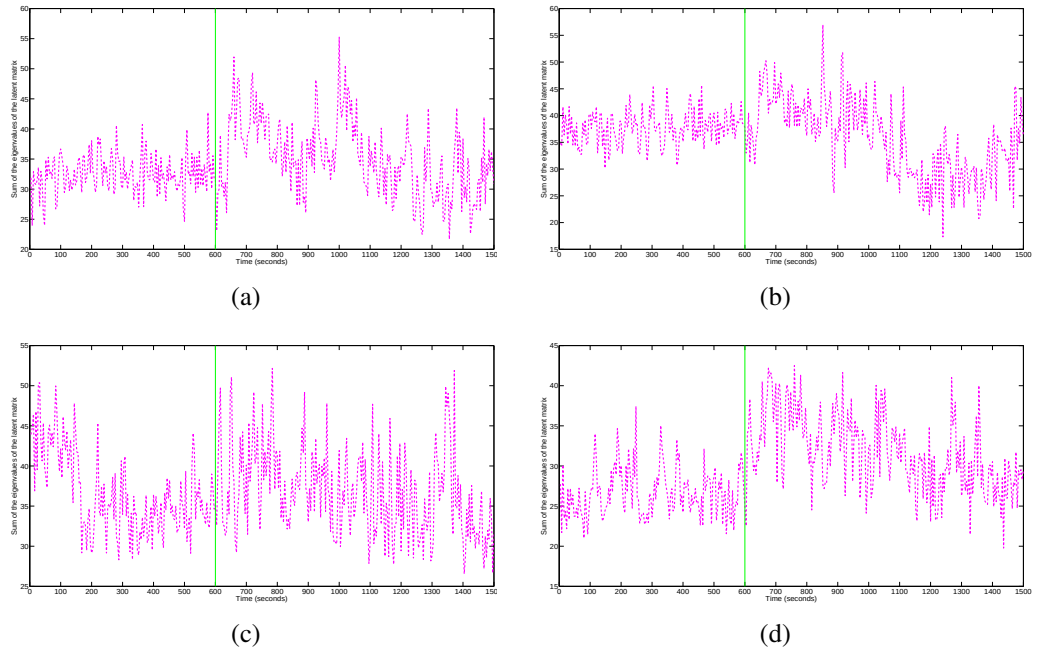

Figure 4.44: Plots of the latent inputs estimated by the SLRPM method for the four group 2 seizures in patient 6. Green lines in all plots denote the seizure onset time.

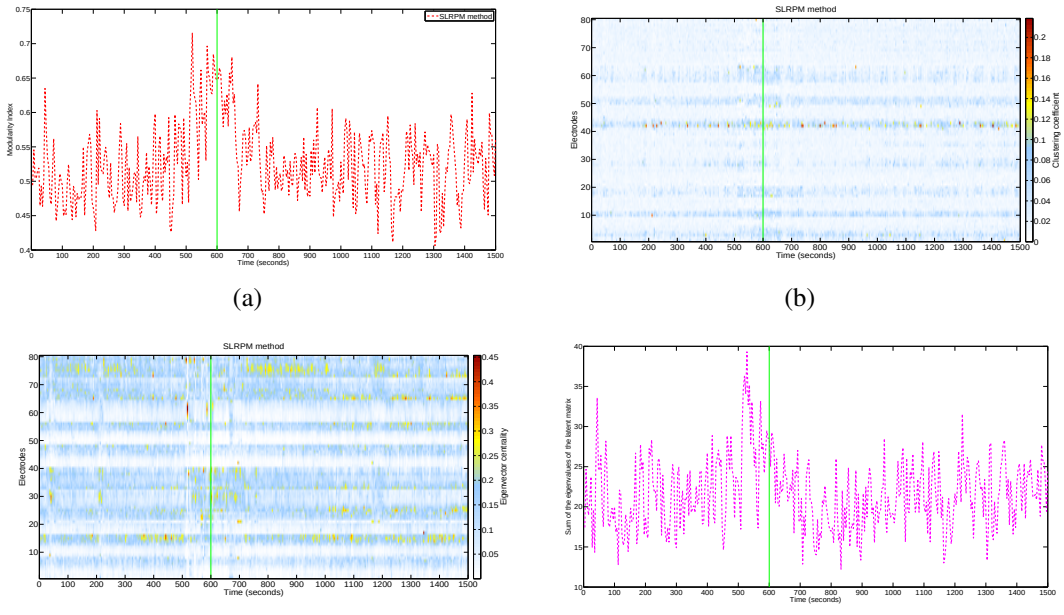

Figure 4.45: Plots of the four measures estimated by the SLRPM method for the one seizure whose characteristic was different from the two groups of seizures in patient 6. Green lines in all plots denote the seizure onset time.

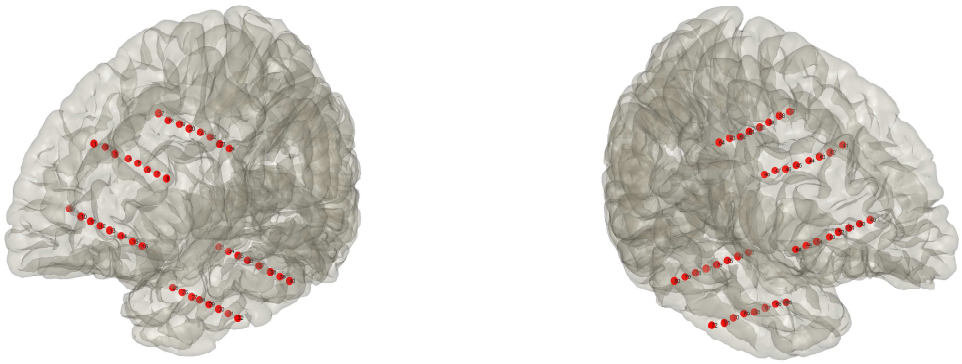

Figure 4.46: Electrode locations in patient 7. (a) Left hemisphere. (b) Right hemisphere.

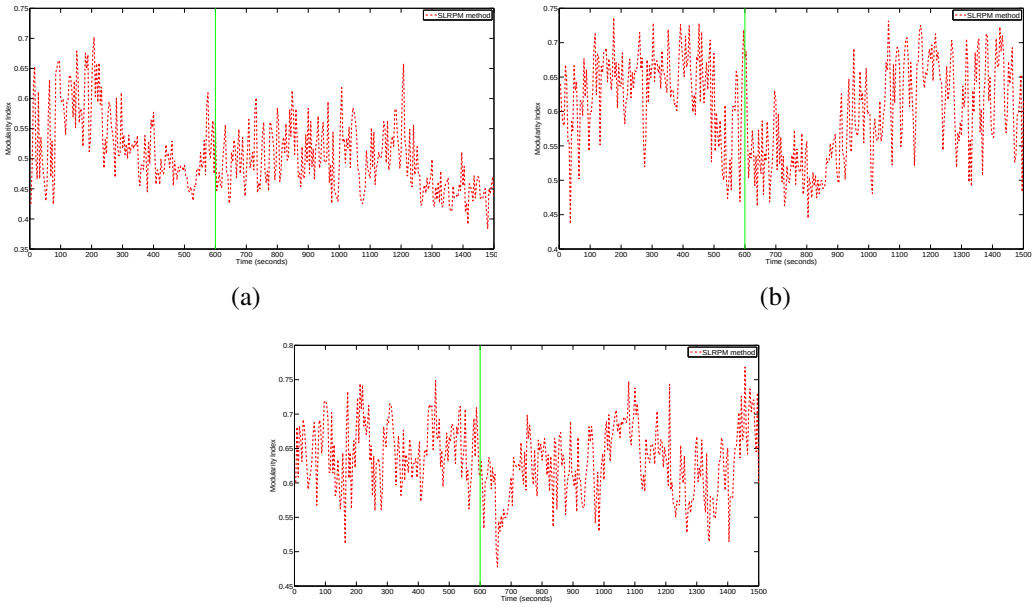

(a) (b)

(c)

Figure 4.47: MI plots for the SLRPM method for 3 seizures in patient 7. Green lines in all plots denote the seizure onset time.

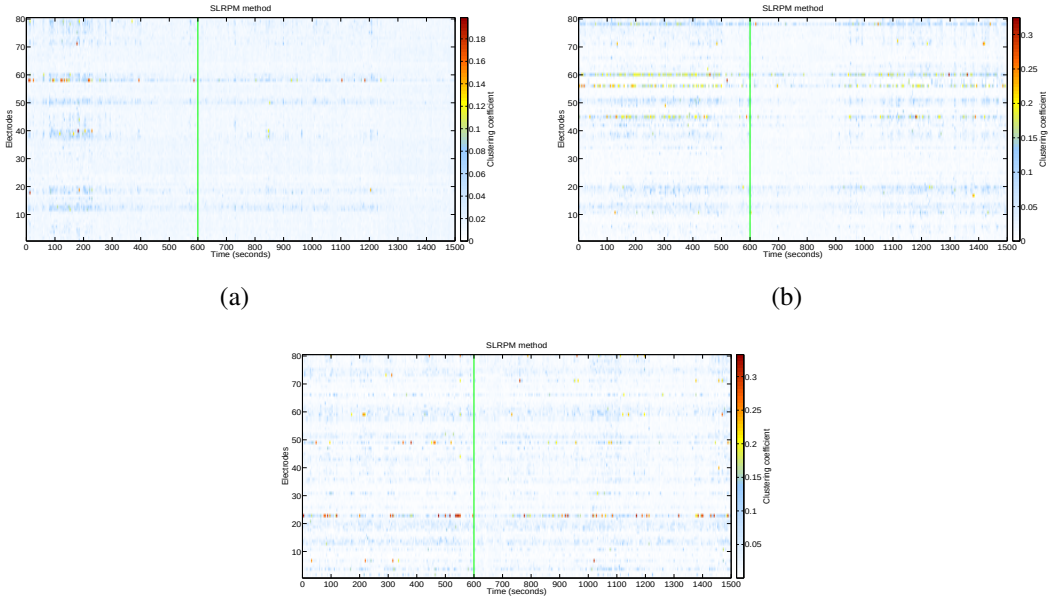

(a) (b)

(c)

Figure 4.48: CC plots for the SLRPM method for 3 seizures in patient 7. Green lines in all plots denote the seizure onset time.

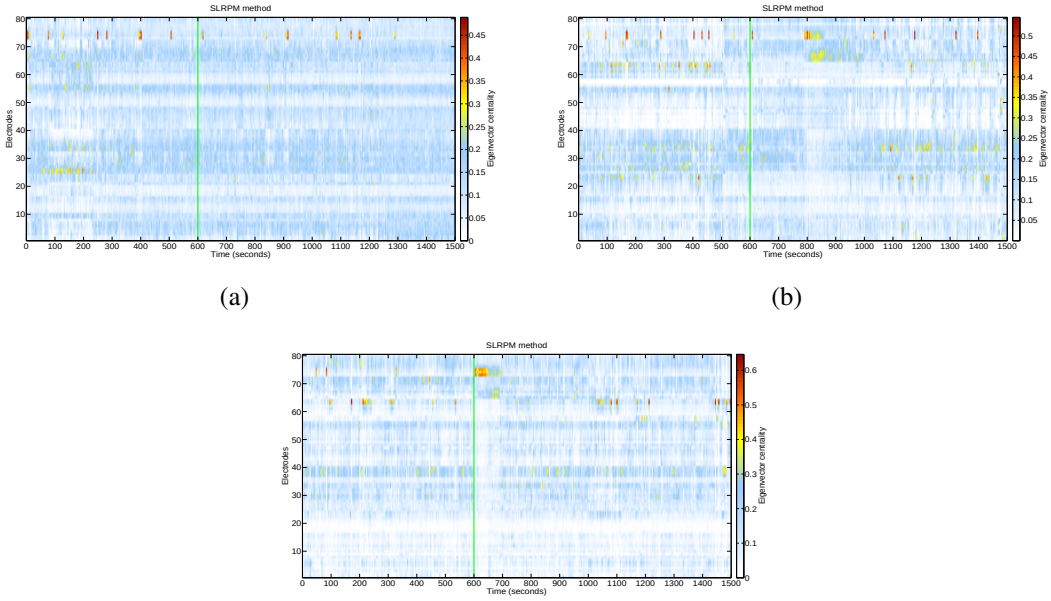

(a) (b)

(c)

Figure 4.49: EC plots for the SLRPM method for 3 seizures in patient 7. Green lines in all plots denote the seizure onset time.

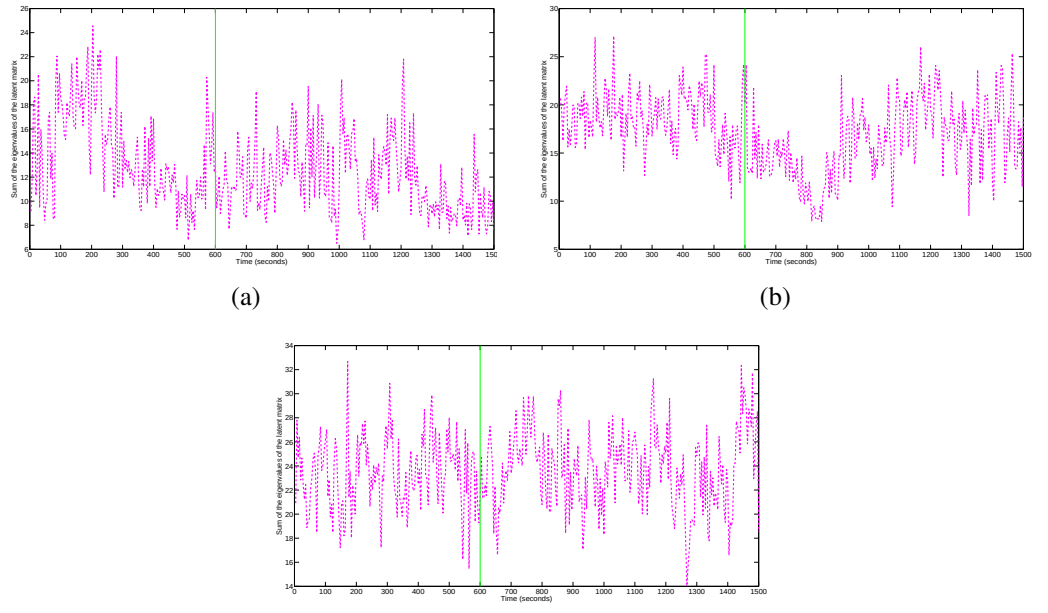

(a) (b)

(c)

Figure 4.50: Plots of the latent inputs estimated by the SLRPM method for 3 seizures in patient 7. Green lines in all plots denote the seizure onset time.

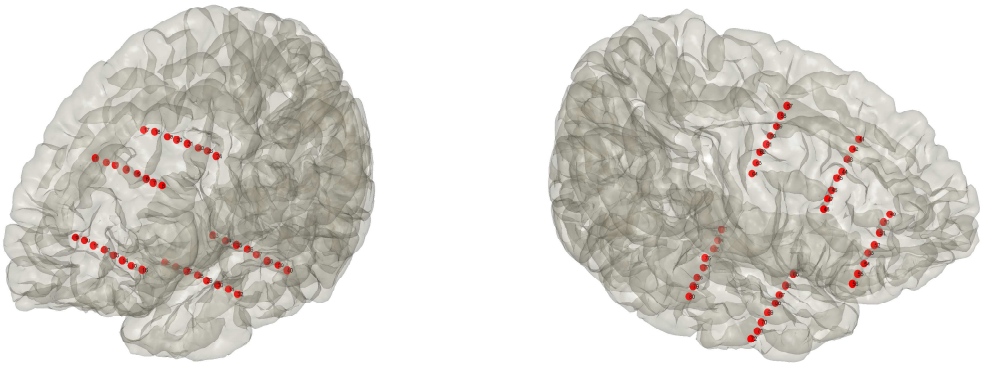

(a) (b)

Figure 4.51: Electrode locations in patient 8. (a) Left hemisphere. (b) Right hemisphere.

Table 4.13: Heterogeneity statistics for seizures in each patient for the SLRPM, SRPM, and correlation methods.

Patient	DH for SLRPM	A/O for SLRPM	DH for SRPM	A/O for SRPM	DH for correlation	A/O for correlation
1	68.51	0/10	55.42	0/10	5.93	0/10
2	42.51	7/9	31.17	6/9	2.08	0/9
3	30.99	2/10	18.04	3/10	6.27	0/10
4	4.89	0/2	9.93	0/2	0.30	0/2
5	32.05	4/9	11.76	0/9	2.92	0/9
6	15.96	1/12	10.61	1/12	3.63	1/12
7	21.72	1/13	10.43	1/13	7.24	3/13
8	48.10	1/6	25.48	3/6	1.72	0/6
9	53.37	12/28	35.53	6/28	13.31	17/28
10	57.53	0/8	36.50	2/8	4.45	0/8
11	11.32	0/8	8.85	0/8	6.31	0/8
12	24.02	0/4	18.36	0/4	2.67	0/4

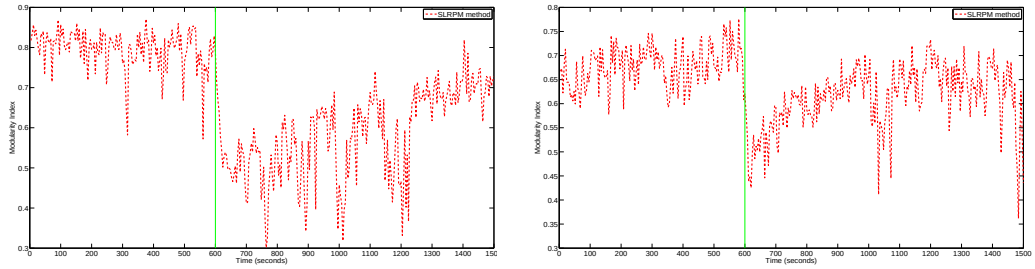

(a)

(b)

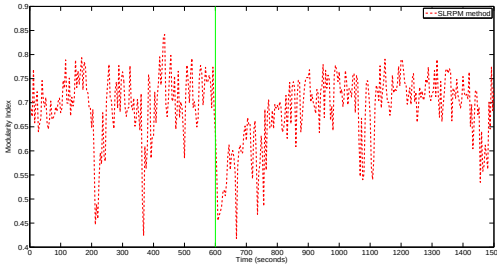

(c)

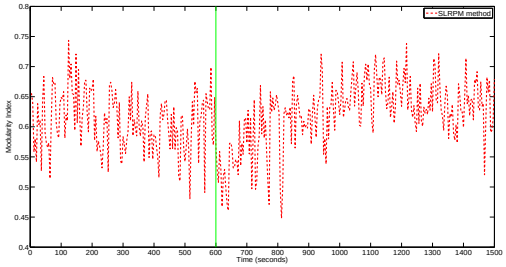

(d)

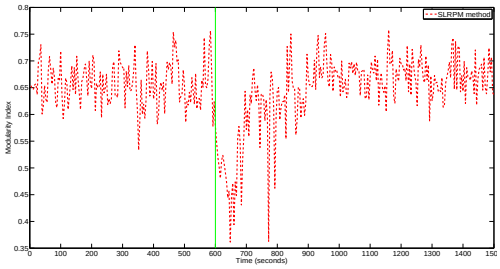

(e)

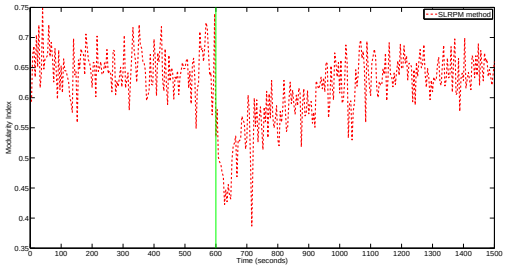

(f)

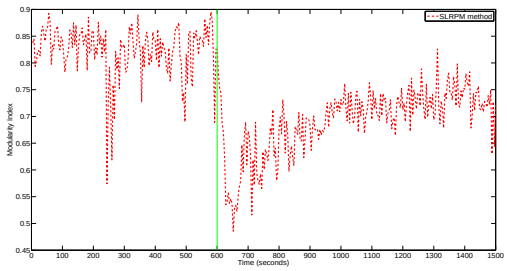

(g)

Figure 4.52: MI plots for the SLRPM method for the 7 clinical seizures in patient 8. Green lines in all plots denote the seizure onset time.

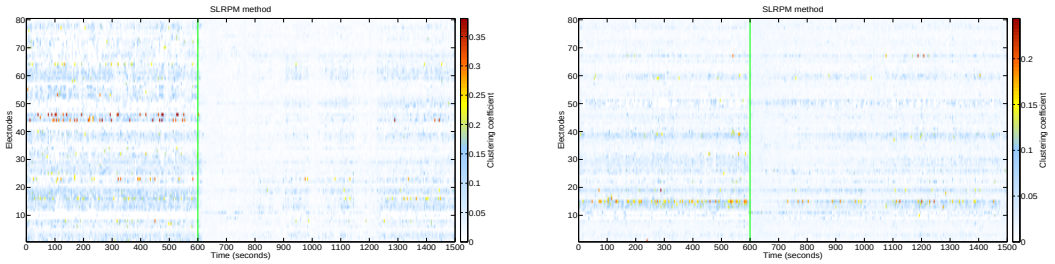

(a)

(b)

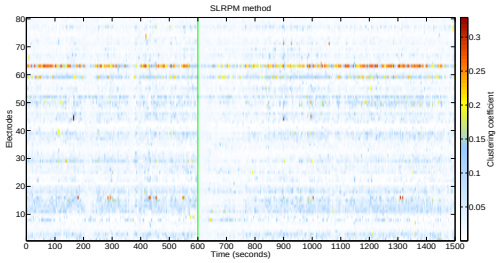

(c)

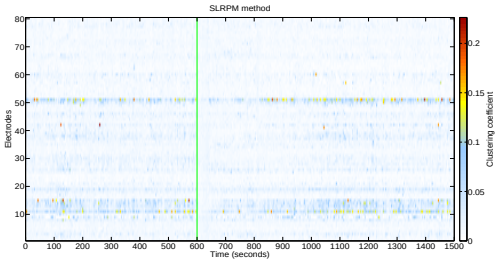

(d)

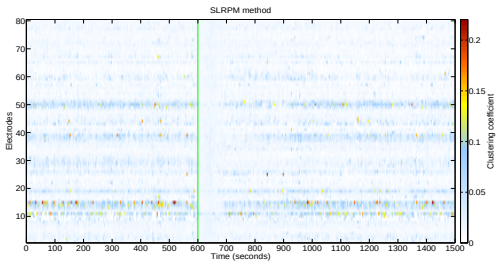

(e)

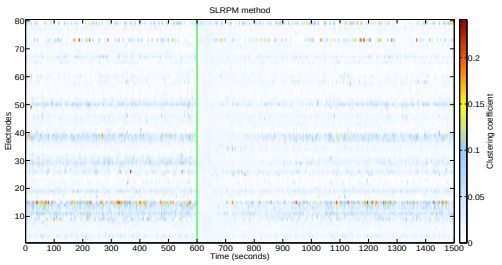

(f)

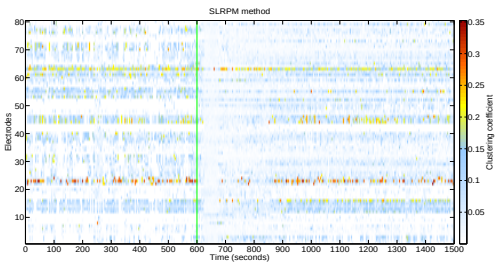

(g)

Figure 4.53: CC plots for the SLRPM method for the 7 clinical seizures in patient 8. Green lines in all plots denote the seizure onset time.

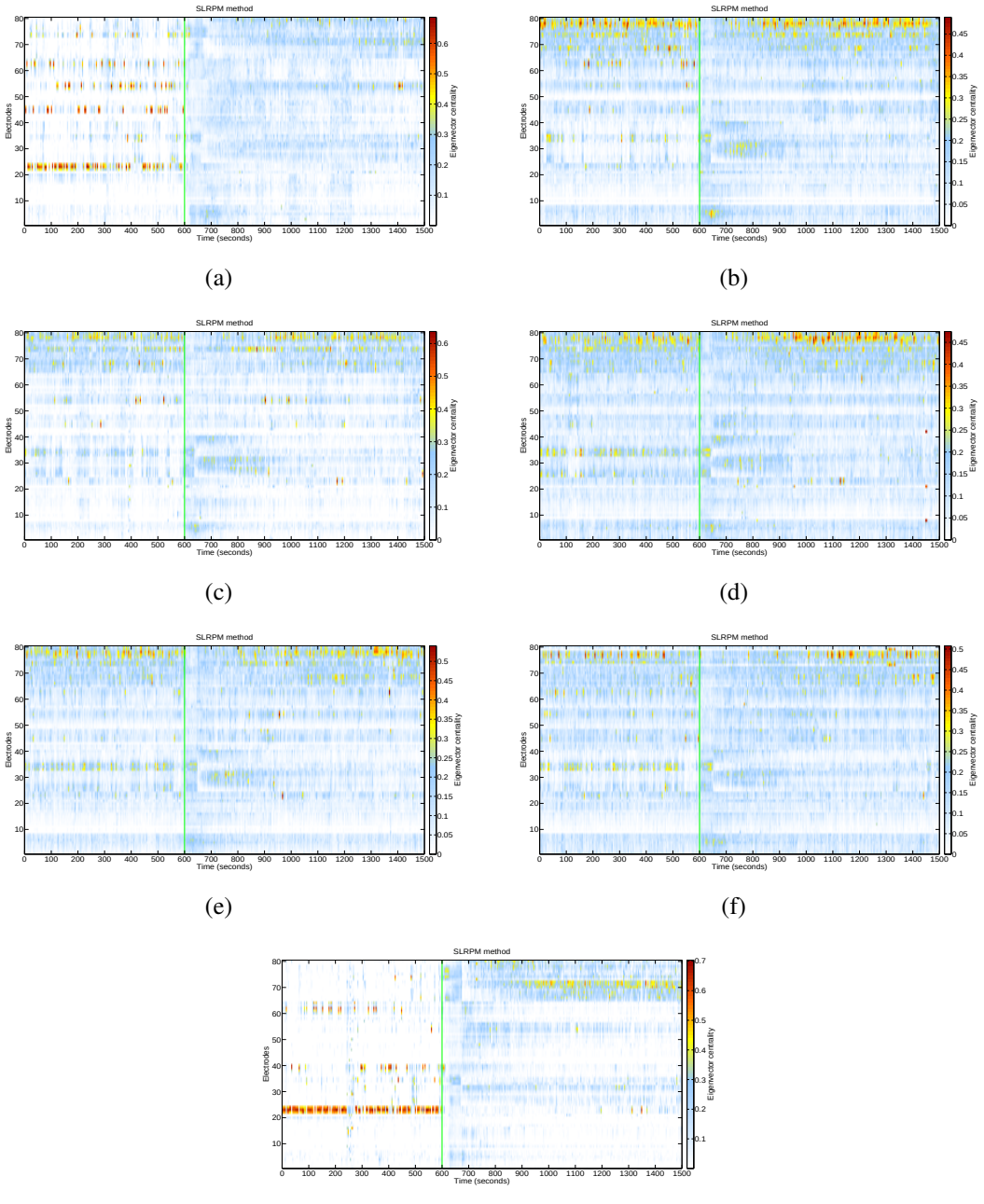

Figure 4.54: EC plots for the SLRPM method for the 7 clinical seizures in patient 8. Green lines in all plots denote the seizure onset time.

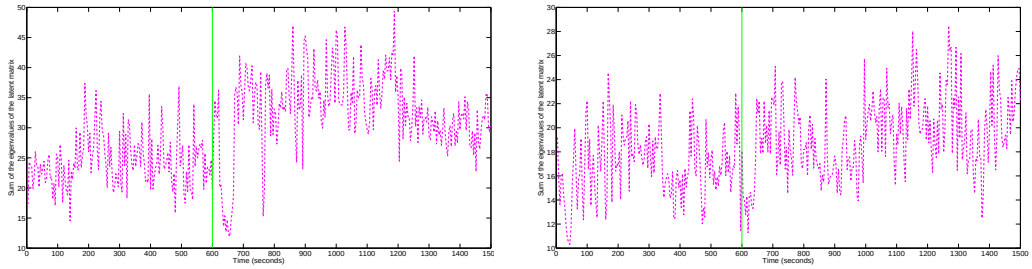

(a)

(b)

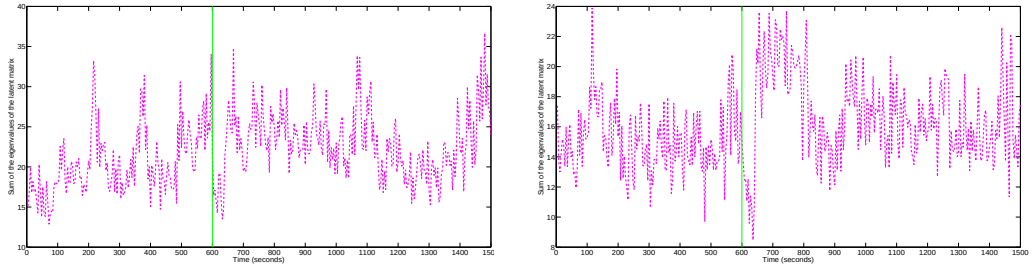

(c)

(d)

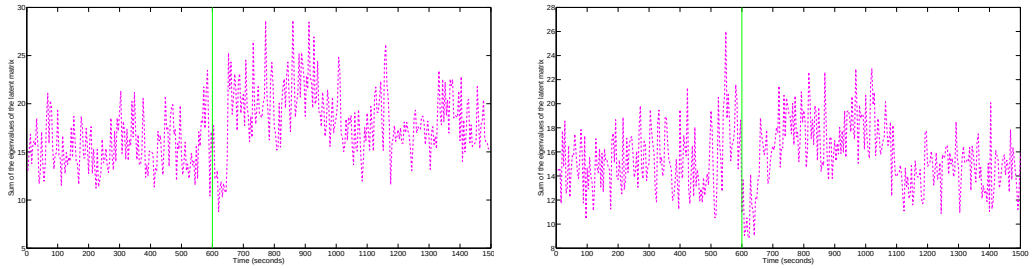

(e)

(f)

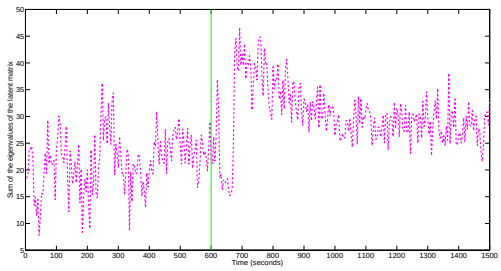

(g)

Figure 4.55: Plots of the latent inputs estimated by the SLRPM method for the 7 clinical seizures in patient 8. Green lines in all plots denote the seizure onset time.

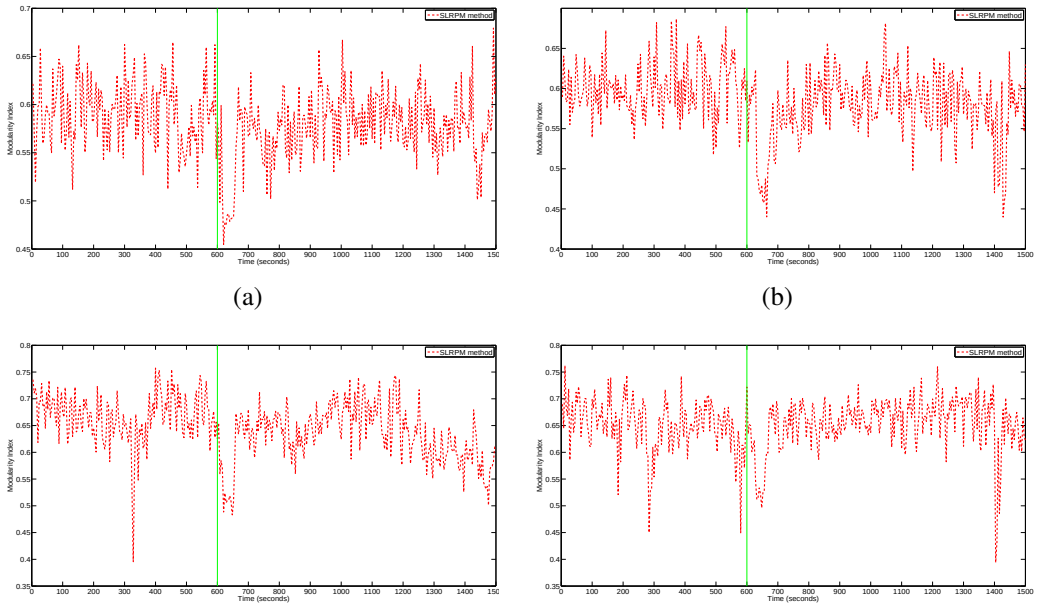

Figure 4.56: MI plots for the SLRPM method for the 4 sub-clinical seizures in patient 8. Green lines in all plots denote the seizure onset time.

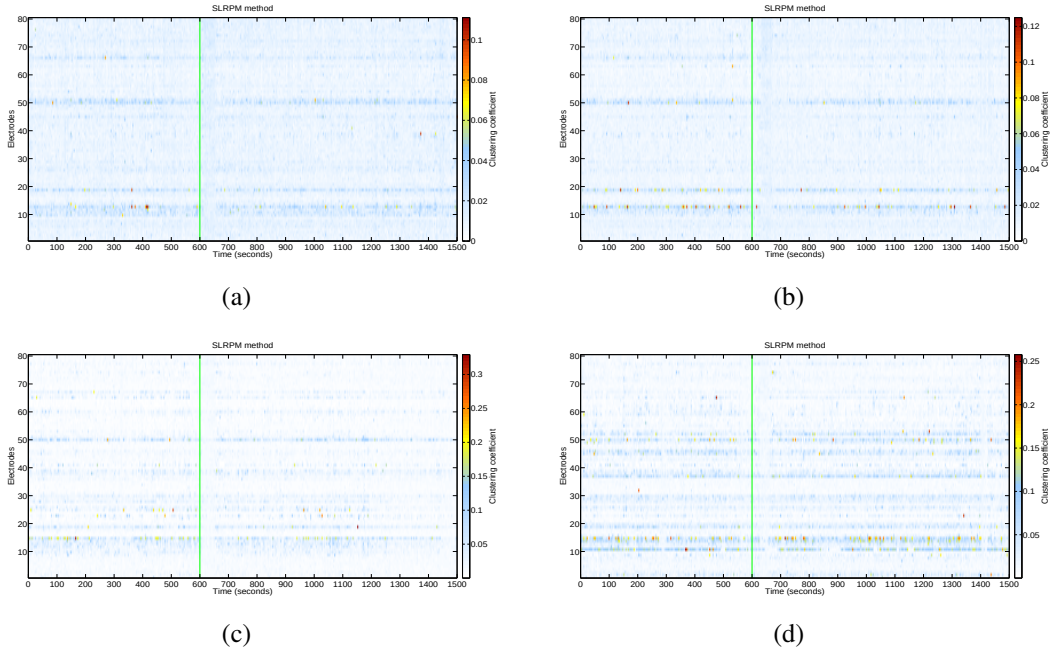

Figure 4.57: CC plots for the SLRPM method for the 4 sub-clinical seizures in patient 8. Green lines in all plots denote the seizure onset time.

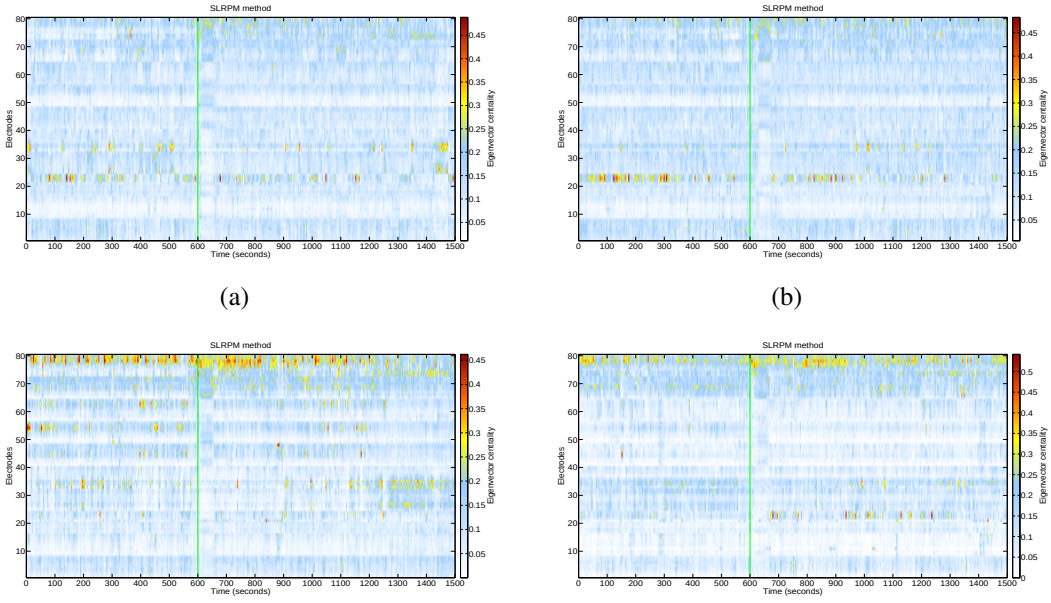

Figure 4.58: EC plots for the SLRPM method for the 4 sub-clinical seizures in patient 8. Green lines in all plots denote the seizure onset time.

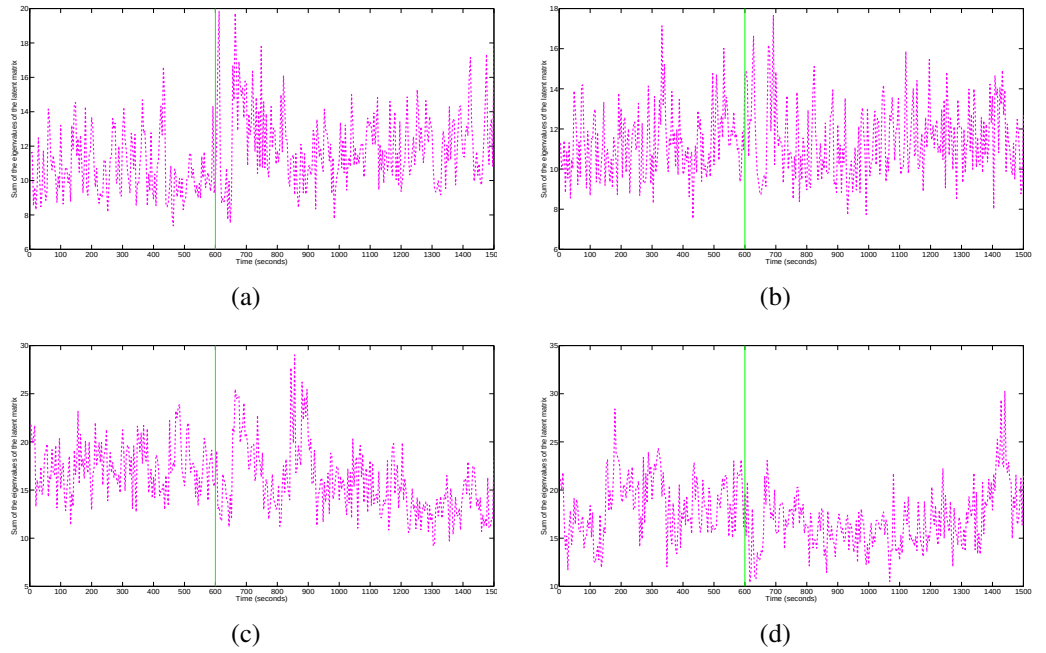

Figure 4.59: Plots of the latent inputs estimated by the SLRPM method for the 4 sub-clinical seizures in patient 8. Green lines in all plots denote the seizure onset time.

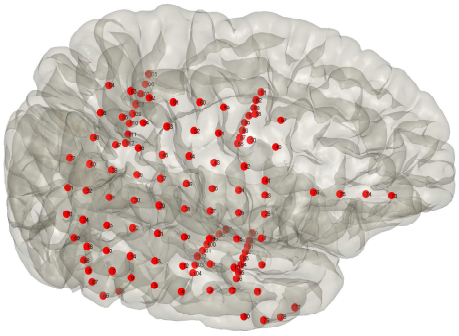

Figure 4.60: Electrode locations in patient 9.

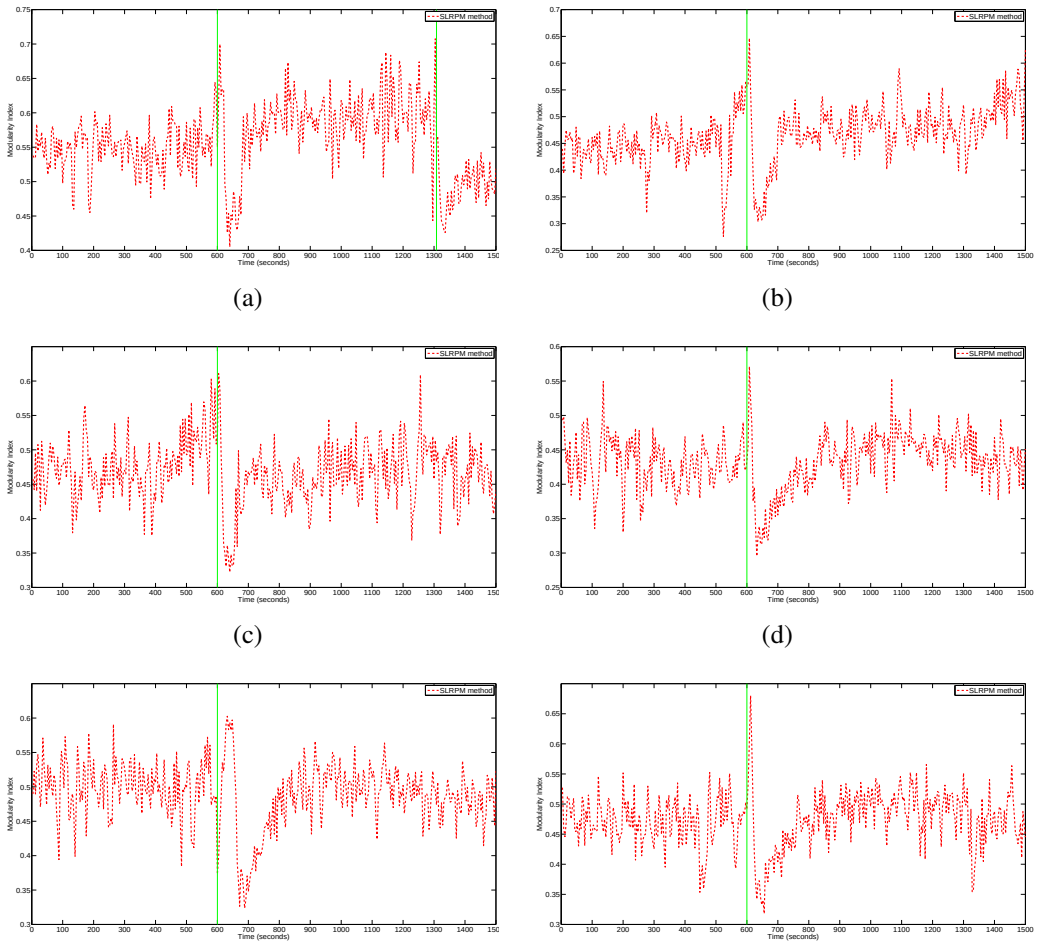

Figure 4.61: MI plots for the SLRPM method for the 7 group 1 seizures in patient 9. Green lines in all plots denote the seizure onset time.

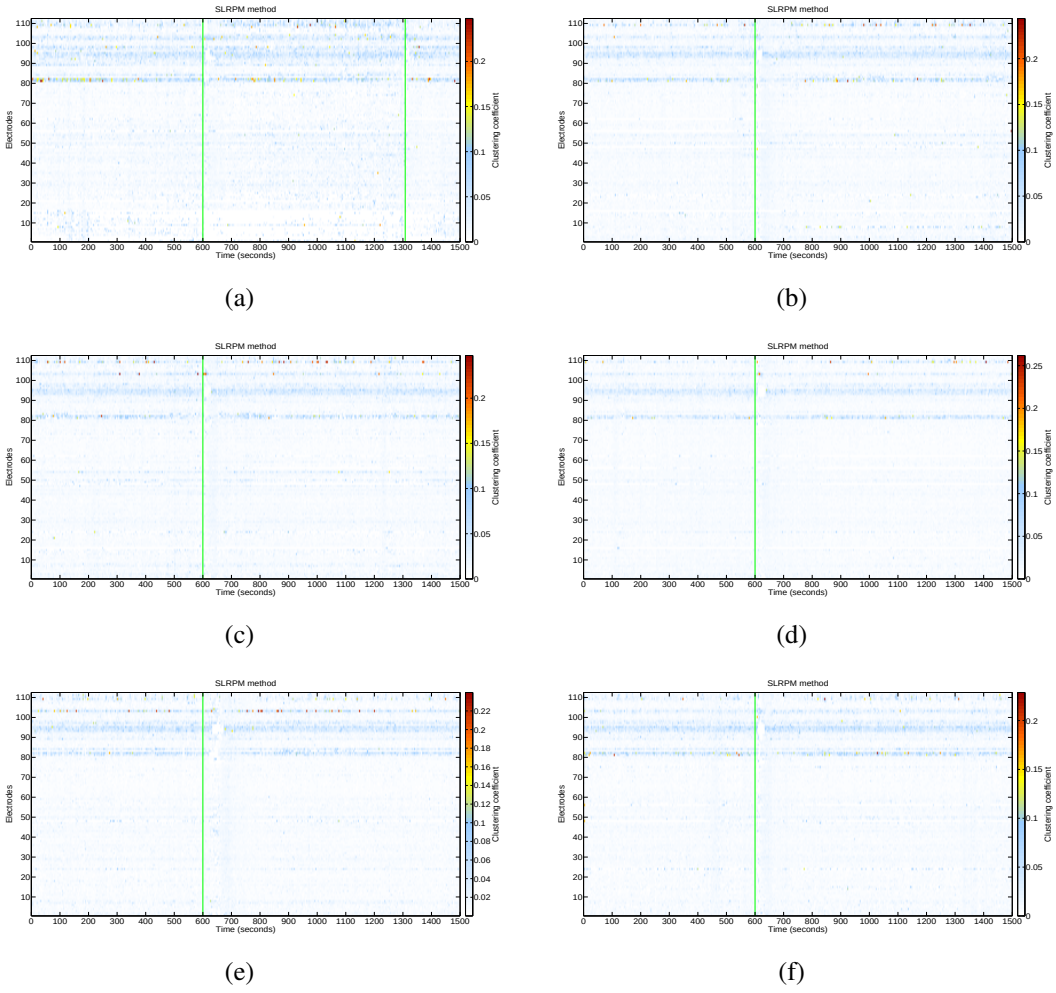

Figure 4.62: CC plots for the SLRPM method for the 7 group 1 seizures in patient 9. Green lines in all plots denote the seizure onset time.

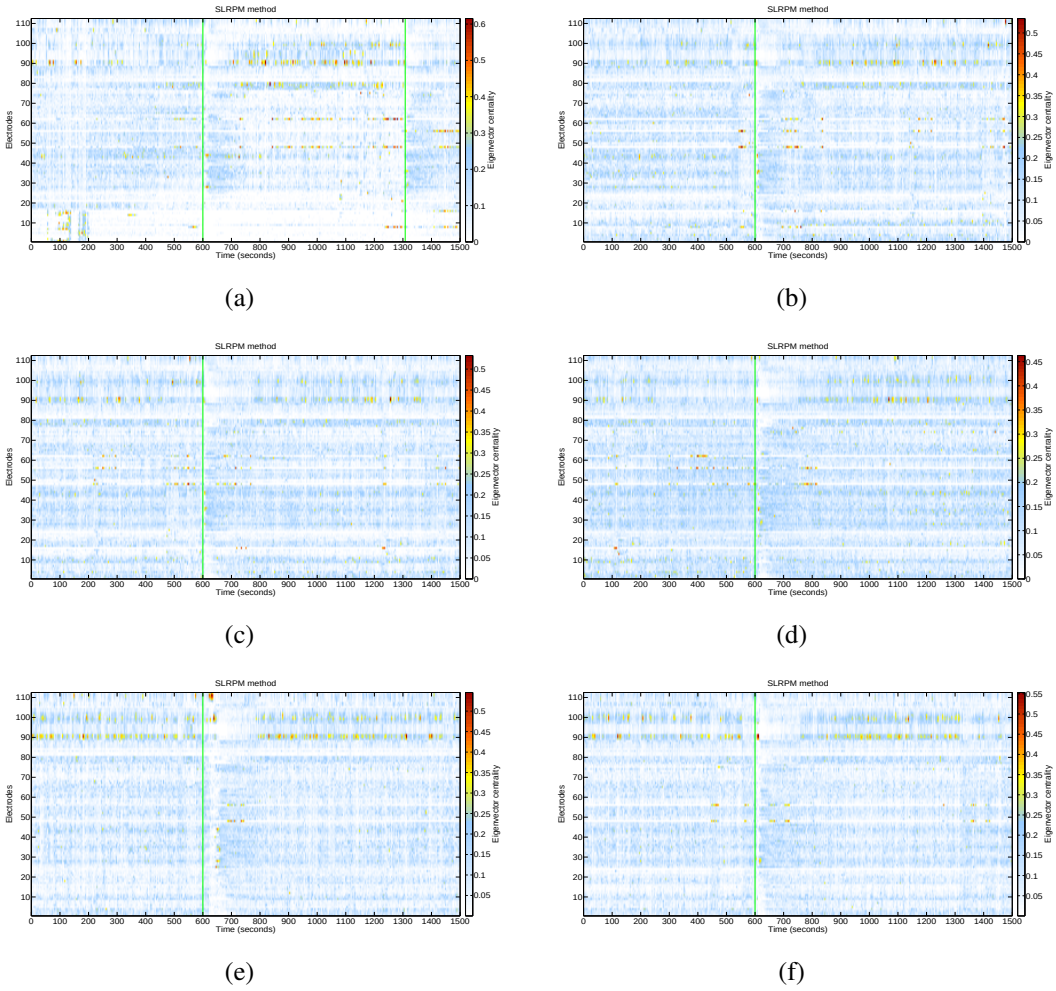

Figure 4.63: EC plots for the SLRPM method for the 7 group 1 seizures in patient 9. Green lines in all plots denote the seizure onset time.

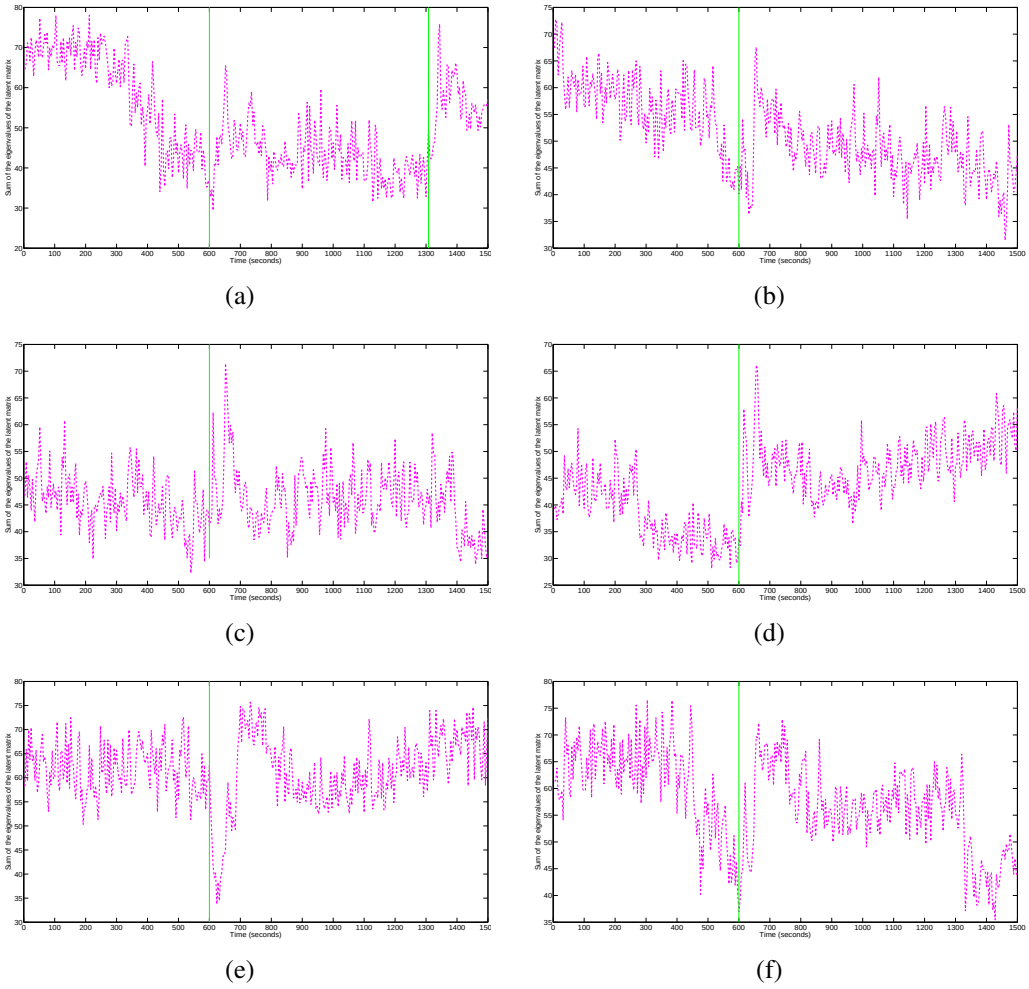

(a) (b)

(c) (d)

(e) (f)

Figure 4.64: Plots of the latent inputs estimated by the SLRPM method for the 7 group 1 seizures in patient 9. Green lines in all plots denote the seizure onset time.

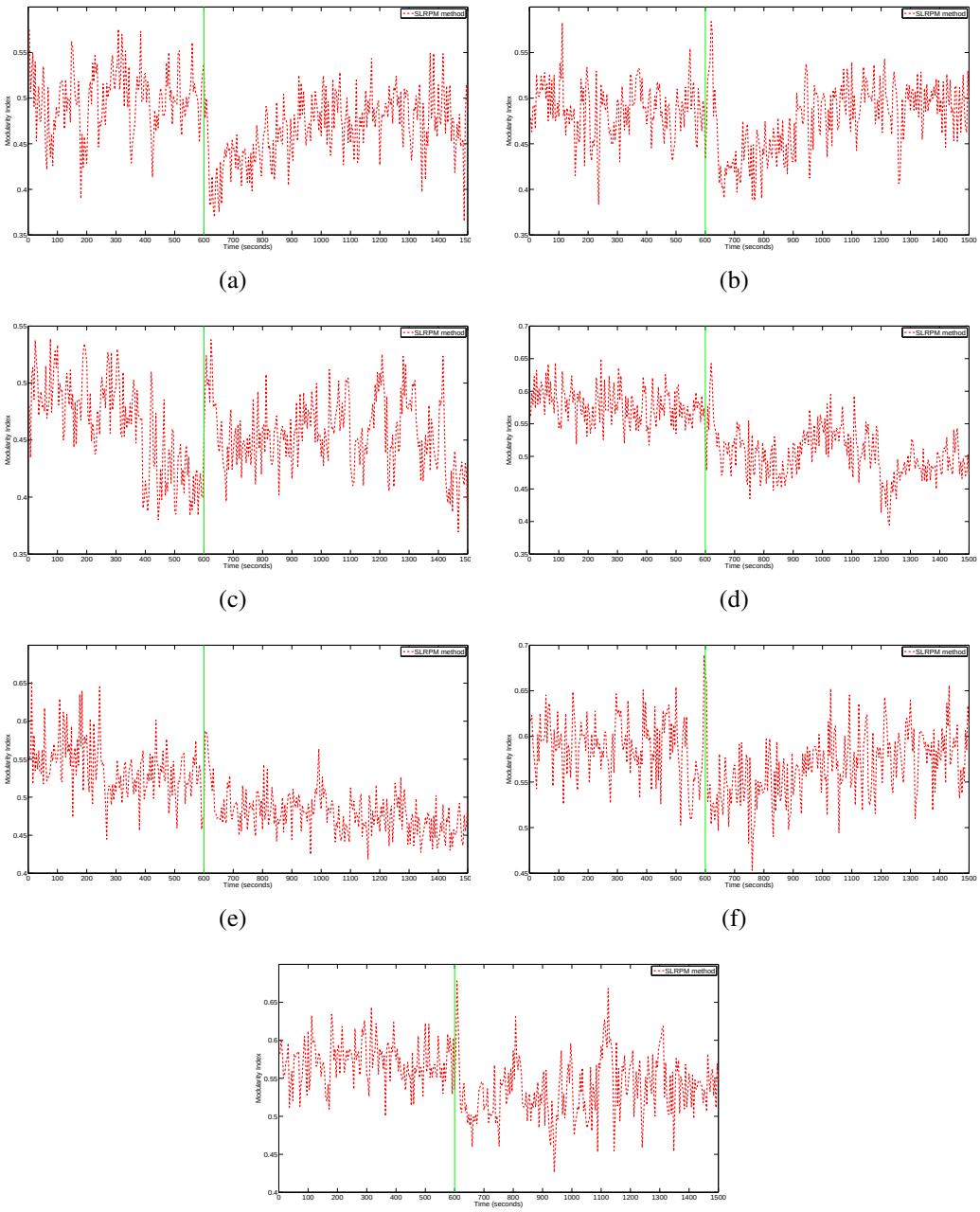

Figure 4.65: MI plots for the SLRPM method for the 7 group 2 seizures in patient 9. Green lines in all plots denote the seizure onset time.

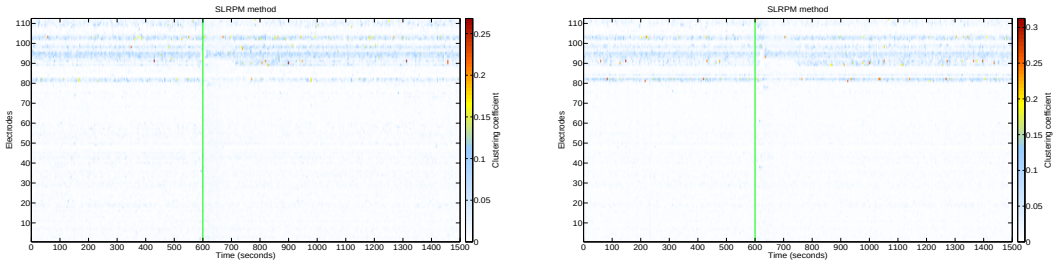

(a)

(b)

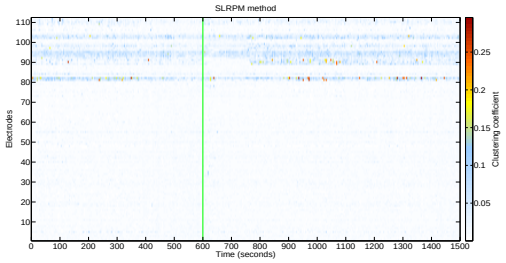

(c)

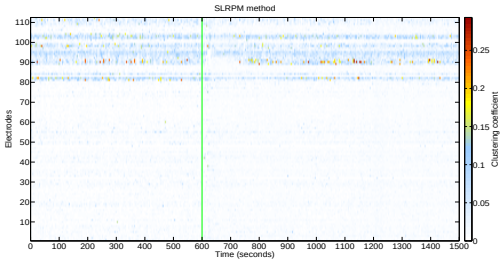

(d)

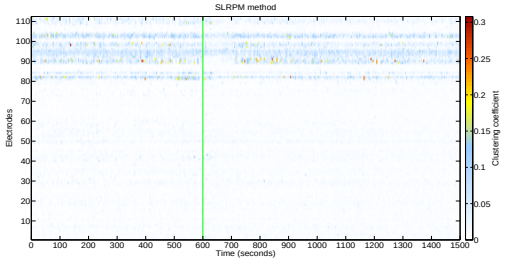

(e)

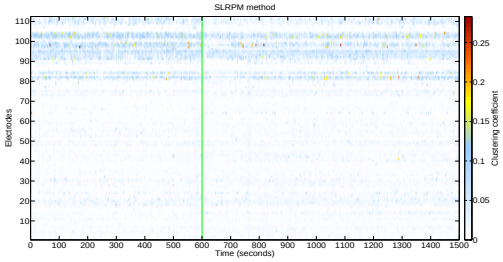

(f)

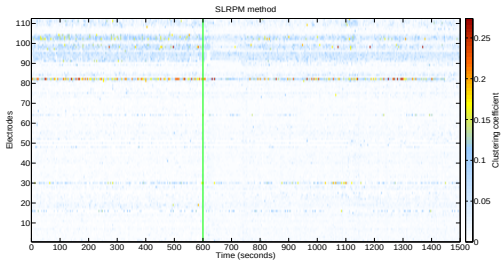

(g)

Figure 4.66: CC plots for the SLRPM method for the 7 group 2 seizures in patient 9. Green lines in all plots denote the seizure onset time.

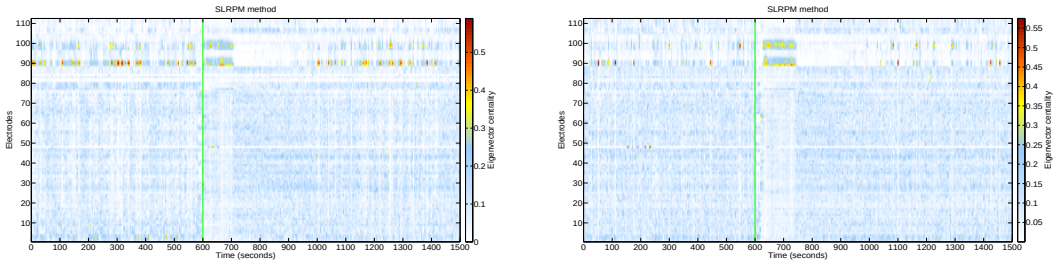

(a)

(b)

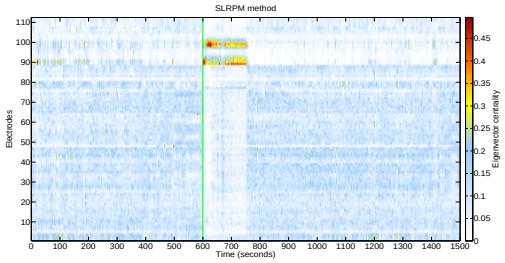

(c)

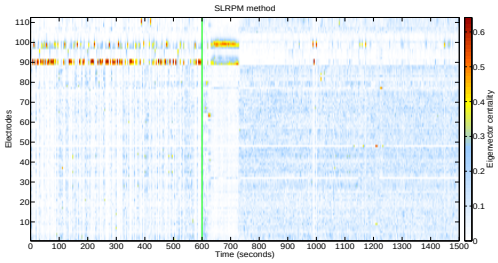

(d)

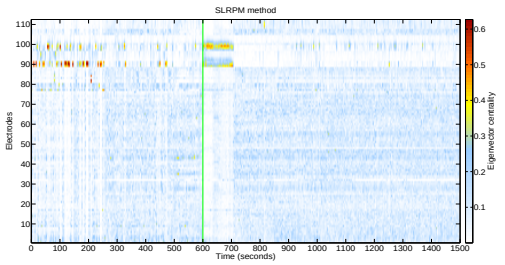

(e)

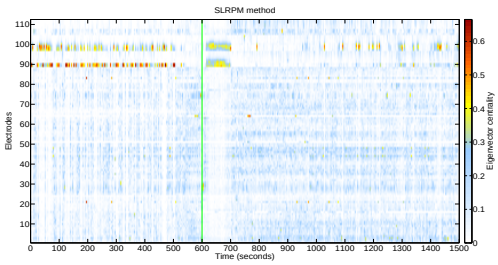

(f)

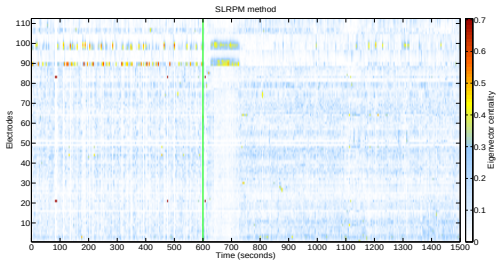

(g)

Figure 4.67: EC plots for the SLRPM method for the 7 group 2 seizures in patient 9. Green lines in all plots denote the seizure onset time.

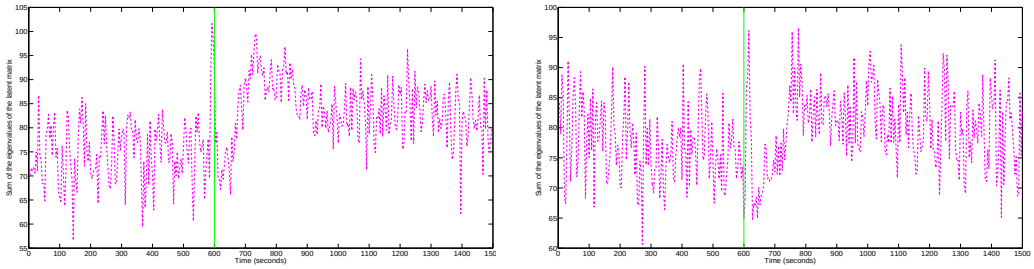

(a)

(b)

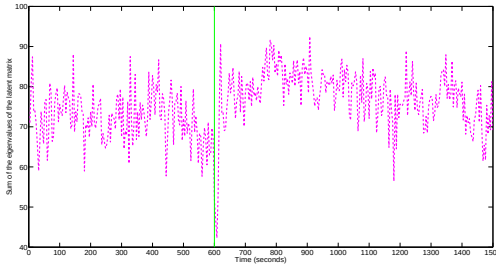

(c)

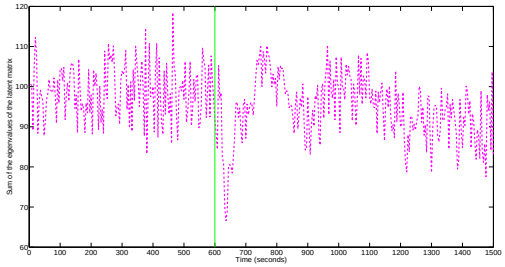

(d)

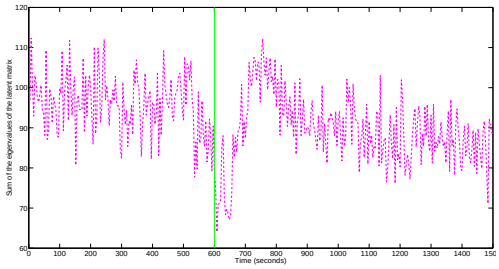

(e)

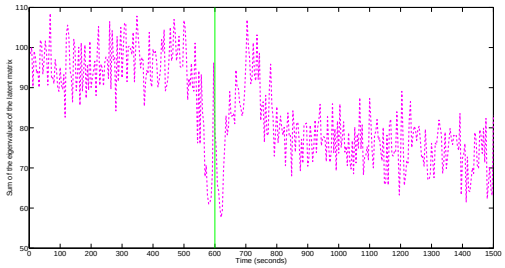

(f)

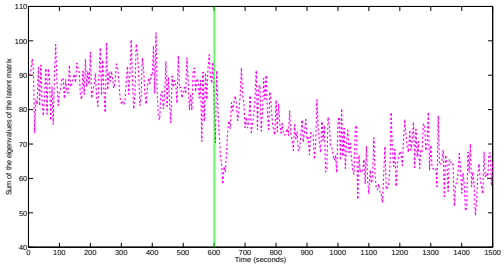

(g)

Figure 4.68: Plots of the latent inputs estimated by the SLRPM method for the 7 group 2 seizures in patient 9. Green lines in all plots denote the seizure onset time.

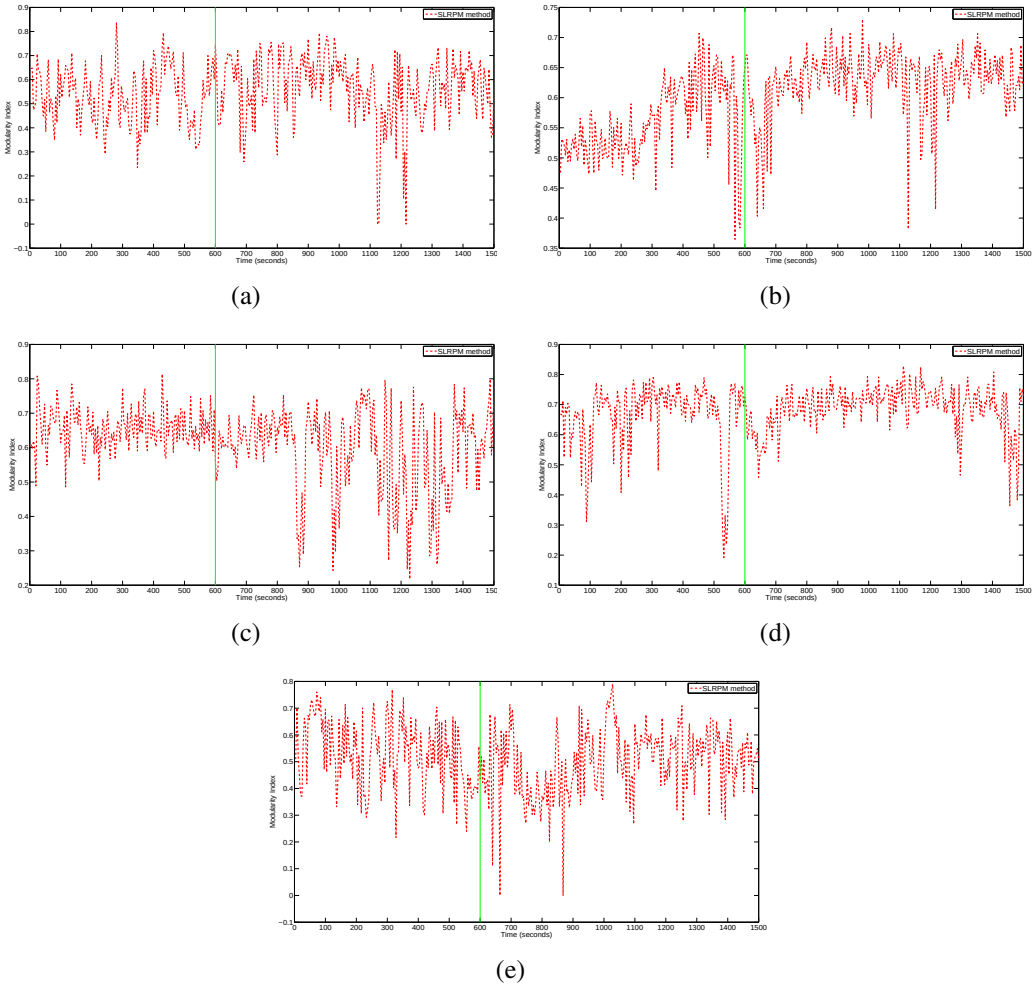

Figure 4.69: MI plots for the SLRPM method for the 5 group 3 seizures in patient 9. Green lines in all plots denote the seizure onset time.

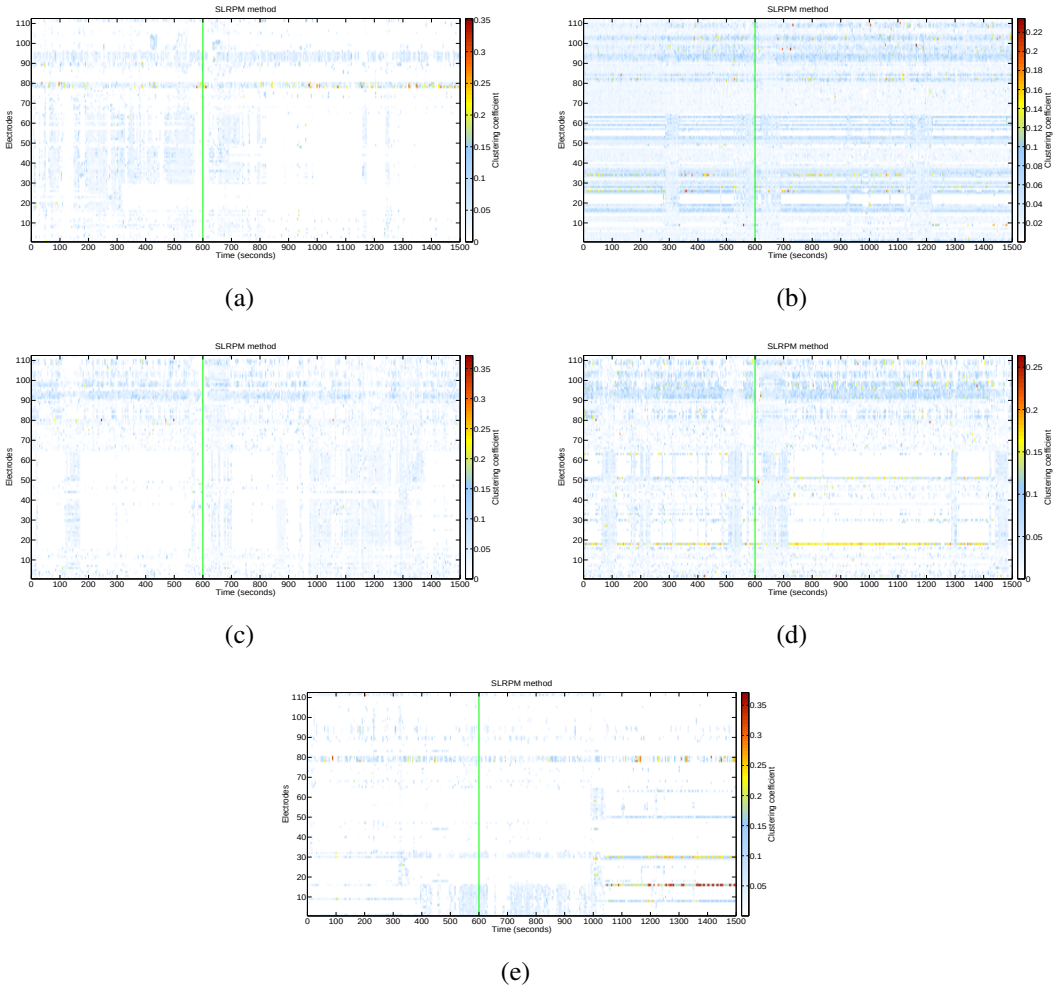

Figure 4.70: CC plots for the SLRPM method for the 5 group 3 seizures in patient 9. Green lines in all plots denote the seizure onset time.

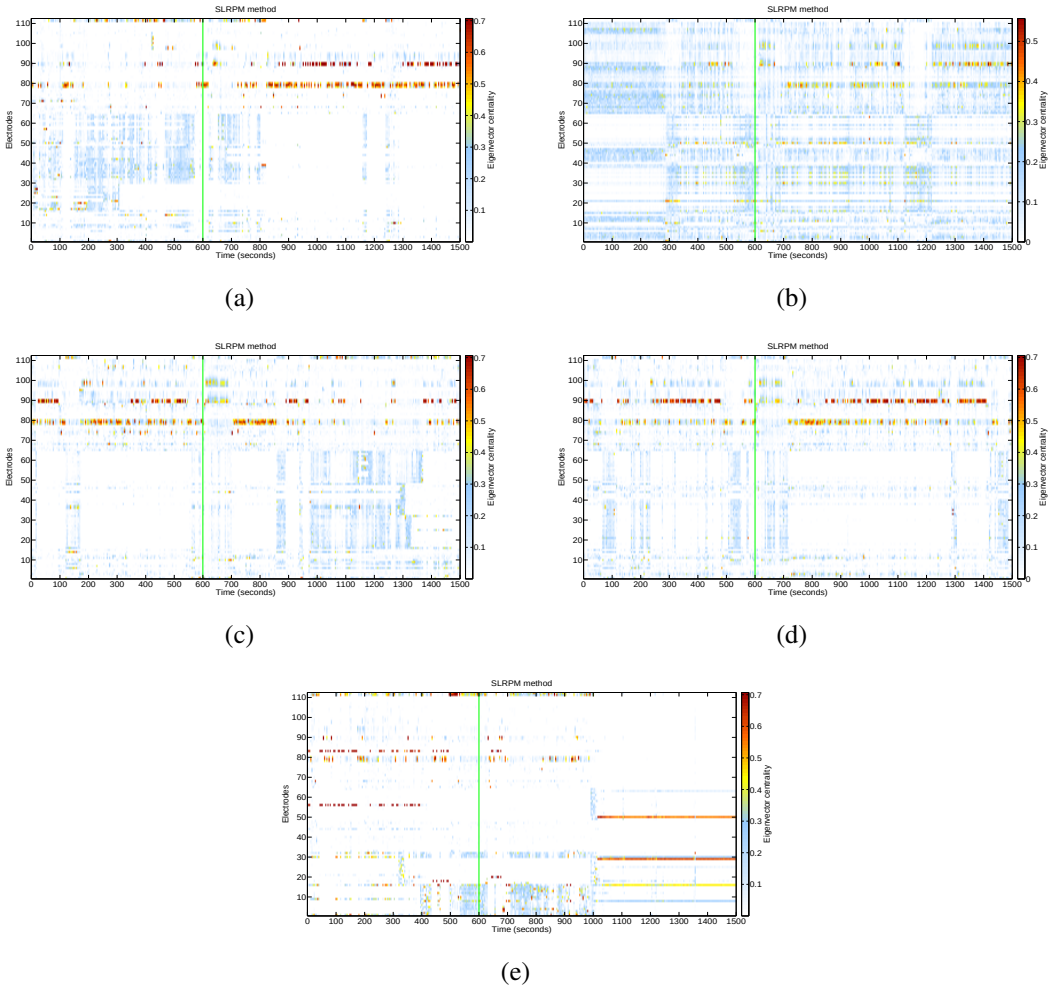

Figure 4.71: EC plots for the SLRPM method for the 5 group 3 seizures in patient 9. Green lines in all plots denote the seizure onset time.

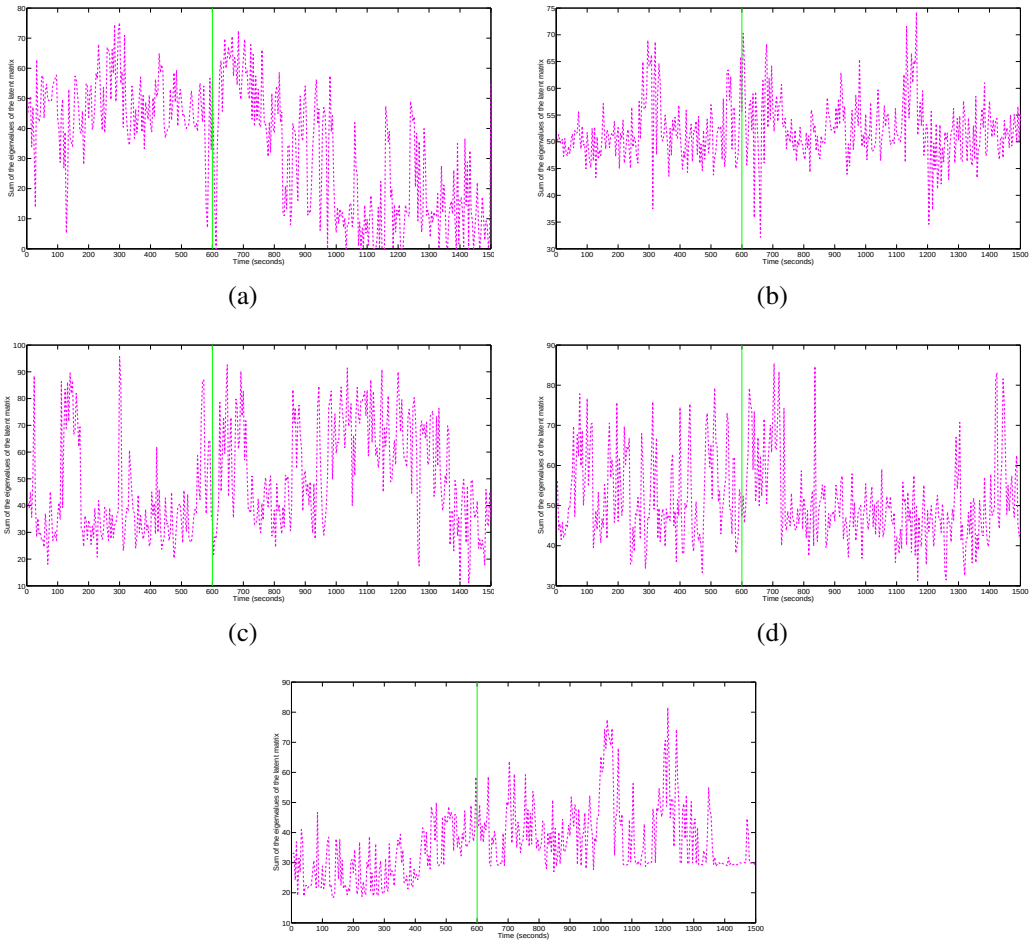

(a) (b)

(c) (d)

(e)

Figure 4.72: Plots of the latent inputs estimated by the SLRPM method for the 5 group 3 seizures in patient 9. Green lines in all plots denote the seizure onset time.

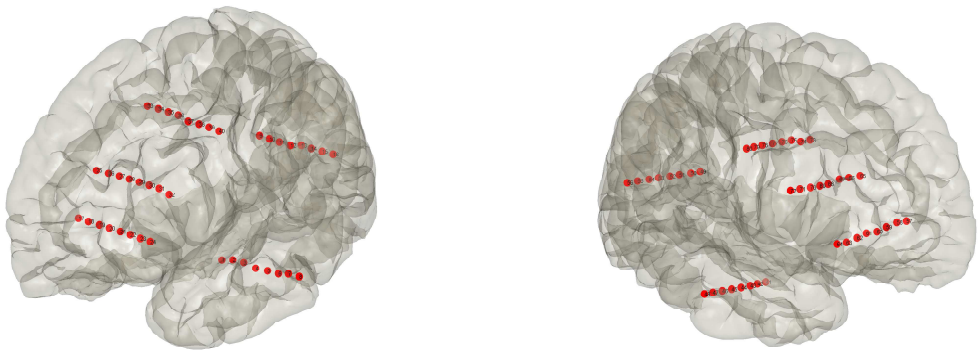

(a) (b)

Figure 4.73: Electrode locations in patient 10. (a) Left hemisphere. (b) Right hemisphere.

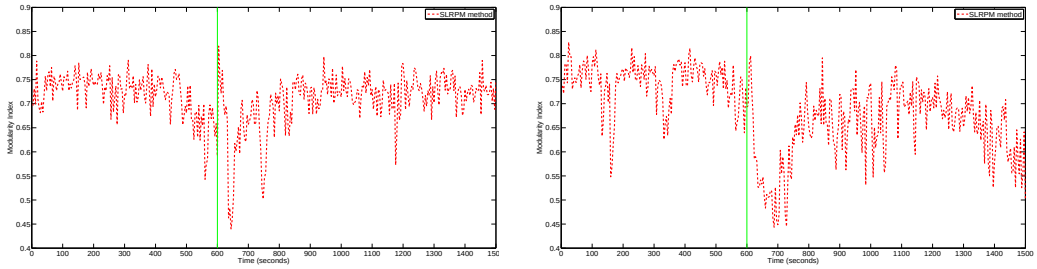

(a)

(b)

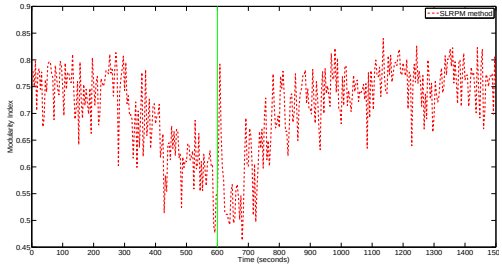

(c)

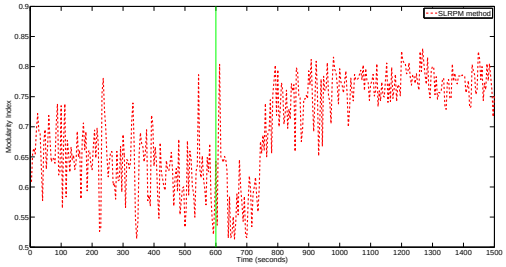

(d)

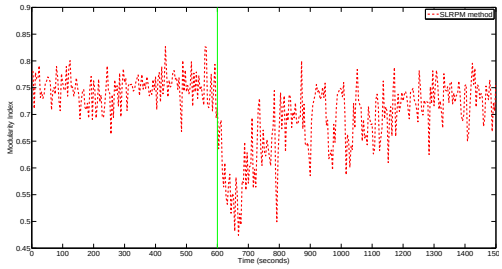

(e)

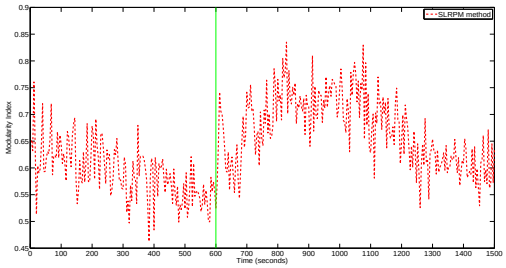

(f)

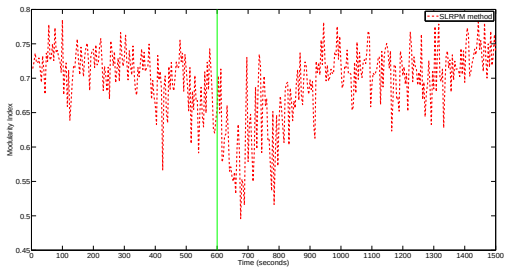

(g)

Figure 4.74: MI plots for the SLRPM method for the 7 group 1 seizures in patient 10. Green lines in all plots denote the seizure onset time.

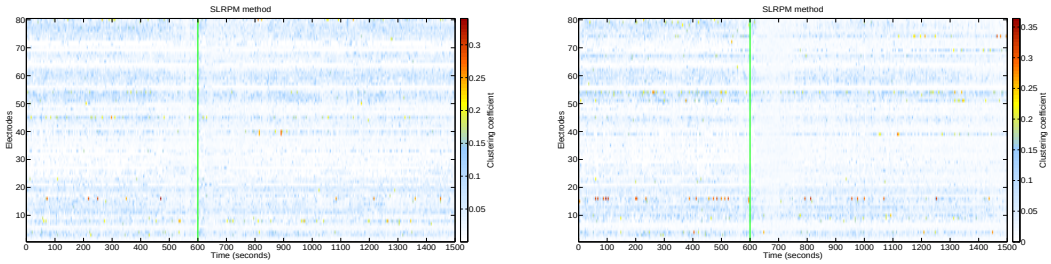

(a)

(b)

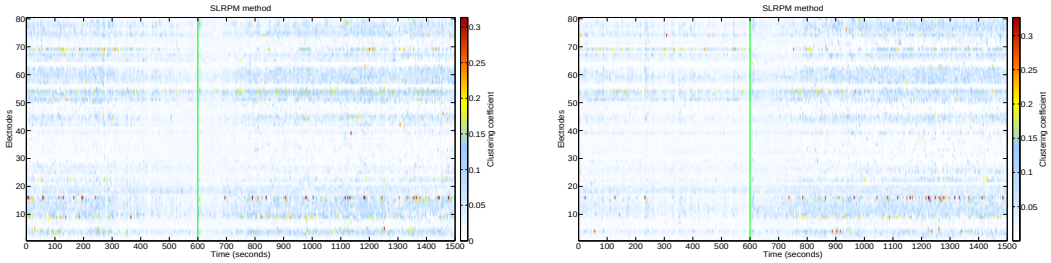

(c)

(d)

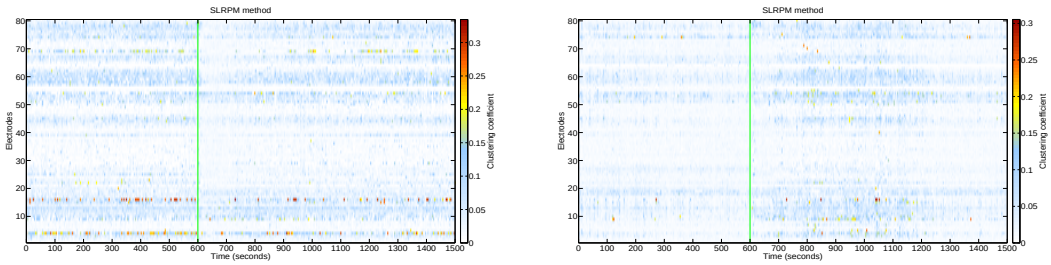

(e)

(f)

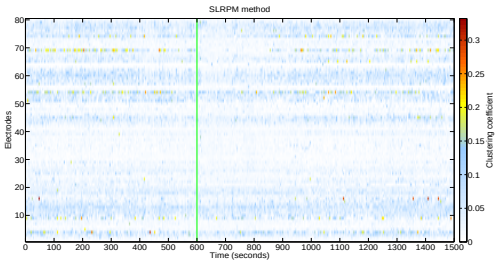

(g)

Figure 4.75: CC plots for the SLRPM method for the 7 group 1 seizures in patient 10. Green lines in all plots denote the seizure onset time.

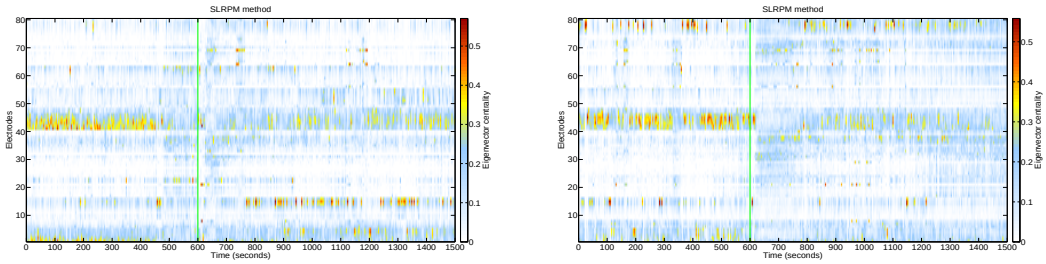

(a)

(b)

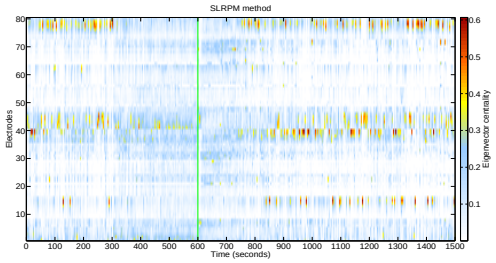

(c)

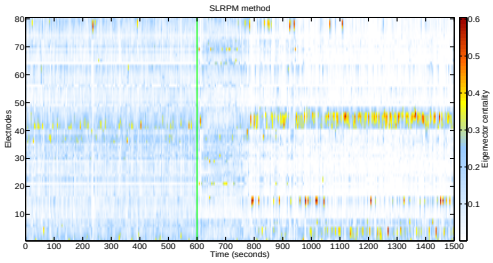

(d)

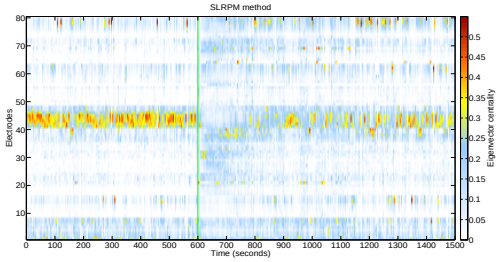

(e)

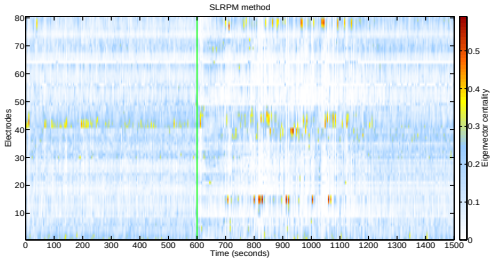

(f)

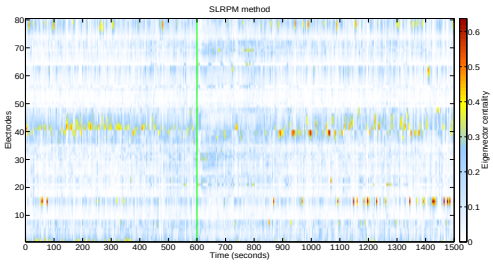

(g)

Figure 4.76: EC plots for the SLRPM method for the 7 group 1 seizures in patient 10. Green lines in all plots denote the seizure onset time.

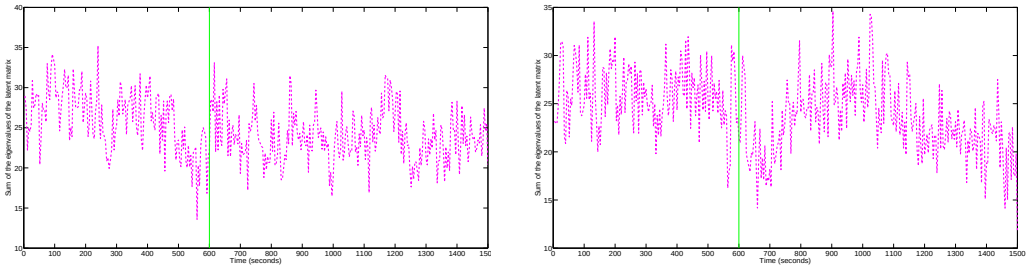

(a)

(b)

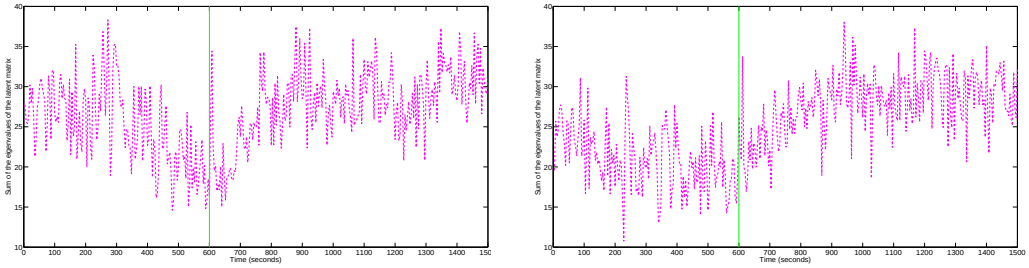

(c)

(d)

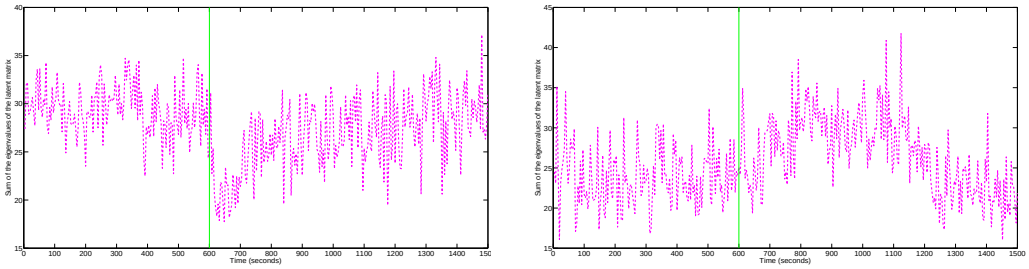

(e)

(f)

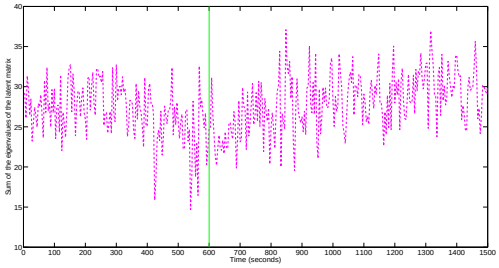

(g)

Figure 4.77: Plots of the latent inputs estimated by the SLRPM method for the 7 group 1 seizures in patient 10. Green lines in all plots denote the seizure onset time.

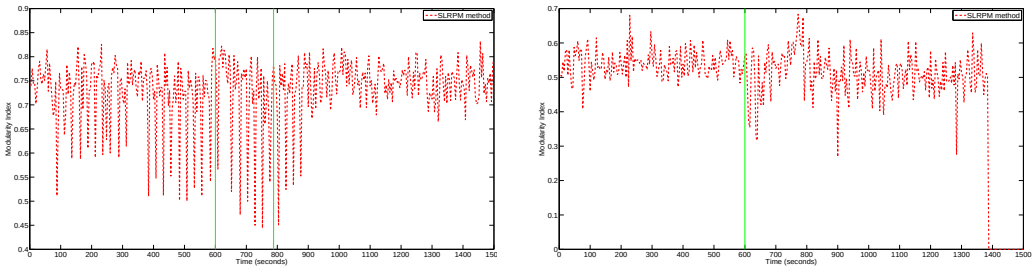

(a) (b)

Figure 4.78: MI plots for the SLRPM method for the 3 group 2 seizures in patient 10. Green lines in all plots denote the seizure onset time.

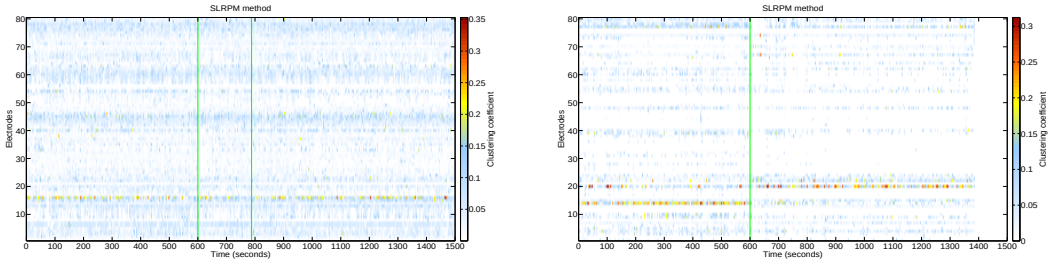

(a) (b)

Figure 4.79: CC plots for the SLRPM method for the 3 group 2 seizures in patient 10. Green lines in all plots denote the seizure onset time.

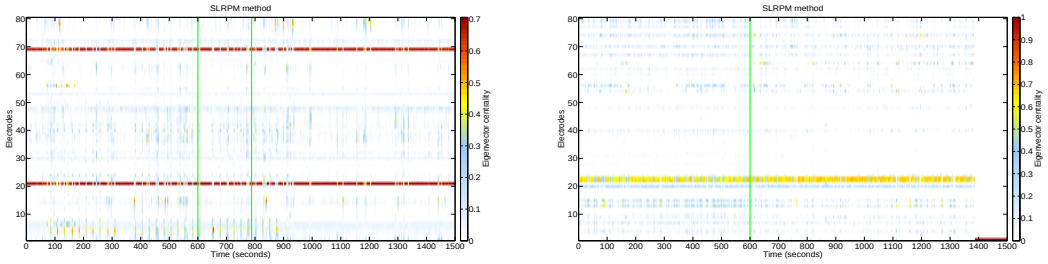

(a) (b)

Figure 4.80: EC plots for the SLRPM method for the 3 group 2 seizures in patient 10. Green lines in all plots denote the seizure onset time.

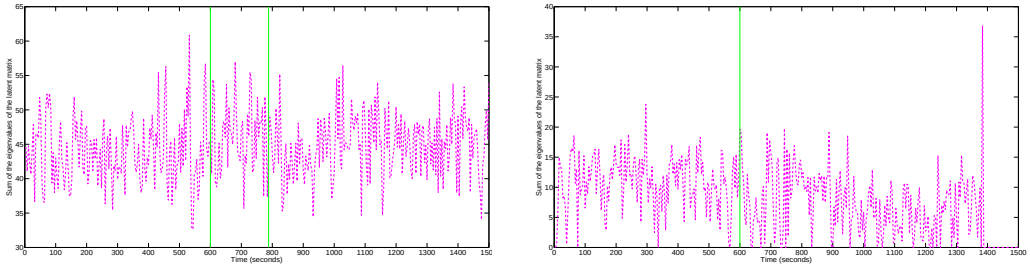

(a) (b)

Figure 4.81: Plots of the latent inputs estimated by the SLRPM method for the 3 group 2 seizures in patient 10. Green lines in all plots denote the seizure onset time.

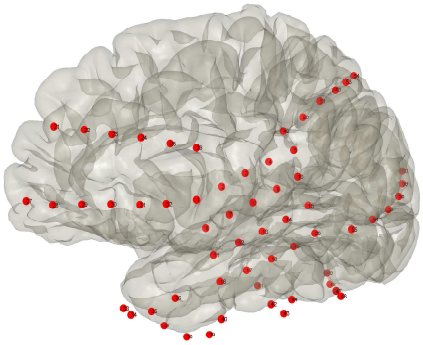

Figure 4.82: Electrode locations in patient 11.

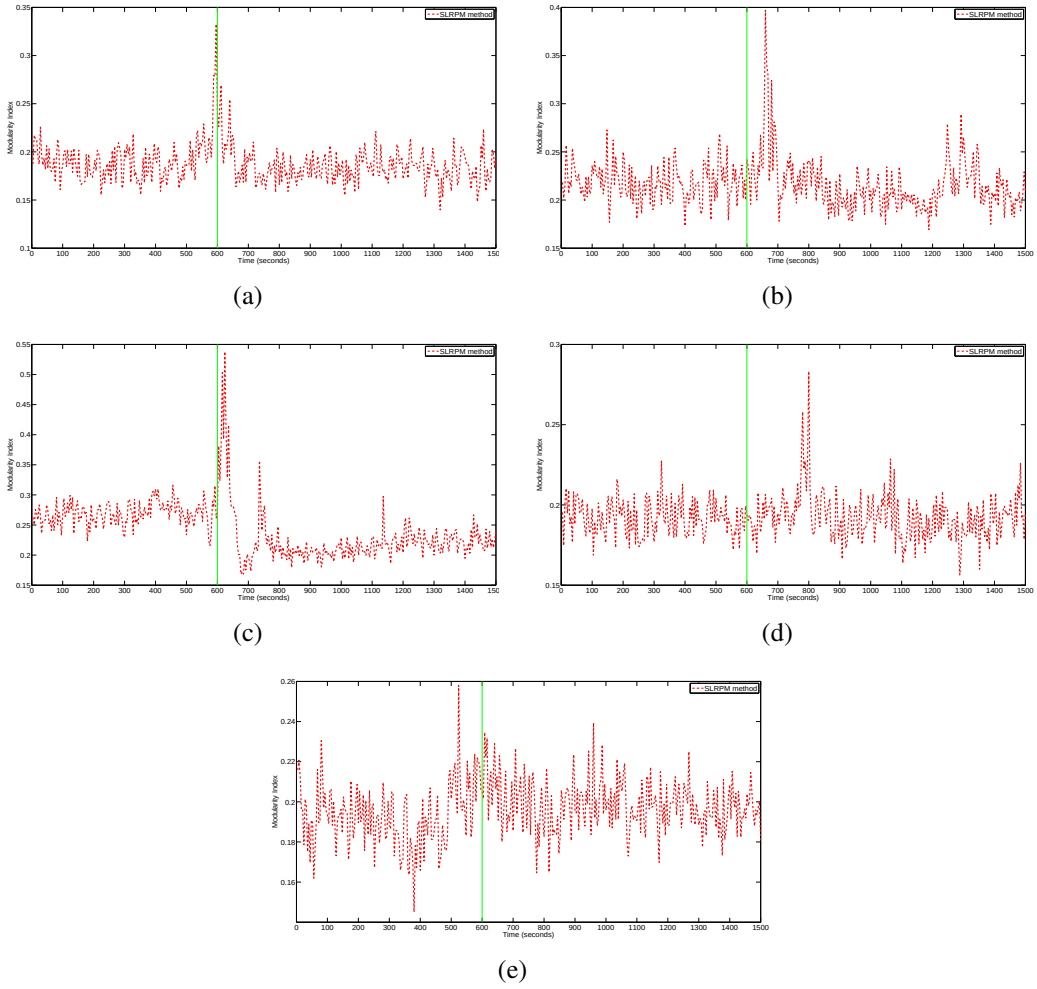

Figure 4.83: MI plots for the SLRPM method for the 5 seizures in patient 11. Green lines in all plots denote the seizure onset time.

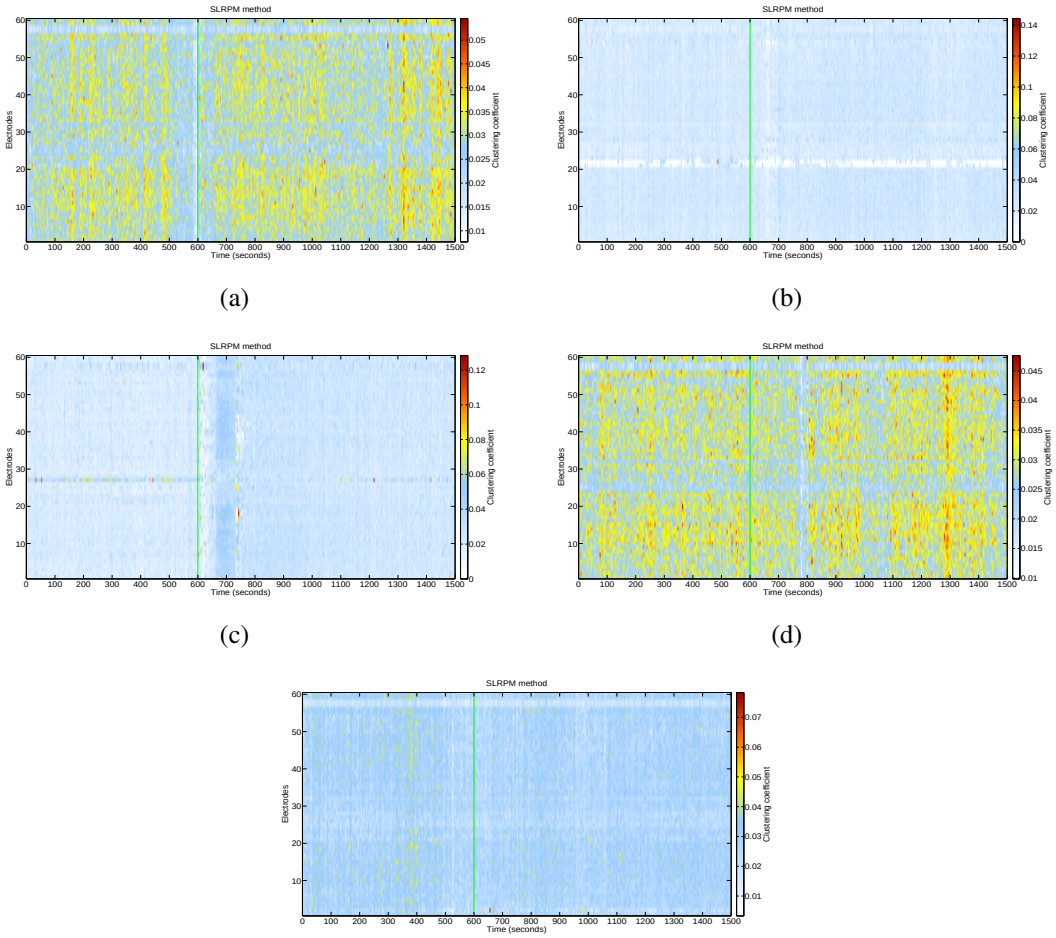

Figure 4.84: CC plots for the SLRPM method for the 5 seizures in patient 11. Green lines in all plots denote the seizure onset time.

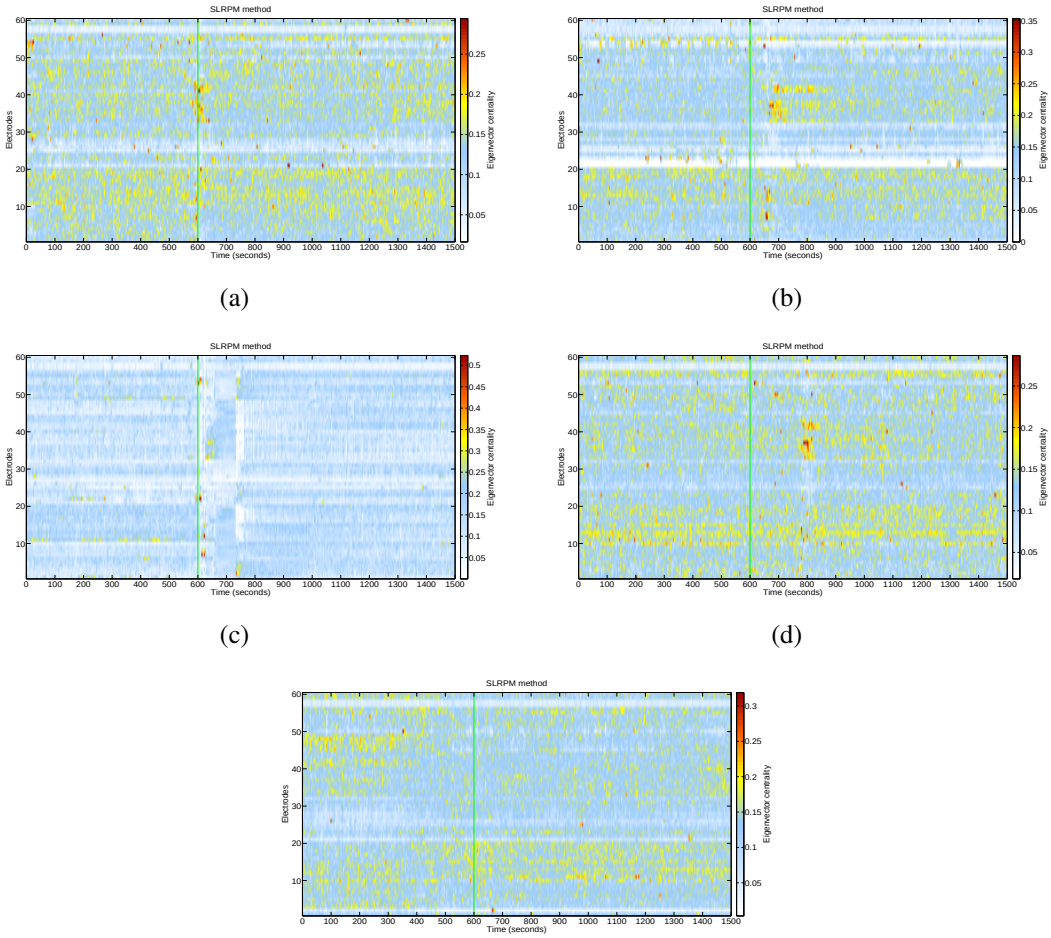

Figure 4.85: EC plots for the SLRPM method for the 5 seizures in patient 11. Green lines in all plots denote the seizure onset time.

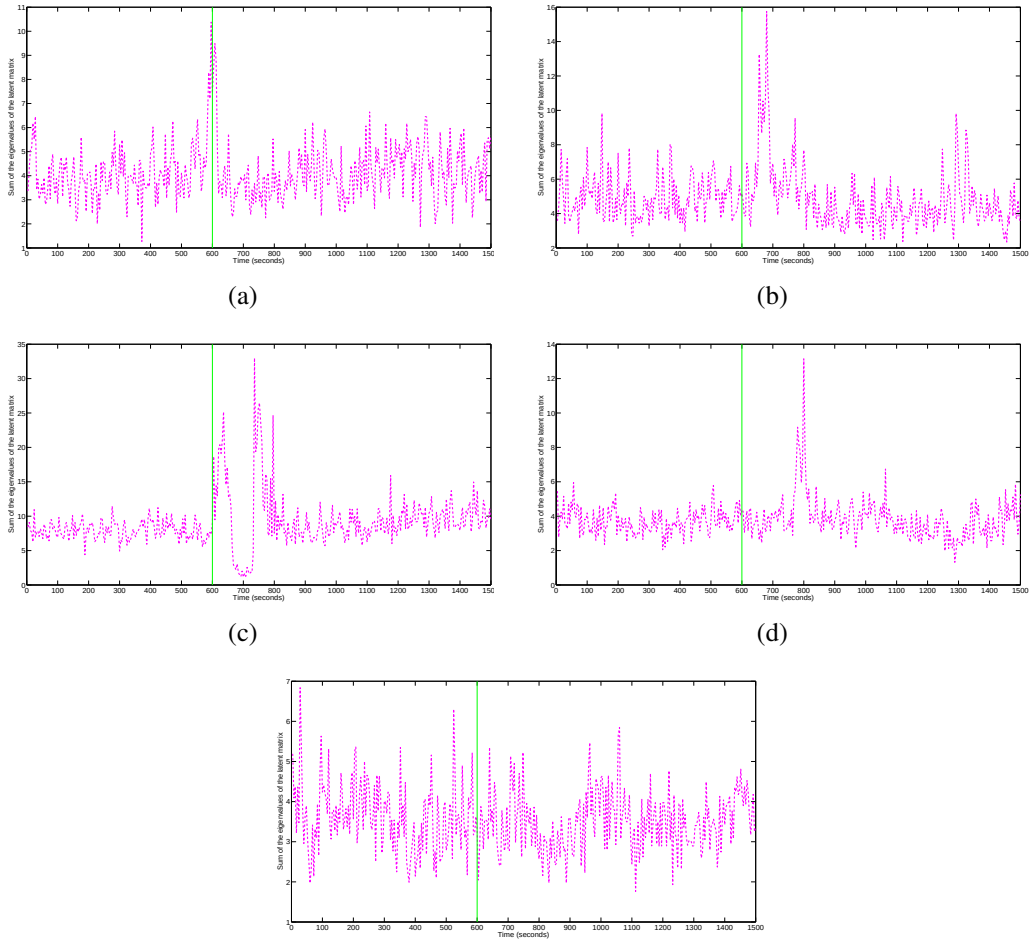

Figure 4.86: Plots of the latent inputs estimated by the SLRPM method for the 5 seizures in patient 11. Green lines in all plots denote the seizure onset time.

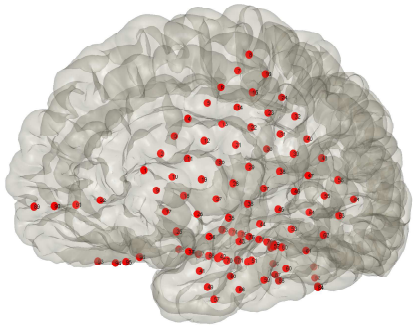

Figure 4.87: Electrode locations in patient 12.

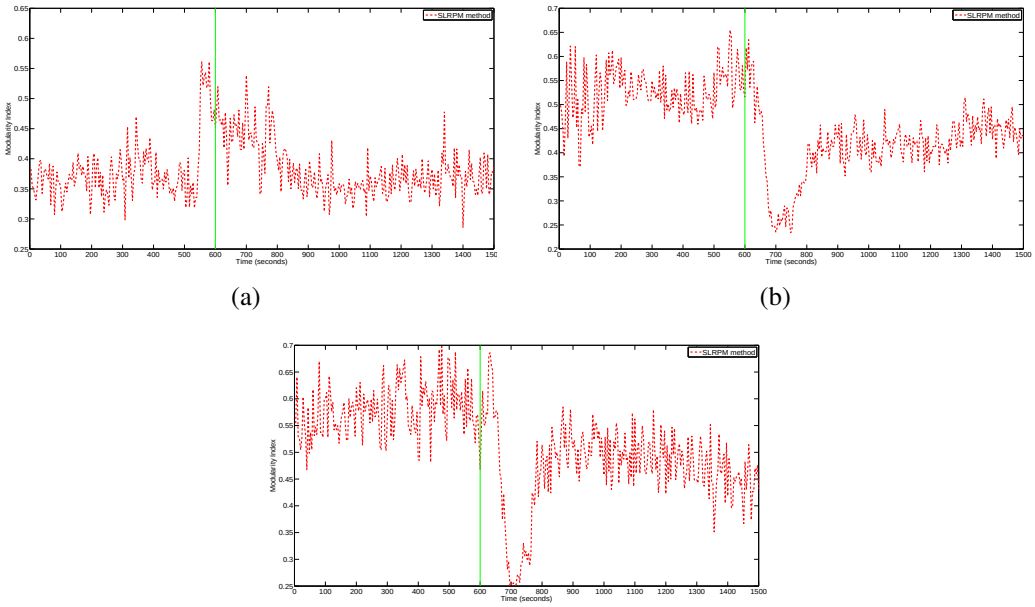

(a) (b)

(c)

Figure 4.88: MI plots for the SLRPM method for the 3 clinical seizures in patient 12. Green lines in all plots denote the seizure onset time.

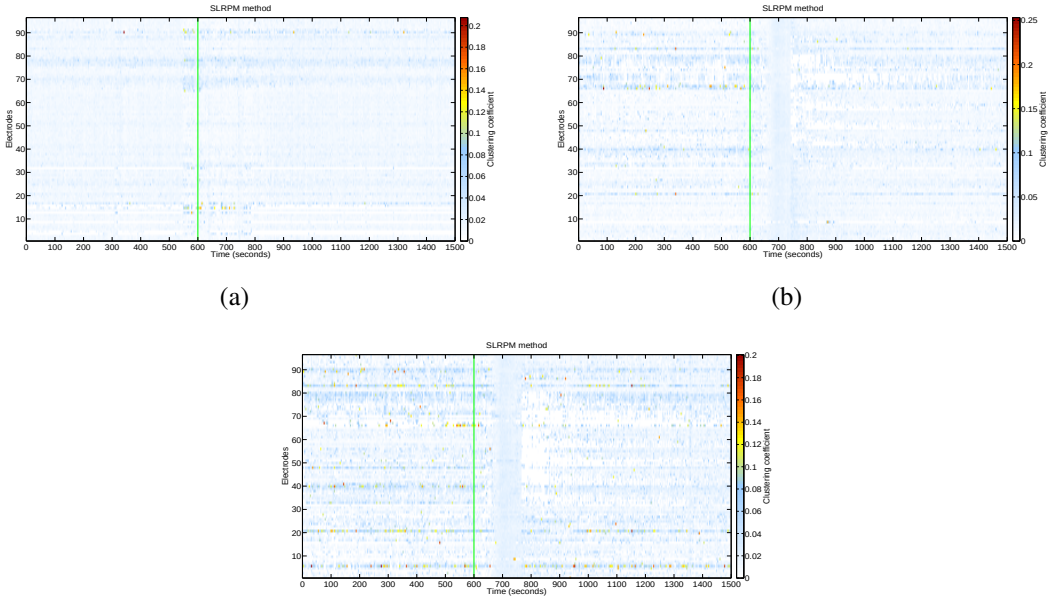

(a) (b)

(c)

Figure 4.89: CC plots for the SLRPM method for the 3 clinical seizures in patient 12. Green lines in all plots denote the seizure onset time.

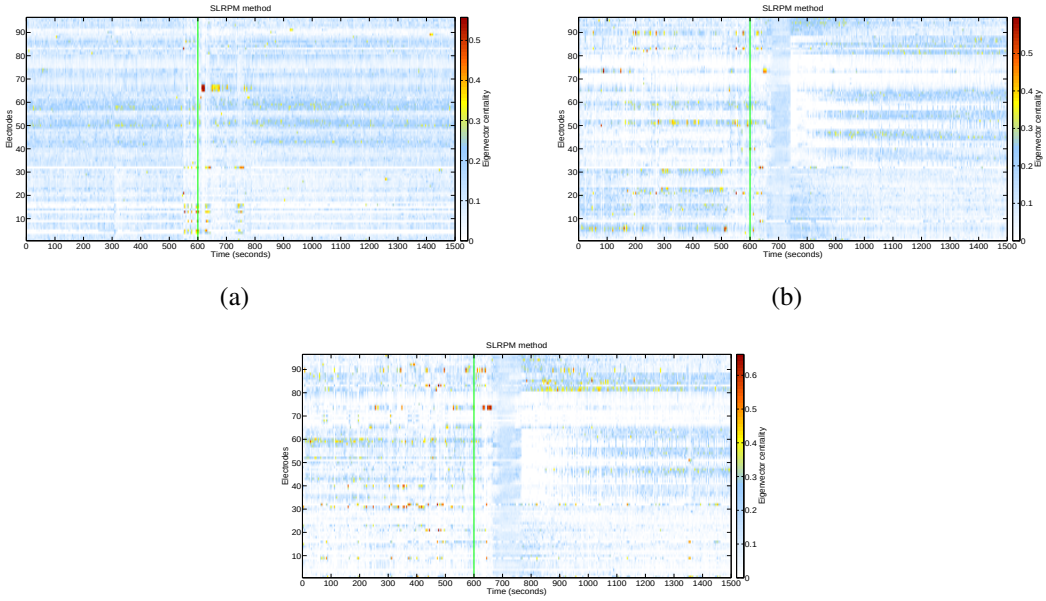

(a) (b)

(c)

Figure 4.90: EC plots for the SLRPM method for the 3 clinical seizures in patient 12. Green lines in all plots denote the seizure onset time.

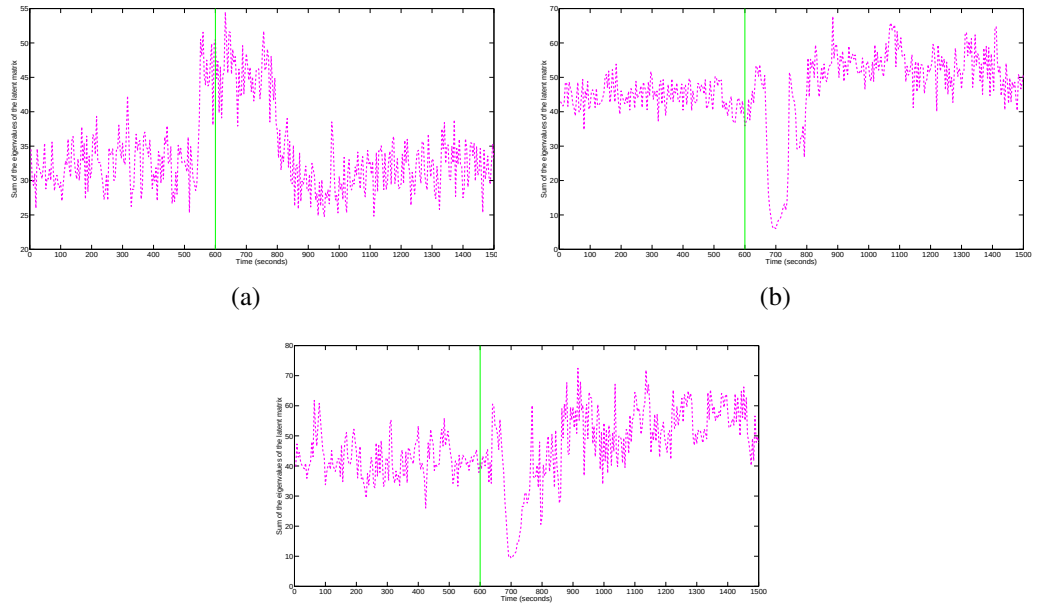

(a) (b)

(c)

Figure 4.91: Plots of the latent inputs estimated by the SLRPM method for the 3 clinical seizures in patient 12. Green lines in all plots denote the seizure onset time.

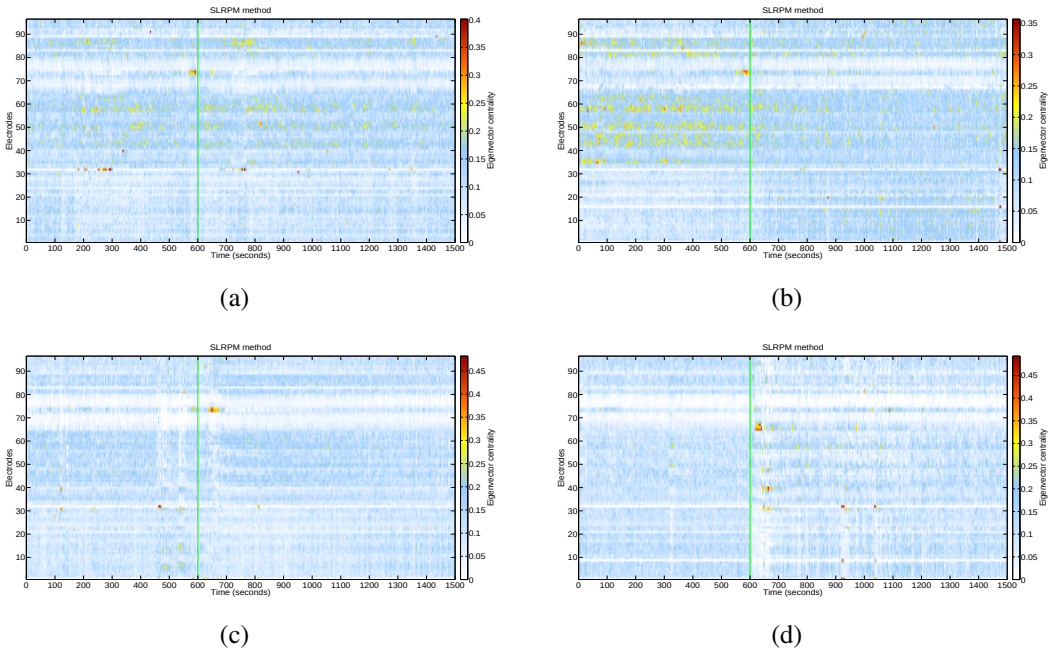

Figure 4.92: EC plots for the SLRPM method for 4 sub-clinical seizures in patient 12. Green lines in all plots denote the seizure onset time.

we see that the SLRPM method is able to identify a relatively more number of onset channels (28) from the preictal active electrodes in all patients than the SRPM (22) and correlation (21) methods. For SLRPM and SRPM methods, in 5 patients, the preictal active electrodes did not correspond to any of the onset channels whereas for the correlation method, this number increased to 9. Also for SLRPM, only 28 preictal active electrodes corresponded to the onset channels whose total number was 119 in all patients. This suggests that not all preictal activity leads to seizure onset. We also have analyzed 1, 2, and 3 hours preictal segments for these patients and observed high DH in some patients. We also notice that there is no direct relationship between DH and A/O for SLRPM. For example, in patient 4, there is a relatively low DH and none of the active electrodes corresponded to the onset channels. But in patients 2 and 9, for which the seizures have a relatively high DH, 7 and 12 active electrodes corresponded to the onset channels respectively. The DH estimated by SLRPM covered a relatively wider range than those estimated by the SRPM and correlation methods indicating that the local cortical connectivity, after excluding the effect of the common latent inputs, can be highly heterogeneous.

4.4 Effect of preprocessing

Here, we study the effect of two of the most important preprocessing steps that we applied on our ECoG recordings. The first is CAR and the other is z-scoring.

4.4.1 Effect of CAR

In our CAR, we subtracted the average signal of all electrodes from each electrode at each time point. However, since the dynamics of the seizure onset electrodes might be different from those of the non-onset electrodes, we tested the SLRPM method by considering only the non-onset electrodes for CAR. We also tested SLRPM by considering a random subset of 40 non-onset electrodes for CAR. We considered the EC measure applied on seizure 1 in patient 1 as an example to test these two CAR procedures and the results are shown in (a) and (b) of Figure 4.93 respectively. For comparison, the EC plot of SLRPM method in Figure 4.4 is reproduced in Figure 4.93 (c) in which we use all electrodes for CAR. We note that both these CAR approaches have minimal effect on the preictal, ictal, and post-ictal dynamics and the dynamics look similar to that in Figure 4.93 (c).

4.4.2 Effect of normalization

For our analysis, we z-scored each channel for the entire 25 minutes time-segment to have a relatively less biased estimation of mean and standard deviation. However, some researchers also use z-scoring in each time-window rather than the entire data (Varsavsky et al., 2010). To test the effect of normalization in each time-window on SLRPM, we considered the EC measure applied on seizure 1 in patient 1 as an example. Figure 4.94 (a) shows the result of this normalization procedure. For comparison, the EC plot of SLRPM method in Figure 4.4 is reproduced in Figure 4.94 (b) in which normalization was applied for the entire time-segment. We note that the preictal dynamics (also see Figure 4.95 for the plot of only the preictal period of Figure 4.94 (a)) in Figure 4.94 (a) is significantly different than that in Figure 4.94 (b) and the ictal and post-ictal dynamics

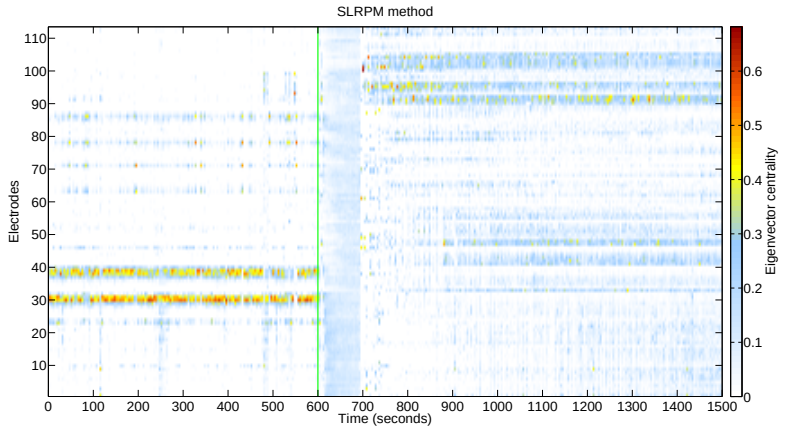

(a)

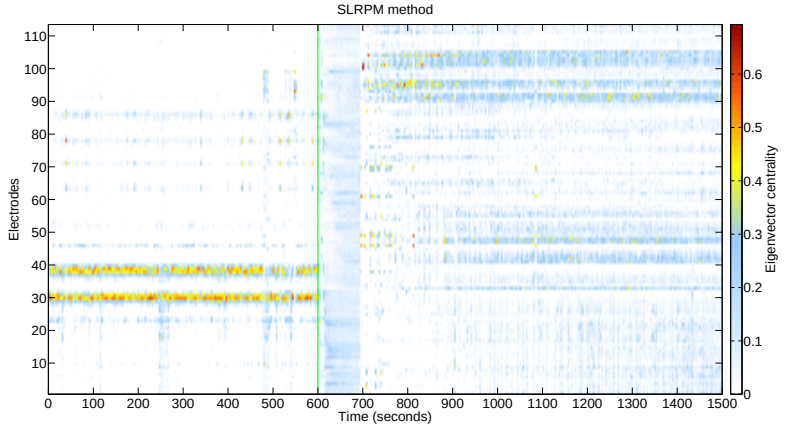

(b)

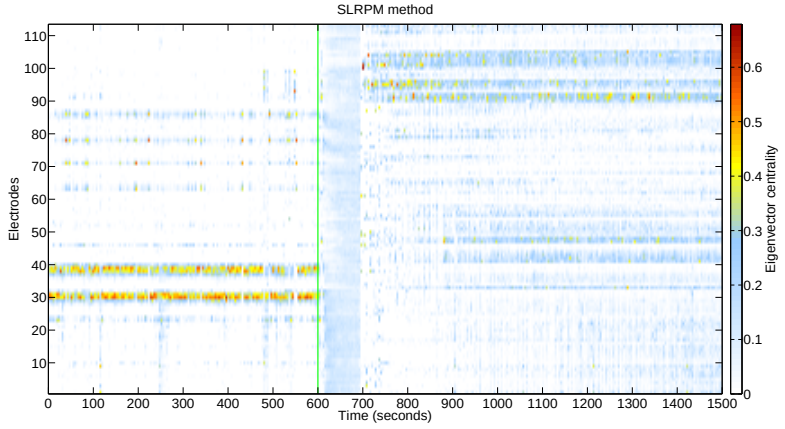

(c)

Figure 4.93: Analysis of effect of CAR on SLRPM method for seizure 1 in patient 1. Green lines in all plots denote the seizure onset time. (a) Non-onset electrodes are used for CAR. (b) A random subset of 40 non-onset electrodes are used for CAR. (c) All electrodes are used for CAR.

are relatively more similar for these two normalization procedures. Moreover, we have applied z-scoring only on the 10 minutes preictal recording and the result is shown in Figure 4.94 (c). Note that, even though the values of the EC measures for the electrodes are different for the preictal period in Figure 4.94 (b) and Figure 4.94 (c), electrodes which were relatively more active than others, can be seen in both. However, both of these are markedly different than the EC measures for the electrodes in the preictal period in Figure 4.94 (a). This shows that two different normalization methods can produce different results and care need to be taken while interpreting the results.

4.5 Discussion

Researchers (Vega-Zelaya et al., 2015; Kramer et al., 2010; Ponten et al., 2007; Schindler et al., 2008) have previously reported increase in ACC after seizure onset. However, in our analysis we do not consider ACC since we found that, in the preictal period, some electrodes are relatively more active than other electrodes and averaging CC across electrodes in this period and comparing the result to that in the ictal period does not provide the picture of the dynamics for individual electrodes. The relative decrease in MI after seizure onset in some seizures is consistent with findings from (Vega-Zelaya et al., 2015). Similar to the authors in (Burns et al., 2014), we also observed change in brain connectivity from the EC measure after the onset of some seizures. There is also evidence of decreased cortical-subcortical interaction during epileptic seizures (Blumenfeld et al., 2012) which explains the relatively decreased latent inputs during the ictal period estimated by the SLRPM method in some seizures.

4.6 Acknowledgement

Chapter 4, in part, is currently being prepared for submission for possible publication of some of the material in Das, Anup; Sexton, Daniel; Lainscsek, Claudia; Cash, Sydney S.; Sejnowski, Terrence J.,“Characterizing brain connectivity during epileptic seizures from human electrocorticography recordings with unobserved inputs”. The author of this thesis is the primary

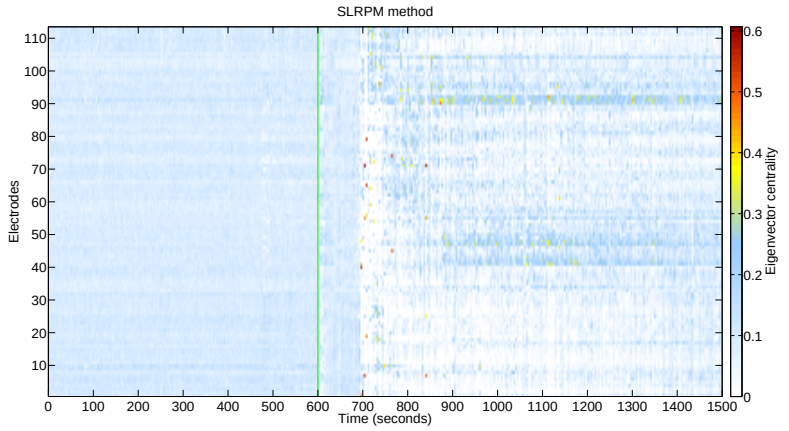

(a)

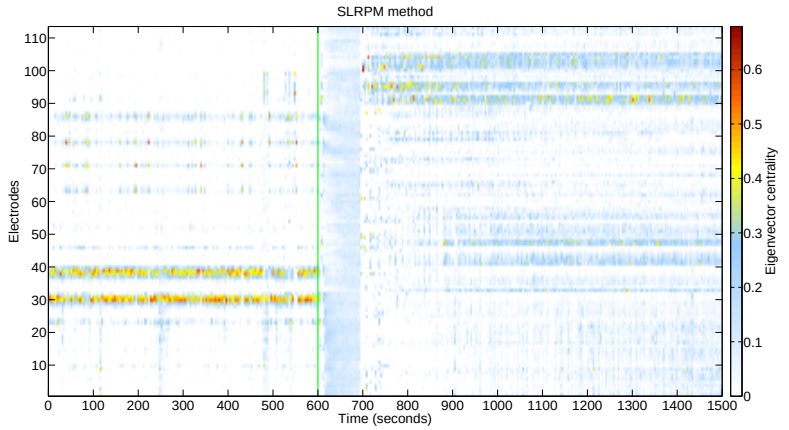

(b)

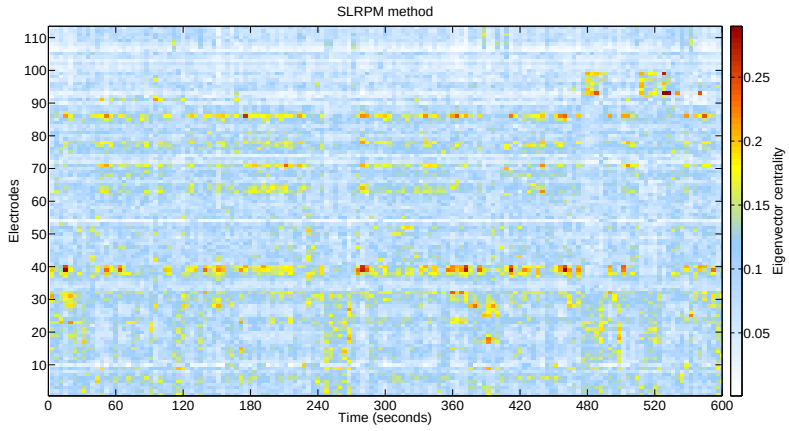

(c)

Figure 4.94: Analysis of effect of normalization on SLRPM method for seizure 1 in patient 1. Green lines in (a) and (b) denote the seizure onset time. (a) Window-wise z-scoring. (b) Z-scoring the entire time-segment. (c) Z-scoring only the preictal time-segment.

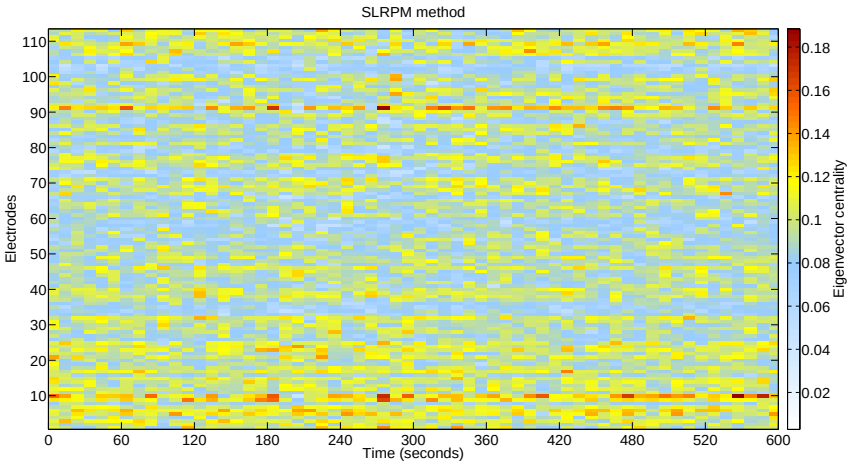

Figure 4.95: Shown here is the preictal period of Figure 4.94 (a) for better visualization of the active electrodes.

author of this material.

Chapter 5

Final remarks

Extensive research work exists in literature in which brain activity has been estimated using the correlation method. However, as we have shown in our thesis, latent inputs can have a significant impact in the inferred connectivity in the cortex. The sparse-plus-latent regularized precision matrix (SLRPM) method provides a way to calculate the local cortical connectivity by conditioning on the latent inputs. The methods that we used in this thesis to analyze electrocorticography (ECoG) recordings could also be applied to single unit recordings, local field potentials, and functional magnetic resonance imaging (fMRI) data. Results and discussions in this thesis may help SLRPM to be used as a standard in brain connectivity analysis in neuroscience applications and provide new insights in to the cortical activity of the human brain which will possibly lead us to find better treatments in epilepsy.

Bibliography

Allen, E. A., Damaraju, E., Plis, S. M., Erhardt, E. B., Eichele, E., & Calhoun, V. D.(2012). Tracking Whole-Brain Connectivity Dynamics in the Resting State. *Cerebral Cortex*, *24*, 663–676.

Anand, A., Li, Y., Wang, Y., Wu, J., Gao, S., Bukhari, L., Mathews, V. P., Alnin, A., & Lowe, M. J.(2005). Antidepressant effect on connectivity of the mood-regulating circuit: an fMRI study. *Neuropsychopharmacology*, *30* (7), 1334–1344.

Andrade, K. C., Spoormaker, V. I., Dresler, M., Wehrle, R., Holsboer, F., Samann, P. G., & Czisch, M.(2011). Sleep Spindles and Hippocampal Functional Connectivity in Human NREM Sleep. *Journal of Neuroscience*, *31* (28), 10331–10339.

Andrillon, T., Nir, Y., Staba, R. J., Ferrarelli, F., Cirelli, C., Tononi, G., & Fried, I.(2011). Sleep Spindles in Humans: Insights from Intracranial EEG and Unit Recordings. *Journal of Neuroscience*, *31* (49), 17821-17834.

Attwell, D., & Iadecola, C. (2002). The neural basis of functional brain imaging signals. *Trends in Neurosciences*, *25* (12), 621–625.

Banerjee, O., El Ghaoui, L., & d'Aspremont, A. (2008). Model Selection Through Sparse Maximum Likelihood Estimation for Multivariate Gaussian or Binary Data. *Journal of Machine Learning Research*, *9*, 485–516.

Basner, M., Griefahn, B., & Penzel, T. (2008). Inter-rater agreement in sleep stage classification between centers with different backgrounds. *Somnologie-Schlafforschung und Schlafmedizin*, *12* (1), 75–84.

Bassett, D. S., Greenfield, D. L., Lindenberg, A. M., Weinberger, D. R., Moore, S. W., & Bullmore, E. T.(2010). Efficient physical embedding of topologically complex information processing networks in brains and computer circuits. *PLoS Computational Biology*, *6* (4), e1000748.

Bassett, D. S., Wymbs, N. F., Porter, M. A., Mucha, P. J., Carlson, J. M., & Grafton, S. T.(2011). Dynamic reconfiguration of human brain networks during learning. *Proceedings of the National Academy of Sciences USA*, *108* (18), 7641–7646.

Biswal, B., Yetkin, F. Z., Haughton, V. M., & Hyde, J. S. (1995). Functional connectivity in the motor cortex of resting human brain using echo-planar MRI. *Magnetic Resonance in Medicine*, *34* (4), 537–541.

Blondel, V. D., Guillaume, J. L., Lambiotte, R., & Lefebvre, E. (2008). Fast unfolding of communities in large networks. *Journal of Statistical Mechanics: Theory and Experiment*, *2008* (10), P10008.

Blumenfeld, H. (2012). Impaired consciousness in epilepsy. *Lancet Neurology*, *11* (9), 814–826.

Brandes, U., Delling, D., Gaertler, M., Gorke, R., Hoefer, M., Nikoloski, Z., & Wagner, D. (2008). On Modularity Clustering. *IEEE Transactions on Knowledge and Data Engineering*, *20* (2), 172–188.

Bruno, J. L., Hosseini, S. M. H., Saggar, M., Quintin, E., Raman, M. M., & Reiss, A. L. (2017). Altered Brain Network Segregation in Fragile X Syndrome Revealed by Structural Connectomics. *Cerebral Cortex*, *27* (3), 2249–2259.

Brunton, B. W., Johnson, L. A., Ojemann, J. G., & Kutz, J. N.(2016). Extracting spatial–temporal coherent patterns in large-scale neural recordings using dynamic mode decomposition. *Journal of Neuroscience Methods*, *258*, 1–15.

Burns, S. P., Santaniello, S., Yaffe, R. B., Jouny, C. C., Crone, N. E., Bergey, G. K., Anderson, W. S. & Sarma, S. V.(2014). Network dynamics of the brain and influence of the epileptic seizure onset zone. *Proceedings of the National Academy of Sciences USA*, *111* (49), E5321–E5330.

Chandrasekaran, V., Parrilo, P. A., & Willsky, A. S.(2012). Latent Variable Graphical Model Selection via Convex Optimization. *The Annals of Statistics*, *40* (4), 1935–1967.

Chu, C. J., Tanaka, N., Diaz, J., Edlow, B. L., Wu, O., Hamalainen, M., Stufflebeam, S., Cash, S. S. & Kramer, M. A.(2015). EEG functional connectivity is partially predicted by underlying white matter connectivity. *NeuroImage*, *108*, 23–33.

Cimenser, A., Purdon, P. L., Pierce, E. T., Walsh, J. L., Salazar-Gomez, A. F., Harrell, P. G., Tavares-Stoeckel, C., Habeeb, K., & Brown, E. N.(2011). Tracking brain states under general anesthesia by using global coherence analysis. *Proceedings of the National Academy of Sciences USA*, *108* (21), 8832–8837.

Cole, M. W., Bassett, D. S., Power, J. D., Braver, T. S., & Petersen, S. E.(2014). Intrinsic and Task-Evoked Network Architectures of the Human Brain. *Neuron*, *83* (1), 238–251.

Cordes, D., Haughton, V. M., Arfanakis, K., Wendt, G. J., Turski, P. A., Moritz, C. H., Quigley, M. A., & Meyerand, M. E. (2000). Mapping functionally related regions of brain with functional connectivity MR imaging. *American Journal of Neuroradiology*, *21* (9), 1636–1644.

Danker-hopfe, H., Anderer, P., Zeitlhofer, J., Boeck, M., Dorn, H., Gruber, G., Heller, E., Loretz, E., Moser, D., Parapatics, S., & others (2009). Interrater reliability for sleep scoring according to the Rechtschaffen & Kales and the new AASM standard. *Journal of Sleep Research*, *18* (1), 74–84.

Das, A., Sampson, A. L., Lainscsek, C., Muller, L., Lin, W., Doyle, J. C., Cash, S. S., Halgren, E., & Sejnowski, T. J. (2017). Interpretation of the Precision Matrix and Its Application in Estimating Sparse Brain Connectivity during Sleep Spindles from Human Electrocorticography Recordings . *Neural Computation*, *29* (3), 603–642.

Dempster, A. P. (1972). Covariance Selection. *Biometrics*, *28* (1), 157–175.

Diessen, E. V., Diederen, S. J. H., Braun, K. P. J., Jansen, F. E., & Stam, C. J. (2013). Functional and structural brain networks in epilepsy: What have we learned? *Epilepsia*, *54* (11), 1855–1865.

Ferrarelli, F., Huber, R., Peterson, M. J., Massimini, M., Murphy, M., Riedner, B. A., Watson, A., Bria, P., & Tononi, G. (2007). Reduced sleep spindle activity in schizophrenia patients. *The American Journal of Psychiatry*, *164* (3), 483–492.

Fogel, S. M., Nader, R., Cote, K. A., & Smith, C. T. (2007). Sleep Spindles and Learning Potential. *Behavioral Neuroscience*, *121* (1), 1–10.

Fogel, S. M., & Smith, C. T. (2006). Learning-dependent changes in sleep spindles and Stage 2 sleep. *Journal of Sleep Research*, *15* (3), 250–255.

Fox, M. D., Corbetta, M., Snyder, A. Z., Vincent, J. L., & Raichle, M. E.(2006). Spontaneous neuronal activity distinguishes human dorsal and ventral attention systems. *Proceedings of the National Academy of Sciences USA*, *26* (103), 10046–10051.

Fox, M. D., Snyder, A. Z., Vincent, J. L., Corbetta, M., Van Essen, D. C., & Raichle, M. E.(2005). The human brain is intrinsically organized into dynamic, anticorrelated functional networks. *Proceedings of the National Academy of Sciences USA*, *102* (27), 9673–9678.

Friedman, J., Hastie, T., & Tibshirani, R. (2008). Sparse inverse covariance estimation with the graphical lasso. *Biostatistics*, *9* (3), 432–441.

Gais, S., & Born, J. (2004). Declarative memory consolidation: Mechanisms acting during human sleep. *Learning & Memory*, *11* (6), 679–685.

Gais, S., Mölle, M., Helms, K., & Born, J. (2002). Learning-Dependent Increases in Sleep Spindle Density. *Journal of Neuroscience*, *22* (15), 6830–6834.

Giorge, F. S., Pizzanelli, C., Biagioni, F., Murri, L. & Fornia, F. (2004). The role of norepinephrine in epilepsy: from the bench to the bedside. *Neuroscience and Biobehavioral Reviews*, *28* (5), 507–524.

Glasser, M. F., Coalson, T. S., Robinson, E. C., Hacker, C. D. Harwell, J., Yacoub, E., Ugurbil, K., Andersson, J., Beckmann, C. F., Jenkinson, M., Smith, S. M., & Van Essen, D. C. (2016). A multi-modal parcellation of human cerebral cortex. *Nature*.

Greicius, M. D., Krasnow, B., Reiss, A. L., & Menon, V. (2003). Functional connectivity in the resting brain: a network analysis of the default mode hypothesis. *Proceedings of the National Academy of Sciences USA*, *1* (100), 253–258.

Hampson, M., Peterson, B. S., Skudlarski, P., Gatenby, J. C., & Gore, J. C. (2002). Detection of functional connectivity using temporal correlations in MR images. *Human Brain Mapping*, *15* (4), 247–262.

Honey, C. J., Sporns, O., Cammoun, L., Gigandet, X., Thiran, J. P., Meuli, R. & Hagmann, P. (2009). Predicting human resting-state functional connectivity from structural connectivity. *Proceedings of the National Academy of Sciences USA*, *106* (6), 2035–2040.

Hsieh, C. J., Sustik, M. A., Dhillon, I. S., & Ravikumar, P. (2011). Sparse Inverse Covariance Matrix Estimation Using Quadratic Approximation. *Advances in Neural Information Processing Systems*, 2330–2338.

Hsieh, C. J., Sustik, M. A., Dhillon, I. S., Ravikumar, P., & Poldrack, R. (2013). BIG & QUIC: Sparse Inverse Covariance Estimation for a Million Variables. *Advances in Neural Information Processing Systems*, 3165–3173.

Iber, C. (2007). The AASM manual for the scoring of sleep and associated events: rules, terminology and technical specifications. *American Academy of Sleep Medicine*.

Joyce, K. E., Laurienti, P. J., Burdette, J. H., & Hayasaka, S. (2010). A New Measure of Centrality for Brain Networks. *Plos One*, *5* (8), e12200.

Kohavi, R. (1995). A Study of Cross-Validation and Bootstrap for Accuracy Estimation and Model Selection. *Proceedings of the 14th international joint conference on Artificial Intelligence*, *2*, 1137–1143.

Kramer, M. A., Eden, U. T., Kolaczyk, E. D., Zepeda, R., Eskandar, E. N., & Cash, S. S. (2010). Coalescence and Fragmentation of Cortical Networks during Focal Seizures. *Journal of Neuroscience*, *30* (30), 10076–10085.

Kramer, M. A., & Cash, S. S. (2012). Epilepsy as a Disorder of Cortical Network Organization. *The Neuroscientist*, *18* (4), 360–372.

Kremliovsky, M. N., & Kadtke, J. B. (1997). Using delay differential equations as dynamical classifiers. *Applied nonlinear dynamics and stochastic systems near the millenium*, *411* (1), 57–62.

Kuhnert, M., Elger, C. E., & Lehnertz, K. (2010). Long-term variability of global statistical properties of epileptic brain networks. *Nature Neuroscience*, *20*, 043126.

Krimer, L. S., Muly, E. C. 3rd, Williams, G. V., & Goldman-Rakic, P. S. (1998). Dopaminergic regulation of cerebral cortical microcirculation. *Nature Neuroscience*, *1* (4), 286–289.

Lado, F. A., & Moshe, S. L. (2008). How do seizures stop? *Epilepsia*, *49* (10), 1651–1664.

Lainscsek, C., Hernandez, M. E., Weyhenmeyer, J., Sejnowski, T. J., & Poizner, H. (2013). Nonlinear dynamical analysis of EEG time series distinguishes patients with Parkinsons disease from healthy individuals. *Frontiers in Neurology*, *4*.

Lainscsek, C., & Sejnowski, T. J.(2015). Delay differential analysis of time series. *Neural Computation*, 615–627.

Lainscsek, C., Weyhenmeyer, J., Hernandez, M. E., Poizner, H., & Sejnowski, T. J.(2013). Nonlinear dynamical classification of short time series of the Rössler system in high noise regimes. *Frontiers in Neurology*, *4*, 182.

Larson-Prior, L. J., Zempel, J. M., Nolan, T. S., Prior, F. W., Snyder, A. Z., & Raichle, M. E. (2009). Cortical Network Functional Connectivity in the Descent to Sleep. *Proceedings of the National Academy of Sciences USA*, *1* (106), 4489–4494.

Laughlin, S. B., & Sejnowski, T. J. (2003). Communication in Neuronal Networks. *Science*, *301* (5641), 1870–1874.

Lauritzen, S. L. (1996). Graphical Models. *Oxford University Press*.

Lohmann, G., Margulies, D. S., Horstmann, A., Pleger, B., Lepsien, J., Goldhahn, D., Schloegl, H., Stumvoll, M., Villringer, A., & Turner, R. (2010). Eigenvector Centrality Mapping for Analyzing Connectivity Patterns in fMRI Data of the Human Brain. *Plos One*, *5* (4), e10232.

Lynall, M., Bassett, D.S., Kerwin, R., McKenna, P. J., Kitzbichler, M., Muller, U., & Bullmore, E. (2010). Functional Connectivity and Brain Networks in Schizophrenia. *The Journal of Neuroscience*, *30* (28), 9477–9487.

Ma, S., Xue, L., & Zou, H. (2013). Alternating Direction Methods for Latent Variable Gaussian Graphical Model Selection. *Neural Computation*, *25* (8), 2172–2198.

MacKay, D. J. C. (2002). Information Theory, Inference & Learning Algorithms. *Cambridge University Press*.

Marrelec, G., Horwitz, B., Kim, J., Pelegrini-Issac, M., Benali, H. & Doyon, J. (2007). Using partial correlation to enhance structural equation modeling of functional MRI data. *Magnetic Resonance Imaging*, *25* (8), 1181–1189.

Marshall, L., & Born, J. (2007). The contribution of sleep to hippocampus-dependent memory consolidation. *Trends in Cognitive Sciences*, *11* (10), 442–450.

Meier-Koll, A., Bussmann, B., Schmidt, C., & Neuschwander, D. (1999). Walking through a maze alters the architecture of sleep. *Perceptual and Motor Skills*, *88* (3), 1141–1159.

Meunier, D., Lambiotte, R., & Bullmore, E. T.(2010). Modular and hierarchically modular organization of brain networks. *Frontiers in Neuroscience*, *4* (200).

Miletics, E., & Molnárka, G. (2005). Implicit extension of Taylor series method with numerical derivatives for initial value problems. *Computers & Mathematics with Applications*, *50* (7), 1167–1177.

Monti, R. P., Hellyer, P., Sharp, D., Leech, R., Anagnostopoulos, C., & Montana, G. (2014). Estimating time-varying brain connectivity networks from functional MRI time series. *NeuroImage*, *103*, 427–443.

Muller, L., Piantoni, S., Koller, D., Cash, S. S., Halgren, E., & Sejnowski, T. J. (2016). Rotating waves during human sleep spindles organize global patterns of activity that repeat precisely through the night. *eLife*, *5*, e17267.

Newman, M. E. J., & Girvan, M. (2004). Finding and evaluating community structure in networks. *Physical Review E*, *69* (2), 026113.

Newman, M. E. J. (2006). Modularity and community structure in networks. *Proceedings of the National Academy of Sciences USA*, *103* (23), 8577–8582.

Newman, M. E. J. (2010). Networks: An Introduction. *Oxford University Press*.

Nunez, P. L., & Srinivasan, R. (2006). Electric Fields of the Brain: The Neurophysics of EEG. *Oxford University Press*.

Onnela, J. P., Saramaki, J., Kertesz, J., & Kaski, K. (2005). Intensity and coherence of motifs in weighted complex networks. *Physical Review E*, *71* (6), 764–772.

Oztoprak, F., Nocedal, J., Rennie, S., & Olsen, P. A. (2012). Newton-Like Methods for Sparse Inverse Covariance Estimation. *Advances in Neural Information Processing Systems*, 764–772.

Petit, D., Gagnon, J. F., Fantini, M. L., Ferini-Strambi, L., & Montplaisir, J. (2004). Sleep and quantitative EEG in neurodegenerative disorders. *Journal of Psychosomatic Research*, *56* (5), 487–496.

Ponten, S. C., Bartolomei, F., & Stam, C. J. (2007). Small-world networks and epilepsy: Graph theoretical analysis of intracerebrally recorded mesial temporal lobe seizures. *Clinical Neurophysiology*, *118* (4), 918–927.

Reichardt, J., & Bornholdt, S. (2006). Statistical Mechanics of Community Detection. *Physical Review E*, *74* (1), 016110.

Ronhovde, P., & Nussinov, Z. (2009). Multiresolution community detection for megascale networks by information-based replica correlations. *Physical Review E*, *80* (1), 016109.

Rosa, M. J., Portugal, L., Hahn, T., Fallgatter, A. J., Garrido, M. I., Taylor, J. S., & Mourao-Miranda, J.(2015). Sparse network-based models for patient classification using fMRI. *NeuroImage*, *105*, 493–506.

Rothman, A. J., Bickel, P. J., Levina, E., & Zhu, J. (2008). Sparse permutation invariant covariance estimation. *Electronic Journal of Statistics*, *2*, 494–515.

Rozman, P. A. (2015). Multi-Unit Activity in the Human Cortex as a Predictor of Seizure Onset. *Doctoral dissertation, Harvard Medical School*.

Rubinov, M., & Sporns, O. (2010). Complex network measures of brain connectivity: Uses and interpretations. *NeuroImage*, *52* (3), 1059–1069.

Rubinov, M., & Sporns, O.(2011). Weight-conserving characterization of complex functional brain networks. *NeuroImage*, *56* (4), 2068–2079.

Ryali, S., Chen, T., Supekar, K., & Menon, V.(2012). Estimation of functional connectivity in fMRI data using stability selection-based sparse partial correlation with elastic net penalty. *NeuroImage*, *59* (4), 3852–3861.

Salvador, R., Suckling, J., Coleman, M. R., Pickard, J. D., Menon, D., & Bullmore, E. (2005). Neurophysiological Architecture of Functional Magnetic Resonance Images of Human Brain. *Cerebral Cortex*, *15*, 1332–1342.

Sampson, A. L., Lainscsek, C., Cash, S. S., Halgren, E., & Sejnowski, T. J. (2015). Nonlinear Dynamical Sleep Spindle Detection Using Delay Differential Analysis. *Society for Neuroscience*.

Saramaki, J., Kivela, M., Onnela, J. P., Kaski, K., & Kertesz, J. (2007). Generalizations of the clustering coefficient to weighted complex networks. *Physical Review E*, *75* (2), 027105.

Sato, A., & Sato, Y. (1992). Regulation of regional cerebral blood flow by cholinergic fibers originating in the basal forebrain. *Neuroscience Research*, *14* (4), 242–274.

Schabus, M., Gruber, G., Parapatics, S., Sauter, C., Klösch, G., Anderer, P., Klimesch, W., Saletu, B., & Zeitlhofer, J. (2004). Sleep Spindles and Their Significance for Declarative Memory Consolidation. *Sleep*, *27* (8), 1479–1485.

Schindler, K. A., Bialonski, S., Horstmann, M. T., Elger, C. E., & Lehnertz, K. (2008). Evolving functional network properties and synchronizability during human epileptic seizures. *Chaos*, *18* (3), 033119.

Scheinberg, K., Ma, S., & Goldfarb, D. (2010). Sparse Inverse Covariance Selection via Alternating Linearization Methods. *Advances in Neural Information Processing Systems*, 2101–2109.

Sejnowski, T. J. (1995). Neural Networks: Sleep and memory. *Current Biology*, *5* (8), 832–834.

Sejnowski, T. J., & Destexhe, A. (2000). Why do we sleep?. *Brain Research*, *886* (1–2), 208–223.

Shafi, M. M., Westover, M. B., Oberman, L., Cash, S. S., & Pascual-Leone, A. (2014). Modulation of EEG Functional Connectivity Networks in Subjects Undergoing Repetitive Transcranial Magnetic Stimulation. *Brain Topography*, *27* (1), 172–191.

Siegle, G. J., Thompson, W., Carter, C. S., Steinhauer, S. R., & Thase, M. E. (2007). Increased Amygdala and Decreased Dorsolateral Prefrontal BOLD Responses in Unipolar Depression: Related and Independent Features. *Biological Psychiatry*, *61* (2), 198–209.

Smith, C., & Macneill, C. (1994). Impaired motor memory for a pursuit rotor task following Stage 2 sleep loss in college students. *Journal of Sleep Research*, *3* (4), 206–213.

Smith, S. M., Miller, K. L., Salimi-Khorshidi, G., Webster, M., Beckmann, C. F., Nichols, T. E., Ramsey, J. D., & Woolrich, M. W. (2011). Network modelling methods for fMRI. *NeuroImage*, *54* (2), 875–891.

Sojoudi, S., & Doyle, J. (2014). Study of the brain functional network using synthetic data. *Proceedings of the 52nd Annual Allerton Conference on Communication, Control, and Computing*, 350–357.

Sojoudi, S. (2016). Equivalence of Graphical Lasso and Thresholding for Sparse Graphs. *Journal of Machine Learning Research*, *17* (115), 1–21.

Spoormaker, V. I., Schröter, M. S., Gleiser, P. M., Andrade, K. C., Dresler, M., Wehrle, R., Sämann, P. G., & Czisch, M. (2010). Development of a Large-Scale Functional Brain Network during Human Non-Rapid Eye Movement Sleep. *Journal of Neuroscience*, *30* (34), 11379–11387.

Sporns, O. (2010). Brain Connectivity Toolbox. *https://sites.google.com/site/bctnet/visualization*.

Sporns, O.(2011). The Nonrandom Brain: Efficiency, Economy, and Complex Dynamics. *Frontiers in Computational Neuroscience*, *5* (5).

Stam, C. J.(2005). Nonlinear dynamical analysis of EEG and MEG: Review of an emerging field. *Clinical Neurophysiology*, *116* (10), 2266–2301.

Stam, C. J.(2014). Modern network science of neurological disorders. *Nature Reviews Neuroscience*, *15*, 683–695.

Steriade, M., McCormick, D. A., & Sejnowski, T. J. (1993). Thalamocortical oscillations in the sleeping and aroused brain. *Science*, *262* (5134), 679–685.

Stevenson, I. H., Rebesco, J. M., Miller, L. E., & Kording, K. P. (2008). Inferring functional connections between neurons. *Current Opinion in Neurobiology*, *18* (6), 582–588.

Stickgold, R., & Walker, M. P. (2005). Memory consolidation and reconsolidation: what is the role of sleep?. *Trends in Neurosciences*, *28* (8), 408–415.

Stickgold, R., & Walker, M. P. (2007). Sleep-dependent memory consolidation and reconsolidation. *Sleep Medicine*, *8* (4), 331–343.

Sun, Y., Danila, B., Josić, K., & Bassler, K. E. (2009). Improved community structure detection using a modified fine-tuning strategy. *Europhysics Letters*, *86* (2), 28004.

Supekar, K., Menon, V., Rubin, D., Muse, M., & Greicius, M. D. (2008). Network Analysis of Intrinsic Functional Brain Connectivity in Alzheimer's Disease. *PLoS Computational Biology*, *4* (6), e1000100.

Takens, F. (1981). Detecting Strange Attractors in Turbulence. *Lecture Notes in Mathematics*, *898*, 366–381.

Truccolo, W., Donoghue, J. A., Hochberg, L. R., Eskandar, E. N., Madsen, J. R., Anderson, W. S., Brown, E. N., Halgren, E.& Cash, S. S. (2011). Single-neuron dynamics in human focal epilepsy. *Nature Neuroscience*, *14* (5), 635–641.

Uddin, L. Q., Kelly, A. C., Biswal, B. B., Castellanos, F. X., & Milham, M. P. (2009). Functional connectivity of default mode network components: correlation, anticorrelation, and causality. *Human Brain Mapping*, *30* (2), 625–637.

Varoquaux, G., Gramfort, A., Jean-baptiste, P., & Thirion, B.(2010). Brain covariance selection: better individual functional connectivity models using population prior. *Advances in Neural Information Processing Systems*, 2334–2342.

Varsavsky, A., Mareels, I., & Cook, M.(2010). Epileptic Seizures and the EEG: Measurement, Models, Detection and Prediction. *CRC Press; 1 edition*.

Vega-Zelaya, L., Pastor, J., de Sola, R. G., & Ortega, G. J.(2015). Disrupted Ipsilateral Network Connectivity in Temporal Lobe Epilepsy. *Plos One*, *10* (10), e0140859.

Vertes, P. E., Alexander-Bloch, A. F., Gogtay, N., Giedd, J. N., Rapoport, J. L., & Bullmore, E. T. (2012). Simple models of human brain functional networks. *Proceedings of the National Academy of Sciences*, *109* (15), 5868–5873.

Volterra, V.(1887). Sopra le funzioni che dipendono da altre funzioni. *Atti della Reale Accademia dei Lincei*, *3*,97–105.

Volterra, V.(1959). Theory of functionals and of integral and integro-differential equations. *Dover Publications, Inc.*.

Walker, M. P., Brakefield, T., Morgan, A., Hobson, J. A., & Stickgold, R. (2002). Practice with Sleep Makes Perfect: Sleep-Dependent Motor Skill Learning. *Neuron*, *35* (1), 205–211.

Wang, Y., Kang, J., Kemmer, P. B., & Guo, Y. (2016). An Efficient and Reliable Statistical Method for Estimating Functional Connectivity in Large Scale Brain Networks Using Partial Correlation. *Frontiers in Neuroscience*, *10* (123).

Wang, Y., Ghumare, E., Vandenberghe, R., & Dupont, P. (2017). Comparison of Different Generalizations of Clustering Coefficient and Local Efficiency for Weighted Undirected Graphs. *Neural Computation*, *29* (2), 313–331.

Warby, S. C., Wendt, S. L., Welinder, P., Munk, E. G. S., Carrillo, O., Sorensen, H. B. D., Jennum, P., Peppard, P. E., Perona, P., & Mignot, E. (2014). Sleep-spindle detection: crowdsourcing and evaluating performance of experts, non-experts and automated methods. *Nature Methods*, *11*, 385–392.

Whittaker, J. (1990). Graphical Models in Applied Multivariate Statistics. *John Wiley and Sons*.

Xiong, J., Parsons, L. M., Gao, J. H., & Fox, P. T. (1999). Interregional connectivity to primary motor cortex revealed using MRI resting state images. *Human Brain Mapping*, *8* (2–3), 151–156.

Yatsenko, D., Josić, K., Ecker, A. S., Froudarakis, E., Cotton, R. J., & Tolias, A. S. (2015). Improved Estimation and Interpretation of Correlations in Neural Circuits. *PLoS Computational Biology*, *11* (3), e1004083.

Yuan, M., & Lin, Y. (2007). Model selection and estimation in the Gaussian graphical model. *Biometrika*, *94* (1), 19–35.

Zhou, D., Thompson, W. K., & Siegle, G. (2009). MATLAB toolbox for functional connectivity. *NeuroImage*, *47* (4), 1590–1607.

Zuo, X. N., Ehmke, R., Mennes, M., Imperati, D., Castellanos, F. X., Sporns, O., & Milham, M. P.(2012). Network centrality in the human functional connectome. *Cerebral Cortex*, *22* (8), 1862–1875.